Exploring the concepts of electrochemical blocking for single entity detection

Zejun Deng

INSTITUT POLYTECHNIQUE DE PARIS

ÉCOLE POLYTECHNIQUE

IP PARIS

NNT : 2020IPPAX059

Thèse de doctorat

Exploring the concepts of electrochemical blocking for single entity detection

Thèse de doctorat de l'Institut Polytechnique de Paris
préparée à École Polytechnique

École doctorale n°626 Ecole Doctorale de l'Institut Polytechnique de Paris (ED IP Paris)
Spécialité de doctorat: Chimie

Thèse présentée et soutenue à Palaiseau, le 18/09/2020, par

M. Zejun DENG

Composition du Jury :

M. Jean-Christophe Lacroix Professeur, ITODYS Université de Paris	Président
M. Frédéric Kanoufi Directeur de Recherche, ITODYS Université Paris Diderot	Rapporteur
M. Emmanuel Maisonhaute Professeur, Université Pierre et Marie Curie (UMR 8235)	Rapporteur
Mme. Kristina Tschulik Prof. Dr. rer. nat., Ruhr-University Bochum	Examinateur
Mme. Estelle Lebègue Maitre de conférence, CEISAM Université de Nantes (UMR 6230)	Examinateur
M. Fouad Maroun Directeur de Recherche, LPMC École Polytechnique	Directeur de thèse
M. Christophe Renault Chargé de Recherche, LPMC École Polytechnique	Co-Directeur de thèse

Acknowledgements

Working in the lab of PMC as a Ph.D. student would definitely be a precious and memorable experience in my life. I would like to express sincere thankfulness, warmth and appreciation to everyone who made my research successful and assisted me at every point to achieve my goal:

First, I would like to express my sincere gratitude to Fouad Maroun, my supervisor, for his vital support and assistance. I appreciate that he always gives me insightful comments and suggestions, no matter in instrumental training, experimental ideas, the analysis of experimental data, or in the process of thesis writing, etc. Besides, his serious attitude towards scientific research will benefit me throughout my life. I would also like to express my deepest appreciation to Christophe Renault, my principle supervisor, for his continuous support and warm encouragement during work and study. He shows great patience to guide me how to perform experiments and simulations, process and present the data scientifically, and teach me the experimental principle as well as fruitful writing skills. I really enjoy every discussion with him; whenever I feel confused, he always gives me very helpful guidance and constructive suggestions. In brief, without their guidance, persistent help and encouragement, this dissertation would not have been possible.

Then, I would like to express my gratitude to Mathis Plapp, the director of the lab, who is always keeping enthusiastic about making PMC become a better place to work and study. Moreover, sincere thanks for acting as my rental guarantor; otherwise, I might have nowhere to live in.

My gratitude also goes to Poggi Mélanie for her help in the SEM training, and to Denis Coupvent-Desgraviers for his help in computer-related technical details.

I would like to say special thanks to Anne-Marie Dujardin for her help in many ways, no matter in administrative matters or on daily issues.

Special thanks also go to China Scholarship Council that funds me to carry out my Ph.D. studies.

I appreciate many others from the group of “electrochemistry and thin films”: Allongue Philippe, Anne Chantal Gouget-Laemmel, Catherine Henry de Villeneuve, Moraillon Anne, François Ozanam, Michel Rosso, Cassiana Andrei, Mathilde Bouvier, Alexandre Da Silva, Yue Feng, Weichu Fu, Ivan Pacheco and Hyeonseok Sim, for their fruitful help and discussions during the past three years. I will keep remembering every moment of joy and happiness.

I also appreciate many others from the lab (I will try to make it in the alphabetical order): Alistair Rowe, André Wack, Alla Gilles, André Blandine, Alireza Kazemi, Bernard Sapoval, Capucine Cleret de Langavant, Claude-Alban Ranély Vergé Depré, Claude Weisbuch, Denis Grebenkov, Debacker Sophie, Daniel Paget, Debacker Sophie, Elodie Chaudan, Fausto Sirotti, Fabian Cadiz, Hervé Henry, Isabelle MAURIN, Jeongmo Kim, Jongwook Kim, Jean-Marie Lentali, Jacques Peretti, Louis-Joseph Alain, Larquet Eric, Lenoir Didier, Lahlil Khalid, Marcel Filoche, Maron Sébastien, Mohammedi Rabei, Nicolas Moutal, Perceval Desforges, Quillard Elodie, Ranély Vergé Dépré Claude-Alban, Sébastien Maron, Raphaël Zanella, Sylvain Knight, Thierry Gacoin, Tusseau-Nenez Sandrine, Thomas Philippe, Wiebke Hahn, Yves Lassailly, Zijun Wang, for their tremendous help in instrumental training, facilities maintenance, and fruitful discussions during the past three years.

Besides, I would like to express my sincere gratitude to my jury members: Prof. Jean-Christophe Lacroix, Prof. Frédéric Kanoufi and Prof. Emmanuel Maisonhaute, Prof. Dr. rer. nat. Kristina Tschulik,

Dr. Estelle Lebègue, for their insightful comments and suggestions, and also for the fruitful questions which can promote me to think deeply and broaden my horizons. Special thanks for my reporters, Prof. Frédéric Kanoufi and Prof. Emmanuel Maisonhaute, for reviewing this thesis manuscript during such a difficult coronavirus period. I would also like to show my most sincere appreciation to Prof. Frédéric Kanoufi, who acts as my reference to support my application for a postdoctoral position.

Finally, I would like to acknowledge my parents for the endless support during these years, and my beloved fiancée Juan Tang for always being by my side and inspiring me to do better. Without their support and encouragement, any of my successes would not have been possible.

Abstract

This dissertation is dedicated to exploring the concepts of electrochemical blocking for single entity detection. Electrochemical blocking is a type of single-entity electrochemical measurement particularly well adapted to the detection of insulating entities, including artificial entities like polymer particles or bioparticles like proteins and bacteria. The size of these entities spans between few nm to several microns, and their electronic structure covers the entire spectrum from insulator to semiconductor and metallic behavior. Currently, the accurate determination of the size of a particle by electrochemical blocking remains an analytical challenge, owing to the uneven current distribution on disk ultra-microelectrodes UMEs (so-called edge effect). The goal of this dissertation is to develop this elegant and straightforward methodology into a versatile and quantitative analytical tool.

In the first part of this dissertation, we describe the use of hemispherical Hg UME to detect individual insulating particles in order to remove the edge effects on disk UMEs. The use of hemispherical Hg UME enables simultaneous measurements of the size distribution *and* concentration of particles in suspension. Using numerical simulations, we deduce the quantitative relation between the magnitude of the current step and the size of the bead. The frequency of collision measured for a given size of bead is then converted into a concentration (in mol/L) by quantification of the relative contributions of migration and diffusion for each size of the bead. Under our experimental conditions (low concentration of supporting electrolyte), migration dominates the flux of bead. The average size of polystyrene beads of 0.5 and 1 μm radius obtained by electrochemistry and scanning electron microscopy (SEM) differs by only -8% and -9%, respectively. The total concentration of polystyrene beads of 0.5 and 1 μm radius obtained by electrochemistry is found in close agreement (<10% of error) with their nominal concentrations (25 and 100 fM).

In the second part of this dissertation, we extend the reach of electrochemical blocking from detection of individual insulating particles to electrically conducting particles. This method, called “electro-catalytic depression” (ECD), enables the detection of particles that are electronically conducting but catalytically inert, such as carbonaceous particles colliding on precious metal UMEs. The ECD method is based on the difference in heterogeneous kinetics of electron transfer for a given inner-sphere reaction to block the current at the surface of a particle made of a material having poor catalytic properties compared to the material of the electrode. We apply this method to detect individual graphene nanoplatelets (GNPs) of few μm long and 15 nm thick. GNPs block the oxidation of hydrazine on a 5 μm radius Pt UME. We studied the influence of the potential on the observed current response for individual GNP detection. We evidence that, at low bias potentials (≤ 0.1 V), an electronically conducting GNP produces a discrete stair-shaped decrease of current (negative steps) similar to the signal obtained with insulating particles like polystyrene beads. We show how the analysis of a “blocking-type” signal originally developed for insulating beads can be extended to the detection of conducting particles. At high potentials (> 0.1 V), where hydrazine oxidation occurs on the GNP, the kinetic difference between GNP and Pt decreases, leading to the decrease of both average and median current step size.

The last part is the understanding of complex current responses of individual GNP collisions by correlated opto-electrochemical measurements. We found the collision behaviors of a 2D object with the UME surface are not always a simple collision event (i.e., adsorption or desorption). We evidence that a simple current spike is attributed to the bouncing of GNP at the electrode surface. Complex current responses can be divided into a couple of signal intervals. During the initial landing process, the

capacitive charge is not the only factor contributing to the rapid current increase. Once the GNP touches the surface of Pt, transient current responses come from the instantaneous increase in the electroactive surface area of GNP. Importantly, the rotation of GNP will cause changes in current transients. The increased steady-state current plateau is attributed to permanent adsorption of GNPs at the perimeter of the surface of Pt, resulting from the increase in the total effective electroactive surface.

Keywords: single entity electrochemistry, electrochemical blocking, electrocatalytic amplification, electro-catalytic depression, opto-electrochemical measurement, nano-electrochemistry, graphene nanoplatelet, ultra-microelectrode

Résumé

Cette thèse est consacrée à l'exploration des concepts de blocage électrochimique pour la détection d'une seule entité. Le blocage électrochimique est un type de mesure électrochimique mono-entité particulièrement bien adapté à la détection d'entités isolantes, notamment des entités artificielles comme des particules de polymère ou des bioparticules comme des protéines et des bactéries. La taille de ces entités s'étend de quelques nm à plusieurs microns, et leur structure électronique couvre tout le spectre de l'isolant au semi-conducteur et au comportement métallique. Actuellement, la détermination précise de la taille d'une particule par blocage électrochimique reste un défi analytique, en raison de la répartition inégale du courant sur les ultra-microélectrodes disques UME (effet dit de bord). Le but de cette thèse est de développer cette méthodologie élégante et simple en un outil analytique polyvalent et quantitatif.

Tout d'abord, nous décrivons l'utilisation de Hg UME hémisphérique pour détecter des particules isolantes individuelles afin d'éliminer les effets de bord sur les UME de disque. L'utilisation de Hg UME hémisphérique permet des mesures simultanées de la distribution granulométrique et de la concentration des particules en suspension. À l'aide de simulations numériques, nous en déduisons la relation quantitative entre la magnitude du pas courant et la taille du cordon. La fréquence de collision mesurée pour une taille de bille donnée est ensuite convertie en concentration (en mol/L) par quantification des contributions relatives de migration et de diffusion pour chaque taille de bille. Dans nos conditions expérimentales (faible concentration d'électrolyte de support), la migration domine le flux de bille. La taille moyenne des billes de polystyrène de 0.5 et 1.0 µm de rayon obtenues par électrochimie et microscopie électronique à balayage (MEB) ne diffère que de -8% et -9%, respectivement. La concentration totale de billes de polystyrène de 0.5 et 1.0 µm de rayon obtenue par électrochimie se trouve en étroite concordance (< 10% d'erreur) avec leurs concentrations nominales (25 et 100 fM).

En outre, nous étendons la portée du blocage électrochimique de la détection de particules isolantes individuelles aux particules électriquement conductrices. Cette méthode, appelée "dépression électro-catalytique" (ECD), permet la détection de particules conductrices électroniquement mais catalytiquement inertes, telles que des particules carbonées entrant en collision avec des UME de métaux précieux. La méthode ECD est basée sur la différence de cinétique hétérogène de transfert d'électrons pour une réaction de sphère interne donnée pour bloquer le courant à la surface d'une particule constituée d'un matériau ayant de mauvaises propriétés catalytiques par rapport au matériau de l'électrode. Nous appliquons cette méthode pour détecter des nanoplaquettes de graphène (GNP) individuelles de quelques µm de long et 15 nm d'épaisseur. Les GNPs bloquent l'oxydation de l'hydrazine sur un rayon Pt UME de 5 µm. Nous avons étudié l'influence du potentiel sur la réponse actuelle observée pour la détection individuelle du PNB. Nous prouvons que, à des potentiels de polarisation faibles (≤ 0.1 V), un GNP électroniquement conducteur produit une diminution discrète en forme d'escalier du courant (étapes négatives) similaire au signal obtenu avec des particules isolantes comme des billes de polystyrène. Nous montrons comment l'analyse d'un signal "de type blocage" développé à l'origine pour les billes isolantes peut être étendue à la détection de particules conductrices. À des potentiels élevés (> 0.1 V), où l'oxydation de l'hydrazine se produit sur le GNP, la différence cinétique entre le GNP et le Pt diminue, conduisant à la diminution de la taille moyenne et médiane des pas de courant.

La dernière partie est la compréhension des réponses actuelles complexes des collisions GNPs individuelles par des mesures opto-électrochimiques corrélées. Nous avons constaté que les comportements de collision d'un objet 2D avec la surface UME ne sont pas toujours un simple événement de collision (c'est-à-dire, adsorption ou désorption). Nous prouvons qu'un simple pic de

courant est attribué au rebond du GNP à la surface de l'électrode. Les réponses de courant complexes peuvent être divisées en deux intervalles de signal. Pendant le processus d'atterrissage initial, la charge capacitive n'est pas le seul facteur contribuant à l'augmentation rapide du courant. Une fois que le GNP touche la surface de Pt, les réponses de courant transitoire proviennent de l'augmentation instantanée de la surface électroactive du GNP. Surtout, la rotation du GNP entraînera des changements dans les transitoires de courant. L'augmentation du plateau de courant en régime permanent est attribuée à l'adsorption permanente de GNP au périmètre de la surface de Pt, résultant de l'augmentation de la surface électroactive effective totale.

Mots clés: électrochimie mono-entité, blocage électrochimique, amplification électrocatalytique, dépression électro-catalytique, mesure opto-électrochimique, nano-électrochimie, nanoplaquette de graphène, ultra-microélectrode

Table of Contents

Lists of Acronyms and Symbols

Acronyms	Definition
Ag NP(s)	Silver Nanoparticle(s)
Au NP(s)	Gold Nanoparticle(s)
AFM	Atomic force microscope
CV	Cyclic voltammogram
DLS	Dynamic light scattering
DI water	Distilled water
ECA	Electrocatalytic amplification
ECD	Electrocatalytic depression
FcMeOH	Ferrocenemethanol
FcDM	Ferrocenedimethanol
HOPG	Highly oriented pyrolytic graphite
HER	Hydrogen evolution reaction
i-t	Current-time
GNP(s)	Graphene nanoplatelet(s)
NTA	Nanoparticle tracking analysis
OCP	Open circuit potential
ORR	Oxygen reduction reaction
PSB	Polystyrene bead
PZC	Point of zero charge
Pt NP(s)	Platinum nanoparticle(s)
r-GO	Reduced graphene oxide
SAM	Self-assembly monolayer
SEE	Single entity electrochemistry
SEM	Scanning electron microscopy
SECM	Scanning electrochemical microscopy
SECCM	Scanning electrochemical cell microscopy
SWCNT	Single-wall carbon nanotube
TiO_2	Titanium dioxide film

TEM	Transmission electron microscopy
TFA	Time of first arrival
UME	Ultramicroelectrode
WE	The working electrode

Symbols	Unit	Definition
α	1	The coefficient of charge transfer
C^*	mol L^{-1}	The concentration of bulk solution
C_i	mol L^{-1}	The concentration of species *i*
C	pF	The total interfacial capacitance
D_i	cm^2 s^{-1}	The diffusion coefficient of species *i*
E	V	The applied potential
E_0	V	The formal potential
e	C	The elementary charge
ε_r	1	Relative permittivity
ε_0	C V^{-1} m^{-1}	Vacuum permittivity
F	C mol^{-1}	The Faraday's constant
f_{bead}	Hz	The overall collision frequency of the bead
f_{bead}^{mig}	Hz	The frequency of collision of the bead by migration
f_{bead}^{diff}	Hz	The frequency of collision of the bead by diffusion
i_p	nA	The peak current
i_{ss}	nA	Steady-state current at a mass-transfer limit
j_{bead}	mol m^{-2} s^{-1}	The flux of bead
k_0	cm s^{-1}	The standard rate constant
k	J K^{-1}	The Boltzman constant
M_r	g mol^{-1}	The molar mass
n	1	The number of electron transfer per molecule
N_a	mol^{-1}	The Avogadro's constant
Q	C	The amount of charge
r_{np}	cm	the radius of the nanoparticle
r_e, r_{elec}	cm	The radius of the electrode
r_{bead}	cm	The radius of the bead
r_h	cm	The hydrodynamic radius of molecules
R	kg m^2 K^{-1} mol^{-1} s^{-2}	The gas constant
R_L	Ω	The resistance of solution
T	K	The absolute temperature

V_i	m^{-3}	The volume of species *i*
z_{bead}	C	The amount of charge of the bead
ρ	g cm^{-3}	The density of the particle
	Ω cm	The solution resistivity
μ_i	m^2 V^{-1} s^{-1}	The mobility of species *i*
σ_{bead}	C m^{-2}	The charge density of the bead
η	Pa s	The dynamic viscosity of the solvent
ξ	mV	Zeta potential

1. Chapter 1 Introduction

Single Entity Electrochemistry, abbreviated as SEE, refers to the study of a single entity, one at a time, using electrochemical methodologies. The term "entity" encompasses a large variety of objects like proteins, molecules, nanoparticles, blood cells, emulsion droplets, vesicles, microbeads – literally anything that can represent a unit of interest.[1] The name "SEE" finds its origin in a Faraday discussion held in the University of York, in early September 2016.[2] During that discussion, scientists from different branches of analytical chemistry and electrochemistry gathered to discuss and explore electrochemical studies of single entities. The theme of that meeting expanded around SEE of interest, including issues of single objects at nanometer-sized scale (e.g., nanoparticles, nanowires), confined techniques at the nanoscale (e.g., nanopores, nanofluidic device), complex reactions at the nanoscale, and molecular analysis at the single-molecule level.

The study of individual entities presents an interest in both fundamental and applied fields. In the field of the food industry, entities, such as titanium dioxide, silica, artificial nanoliposomes, vesicles, are widely used as food additives and packaging materials.[3] In the field of catalysis and energy, nanomaterials (e.g., nanoparticles and nanotubes) are playing a critical role in the conversion and storage of energy due to their high specific surface area, adjustable physicochemical properties (e.g., size-dependent and surface-dependent properties).[4-5] Organic nanoparticles, having the diversity of molecular structures and capabilities of compounding with other materials, have become increasingly prominent in applications of biopharmaceutical and bioimaging fields.[6-7] More importantly, natural nanoparticles, such as proteins, vesicles and viruses, play an indispensable role in the metabolism of life as well as the physiological and pathological processes.[8-9] The properties of single entities are closely related to their morphology, size, charge density and surface-chemical properties. Therefore, it is of great significance to develop the methods of single entity detection and analysis for understanding the relationship between structure and function.

1.1 Overview of single entity electrochemistry

1.1.1 Why do we strive to develop single entity measurements via electrochemistry?

To answer this question, I will split it into two separate questions. First, why do we need to observe single entities? Second, why use electrochemistry to conduct single entity measurements?

Why do we need to study single entities? In traditional ensemble-based studies, the activity is measured by averaging the responses of millions or billions of individual entities. The chemical and physical properties of individual entities are prone to be hindered among ensemble studies because a real system is usually heterogeneous. This point is elegantly illustrated by the following analogy (source from Dr. Jeffery E. Dick): "Image a scenario, you have never heard of fireflies. If one places millions or billions of fireflies in a large jar and then asks another person to study the light intensity given off by these fireflies. After observing the jar for a few minutes in the dark, the observer can find that the light intensity coming out of the jar does not vary significantly with time, but scales linearly with the number of fireflies in the jar. Based on visual observation, one can reach a rough conclusion that fireflies continuously light due to bioluminescence. This is not the negligence of the observer since the observer does not study one firefly at a time. What is the possibility for these fireflies will blink on and off at the same time? Nearly zero. Later, scientists experimentally confirmed that the fluorescence of single proteins is not continuous." Thus, the study of a single entity (like a firefly, single nanoparticle or

molecule) allows studying variation in populations. Note that these variations may be temporal (like the firefly) but also caused by heterogeneities in local environments or even internal variations between entities (that is an entity does not look exactly the same as another).

More importantly, from an analytical standpoint, single entity detection offers access to the ultimate sensitivity in analytical science, that is, a limit of detection of one entity at a time. Early detection of very dilute species for disease diagnosis helps to improve patient outcomes and potentially predict or even eradicate the progression of the disease. For example, the detection of a circulating tumor cell at the sub-femtomolar level ($\leq 10^{-15}$ M) in the blood is made possible by the technique of single entity detection.[10-11]

Finally, the observation of one entity at a time can considerably simplify the comprehension of a system where (multiple) coupling(s) between a large number of entities affects the overall response. For example, the current response of composite electrodes made of nanoparticles assembled by compaction or using binders may depend on a large extent of the assembly of particles and not the internal structure of these latter.

Why use electrochemistry? Currently, common technologies used for particle detection mainly include electron microscope technology and spectroscopic techniques. For the former, two types of microscopes, scanning electron microscope and transmission electron microscope, are widely used to observe the morphology of particles and explore their structural information. However, such methods are still very difficult to be directly used for real-time detection of single particles in solution to acquire abundant information. As for the technology of dynamic light scattering technology (DLS), in principle, it can be used for real-time in-situ detection of particles in a solution ranging from few nm to several μm. However, it still provides the statistical results of the particles in the entire system, which can easily mask the fundamental properties of individual entities. The presence of large agglomerated particles or impurities in the system will interfere with the detection results. More importantly, it is generally more complex to obtain the concentration of particles in solution.[12-13] Among those rare analytical tools that can accurately measure particle size and concentration, one can find the method of single nanoparticle tracking analysis (NTA). NTA tracks the scattering signal of individual particles to reconstruct trajectories and count them in a fast and accurate manner.[14] However, the cost, size and fragility of this equipment limit its use in large facilities.

Single entity electrochemistry measurement is usually performed at small-sized electrodes (e.g., ultramicroelectrodes, nanoelectrodes and nanopore-based electrodes), and the background current noise is extremely low (down to few picoamperes or even below). Thanks to the instrumental and methodological developments, a low-noise electrochemical potentiostat, with the high temporal and current resolution, allows rapid and sensitive measurements at the level of a single entity, one at a time. SEE is considered as one of the most sensitive and desirable measurements in analytical science. The limit of quantitation of the analytes can be traced down to ranges of picomolar, femto- and even attomolar concentrations.[15] SEE is also a label-free, high-throughput and low-cost technique for the detection of entities. Besides, SEE can probe intrinsic electrochemical activities of analytes at the individual entity level with the help of other technologies (i.e., optical microscopes and scanning probe-based microscopes). Therefore, electrochemists and analytical scientists are striving to develop and explore the field of SEE and its applications over the past decades.

1.1.2 What entities were studied?

SEE is pushing electro-analytical chemistry to a digital era that allows the study of a single entity one at a time. A single entity can be anything, such as individual nanoparticles,[16-17] molecules,[18] emulsion droplets,[19-20] vesicle,[21-22] micelles,[23] proteins,[24] and bacteria,[25] etc. From the view of sizing determination, SEE can measure entities on a scale of 100 microns to nanometers and even angstroms. Detection of sub-nanometer sized molecules (e.g., single-stranded DNA) is usually performed using biological nanopores with a diameter of less than 1 nm (e.g., aerolysin[26-27]) based on the resistive

sensing. In order to focus on the main issues in this dissertation, a wealth of work about nanopore-based studies including solid-state nanopore (e.g., nanopipette,[28-30] SiN_x,[31-32] nanotubes,[33-34] and graphene[35]), and biological nanopores (e.g., α-hemolysin,[36-37], phi29 motor[38-39] and aerolysin[40-41]) is not included in this table, and one can refer to the mentioned representative works or reviews.[42-43]

Table 1.1 lists various types of entities detected on ultramicroelectrodes or nanoelectrodes, including atoms, metal nanoparticles (e.g., Pt, Au, Ag, Cu), metal oxides (e.g., Fe_3O_4, TiO_2, ZnO), bioparticles (e.g., DNA, molecules, virus, enzymes, cells), soft particles (e.g., emulsion droplets, liposomes, micelles), carbonaceous particles (e.g., carbon nanotubes (CNT), graphene, graphene nanoplatelets), as well as other hard particles like polystyrene beads and silica beads, etc. These entities are electrochemically detected on ultra-microelectrodes and nanoelectrodes. There are several reviews to introduce a variety of single entities from different viewpoints. The general perspectives and prospectus on SEE can refer to recent reviews by Bard *et al.*,[44] Crooks *et al.*,[2] Tao *et al.*,[45] Baker *et al.*,[1] Lemay *et al.*,[46] Long *et al.*,[18, 47-48] Kanoufi *et al.*,[49] Compton *et al.*,[50] Tschulik *et al.*,[51] Zhang *et al.*,[52] and Dick *et al.*,[53] etc., for the recent developments. The specific issues on SEE can refer to the following reviews, such as the nanopipette-based single nanoparticle detection given by White *et al.*[54], electrochemical kinetics and dynamics at the nanoscale by White *et al.*,[55] emerging tools for single entity electrochemistry by Tao *et al.*,[45] three-dimensional holographic microscopy for single nanodomain electrochemistry by Kanoufi *et al.*,[49] and mass-transport influenced electrolysis at the nanoscale via numerical simulation by Compton *et al.*,[50] etc.

Table 1.1. Categories of single entities detection by electrochemical methods

Types of entities	Size scale	Electrode	Reaction indicator	Ref.
Single isolated atoms				
Single Pt atom	0.23 nm	Pb UME	HER	[56-57]
Single Pt atom	0.25 nm	Bi UME	HER	[56]
Single cobalt oxide	0.21 nm	CFE	OER	[58]
Metal nanoparticles				
Pt NP	3 ~ 5 nm	C or Au UME	Hydrazine oxidation	[16-17, 59-61]
Au NP	7 ~ 60 nm	CFE or C UME	HER or ORR	[62-63]
Ag NP	5 ~ 60 nm	C UME	Silver oxidation	[63-66]
Cu NP	~ 41 nm	CFE	Copper oxidation	[67]
Metal oxides nanoparticles				
Fe_3O_4 NP	~ 4 nm	GC electrode	$[Fe(CN)_6]^{4-}/[Fe(CN)_6]^{3-}$	[68]
TiO_2 NP	~ 54 nm	Pt UME	Methanol oxidation	[69]
ZnO NP	~ 4 nm	TiO_2@Au UME	Water splitting	[70]
IrO_x NP	~ 28 nm	Pt UME	Water oxidation	[71]
CeO_2 NP	10 ~ 20 nm	Pt microelectrode	CeO_2 reduction	[72]
Bioparticles				
Cytomegalovirus	100 ~ 200 nm	Pt UME	$K_4[Fe(CN)_6]$ oxidation	[15]
Enzymes/antibodies	~ 10 m	Pt UME	$[Fe(CN)_6]^{4-}/[Fe(CN)_6]^{3-}$	[24]
Plasmid DNA	~ 30 nm	Pt UME	$[Fe(CN)_6]^{4-}/[Fe(CN)_6]^{3-}$	[24]
Red blood cell	~ 3 μm	CFE	ORR	[73]
Soft particles				
Toluene droplets	400 ~ 600 nm	Au UME	FcMeOH oxidation	[19]
Liposomes	40 ~ 200 nm	GC electrode	Sodium ascorbate oxidation	[74]
Micelles	~ 41.2 nm	GC electrode	Oxidation of free Br^-	[23]
Vesicles	120 ± 30 nm	Pt UME	$[Fe(CN)_6]^{4-}/[Fe(CN)_6]^{3-}$	[22]
Emulsion droplet	650 ~ 900 nm	C UME	Reduction of TCNQ	[75]
Carbonaceous particles				
r-GO	~ 100 nm	Au/SAM UME	$Ru(NH_3)_6^{3+}$ reduction	[76]
GNP	~ 16.5 μm	CFE	HER or water oxidation	[77]

SWCNT	Tens of nm	Pt nanoelectrode	FcMeOH oxidation	[78]
Nano-C_{60} NP	19 ± 4 nm	Au UME	Nano-C_{60} reduction	[79]
Other hard particles				
Polystyrene nanosperes	~ 22 nm	Pt UME	$[Fe(CN)_6]^{4-}/[Fe(CN)_6]^{3-}$	[24]
Polystyrene spheres	310 ~ 530 nm	Pt UME	FcMeOH oxidation	[80]
Silica beads	~ 310 m	Pt UME	FcDM oxidation	[81]
Carboxylated PSB	~1 μm	Pt UME	FcMeOH oxidation	[82]

* CFE: carbon fiber electrode; HER: hydrogen evolution reaction; ORR: oxygen reduction reaction; GC: glassy carbon macro-electrode; TiO2@Au UME: passivation of the underlying gold electrode by deposition of TiO2; r-GO: flakes of reduced graphene oxides; Au/SAM: SAM modified Au microelectrodes; GNP: graphene nanoplatelets; SWCNT: single-wall carbon nanotubes; FcMeOH: Ferrocenemethanol; TCNQ: 7,7,8,8-tetracyanoquinodimethane; FcDM: 1,1′-ferrocenedimethanol; PSB: polystyrene bead.

1.1.3 How to detect entities electrochemically?

The detection methods are mainly divided into three categories based on: (i) resistive sensing (e.g., Coulter counter, Patch-Clamp), (ii) electrochemistry combined with other techniques and (iii) particle-micro/nanoelectrode collision. In this section, we will briefly introduce the history and representative works in these three categories.

1.1.3.1 Resistive sensing

In the early history of SEE, Wallace H. Coulter's filed a pioneering patent in 1949, during which an analytical method was put forward based on the resistive-pulse sensing to count and analyze micron-scale objects such as bacteria, cells and particles.[83] The Coulter counter consists of two separate compartments connected by a single sensing ion channel with the diameters of 2 ~ 20 μm, as shown in Figure 1.1A and more schematically in Figure 1.1B. The Coulter counter is a resistive pulse technique. The compartments are filled with the electrolyte solution, and two Ag/AgCl electrodes are placed in each compartment to monitor ion current. By applying a potential difference between these two electrodes, the ionic current flows through the sensing channel. Driven by the applied electric field predominately, the analyte with a suitable size (blood cells in Coulter's patent) transits through the sensing channel. The analyte enters the channel and occupies a volume space in the channel, blocking the ionic conduction through the channel. As a result, a decrease in current is observed.

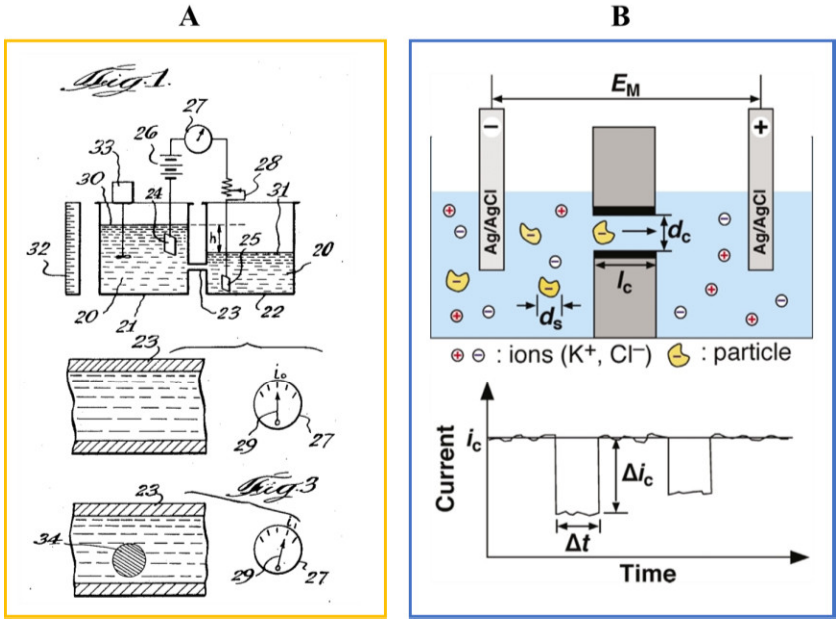

Figure 1.1. (A) ***The Coulter Counter***. Schematic illustration from Wallace H. Counter's patent in 1949 to count particles suspended in a fluid via resistive sensing. As shown in the apparatus, two-fluid vessels are connected by a narrow channel. By applying a potential difference, ion current will be generated across the channel. An analyte that transverse through the channel

occupies the space of the liquid solution and results in a transient current change. Reproduced from US patent.[83] (B) A schematic to illustrate the Coulter Counter. The current-time trace changes with respect to the presence of a particle in the single channel. The analysis of current magnitudes (Δi_c) and the width of signal (Δt) allow counting the size of single analytes and the particle transit time through the channel, respectively. Reproduced from Ref. [84]. Copyright 2004, Royal Society of Chemistry.

The pulse signal caused by the current attenuation change can be recorded by the *i*-*t* curve (see the bottom curve in Figure 1.1B). The magnitude of current responses, Δi_c, depends on the particle size (with respect to the size of the channel) and the width of the signal (the duration in the channel), Δt, relies on the charge and mobility of particles. The number concentration of analytes can be counted by the frequency of the resulting current responses. This simple and effective technique, having label-free features and advantages of high sensitivity to a single analyte, represents a great breakthrough in the field of analytical electrochemistry and has been widely applied in practice for single particle analysis. With the development of nanofabrication technology, the size of the channel can be reduced down to nanometers to detect nano-sized particles.

Later in 1970, R. W. Deblois and C. P. Bean narrowed down the channel size to just 450 nm using a polycarbonate plastic sheet as the template, followed by irradiation etching to form a submicron-meter sized pore.[85] This submicron channel allows detecting polystyrene beads as small as 90 nm in diameter, with a limit of detection of ~60 nm. A few years later, Delbois developed this resistive-pulse technique to detect individual viruses with diameters above 60 nm.[86]

In 2000, based on the concept of Coulter counter, Crooks's group used the artificial nanopore, multiwall carbon nanotube, as the sensing channel. The carbon nanotube nanopore, having uniform structure and absence of surface charge on its interior, can not only measure the concentration and size of particles with diameters around 50 nm but also quantitively assess the surface charge of single particles.[87]

At almost the same time as Crooks's experiments, Kasianowicz and coworkers were using a different approach, biological nanopore, to study the translocation of individual polynucleotide molecules (DNA).[37] Instead of using artificial nanopores, they used a peptide toxin, α-hemolysin, which having a pore diameter of 2.6 nm in its center, as the sensing nanopore. The α-hemolysin can self-assemble into a kind of lipid bilayer membrane and form a single nanochannel on the lipid membrane, as shown in Figure 1.2A.[88] The magic of α-hemolysin biological nanopore is that the narrowest diameter of the pore is ~ 1.4 nm that only allows one biological macromolecule to pass through at a time, achieving analysis of single molecule. Taking DNA as an example, the α-hemolysin nanopore allows single-stranded DNA (ssDNA) with a diameter of 1.2 nm to transit through but keeps away the large double-stranded DNA (~2 nm). Kasianowicz and coworkers found that ssDNA passing through the α-hemolysin nanopore produced four kinds of blockade signals.[37] The analysis of blockade signals can quickly obtain DNA sequence information, as shown in Figure 1.2B. In the past two decades, apart from α-hemolysin, many types of biological nanopores with various critical dimensions, e.g., OmphG, AeL, Phi29 motor and ClyA, are commonly utilized for biological molecules sensing.[42] More in-depth analysis of biological and artificial nanopores, one can refer to recent reviews.[42, 89-90]

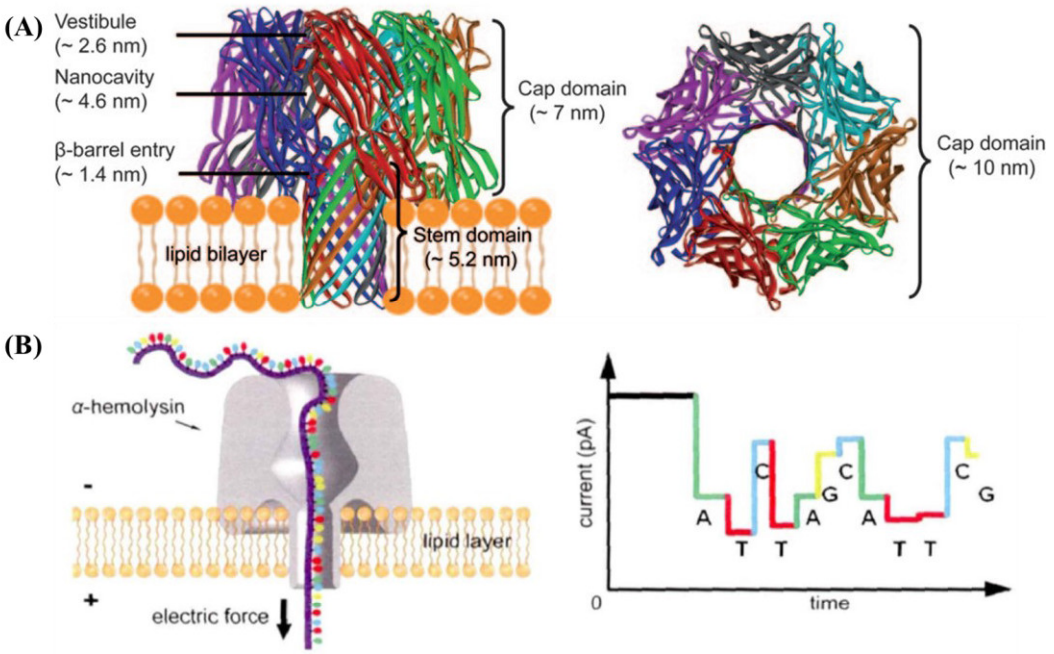

Figure 1.2. Schematic illustration of biological nanopores and its applications. (A) The schematic structure of α-hemolysin nanopore. The mushroom-like hemolysin nanochannel consists of a large vestibule (~ 2.6 nm) and a transmembrane stem with a β-barrel structure (~ 1.4 nm). (B) DNA sequencing by an α-hemolysin nanopore. Reproduced from Ref. [88]. Copyright 2010, John Wiley & Sons, Inc.

Another well-known methodology based on resistive sensing is the Patch Clamp electrophysiology that was first reported by Neher and Sakmann in 1976. Patch Clamp showed the opportunity to measure single proteins in the form of ion channels at a relatively early time.[91] Figure 1.3A shows the schematic diagram of the detection principle that the tip of a glass pipette (P) filled with high-resistance Ringer's solution penetrates and forms contact with the muscle fiber. The tip opening of the glass pipette having 3-5 μm diameter isolates the contacting area electrically. The discrete current changes are ascribed to the opening and closing of membrane channels stimulated by the additions (see Figure 1.3B).

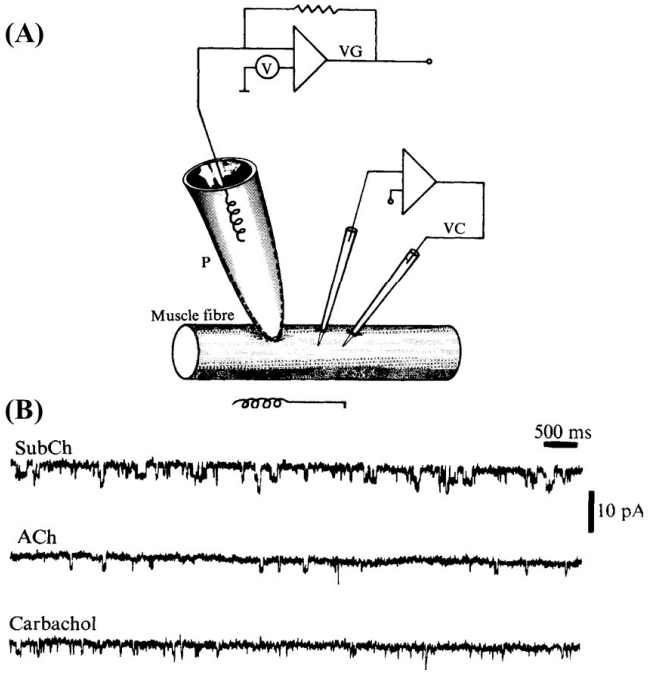

Figure 1.3. Patch-clamp electrophysiology. (A) A glass pipette (P) with a 3-5 μm diameter opening is sealed into the membrane of a cell, allowing the measurement of a single ion channel. The membrane potential across the muscle fiber is locally clamped

to a fixed value by a two-microelectrode voltage clamp. (B) The ion current-time trace for ionic channel activity is stimulated by the addition of the suberyldicholine (SubCh), the acetylcholine (Ach), and carbachol in the filled solution. Reproduced from Ref. [91]. Copyright 1976, Nature Publishing Group.

The key to the high resolution from this methodology lies in limiting the membrane area where the ion current (at the level of pA) is measured at a small patch. Thus, the background current noise is significantly decreased. This work inspires electrochemists to use low-noise and high-bandwidth amplifiers to detect single entities and develop laser-based micropipette puller to fabricate microscale electrodes and sensing channels for electroanalytical or electrochemical studies.[1] Patch-clamp technology is evolving as a conventional method in modern cell electrophysiology, no matter in biomedical research or directly or indirectly clinical research.

1.1.3.2 Electrochemistry combined with other techniques

In recent years, SEE has been developed for the analysis of single particles through the combination of electrochemistry and other technologies, including optical microscopy (e.g., dark-field and bright-field fluorescence microscopies) and spectroscopy (e.g., surface plasmonic resonance and Raman scattering techniques), as well as scanning probe microscopes (e.g., scanning electrochemical microscope and scanning tunneling microscope). SEE measurements are offering new insights into electrochemical reactions at heterogeneous/homogenous interfaces and in-depth studies of electrochemical activities at the level of single entities. The field of SEE is dynamic, diverse and broad, and thus it is extremely difficult to provide a comprehensive introduction to the entire field. In this section, some of the common tools that are used to study individual metallic particles will be highlighted. The systematic and thorough reviews on other analytes (e.g., single molecules, single bioparticles or others) can refer to recent publications.[46, 92-93]

Scanning probe-based techniques provide high spatial resolution, and combining scanning probe techniques with electrochemistry offers new capabilities to understand the local electrochemical behaviors of heterogeneous interfaces. Bard and coworkers pioneeringly developed the technique of scanning electrochemical microscopy (SECM) in which the current flows through a microscale-sized electrode near the substrate electrode.[94] A fruitful variant of SECM is to use micro/nano-pipettes as the detector instead of microelectrodes. The tip of pipettes filled with the solution forms a tiny meniscus or droplet (tiny electrochemical cell) that is in contact with the substrate electrode.[95-96] Very recently, White and coworkers used such technique (SECCM, scanning electrochemical cell microscopy) to study hydrogen evolution reaction (HER) at the localized surface of a single Pt nanoparticle (Pt NP) buried in Nafion film.[97] Pt NP is pre-deposited on the highly oriented pyrolytic graphite (HOPG) electrode, as shown in Figure 1.4A. Owing to the fast kinetics of HER on the surface of Pt NP, the Pt-immobilized HOPG electrode exhibits enhanced current responses and the lower onset potential than those observed at the HOPG (See Figure 1.4B). Then, the local electro-catalytic activity at surface of Pt NP is measured in a point-by-point manner at a constant potential of -1 V vs. Ag/AgCl, visually shown in Figure 1.4C. The current map not only provides information on both the activity and the size of the buried Pt NP.

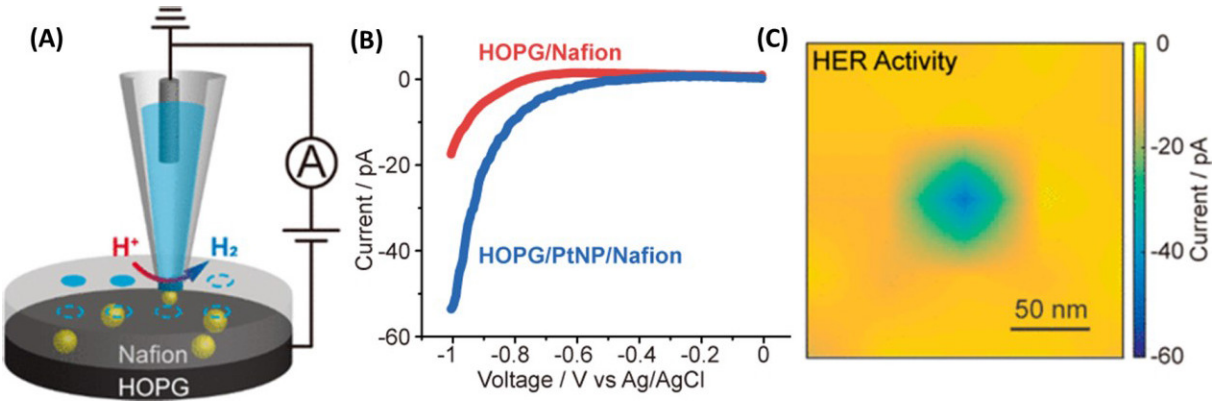

Figure 1.4. (A) Schematic illustration of proton reduction on the surface of a Pt NP (70 nm in diameter) buried in a Nafion film with a thickness of 150 nm. The nanopipette (100 nm diameter of the tip) contains 25 mM $HClO_4$. (B) Linear sweep voltammetry of HER on HOPG/Nafion (red) and HOPG/PtNP/Nafion (blue) at a scan rate of 0.1 V/s. (C) Imaging local activity of HER at each site on the surface of a Pt NP measured at the constant potential of -1 V vs. Ag/AgCl. Reproduced from Ref. [97]. Copyright 2020, American Chemical Society.

Optical imaging technology can provide a high temporal resolution to characterize dynamic collision behaviors of single nanoparticles, and ultimately establish a structure-activity relationship at the level of single nanoparticles. Common optical imaging technologies summarized here are three-dimensional (3D) holography microscopy, fluorescent microscopy, and plasmonic-based electrochemical current microscopy (P-ECM). These correlated techniques with electrochemistry were used to investigate dynamic oxidation behaviors of single silver nanoparticles (Ag NPs) upon contact with the electrified substrate electrode.

Kanoufi and coworkers correlated 3D holography imaging technology with electrochemical measurements to reveal the chemical reactivity of single Ag NPs.[98] The principle of the holographic microscope is to use a beam of light to irradiate the sample under the condition of total internal reflection. The light scattered by the particles interferes with another reference beam to provide 3D localization information of the particles (the spatial localization range is $100 \times 100 \times 30$ μm^3). By simultaneously monitoring the optical information and electrochemical signals of single Ag NPs over the dissolution process, one can determine that the dissolution of Ag particle did not take place immediately upon contact with the Au UME, but occurred after a few seconds (the brown line in Figure 1.5A). The authors propose two possible reasons for these interesting results: Ag NPs might land on a region with a poorly electrocatalytic site, requiring a quite long time for itself to diffuse to a reactive site at the surface of UME; the near-wall hindered diffusion freezes or slows down the movement of Ag NPs within < 10 nm from the surface of UME, and 3D super-resolution holography cannot distinguish the contacting Ag NP or one within 10 nm. Separate studies concerning the diffusiophoretic transport of Ag NPs to the surface of UME and the kinetics of Ag NP dissolution were done by the same authors.[49, 99] They also compared the total exchanged charge (brown) during individual Ag dissolution with the scattered optical intensity (blue), and further confirmed that the starting position and kinetic information of Ag dissolution were consistent (see the left in Figure 1.5B). The optical evidence of partial oxidation of Ag NPs was observed experimentally, as shown in the right in Figure 1.4B. This correlated technique was successfully applied to the study of complex chemical processes at the level of single NPs.

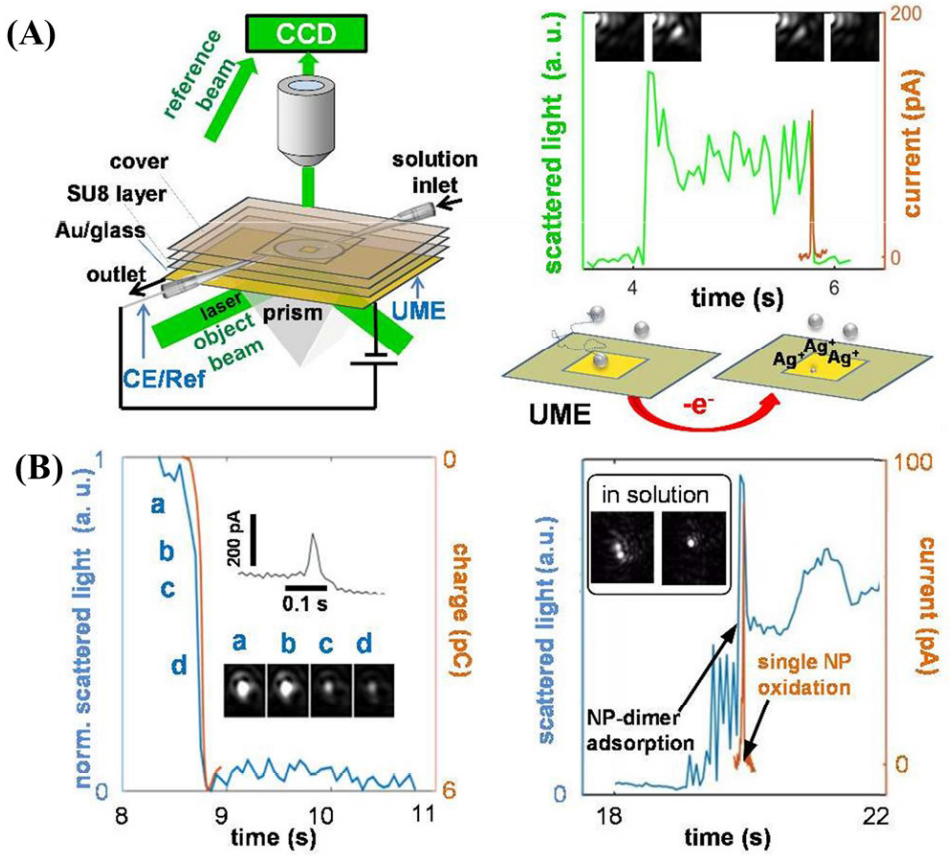

Figure 1.5. 3D super-resolution holography coupled with electrochemistry. (A) left: Schematic fluidic device combines electrochemical setup and 3D holographic micro-imaging technology to achieve optical 3D localization of Ag NPs impacting with the Au UME. Right: Green trace: light scattered by an individual Ag nanoparticle in KNO_3, with the increase of scattered light during its landing and the disappearance of the current peak caused by its dissolution. (B) Correlated opto-electrochemical signals for the electro-dissolution of Ag NPs in the KNO_3 solution. Left: comparison between scattered optical intensity (blue) and total exchanged charge (brown). Right: Agglomerate formation and oxidation of two Ag NPs in solution, coupled with the optical evidence of partial dissolution of Ag NP. Adapted with permission from Ref. [98]. Copyright 2016, American Chemical Society.

Zhang and coworkers designed a unique nanopipette electrochemical nanocell that enables optical monitoring of the dynamic motion of single Ag NPs during collisions at the confined surface (see Figure 1.6).[100] A Pt NP is pre-deposited at the tip of a nanopipette to form an electrochemical nanocell in which a bipolar reaction happens that the proton reduction on the external surface of Pt is electrically coupled with the Ag NP oxidation inside the nanocell. When the colliding Ag NP is partially oxidized to form Ag_2O, the oxidation product undergoes photocatalytic decomposition, which results in the formation of fluorescent small Ag clusters generating strong fluorescence signals. The successful observation of fluorescence images is attributed to the confined volume inside the microfabricated nanocell (~ 50 attoliters), which limits the motion of Ag NP to one dimension (within 1 μm along the nanocell) and reduces the background fluorescence signal. The authors attributed the repeated motions of single Ag NP at the confined nanocell to the electrostatic interaction between Ag NP, the walls of the nanocell and the Pt nanoelectrode.

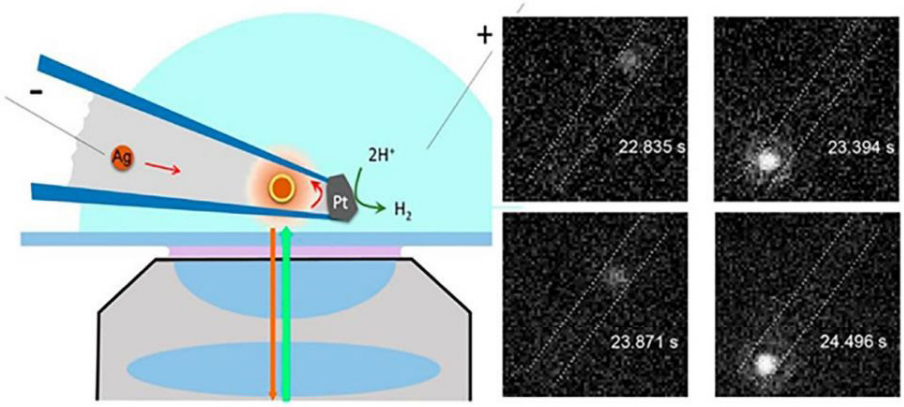

Figure 1.6. Fluorescent microscopy coupled with electrochemistry. Schematic illustration of the experimental setup to monitor the oxidation behaviors of individual Ag NP in a 100 nm diameter nanopipette nanocell. Pt NPs were pre-deposited at the tip of the quart to form a Pt nanoelectrode in the confined nanocell (100 nm in diameter). Fluorescent microscopy placed right below the nanocell to image the dynamic oxidation behaviors of single Ag NP at the confined region. Once the colliding Ag NP is partially oxidized to form Ag_2O, the photo-decomposition of this oxide layer leads to the formation of fluorescent small silver clusters, resulting in a strong fluorescence signal. The Ag oxidation inside the confined nanocell is electrically coupled to proton reduction on the other side of Pt. Reproduced from Ref. [100]. Copyright 2017, American Chemical Society.

Tao and coworkers developed the technique of plasmonic-based electrochemical current microscopy (P-ECM) to image the oxidation of individual Ag NPs deposited on the Au substrate, as shown in Figure 1.7A.[100] The Au electrode was held at a sufficient potential (-50 mV vs. Ag/AgCl) to oxidize single Ag NP. The intensity of the plasmonic image decreases with the oxidation of Ag NP, $Ag + 2\,SCN^- = Ag(SCN)_2$. When a single Ag NP is completely oxidized, the intensity returns to the baseline, as shown in Figure 1.7B. Meanwhile, the number of oxidized atoms from the nanoparticle equals to the amount of charge transfer during oxidation, then the transient radius of nanoparticle $r(t)$ is given by:

$$r(t) = r_0 - \frac{m_{Ag} N_A}{\rho} k_0 e^{\alpha \frac{nF}{RT}(E-E_0)} t \tag{1.1}$$

where r_0 is the initial radius of Ag NP, m_{Ag} is the mass of Ag atom, N_A is the Avogadro constant, and ρ is the density of Ag. The parameters of k_0, α, n, F, R, T, E, and E_0 are the standard rate constant, the coefficient of charge transfer, the number of electron transfer per atom, the Faraday constant, the gas constant, the absolute temperature, the applied potential and the formal potential, respectively. At a constant applied potential, the Eq. (1.1) describes the relationship of nanoparticle size with time.

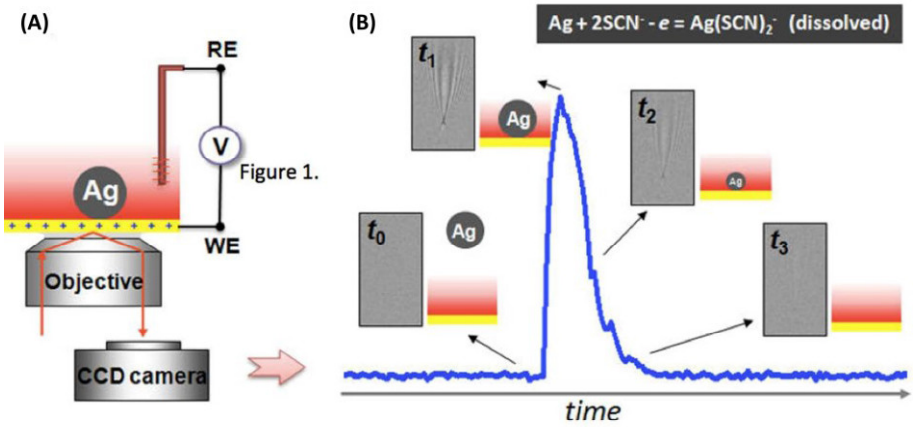

Figure 1.7. Single nanoparticle detection by the technique of P-ECM. (A) Schematic representation of the P-ECM imaging setup. The gold chip works as the working electrode and Ag/AgCl acts as the reference electrode. Incident light that comes from a super luminescent light-emitting diode passes through an optical microscope objective and directly irradiates Ag NP to excite surface plasmons. The reflected light is then collected by the CDD camera to form a surface plasmon resonance image.

(B) The transient intensity of surface resonance image (blue curve) changes with the electrochemical dissolution of single Ag NP. Reproduced from Ref. [101]. Copyright 2014, American Chemical Society.

The P-ECM technique is capable of studying localized electrochemical reactions with high throughout and temporal resolution, which has been widely used to study various nanomaterials, including silver nanoparticles,[102] metal oxide,[45] bacteria,[103] and viruses,[104] etc. The imaging technique is fast, label-free and noninvasive, but the spatial resolution of this technique is limited by optical diffraction, with a fraction of μm.[45]

1.2 Electrochemical methodologies for single particle detection

The developments of the ultramicroelectrode and relevant instrumentation in the 1980s started a new chapter in electrochemical science. R.N. Adams and coworkers in 1979 reported the use of UME doing electrochemistry in rat brain.[105] Later in the mid-1980s, the independent work from Wightman *et al.*[106] and Fleischmann *et al.*[107] introduced UMEs to the field of electroanalytical chemistry. At the same time, the invention of SECM significantly influenced electrochemical measurements and imaging in small volumes.[108-109] These unprecedented advances have greatly pushed forward the development of electroanalytical science. Ultramicroelectrode or nanoelectrodes are extremely important for single entity measurements. The background current associated with electrochemical double layer scales with the electrode area and the electrochemical current response from an individual entity is usually small and easily overwhelmed by a relatively large background current. Those electrodes with tiny surfaces exhibit an extremely low background current, making it possible to detect single nanometric entities.

In recent years, under the active exploration of many scientists, like Serge G. Lemay, Allen J. Bard, Richard G. Compton, Richard M. Crooks, Henry S. White, to name but a few, the field has continued to develop and achieved remarkable research results. Through the real-time study of the collision process between single particles and electrodes, many issues can be explored, including the frequency of collision, size distribution and concentration, morphological characteristics, and charge, etc. Electrochemical techniques for single particle detection can be divided into four main categories: (i) potentiometric technique; (ii) capacitance feedback response; (iii) fast-scan cyclic voltammetry; (iv) amperometric technique. In this section, we will first make a simple introduction for the first three techniques and then describe in detail the amperometric technique.

In 2012, Bard and coworkers first reported a potentiometric technique for single nanoparticle detection. This technique takes advantage of the difference in kinetics between Pt NP and the Au surface for hydrazine oxidation, which is, to some extent, similar to electrocatalytic amplification. The difference between both techniques is that the potentiometric technique is performed by measuring the changes in open circuit potential (OCP) rather than current changes described in the electrocatalytic amplification. OCP of the electrode is measured at which the net current equals zero and is related to the nature of the electrode itself. Figure 1.8A shows the difference in OCP between the Au UME and the Pt UME in the solution containing 15 mM hydrazine and 50 mM phosphate buffer (pH = 7), being ~ 400 mV vs. Ag/AgCl. Pt is a better electrocatalyst for hydrazine oxidation than Au. Figure 1.8B schematically shows the shift in OCP upon adsorption of a Pt NP on the surface of Au. When a Pt NP absorbs on the surface of Au, Pt catalyzes oxidation of hydrazine generating enhanced anodic current. In order to keep the net current being zero, OCP would shift negatively to reduce down the oxidation reaction rate and increase cathodic current to counteract the current amplification by the Pt NP. Figure 1.8C shows a representative potential-time trace to record consecutive Pt NP collisions on a 5 μm radius Au UME. The magnitude of the changes in OCP (staircase-shaped changes in potentials) is related to the ratio of the size of Pt NP to the electrode radius and the concentration of hydrazine. The collision frequency measured by this potentiometric technique (0.002 $pM^{-1}s^{-1}$) is six times lower than that by amperometric technique (0.012 $pM^{-1}s^{-1}$) under the same condition. Although the authors claimed that the OCP technique has simpler apparatus, higher sensitivity and fewer problems associated with NP deactivation than the amperometric technique, there is no further quantitative analysis of OCP to correlate the magnitudes of potential steps to the size of Pt NP.

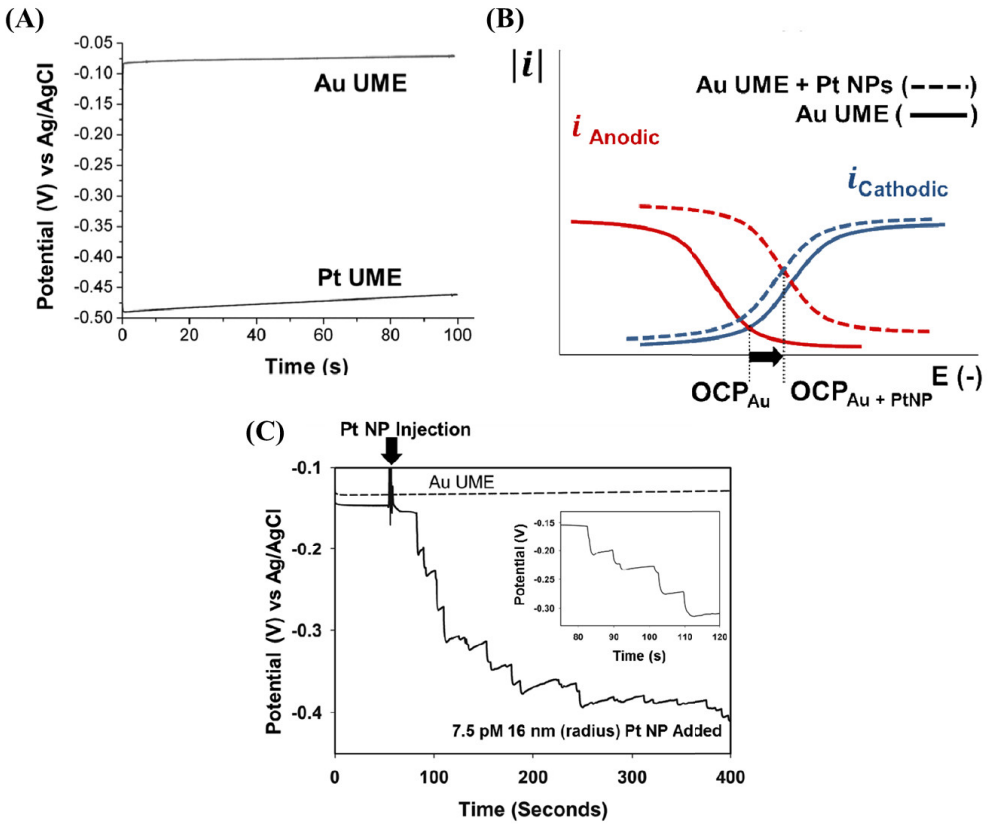

Figure 1.8. Single nanoparticle detection by the potentiometric technique. (A) OCP values of 5 µm radius Au and Pt UMEs in 15 mM hydrazine and 50 mM phosphate buffer solution (pH = 7). (B) Schematic illustration of the shift in OCP before (solid line) and after (dash line) adsorption of a Pt NP on the surface of Au. Note that currents (y-axis) are shown in absolute values. (C) OCP-time trace for Pt NPs colliding on the surface of Au in the presence of 7.5 pM Pt NPs in 15 mM hydrazine and 50 mM phosphate buffer (pH = 7). The magnified staircase-shaped potential response is shown in the inset. Reproduced from Ref. [110]. Copyright, 2012 American Chemical Society.

In 2016, Zhang and coworkers reported the use of a voltammetric approach, fast-scan cyclic voltammetry (FSCV), to study single particle collision.[61, 111] Schematic illustration of the principle of FSCV is shown in Figure 1.9A. It makes use of electroactive metal NPs to catalyze hydrazine oxidation when colliding on an inert electrode, generating an enhanced current. The characteristic of this method is to use a very fast CV scan (60 ms per scan) to record separate voltammograms for each nanoparticle. Figure 1.9B shows five separate collision events on a 60 s recording during Au NPs collisions on the surface of carbon. A straightforward observation showing five collision events is illustrated in Figure 1.9C where a current-time trace is taken from Figure 1.9B indicated by the black line. Each current increment comes from the collision of separate Au NPs. Meanwhile, the current-potential voltammograms for each Au NP are shown in Figure 1.9D. The events 1, 2 and 4 show characteristic sigmoidal CVs, indicating hydrazine oxidation on Au is performed at a diffusion-limited mass transfer, while event 3 needs a higher potential to reach a diffusion-limited steady state. The limiting current in the sigmoidal CV can be utilized to estimate the size of the spherical nanoparticle, given by:

$$i_{ss} = 4\pi \ln(2)\, nFDC^{*}r \tag{1.2}$$

where i_{ss}, n, F, D, C^{*} and r are the limiting current, the number of electron transfer per molecule, the Faraday constant, the diffusion coefficient, the bulk concentration and the particle radius. Furthermore, combining with the finite element simulation by COMSOL and Bulter-Volmer equation, the standard rate constant and the charge transfer coefficient can be obtained.

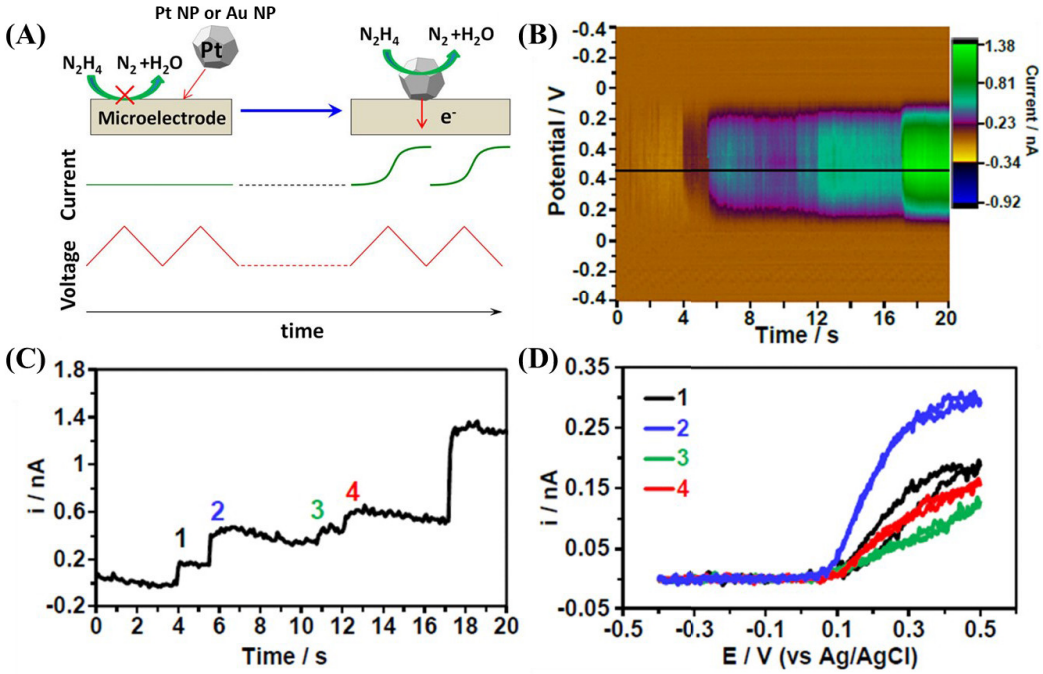

Figure 1.9. Single nanoparticle detection by FSCV. (A) Schematic illustration of the use of FSCV. A triangular voltage waveform is scanning continuously on the inert electrode (e.g., carbon UME), showing no reactive current for hydrazine oxidation. When an active nanoparticle (e.g., Pt NP or Au NP) collides on the inert electrode, hydrazine oxidation takes place at a Pt NP generating steady-state voltammetry at a mass-transfer limit. Reproduced from Ref. [61]. Copyright 2014, American Chemical Society. (B) A representative FSCV color plot during Au NPs collision on the surface of carbon. (C) *i-t* trace taken from (B) at the potential of 0.465 V in the forward scan (along the black line). (D) Single-nanoparticle voltammograms in numbers marked in (C) at a fast scan rate of 25 V/s. The solution contains 10 mM hydrazine, 50 mM PBS and ~12.5 pM Au NPs. Reproduced from Ref. [111]. Copyright 2016, American Chemical Society.

Lemay and coworkers reported the detection of BEAS THP1 and MCF7 cancer cells in real time via a high-frequency nanocapacitor array.[112-113] The authors used a specific electrochemical biosensing platform, consisting of a 90 nm complementary metal-oxide-semiconductor chip with an array nanoelectrode array, to perform capacitive imaging. This on-chip measurement platform enables measurements of only few attofarad resolution (see Figure 1.10). Depending on the frequency of the measurement, they can probe the capacitance of the electrical double layer or the permittivity of the solvent and thus detect the collision of an insulating object. Nano- and microbeads of polystyrene as well as micro-droplets of organic solvents and ionic liquid were also imaged using this platform.

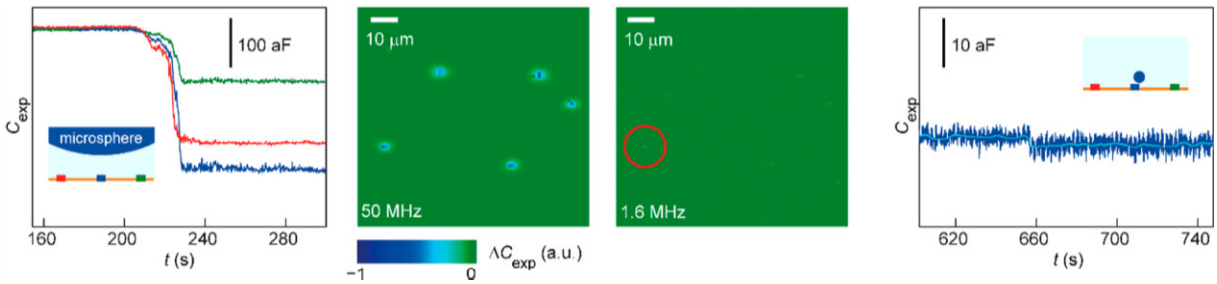

Figure 1.10. From left to right: capacitance as a function of time measured for three neighboring nanoelectrodes in response to the sedimentation of a 4.4 μm radius polystyrene bead. Spatial maps of the change of capacitance obtained at 50 MHz and 1.6 MHz and capacitance change measured upon binding of a 28 nm diameter particle on a nanoelectrode. Reprinted with permission from Ref. [112-113]. Copyright 2016, American Chemical Society.

Recently, Long and coworkers also reported the detection of nanoparticles based on the mechanism of capacitance feedback response (CFR) but the signal is recorded as a current.[114] They used the closed-typed wireless nanopore electrode (CNE) that was fabricated by a coupled chemical-electrochemical approach to detect single Au NPs (see Figure 1.11A). The porous Au layer was first generated at the tip

area by the chemical reaction of $AuCl_4^-$ and BH_4^-, followed by electrochemical reduction of $AuCl_4^-$ to form a continuous prolonged nanotip. CNE having a comparable size to nanoparticles exhibits a low current noise of 0.6 ± 0.1 pA, and the temporal resolution for single transient collision is as low as 10 µs. The features of high temporal resolution and high current resolution of CNE have at least two orders of magnitudes higher signal frequency than the conventional UMEs in single particle analysis. The CFR sensing mechanism can distinguish the size-dependent interactions between Au NPs and the WNE during the dynamic collision process (see Figure 1.11B). The distribution of current peak recorded by 13 and 60 nm diameter Au NPs locates at 5 and 15 pA during separate measurements, respectively. During collisions with two mixture sizes of Au, two distinguishable peaks locating at 5.2 and 16.1 pA are observed, without any overlap between two sizes of Au NPs. The authors proposed the equivalent circuit of the CNE to explain the sensing mechanism (see Figure 1.11C). The negatively charged Au NPs during collisions can modulate the charging-discharging process of interfacial capacitance (circuit element Ce2 in Figure 1.11C), leading to a current spike. However, the CFR is based on the capacitive feedback response mechanism, which requires the analyte to have a high charge density to ensure a sufficient current response; otherwise, it is easily overwhelmed by the background current.

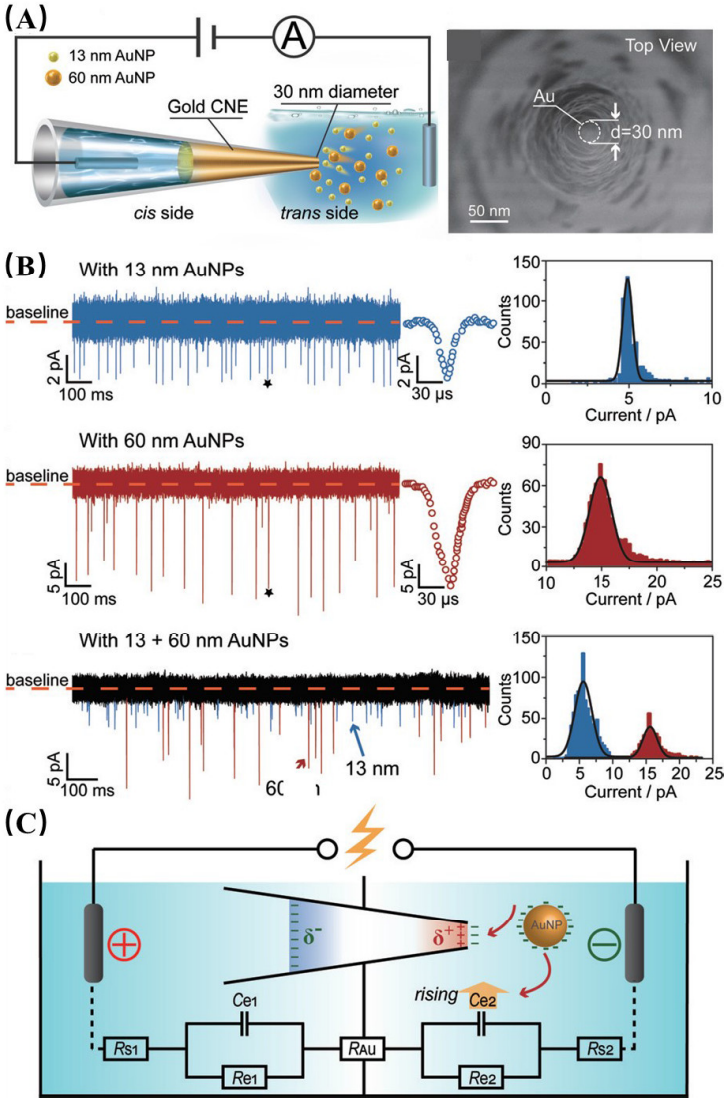

Figure 1.11. Capacitance feedback response for single nanoparticle detection. (A) Schematic illustration of closed-typed wireless nanopore electrode for single Au NP detection. A pair of Ag/AgCl electrode was used to apply the bias potential, and the nanopore electrode was polarized at 0.3 V vs. Ag/AgCl. The right SEM image shows the top view of Au WNE. (B) The raw current spikes (left) and the histograms (right) of individual Au NPs (13 nm and 60 nm in diameter) and the Au NPs mixture. The stars correspond to magnified current spikes shown on the right. The bias potential is +0.3 V vs. Ag/AgCl at

which Au NPs would not be oxidized. (C) The equivalent circuit model of Au WNE for particle detection. Reproduced from Ref. [114]. Copyright 2018, John Wiley & Sons, Inc.

The most common technique used for single particle detection is the amperometric technique, which can be divided into the following categories, such as electrocatalytic amplification, tunneling electrodes, direct electrolysis, enzymatically enhanced collisions and electrochemical blocking, etc. The schematic illustration, the form of current signals, the benefits and limits are summarized in Figure 1.12. Next, we will review some representative work for these methodologies.

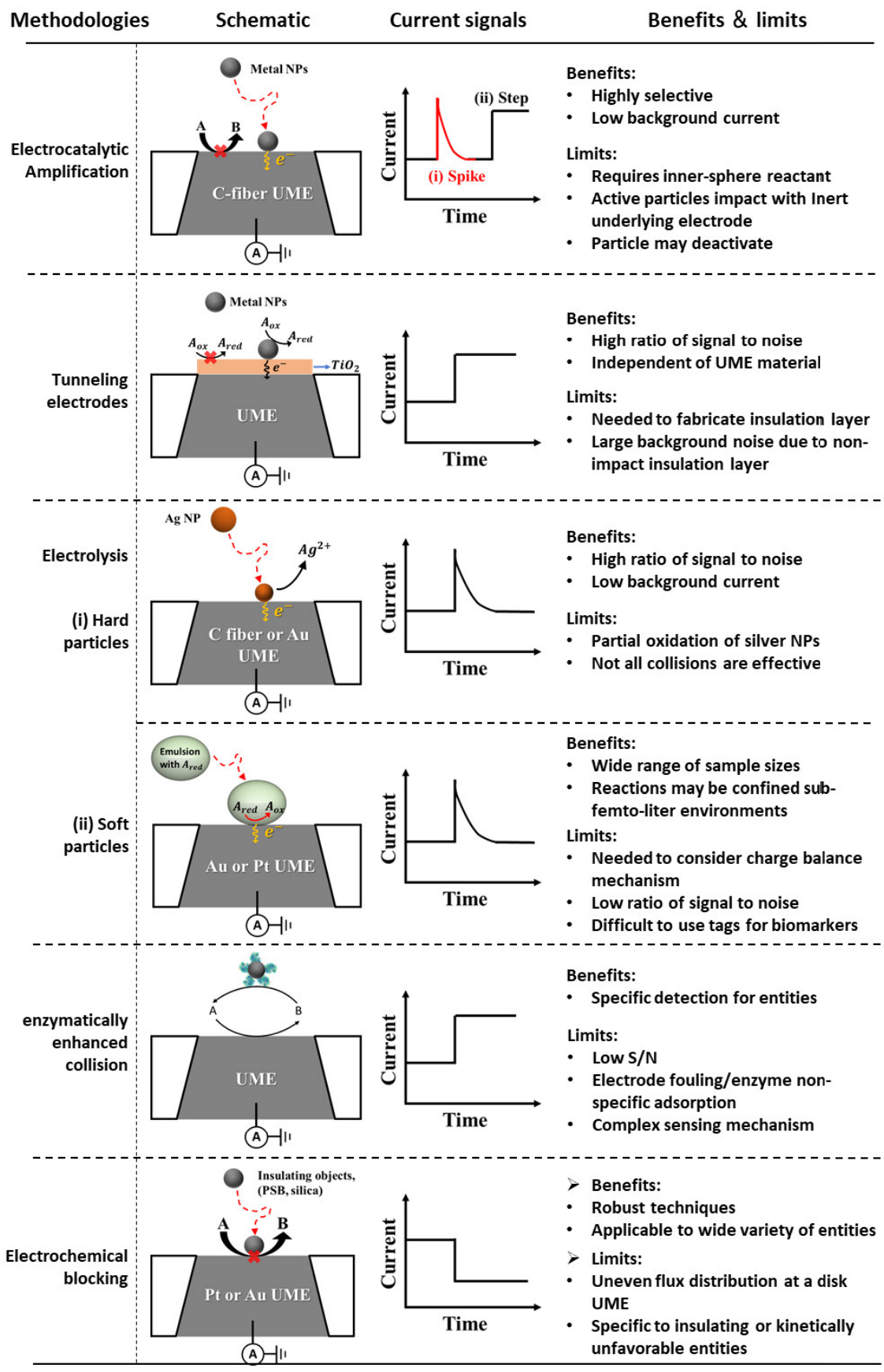

Figure 1.12. Schematic of various amperometric techniques for single particle detection discussed in section 1.2.

1.2.1 Electrocatalytic amplification

In 2007, Xiao and Bard, for the first time, reported a method called electrocatalytic amplification (ECA) to detect single particles made of a material that possesses, for a given inner-sphere reaction, "good" catalytic properties compared to the material of the electrode.[16-17] Figure 1.13A illustrates how a single catalytic particle is detected by the method of ECA. For a typical inner-sphere hydrazine oxidation reaction, based on the difference in kinetics of two materials (e.g., Pt and Au), one can choose an appropriate potential at which the faradaic reaction does not occur on itself while the reaction is "switched on" when a catalytic Pt NP absorbs on the surface of Au, as shown in Figure 1.13B. In the *i-t* trace, an increased current step is observed (see Figure 1.13C, beware of the "Texas" convention where anodic currents are negative). The magnitude of the current increment, *i*, generated by a spherical particle at a mass-transfer limit abides by the Eq. (1.2). Thus, the size of Pt NP can be deduced from the magnitude of the current step. Pt NPs of as small as ~3.6 nm can be detected by ECA, demonstrating the extreme sensibility of this method. Recent reports of possibly single atoms of catalyst (e.g., Pt, CoO_x) can be found.[115-117]

For the method of electrocatalytic amplification, besides the electro-oxidation of hydrazine,[118-121] the other inner-sphere reactions, such as electro-reduction of proton[16-17, 122] or oxygen[123-124], and the electro-oxidation of hydrogen[125-126] or water[71], etc., can also be chosen as the redox indicator reactions. However, among eighteen examples of catalytic amplification[51, 122], only four cases (i.e., a combination of NP and catalytic reactions) show ideal step-like events[17, 119-120, 127] while the others report spike-shaped current events.

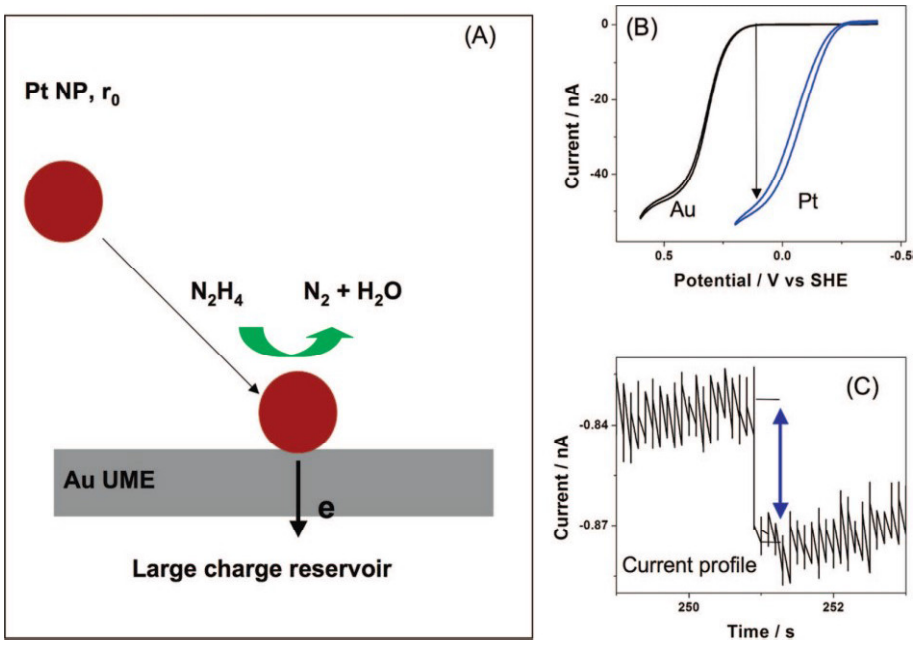

Figure 1.13. Single particle detection by the method of ECA. (A) Schematic of catalytically active Pt NP colliding at the surface of Au UME. (B) Cyclic voltammograms of hydrazine oxidation recorded on the surface of Pt and Au. Taking advantage of the difference in kinetics of Pt and Au, one can choose an appropriate potential at which the reaction rate is fast on Pt but extremely slow on Au. (C) A typical current step observed upon adsorption of single Pt NP at the surface of Au. Reproduced from Ref. [17]. Copyright 2008, American Chemical Society.

Later in 2010, Bard and coworkers reported typical spike-shaped current signals during collisions of single iridium oxide (IrO_x) at the surface of Pt UME, schematically shown in Figure 1.14A. The Pt UME is biased at 0.8 V vs. Ag/AgCl, during which no water oxidation takes place. When an IrO_x NP collides on the surface of Pt, an increasing spike-shaped current signal appears. Figure 1.14B shows representative chronoamperograms recorded on a 10 μm diameter Pt UME in the absence (black curve) and presence (red curve) of 4 pM IrO_x nanoparticles. These current spikes show a fast increase and a slow decay (see the inset in Figure 1.14B). The authors claimed that the fast increase is due to the contact

of IrO_x NP on the surface of Pt; in contrast, the blockage of active sites on nanoparticles by impurities or product, nanoparticle decomposition or detachment from the surface of Pt may be responsible for such a slow decay of transient behavior.

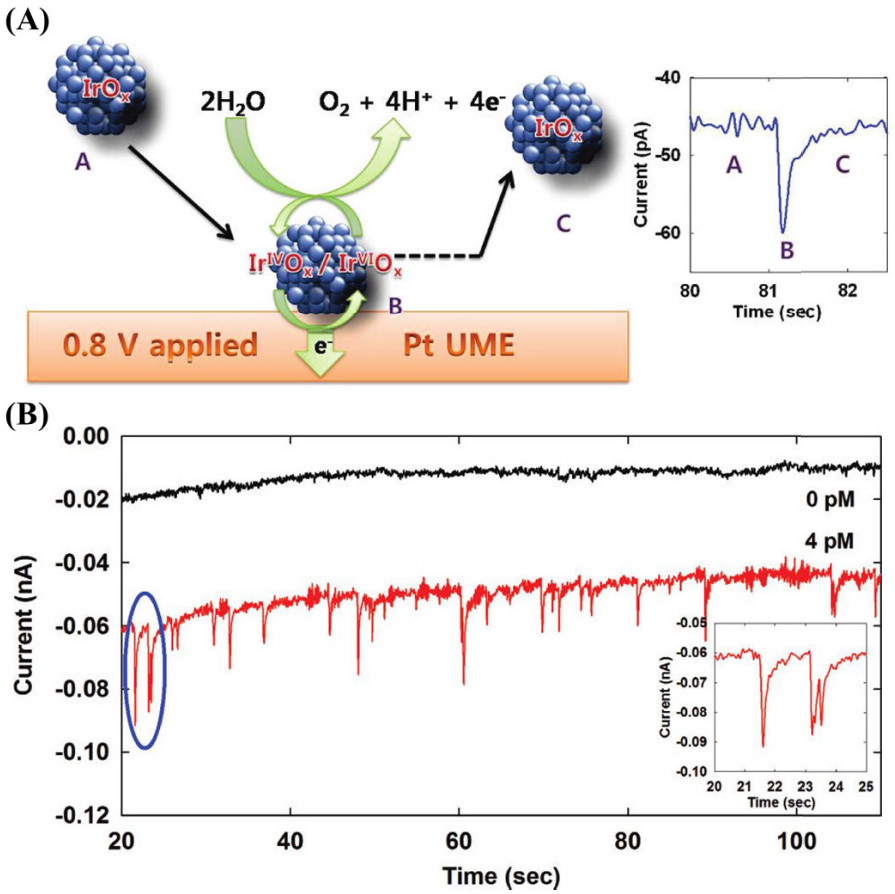

Figure 1.14. Spike-shaped current signals during single IrO_x Np collisions. (A) Schematic illustration of detecting single IrO_x NP at a 10 μm diameter Pt UME. If an IrO_x NP collides on the surface of Pt, the water oxidation is catalyzed, generating a spike-shaped current enhancement. (B) *i-t* trace recorded at Pt without (black curve) and with (red curve) 4 pM IrO_x NPs in solution. Zoom in the inset. [Bias potential] = 0.8 V vs. Ag/AgCl, [Data acquisition] = 50 ms. Reproduced from Ref. [71]. Copyright 2010 American Chemical Society.

Almost at the same time, Bard and coworkers reported the method of surface modification to inactivate the active electrode instead of directly using the inert electrode (e.g., carbon fiber UME). Through anodization of a Pt electrode, a thin layer of oxide (PtO_x) is grown on the surface of Pt. The PtO_x layer inhibits the inner sphere reaction, $NaBH_4$ oxidation, but still allows electron tunneling, as shown in Figure 1.15A. When the electrode is held at a potential at which the PtO_x layer was maintained (e.g., 0 V vs. Ag/AgCl), after injection of 14 nm diameter Au NPs the $NaBH_4$ oxidation is "switched on" and a discrete of increasing current spikes were observed (see Figure 1.15 B and C). The authors also confirmed that the oxidized Pt and Au are electro-catalytically inactive toward the inner-sphere reaction, including $NaBH_4$ oxidation and hydrogen oxidation.

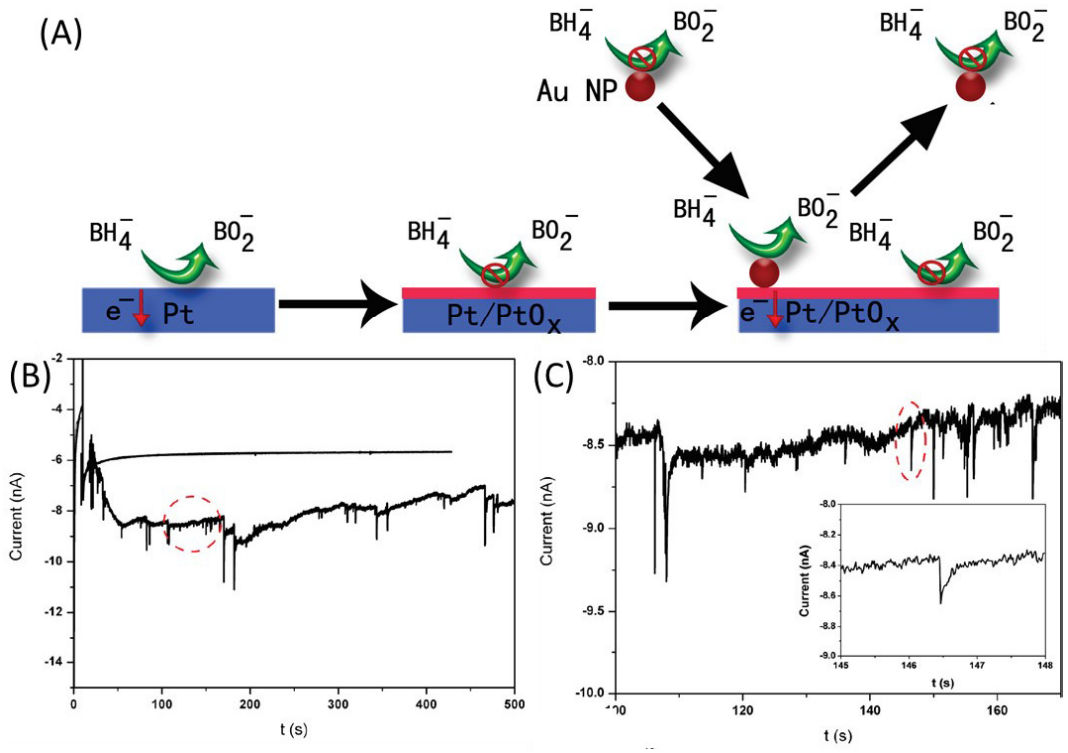

Figure 1.15. Deactivation of active Pt UME via surface modification (pre-oxidation). (A) Schematic illustration of detecting Au NPs on a pre-oxidized Pt UME (Pt/PtO_x UME). (B) *i-t* trace recorded at the surface of Pt/PtO_x in the absence (upper curve) and presence (bottom curve) of 24 pM Au NPs in a solution containing 10 mM $NaBH_4$ and 0.1 M NaOH. The Pt UME (10 μm in diameter) was biased at 0 V vs. Ag/AgCl. (C) Zoom in on panel (B). Reproduced from Ref. [128]. Copyright 2010, American Chemical Society.

Recently, Zhang and coworkers developed the "microjet collision system" to investigate the chemical reactivity of HER on the surface of single Pt NP. This system used a pressure-driven flow to deliver single Pt NPs from a glass micropipette onto a closely positioned carbon fiber UME (see Figure 1.16A). Even in high acid concentrations up to 3 M, single Pt NPs did not undergo significant nanoparticle aggregation. The microjet collision system allows continuous recording of thousands of spike-shaped collisions in highly concentrated acid solution with the collision frequency as high as 10 Hz, as shown in Figure 1.16B. Current spikes are attributed to the proton reduction catalyzed on the surface of Pt NPs. They further studied potential-dependent nanoparticle collisions from +0.1 V to -0.7 V, as shown in Figure 1.16C. At a relatively low overpotential for HER (less than -0.4 V), singular fast spikes (~ 50 μs) were observed while at high overpotential (e.g., -0.7 V), a fast spike associated with a slow decay (seconds long) were observed. The authors proposed that fast current spikes result from the initial hydrogen adsorption ($H^+ + e^- = H_{ads}$), while a slow decay is attributed to the hydrogen evolution ($H^+ + H_{ads} + e^- = H_2(g)$, or $H_{ads} + H_{ads} = H_2(g)$), as shown in Figure 1.16D. Owing to the existence of repetitive collisions of Pt NPs before sticking on the electrode surface, and the overlapping of the process of hydrogen adsorption and hydrogen evolution, there is no further analysis of the full charge to the size of colliding Pt NPs.

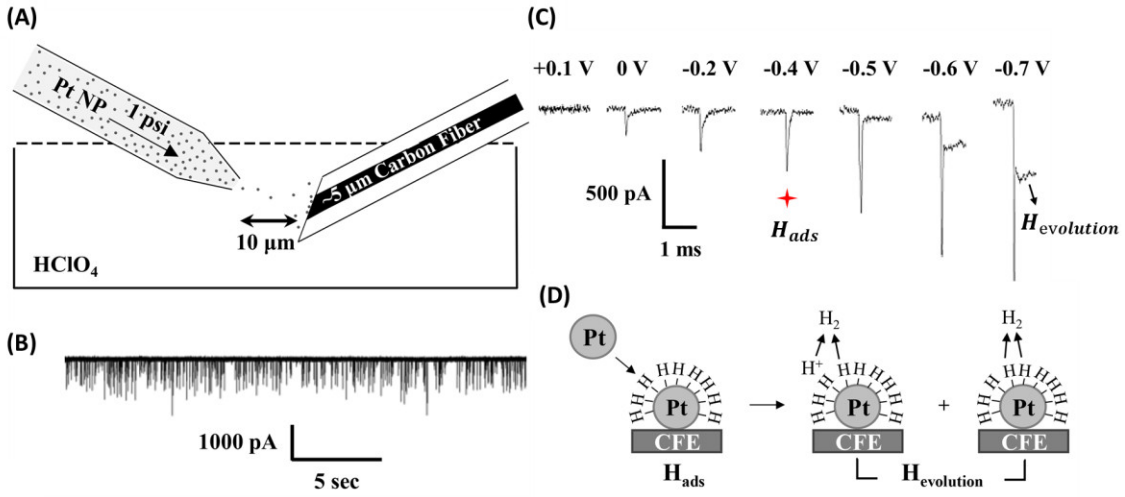

Figure 1.16. Ultrafast hydrogen adsorption (H_{ads}) and hydrogen evolution ($H_{evolution}$) on the surface of single Pt NP. (A) Schematic illustration of microjet setup used to deliver Pt NPs under the pressure of 1 PSI through a concentrated acid solution (1.25 mM to 750 mM) onto a C-fiber UME (5 µm in diameter). (B) *i-t* trace of nanoparticle collisions using the microjet system (A) at – 400 mV. [$HClO_4$]=25 mM, [Pt diameter] = 30 nm. (C) Potential-dependent Pt NP (30 nm in diameter) collisions under various potentials from +0.1 V to -0.7 V in 25 mM $HClO_4$ solution. (D) The proposed mechanism to explain the ultrafast collision peaks at various potentials. The initial fast peak is caused by the hydrogen adsorption around Pt NPs at the surface of C-fiber UME, while the subsequent slow decay is attributed to the hydrogen evolution. Reproduced from Ref. [122]. Copyright 2019, American Chemical Society.

1.2.2 Tunneling electrodes

In order to develop a highly sensitive detector for scanning electrochemical microscopy, Bard and coworkers fabricated a tunneling electrode with the dimension to the nanometer scale by electrodeposition of an insulating titanium dioxide (TiO_2) film, followed by capturing metal nanoparticles on the film surface, as shown in Figure 1.17A.[60, 129] A constant potential is applied to electrodeposit a single Pt NP on the TiO_2 film surface from the acidic precursor solution (H_2PtCl_6). The TiO_2 film blocks the electron transfer from the surface of Pt to the solution species. Meanwhile, the thickness of TiO_2 film (1.0 nm to 2.2 nm) is thin enough to restore electron transfer to the solution species via facile electron tunneling once the attachment of Pt NPs at the film surface. After attachment of Pt NPs on the surface of Pt UME/TiO_2 surface, a sharp current increase is observed in the *i-t* trace (not shown) and typical sigmoidal-shaped voltammetry for $Fe(CN)_6^{3-}$ reduction appeared. The method of electrodeposition benefits the monitoring of the formation and growth of a single Pt NP by recording *i-t* transients over the deposition process. A representative SEM image of the tunneling UME with the attachment of Pt NP is shown in Figure 1.17B. Figure 1.17C shows voltammetric behaviors of the tunneling UME with various radii in the solution containing 5 mM $Ru(NH_3)_6^{3+}$ and 0.1 M KNO_3. The radii of Pt NPs are estimated based on the limiting current assuming a spherical geometry for single Pt NPs, is also described by the Eq. (1.2). Once knowing the radius of single Pt NPs, the kinetic information can be extracted from the steady-state voltammograms using the proposed Kotecký-Levich method. They further used the finite element analysis based on COMSOL Multiphysics to establish the simulated voltammograms. The simulated kinetic parameters are in good match with the experimental results.

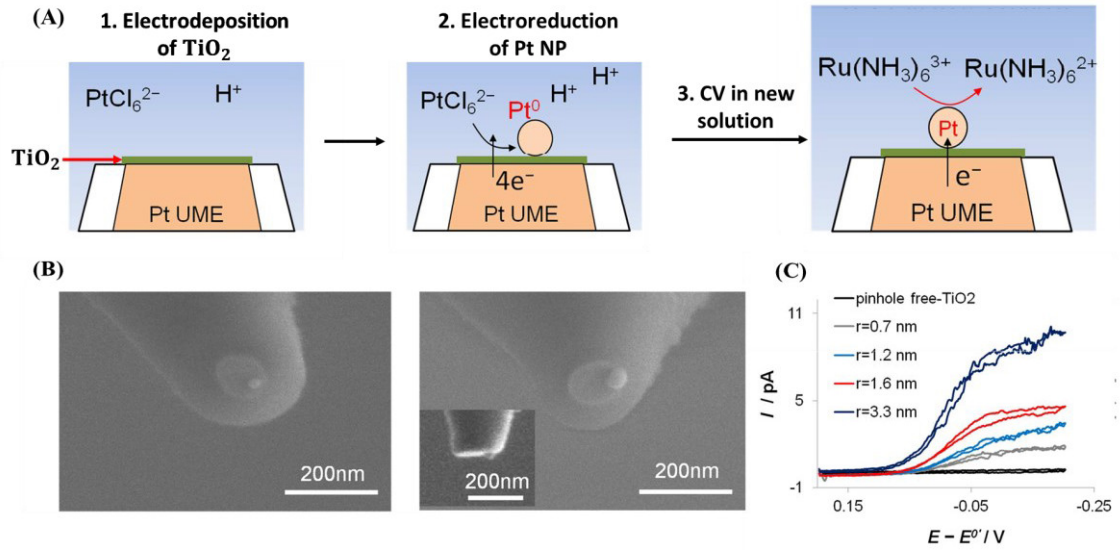

Figure 1.17. Tunneling ultramicroelectrodes. (A) Schematic illustration showing electro-reduction of single Pt NP at the surface of TiO_2 film and $Ru(NH_3)_6^{3+}$ reduction on the surface of single Pt NP. (B) SEM image showing the attachment of single Pt NPs on the surface of a tunneling UME. The inset is the side view of Pt NP. (C) Cyclic voltammetric behaviors of reduced Pt NPs with various radii at the surface of the tunneling UME. Reproduced from Ref. [129]. Copyright 2014, American Chemical Society.

Chen and coworkers reported the fabrication of graphene nanoelectrodes by the method of tunneling electrodes, schematically shown in Figure 1.18A. They first modified the surface of Au via the formation of a self-assembled monolayer (SAM) by soaking in $C_{12}H_{25}SH$ solution for 48 hours at room temperature. The graphene nanoelectrodes were fabricated via immobilization of reduced graphene oxide (r-GO) flakes onto the Au/SAM surface by quick dipping in r-GO suspensions. The SAM layer blocks electron transfer for the reduction of $Ru(NH_3)_6^{3+}$, while graphene enables electron tunneling to the redox species. Figure 1.18B shows the steady-state voltammograms of graphene tunneling nanoelectrodes with various sizes, and representative AFM images of r-GO flakes are shown in Figure 1.18C. Before the quantitative calculation of heterogeneous kinetics of electron transfer at the surface of r-GO flakes, they assumed the flake has a disk shape, with an effective diameter determined by the dimensionless limiting current shown in Figure 1.18B. Based on the numerical fitting of the voltammetric responses, the standard rate constant (k^0) of reduction at the surface of r-GO flakes can be extracted via the Butler-Volmer equation. The obtained k^0 value is as high as 9-10 cm/s, which is close to that on metal electrodes and much higher than those reported on the basal planes of HOPG.

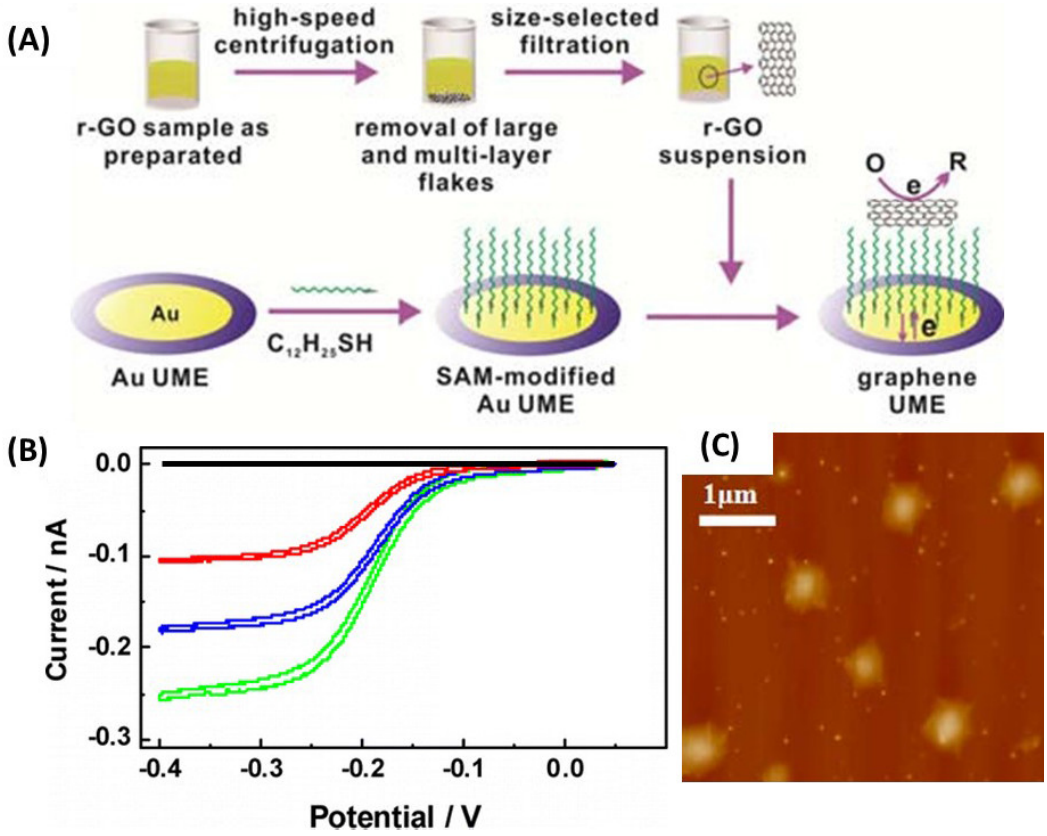

Figure 1.18. Graphene tunneling nanoelectrodes. (A) Schematic diagram of fabricating graphene UME. (B) Cyclic voltammograms recorded at the bare Au/SAM electrode (black curve) and graphene-modified Au/SAM UMEs with different sizes (red, blue and green curves represent the increasing size of graphene). The solution contains 10 mM $Ru(NH_3)_6^{3+}$ and 1 M KCl. [scan rate] = 10 mV/s. (C) Representative AFM images of r-GO in suspensions. Reproduced from Ref. [76]. Copyright 2013 American Chemical Society.

Unwin and coworkers employed the micropipette as a fluidic device to deliver Au NPs to the surface of SAM modified Au substrate electrode in order to study Au NP mediated faradaic reactions, as schematically shown in Figure 1.19A. Meniscus contact forms between the micropipette and the substrate electrode, resulting in the formation of an electrochemical cell. This technique is known as scanning electrochemical cell microscopy (SECCM). The oxidation of $Fe(CN)_6^{4-}$ to $Fe(CN)_6^{3-}$ is hindered on various SAM/Au electrodes while typical redox peaks of species are recorded at the bare Au (see Figure 1.19B). In the presence of Au NPs in the micropipette, electron tunneling is mediated and clear distinctive current spikes are observed at a passivated substrate electrode, as shown in Figure 1.19C. The authors combined SECCM with AFM force measurements to study the impact of surface chemistry on nanoparticle-electrode interactions. Three SAMs are compared with different terminal groups, two hydrophilic groups (OH_{SAM} and $COOH_{SAM}$) and one hydrophobic group ($CH_{3,SAM}$). They found the interaction forces have significant effects on NP collisions: when Au NPs interact weakly with OH_{SAM} surfaces, the frequency of collision ($12.80 \times 10^4\ s^{-1}pM^{-1}cm^{-2}$) is relatively high due to the hydrophilic interface (lack of repulsion); when some repulsion is observed between Au NPs and $COOH_{SAM}$ interface, the frequency of collision ($4.30 \times 10^4\ s^{-1}pM^{-1}cm^{-2}$) is lower than that observed with OH_{SAM} surface, and this influence is emphasized at the hydrophilic $CH_{3,SAM}$ interface ($0.16 \times 10^4\ s^{-1}pM^{-1}cm^{-2}$) with strong repulsion.

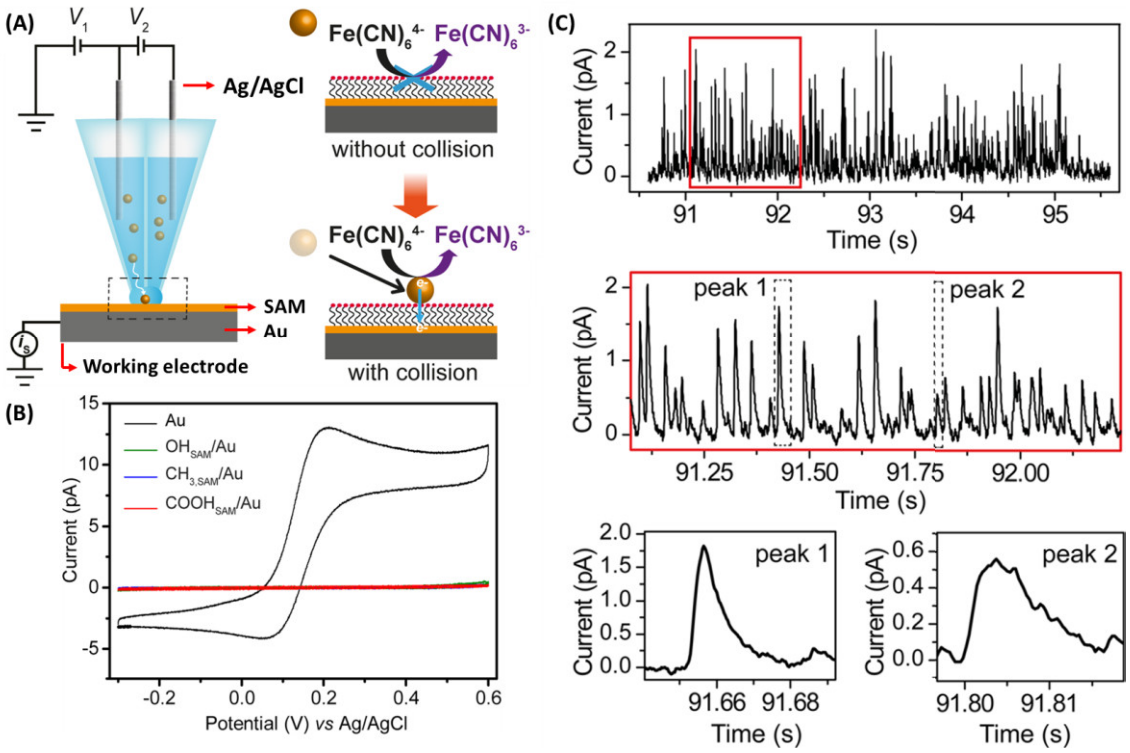

Figure 1.19. (A) Left: schematic illustration of SECCM setup. V_1 is the potential of the two reference electrodes relative to the working electrode connected to the ground. V_2 is the applied potential between two reference electrodes (Ag/AgCl) in the pipet, which is used to check the resistance of electrolyte and serve as an indicator of the droplet size. The diameter of the pipet is 3 μm. Right: schematic illustration of single Au NP detection on an SAM/Au electrode. The SAM layer inhibits electron transfer of redox species (top) while the Au NP can mediate electron transfer (bottom). (B) Microscale CVs measured at a bare Au (black line) and various SAM/Au electrodes (colored lines) in the presence of 1 mM $K_4Fe(CN)_6$ and 20 mM KCl at a scan rate of 100 mV s^{-1}. (C) *i-t* trace recorded at a hydrophilic group (11-mercapto-1-undecanol, denoted as OH_{SAM}) modified SAM/Au electrodes biased at 400 mV. The two bottom curves are zoom-in the current trace. Reproduced from Ref. [130]. Copyright 2015, American Chemical Society.

1.2.3 Electrolysis

Depending on the nature of particles, single particle electrolysis can be divided into hard particles (e.g., Ag NP, Au NP, Pt NP) and soft particles (e.g., emulsion droplet, micelles, vesicles). We will separately review the representative works in both types.

1.2.3.1 Single particle electrolysis (hard particles)

In 2011, Compton and coworkers first proposed to quantify the size of Ag NPs based on Faraday's law of electrolysis.[64] They applied a sufficient potential to achieve direct oxidation of Ag NPs upon contact with the substrate electrode, generating a spike-shaped current signal, as shown in Figure 1.20 A and B. The frequency of collisions scales linearly with the increasing concentration of Ag NPs (see Figure 1.20C). The total charge passed is obtained by the integration of the current spike. Assuming Ag NP is spherical and undergoes complete oxidation, the integration of each current event provides an amount of charge (Q), which can be used to deduce the size of the silver nanoparticle by the following equation:[131]

$$r = \sqrt[3]{\frac{3MQ}{4\pi Fz\rho}} \tag{1.3}$$

where M, Q, F, z, ρ and r are the molar mass, the amount of charge, the Faraday's constant, the number of electron transfer per atom, the density and the radius of the particle, respectively. The Eq. (1.3) is only valid when the particle is spherical and undergoes complete oxidation. Similar studies can also be

extended to the detection and quantification of other metallic nanoparticles, such as Cu[67], and Au[132-133].

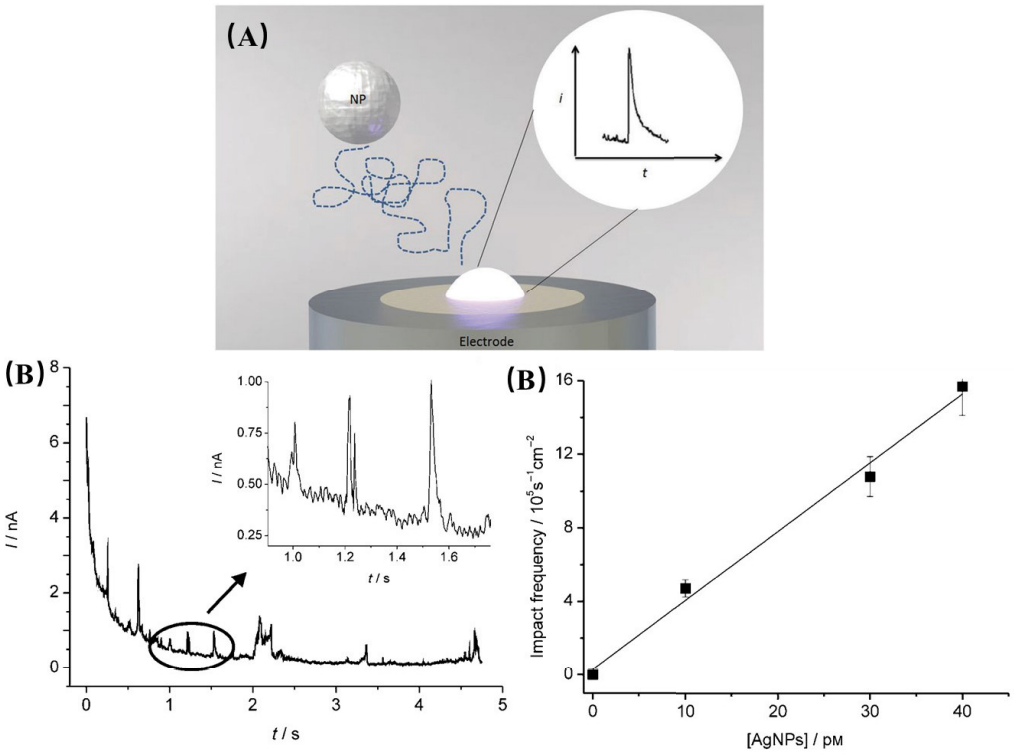

Figure 1.20. (A) Schematic of nanoparticle collisions with a relatively inert UME. Reproduced from Ref. [131]. Copyright 2017, Royal Society of Chemistry. (B) A representative chronoamperometric curve showing the oxidative collisions of Ag NPs at a glassy-carbon UME in citrate solutions. (C) The collision frequency vs. the number concentration of Ag NPs. Reproduced from Ref. [64]. Copyright 2011, John Wiley & Sons, Inc.

In terms of particle diameters ranging from 5 to 50 nm, Ag nanoparticles can undergo complete oxidation.[134-135] For larger particles, however, there exists a great controversy because those Ag NPs colliding with the electrode undergo incomplete oxidation. In 2017, the dynamic multipeak oxidation behaviors of individual Ag NPs during collisions were nearly simultaneously reported by the research groups of Long[66], Zhang[65] and Unwin[136]. These works are indicative of a complex nano-motion mechanism at the interface of nanoparticle-electrode, which is different from Compton's reported mechanism of full oxidation upon collision. Figure 1.21A shows the oxidation dynamics of single Ag NPs, where those observed multipeak behaviors consist of rapid and consecutive small peaks with the separated spacing of a few milliseconds (see the bottom curve).[65] Besides, the experimental conditions of the applied low-pass filtering frequency is also considered as an important factor for the multipeak studies (see Figure 1.21B).[137] High applied frequencies increase accordingly the temporal resolution of the measurement, but the total charge transferred (used to quantify the particle size) during dynamic collisions is theoretically independent of the applied filter frequency.[138] Considering the significantly high noise at the high applied frequency, the Compton's group suggested a small filtering frequency of 100 Hz should be applied for accurate size quantitation because of low background noise.[139]

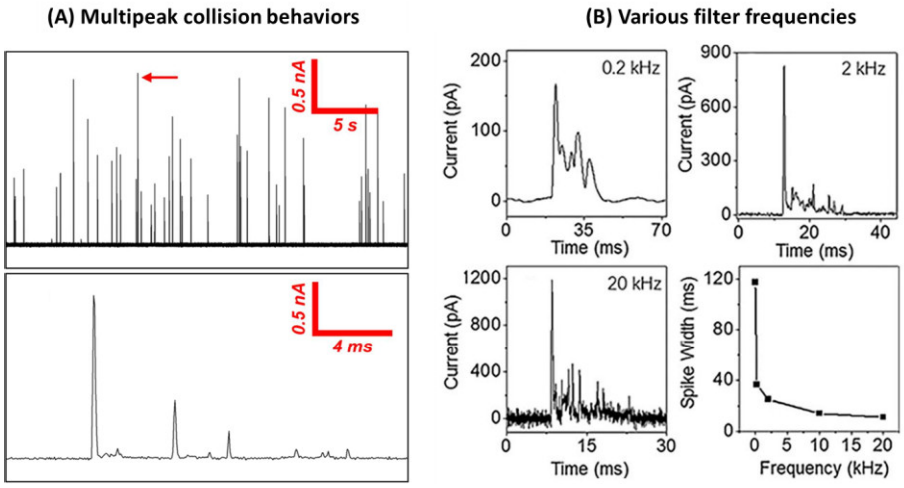

Figure 1.21. Multiple oxidative collision behaviors of single Ag NPs. (A) The representative multiple collision behaviors of 60 nm diameter Ag NPs on the surface of Au at 0.6 V vs. Ag/AgCl. The bottom curve is zoom-in trace of the event (in the upper curve) indicated by the red arrow. Reproduced from Ref. [65]. Copyright 2017, American Chemical Society. (B) Complex oxidative collision behaviors of Ag NPs on the surface of Au at 0.6 V vs. Ag/AgCl at various filter frequencies ranging of 0.2 kHz, 2 kHz and 20 kHz. The relation is shown in the bottom right between the spike width and the filter frequency of a low-pass Bessel filter. Reproduced from Ref. [137]. Copyright 2017, American Chemical Society.

Unwin and coworkers proposed the continuous striping process of single Ag NP at the surface-confined area to explain the periodic current-time pattern (see Figure 1.22). The Ag NP first enters the tunneling region, and the part in closer contact with Au UME undergoes electro-oxidation, followed by being pushed away by electrochemical propulsion. Then the oxidation process occurs again and repeats until Ag NP is completely consumed.[136] However, the dynamic nano-motion mechanism of electrochemical behaviors of individual silver nanoparticles is still under active investigation.[140]

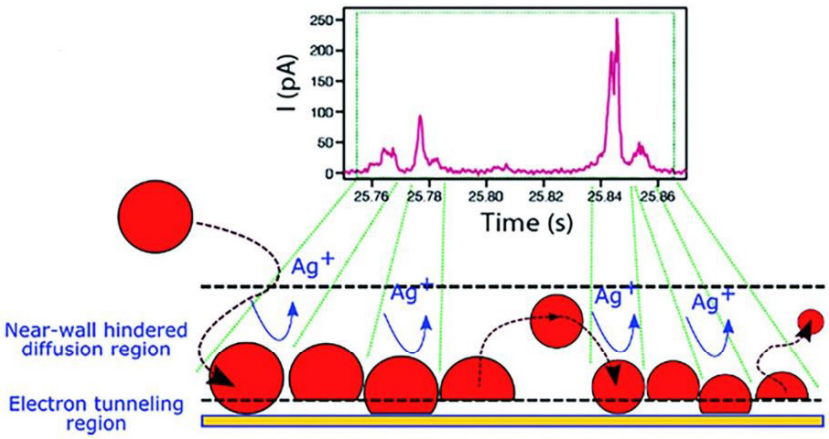

Figure 1.22. Schematic illustration of multipeak behaviors due to the electrochemical dissolution of single Ag NP on the Au electrode. An exemplar i-t trace reflecting the nano-motion of Ag NP is shown above. Reproduced from Ref. [136]. Copyright 2017, Royal Society of Chemistry.

Very recently, Long and coworkers investigated the interaction-modulated dynamic electrochemical behaviors, based on the theoretical predictions, of the oxidation of single Ag NP.[140] They first used density functional theory calculations to predict the interactions of nanoparticles based on their adsorption properties, and then established an experimental framework to test the prediction. According to the theoretical calculations, the oxidized product AgO_x has strong interaction with the surface of Au, and the oxidized Ag^+ has medium interaction with the surface of Au but higher than with the surface of C, as shown in Figure 1.23A. Under the weak interaction between single Ag NP and C UME, the oxidation of single Ag NP shows typical multipeak collision behaviors; in contrast, under the medium interaction, the oxidation of Ag NP showed two major current patterns, a single large spike and a spike

with undulating terrain, respectively. For both cases, Ag NP undergoes incomplete dissolution in an alkaline solution. The current features are attributed to the transient weakly bound state between adsorption and desorption due to the weak adsorption. In contrast, under the strong interaction between AgO_x and Au UME, the Ag NP undergoes complete oxidation showing a spike with an undulating terrain, and the electro-oxidation of Ag NP is evidenced as the rate-determining step. They performed electrochemical size measurements of single Ag NPs under the case of the strong interaction, showing that the median sizes measured by electrochemistry (Figure 1.23B) match well with the TEM results (Figure 1.23C). During their studies, the maximum size of single Ag NP undergoing full oxidation is pushed to ~75 nm. Bringing closer comparison, size distribution by electrochemical measurements always underestimate the results by TEM. The authors explained that the electrochemical measurements were recorded at a sampling rate of 100 kHz and an internal low-pass Bessel filter frequency of 5 kHz, having the time resolution of 66 µs and the background noise of 20 pA. Collision events shorter than 66 µs and the current signals less than 60 pA cannot be acquired accurately. Moreover, the generality and applicability of this surface-confined collision strategy to other metal nanoparticles are yet to be studied.

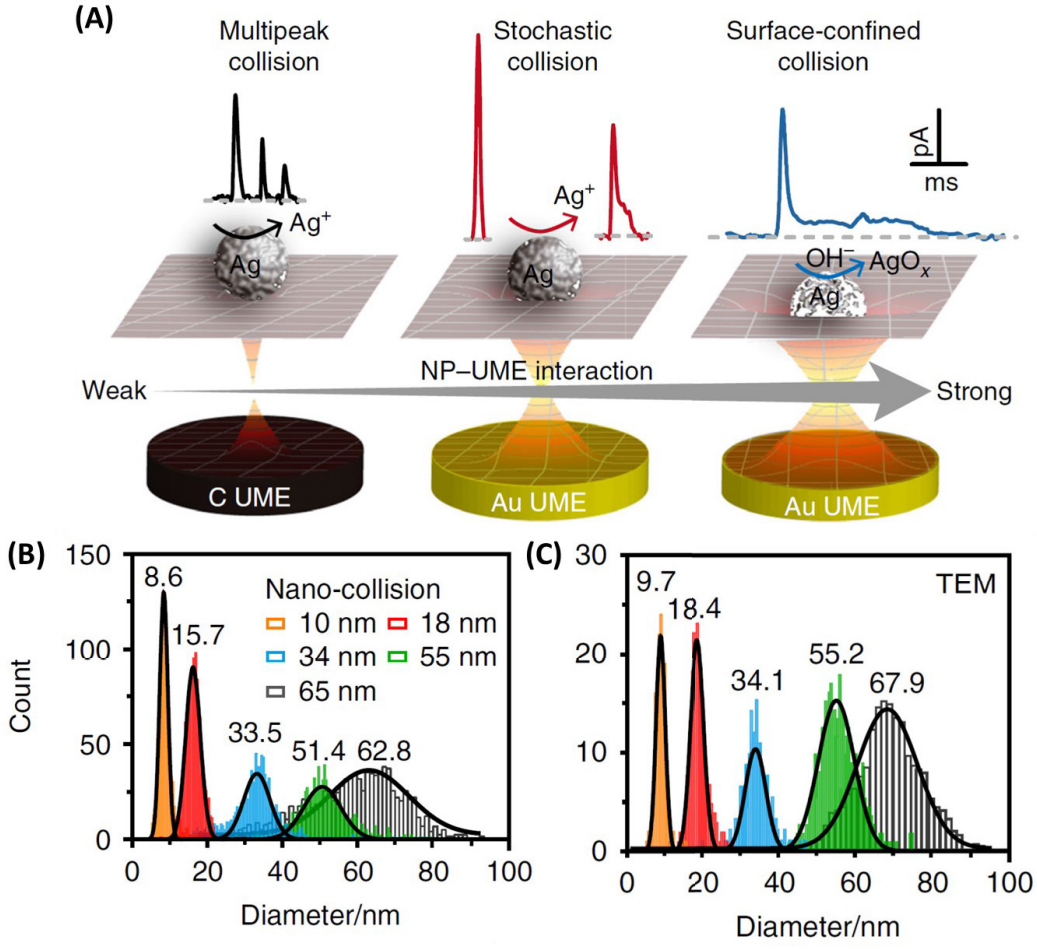

Figure 1.23. (A) Schematic illustration of various collision behaviors due to interaction-modulated dynamic electro-oxidation behaviors of individual Ag NPs. Three types of oxidative collision signals are observed due to the strength of interactions between Ag NPs and the substrate electrode. Comparison of (B) electrochemical size measurement of Ag NPs by surface-confined collisions and (C) the standard method of the size measurement by TEM. Reproduced from Ref. [140]. Copyright 2020, Nature Publishing Group

1.2.3.2 Single droplet electrolysis (soft particles)

In 2014, Bard and coworkers reported the study of electrochemical collisions of single "soft particles", for example, emulsion droplets.[19] Electrochemically active redox molecules (e.g., ferrocene) are added to a toluene-in-water emulsion droplet in the dispersed phase (see Figure 1.24A). The emulsion droplet serves as a reactor for redox species, and under an appropriate bias potential (e.g., +0.5 V vs. Ag/AgCl),

ferrocene oxidation occurs once the droplet collides with the surface Au, generating spike-shaped current enhancement (see Figure 1.24B). Under the premise of spherical droplets, the droplet diameter of the emulsion droplet can be estimated by the integration of charge in each current spike according to the Faraday's law of electrolysis shown in the Eq. (1.3), which is similar to the analysis of hard particles mentioned previously. The rate of droplet arrival to the electrode surface can be calculated by the frequency of the spikes.

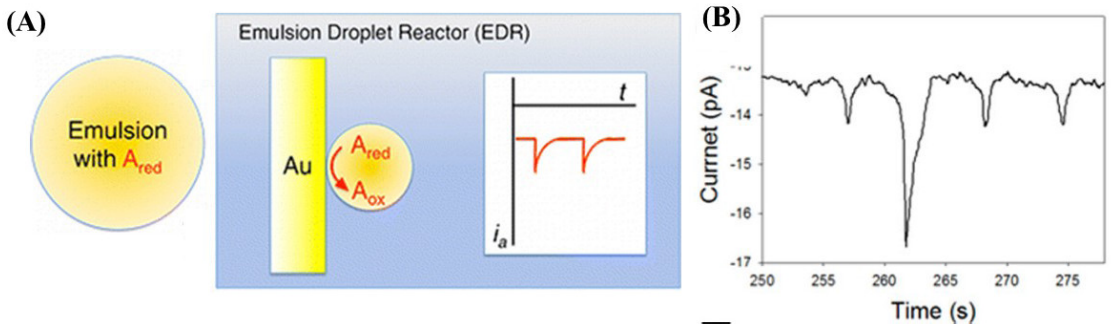

Figure 1.24. Schematic illustration of single emulsion droplet colliding at an Au UME. (A) The emulsion droplet (ED) contains a redox species A_{red}, e.g., ferrocene. When applying a high bias potential that is capable of electrochemically oxidizing the redox molecule inside an emulsion, a spike-shaped current increase is observed. (B) Magnified *i-t* trace showing clear current spikes. Reproduced from Ref. [19]. Copyright 2014, American Chemical Society.

Later, Kim and Bard reported newly extended results based on the previous emulsion droplet reactor.[75] They prepared oil in water emulsion droplets, where 7,7,8,8-tetracyanoquinodimethane (TCNQ) acts as the redox species and nitrobenzene (NB) serves as the emulsion material. At an appropriate potential (e.g., -0.45 V vs. Ag/AgCl), TCNQ is selectively electrochemically reduced inside the droplet at the surface of carbon UME (C-UME), as shown in Figure 1.25A. Under the high negative bias potential (e.g., -0.65 V vs. Ag/AgCl), the reduction of NB emulsion droplets to phenylhydroxylamine (PHA) occurs inside the NB/water emulsion (see Figure 1.25B). Both electrolysis of TCNQ or NB in each separate experiment produced a similar current spike with a slow decay. The corresponding *i-t* decay behaviors for the electrolysis of TCNQ and NB are described by Eqs. (1.4) and (1.5) respectively. The effective contact radius between droplet and UME, and the diameter of the emulsion droplet (d_{drop}) are estimated by Eqs. (1.6) and (1.7), respectively.

$$i(t) = i_p e^{-\frac{mA}{V}t} \tag{1.4}$$

$$i(t) = i_p e^{-\frac{k_{\text{eff}}A}{V}t} \tag{1.5}$$

where i_p is the peak current, m is the coefficient of mass transfer for a disk UME, A is the effective contact area between droplet and UME calculated from the corresponding effective contact radius (r_e), V is the volume of droplet, t is the electrolysis time, and k_{eff} is the effective kinetic constant.

$$m = \frac{4D_{TCNQ}}{\pi r_e} \tag{1.6}$$

$$d_{drop} = 2\sqrt[3]{\frac{3Q}{4\pi nFC_{redox}}} \tag{1.7}$$

where D_{TCNQ} is the diffusion coefficient of TCNQ in droplet, Q is the integration of charge, n is the number of electron transfer per molecule, F is the Faraday constant and C_{redox} is the concentration of redox molecules inside the droplet. The technique of a single emulsion droplet can apply to the study of a tiny electrochemical reactor and selective surface modification for the substrate electrode via a redox reaction of species inside the emulsion droplet, etc.

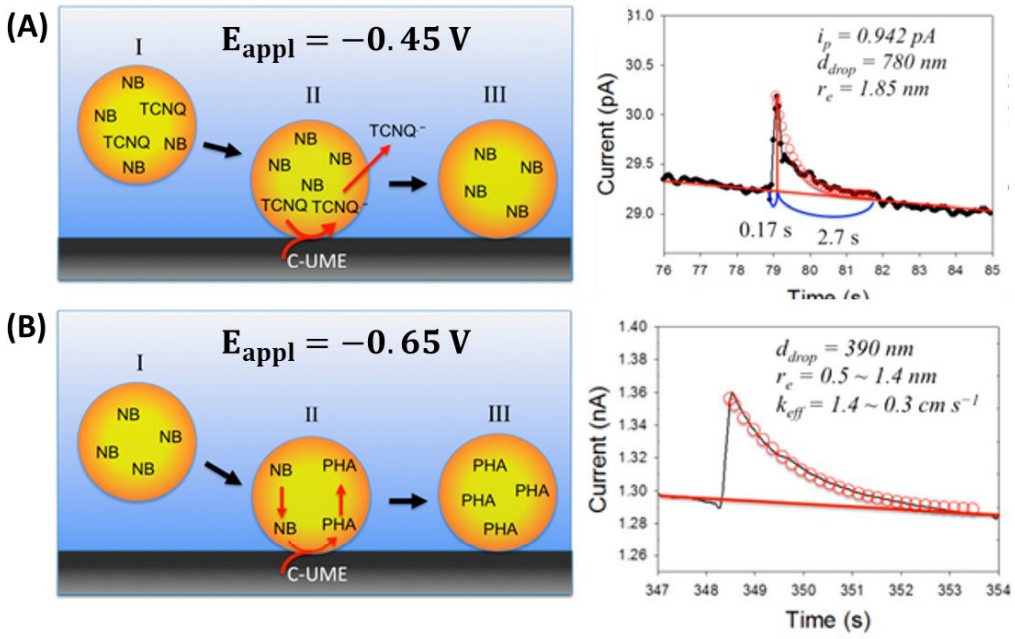

Figure 1.25. Electrochemistry inside the tiny electrochemical reactor. Left: Schematic illustration of (A) Selective electrochemical reduction of 7,7,8,8-tetracyanoquinodimethane (TCNQ) in single emulsion droplet at -0.45 V, and (B) complete electrolysis of single nitrobenzene (NB) emulsion droplet at -0.65 V at a carbon UME (C-UME). Right: Magnified *i-t* trace coupled with the superimposition of simulated *i-t* decay behavior (red circles). Reproduced from Ref. [75]. Copyright, 2014, American Chemical Society.

1.2.4 Enzymatically enhanced collisions

Bard and coworkers reported the enzymatically enhanced collisions for specific detection of single viruses (murine cytomegalovirus, MCMV) on a 1 µm diameter Pt UME.[15, 141] Figure 1.26A shows the anatomy of the virus that was incubated with the antibody and glucose oxidase conjugate (antibody/GOx). The antibody/GOx enzyme can catalyze the oxidation of glucose to gluconolactone while reducing ferricenium molecules back to ferrocene (see Figure 1.26B) at the electrified electrode surface. During their previous study, when FcMeOH oxidation reaction occurs at the electrode, the adsorption of unlabeled MCMV would effectively block the reaction, generating a staircase-shaped current decrease in the *i-t* trace.[15] After the attachment of multi GOx-conjugated antibodies to the side of the virus, an enzymatically enhanced collision of the antibody/GOx-coated MCMV is observed, resulting in a discrete of the current increase in the *i-t* trace (see Figure 1.26 C and D). Indeed, the single GOx enzyme cannot produce a detectable faradic current (ca. 0.2 fA) against the background noise (ca. 10-100 fA). However, through the attachment of GOx to a specific antibody by the covalent bond, the other side of the GOx-conjugated antibody in turn can bond to epitopes around MCMV. Then, GOx is highly and specifically concentrated around the surface of MCMV, producing the order of magnitudes of picoamperes.

Based on the antibody-epitope interaction, the enzymatically enhanced collision has high specificity, and the amplified current signals rely on the conjugation of the GOx enzyme to the primary antibody. During conventional potentiostat, one GOx enzyme cannot produce detectable current singles, and thus, the preconcentration of GOx enzymes around the virus should be used to amplify the current signal. In other words, a critical number of conjugated enzymes around the virus is required to achieve observable signal amplification. This is the first example of specific detection in the field of SEE, opening interesting perspectives in sensing.

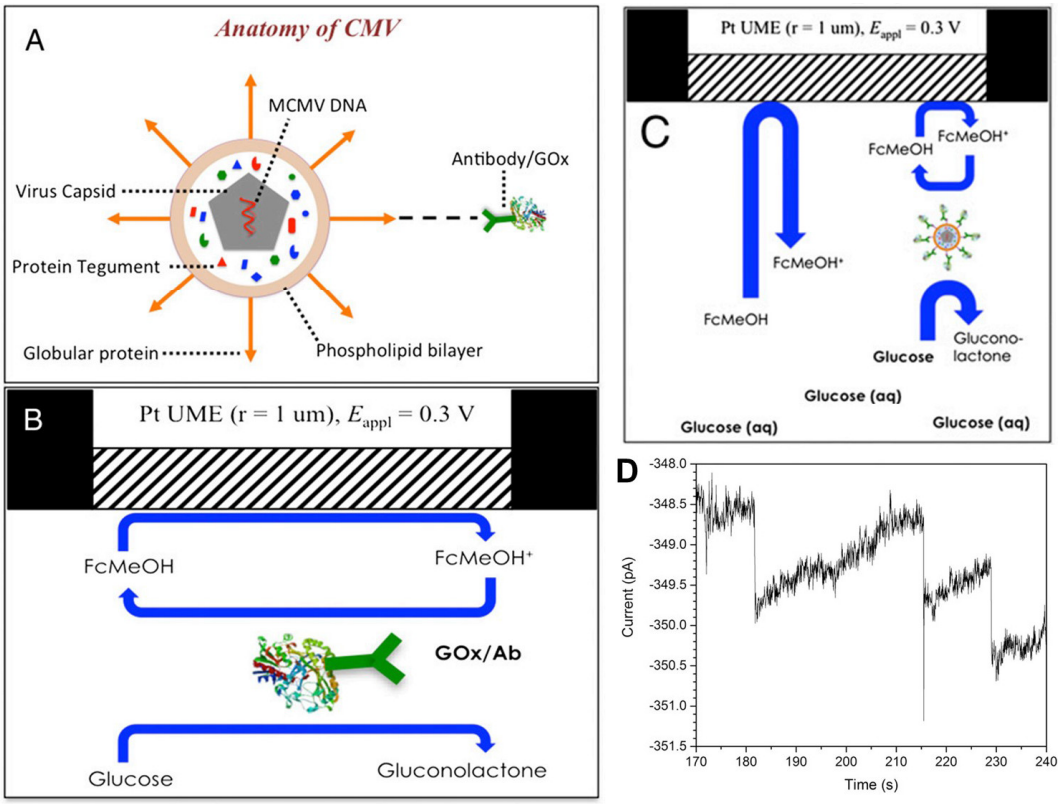

Figure 1.26. (A) Schematic structure of single murine cytomegalovirus (MCMV) viron and the interaction of its surface globular protein with an antibody modified glucose oxidase (Antibody/GOx). (B) Schematic illustration of the antibody and GOx conjugate that catalyzes the glucose oxidation while reducing ferrocenium back to ferrocene. (C) Schematic illustration of the current feedback mechanism from a virus covered by GOx. (D) Staircase-shaped current increases are observed experimentally. The solution contains 50 mM glucose and 1 mM ferrocene methanol (FcMeOH). Reproduced from Ref. [141]. Copyright 2016, National Academy of Sciences of the USA.

In summary of the first part, no matter in electrocatalytic amplification, tunneling electrodes, single droplet electrolysis (hard particles and soft particles) or in an enzymatically enhanced collision, these methods are mainly focused on redox-active nanoparticles. The study of these particles unravels catalytical properties for redox reactions, size, concentration, etc. In the next section, we will introduce collisions and analysis of single non-conducting particles, e.g., insulating polystyrene beads, silica spheres.

1.3 Fundamentals of electrochemical blocking for single entity detection

1.3.1 State-of-the-art

The methodology of "electrochemical blocking can be used to detect insulating objects. In 2004, Lemay and coworkers first demonstrated the time-resolved electrochemical blocking experiment to detect insulating particles by blocking the diffusion flux of a redox molecule to the surface of a UME,[142] although the earlier work by Gorschlüter and coworkers first proposed to use the diffusion blocking to detect single particles.[143] The blocking experiment was then revisited by Bard and later by Crooks and coworkers, etc. Figure 1.27 shows the principle of a typical electrochemical blocking experiment.[80] The UME is held at a suitable potential in which redox molecules (here ferrocene oxidation) are oxidized at a mass-transfer limited current (e.g., +0.5 V vs. Ag/AgCl for ferrocene oxidation). Upon stochastic collision and subsequent irreversible adsorption of an individual insulating object (e.g., silica or polystyrene beads), a portion of the surface area of the electrode is blocked and a discrete decrease of current (a "current step") is observed.

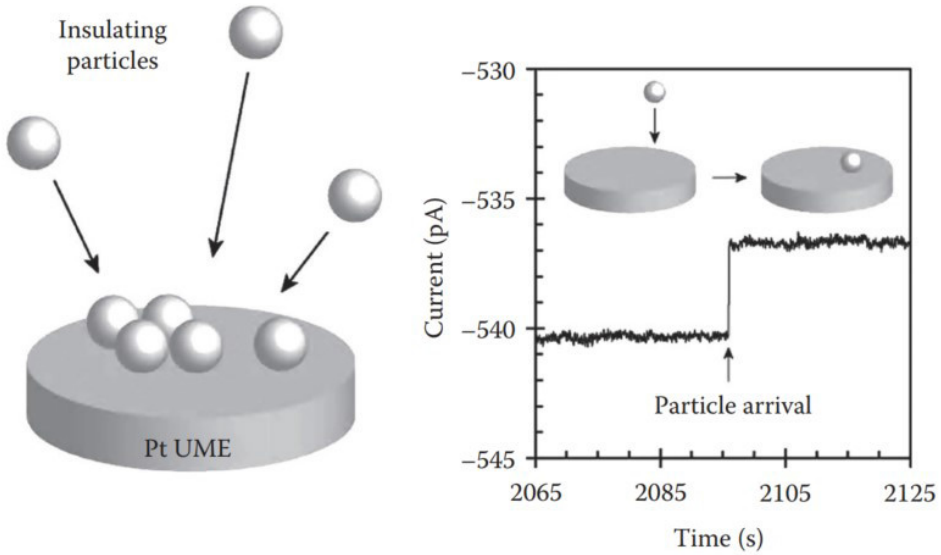

Figure 1.27. Schematic illustration of single insulating particle (e.g., silica or polystyrene beads) detected by electrochemical blocking. When insulating particles irreversibly absorb on the Pt UME, the active surface area of the Pt is partially blocked, and a staircase-shaped current decrease is observed on the *i-t* trace (the right curve). The Pt UME (2 μm in diameter) is biased +0.5 V vs. Ag/AgCl, and the solution contains 50 fM silica spheres (310 nm in diameter) and 2.5 mM FcMeOH. Reproduced from Ref. [80]. Copyright 2012, American Chemical Society.

The methodology of electrochemical blocking can also extend to the detection of single soft particle (e.g., emulsion droplet). As schematically shown in Figure 1.28A, the Au UEM is held at a low potential in which FcMeOH oxidation cannot occur inside the emulsion droplet reactor. If the emulsion droplet collides and irreversibly absorbs to the surface of Au, a staircase-shaped current decrease is observed on the *i-t* trace (see Figure 1.28B). This kind of collision behavior is similar to insulating particles, for example, carboxy lated spheres, polystyrene beads, silica beads.[82, 142, 144]

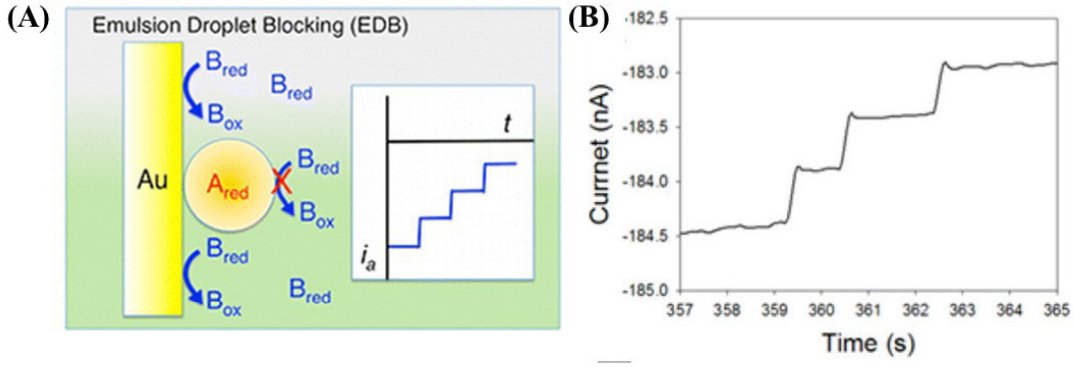

Figure 1.28. (A) Schematic illustration of emulsion droplet blocking. The Au UME is biased at a potential (e.g., 0.2 V Ag/AgCl) in which FcMeOH molecules cannot be oxidized inside the emulsion droplet. The irreversible adsorption of the emulsion droplet at the surface of Pt hinders the flux of redox molecule (here potassium ferrocyanide) to the surface of Au, leading to the staircase-shaped current decrease. Reproduced from Ref. [19]. Copyright, 2014, American Chemical Society.

Bard and coworkers later extended the blocking experiment to detect electrochemically inactive single molecules, such as antibodies, DNA molecules and enzymes, on UMEs (radius ≤ 150 nm). A schematic illustration of the blocking experiment by adsorption of inactive single biomacromolecules at the surface of UMEs is shown in Figure 1.29A. A 100 nm diameter Pt UME is held at a potential to allow oxidation of $Fe(CN)_6^{4-}$ to $Fe(CN)_6^{3-}$ under diffusion-controlled conditions, leading to a steady-state oxidation current (middle curve in Figure 1.29A). If an inactive biomacromolecule absorbs at the surface of a UME, it will partially block the oxidation of $Fe(CN)_6^{4-}$, producing a staircase-shaped current decrease in the *i-t* trace. Apart from insulating polystyrene (PS) beads, the blocking collision behaviors are also observed in the presence of various inactive molecules, including mouse monoclonal antibody (IgG), catalase (CAT), glucose oxidase (GOx), horseradish peroxidase (HRP), and plasmid DNA

(pDNA), as shown in Figure 1.29B. All the *i-t* curves (both the reference PS beads and protein molecules) produce typical staircase-shaped current decreases. The authors suggested a first approximation to convert the magnitude of current steps to the apparent radius of insulating biomolecules using the following expression:

$$r_{\Delta i} = r_{\mathrm{UME}} \sqrt{\frac{\Delta i_{ss}}{i_{ss}}} \tag{1.8}$$

Where $r_{\Delta i}$ is the apparent radius of biomolecules, r_{UME} is the electrode radius, Δi_{ss} is the average magnitudes of current steps, and i_{ss} is the steady-state current for species oxidized at the UME. The Eq. (1.8) provides a simple estimate of $r_{\Delta i}$, regardless of the edge effect on disk-shaped UMEs and the shape of the object. In the second estimation, considering that the concentration of potassium ferrocyanide is as high as 400 mM, migration is not the dominant mode of mass transfer. Then the authors assumed that the flux of redox molecules toward UME is diffusion-controlled. Then, the frequency of collision by diffusion, f_{diff}, can be used to estimate the hydrodynamic radii of biomolecules (r_h) in solution, given by:

$$f_{\mathrm{diff}} = 4DCr_{\mathrm{UME}}N_A \tag{1.9}$$

$$r_h = k_B T(6\pi\eta D)^{-1} \tag{1.10}$$

Where D is the diffusion coefficient of redox molecules, C is the bulk concentration, N_A is Avogadro constant, k_B is Boltzmann constant, T is absolute temperature, and η is the viscosity of the solution. The values of $r_{\Delta i}$ and r_h for each molecule are summarized in Figure 1.29C, in comparison with the nominal protein radii r_{PDB} from the Protein Data Bank. Compared to the values of $r_{\Delta i}$, the estimated average radius r_h is always higher than $r_{\Delta i}$ for most molecules, except the smallest one (GOx); the standard deviation for r_h is smaller than that for $r_{\Delta i}$. For ideal spherical beads (PSB), the value r_h is closer to the nominal radii r_{PDB} than $r_{\Delta i}$.

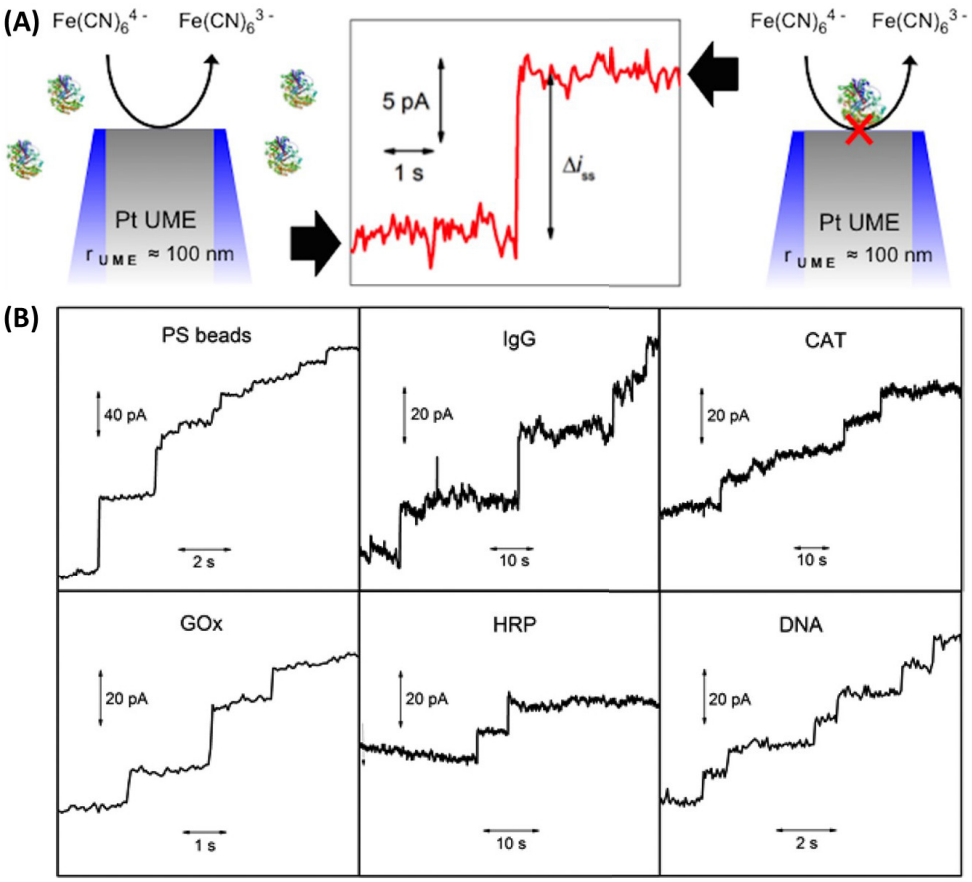

(C)

Table 1. Experimental Results from Electrochemical Collision Experiments

adsorbate	r_{PDB} (nm)	$r_{\Delta i}$ (nm)	r_h (nm)	Δi_{ss} (pA)	r_{UME} (nm)
PSB	11 ± 1	5.9 ± 3.7	12.5 ± 3.5	30 ± 7	140
HRP	1.5	2.2 ± 1.4	3.5 ± 0.5	10 ± 2.1	100
GOx	4	6.8 ± 3.4	4.5 ± 1.5	18 ± 2.3	120
CAT	6	4.6 ± 2.5	7 ± 1	20 ± 5	80
IgG	7.5	6.5 ± 4.5	9.5 ± 2.5	15 ± 2	150

Figure 1.29. The typical blocking experiment by collisions of bioparticles on UMEs. (A) Schematic illustration of a blocking experiment. An insulating bioparticle collides and absorbs at the surface of Pt UME (150 nm in diameter). The oxidation of ferrocyanide is partially blocked and a staircase-shaped current decrease in the *i-t* trace is observed. (B) Representative *i-t* curves recorded in the presence of various analytes, including 7 pM polystyrene (PS) beads, 2 pM mouse monoclonal antibody (IgG), 2 pM catalase (CAT), 2 pM glucose oxidase (GOx), 2 pM horseradish peroxidase (HRP), and 300 pM plasmid DNA (pDNA). The solution contains 400 mM $Fe(CN_6)_3^{4-}$ and the Pt UME is held at 0.8 V vs. Ag/AgCl. (C) Comparison between the data from the Protein Data Bank (PDB) and experimental results from electrochemical collisions experiments. r_{PDB}, $r_{\Delta i}$, r_h, Δi_{ss} and r_{UME} are the data from PDB, the apparent radius of adsorbates, the hydrodynamic radius of biomolecules, the average magnitudes of current steps and the radius of UME. Note that r_{diff} shown in the original publication is changed to r_h in order to better follow by the readers. Reproduced from Ref. [24]. Copyright 2015, American Chemical Society.

From Eq. (1.9) we can know the collision frequency by diffusion is expected to vary linearly with the concentration of molecules. The authors further performed collision experiments for a series of biomolecule concentrations, and a linear relation between collision frequencies and the concentration of biomolecules was obtained (see Figure 1.30).

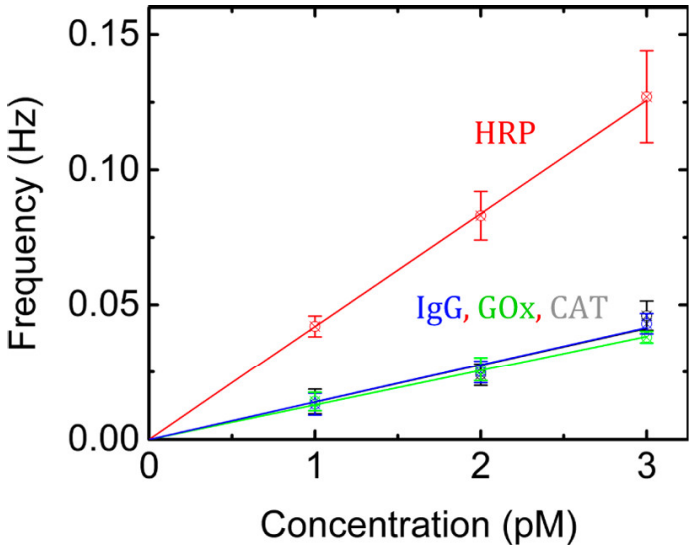

Figure 1.30. The frequency of collisions as a function of concentration for each biomolecule. Each point was averaged from at least three individual measurements and the straight lines are the linear fits of the experimental results. Reproduced from Ref. [24]. Copyright 2015, American Chemical Society.

Recently, Renault and Lemay employed the electrochemical approach to electrochemically detect single two-dimensional (2D) graphene oxide (GO) sheets (250 nm ~ 2000 nm in diameter). The GO sheets having a high electrical resistivity (> 10^3 Ω·cm) should block electron transfer for FcMeOH oxidation. This work raises an interesting issue of whether or not a 2D sheet is better at blocking than a 3D sphere with the same projected area. Figure 1.31A shows the simulated concentration profiles of FcMeOH oxidation oxidized at a diffusion-controlled regime on a UME after adsorption of a 2D sheet (top) and a 3D sphere (bottom). The concentration profiles at a sheet and a sphere are significantly different. The concentration of FcMeOH molecules at the surface of the sheet center is higher than that at the edges having a strong concentration gradient there (yellow color), while the FcMeOH concentration between a sphere and the electrode is almost constant and relatively low (blue color). This difference in the concentration gradient between a 2D object and a 3D object is emphasized in Figure 1.31B. For the bare electrode (red curve), the flux increases along with the radial direction from the center to the edge. This phenomenon is known as the “edge effect” on disk-shaped UMEs. When a 2D sheet collides at the electrode surface (green curve), the flux is almost null right above the sheet surface, but the flux at the sheet edges increases significantly. When a 3D sphere collides at the same location as a sheet (blue curve), the flux is not null under the sphere but lower than the bare UME, except for the contact region between sphere and UME. There is only a slight increase in diffusion flux at the edge of the sphere. Thus, a sphere is expected to block more diffusion flux than a sheet. Indeed, the simulated magnitudes of relative current steps caused by the 2D sheet and the 3D sphere are 0.87% and 3.77%, respectively. This article also highlights the fact that an object not in contact with the electrode surface will also produce an effective blocking step. In other words, an object that can block the volume of diffusion flux above the electrode surface will produce a blocking step.

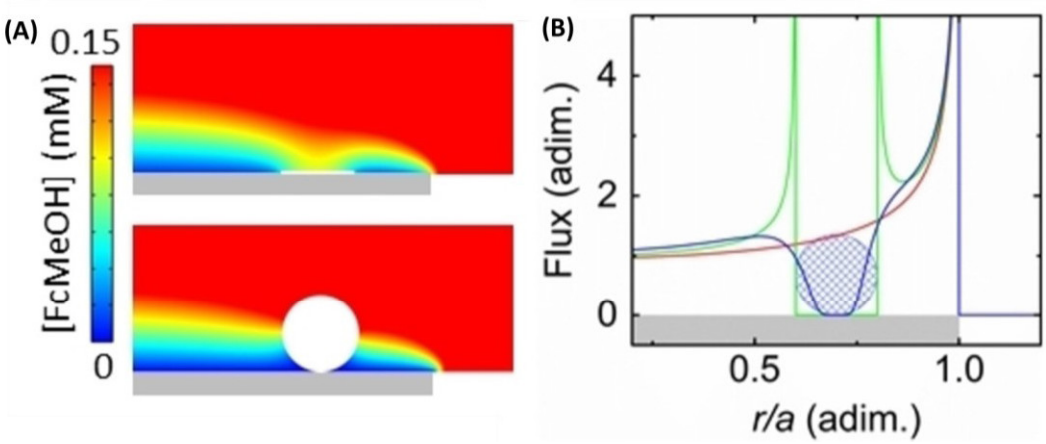

Figure 1.31. (A) Simulated concentration profiles of ferrocene methanol (FcMeOH) molecules blocked by a 2D sheet (top) and a 3D sphere (bottom). FcMeOH (the bulk concentration is 1 mM) is oxidized at diffusion-controlled regime on a UME. The grey rectangle, the yellow rectangle (over the grey rectangle at the top figure) and the white color represent the UME, the graphene oxide sheet and the blocking sphere. The left color scale is adjusted to 0.15 mM in order to emphasize the concentration gradient near/above the electrode surface. (B) Simulated diffusive flux profiles of FcMeOH at the electrode surface versus the radial position, *r*. The adimensional flux is normalized by the flux at the UME center (450 $\mu mol \cdot m^2 \cdot s^{-1}$), and the radial position is normalized by the electrode radius (a = 1μm). The red curve represents the flux at the bare electrode, and the green and blue curves correspond to the flux after adsorption of a 2D sheet and a 3D sphere at the electrode surface, respectively. Reproduced from Ref. [145]. Copyright 2019, John Wiley & Sons, Inc.

1.3.2 Interpretation of current step features

During electrochemical blocking experiments, the magnitude of current steps depends on the ratio of the particle size to the electrode radius, the concentration of redox molecules, the landing position and the surface coverage by previously adsorbed particles on the electrode. An *i-t* trace recorded on a 2 μm Pt UME at +0.5 V vs. Ag/AgCl shows magnitudes of current steps over the timescale of up to 5000 s (see Figure 1.32A). The solution contains 50 fM silica spheres (310 nm in diameter), 2.5 mM FcMeOH and the supporting electrolyte of 1 mM KCl.

At long recoding times (≥ 1000 s), hundreds of collision events were observed from the *i-t* trace. However, the minimum number of silica spheres to pave the entire surface of UME (formation of a monolayer) is calculated to be 10. Thus, the multi-layer adsorption of the silica sphere should be considered at long times. The average magnitudes of current steps continue to decrease with the adsorption of silica spheres until approaching roughly 60% of the diffusion-limited steady-state current recorded in the absence of silica beads (see the inset in Figure 1.32A). The decrease in the current step magnitude with time reflects the increasing surface coverage by insulating spheres; as additional silica spheres irreversibly adsorb at the electrode surface, the total flux to the electrode surface becomes dominated by the voids in the multi-layer spheres rather than the surface area of the bare electrode. Thus, the amount of relative bocking volume decreases with time.

A plot of magnitudes of current steps with time recorded in a high concentration of supporting electrolyte, 5 mM KCl, is shown in Figure 1.32B. The magnitude of current steps decreases more slowly than that measured in 1 mM KCl. At a high concentration of supporting electrolyte, the collision frequency (0.016 Hz) is smaller than that measured at 1 mM KCl (0.075Hz). Thus, the bead surface coverage at the electrode surface for 5 mM KCl should be smaller than that for 1 mM KCl. The decreasing trend of current step magnitudes with time at a high concentration of the electrolyte is accordingly relatively slow.

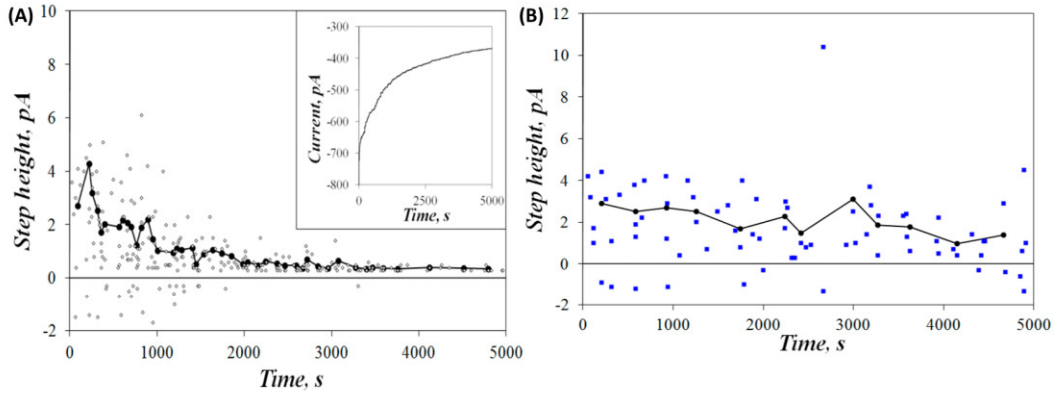

Figure 1.32. *i-t* trace showing the decreasing trend of current step magnitudes with time recorded at a 2 μm diameter Pt UME held at +0.5 V vs. Ag/AgCl. The solution contains 50 fM silica spheres (310 nm in diameter), 2.5 mM FcMeOH and either (A) 1 mM KCl, and (B) 5 mM KCl supporting electrolyte. Each point represents one current step event and current steps are counted by the time sequence of occurrence. The black dots show the average of every five current steps in sequence. Reproduced from Ref. [80]. Copyright 2012, American Chemical Society.

Apart from typical current steps, unusual current oscillating features are occasionally observed, as shown in Figure 1.33. These oscillating features cannot be simply explained by irreversible adsorption or bouncing at the UME surface. Figure 1.33A presents one case where one decreasing current step feature is observed following by an increasing step feature having an equal magnitude of the current step to the decreasing magnitude. This reversal step feature is ascribed to the adsorption and desorption of the same particle at the electrode surface. Figure 1.33B presents a single step punctuated by two small steps, and no additional step features are observed adjacently. The authors thought that such tightly spaced current step features do not result from adsorption of multiple beads at the electrode, but the dynamic movement of one particle from one location to the other locations at the electrode, eventually stopping at a relatively stable adsorption site. Such features can reflect the adsorption and the rearrangement of particles landing on the surface. Figure 1.33C shows a typical oscillating current feature due to the apparent instability of absorbed particles at the electrode surface. These oscillations are occasionally observed only for small spheres (310 nm diameter silica spheres), rather than large spheres (520 nm diameter PS beads). Lemay and coworkers also observed such oscillating features with nanometer-scaled beads (e.g., 50 nm diameter CdSe spheres and 300 nm diameter carboxylated latex beads), but not for micrometer-scaled beads (1 μm diameter spheres). Bard *et al.* thought these oscillations might reflect apparent instability of absorbed particles at the electrode surface as it moves between two closely spaced adsorption sites, for example, the surface defects or collections of particles. Lemay *et al.* attributed such current oscillations to the repetitive competition between electroosmosis and Brownian motion for nanometer-scaled beads, while for large particles, Brownian motion is overwhelmed by electrostatics at the electrode surface, and thus only stable current steps were observed.[142] It seems that the step oscillations due to particle movement or rearrangement might be size-dependent.

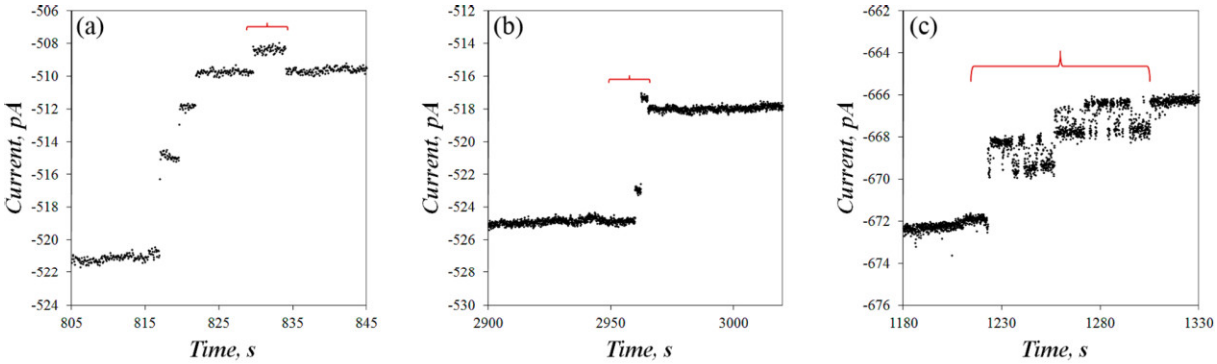

Figure 1.33. Highlighted oscillating features found in chronoamperograms due to the particle movement at a 2 µm diameter Pt UME. The solution contains 2.5 mM FcMeOH and 1 mM KCl. (a) Adsorption and desorption of particle; (b) Movement of one particle; (c) apparent instability of one or more adsorbed particles at the electrode surface. Reproduced from Ref. [80]. Copyright 2012, American Chemical Society.

Later, Crooks and coworkers developed correlated optical and electrochemical measurements to carry out detect single fluorescent microbeads at a 10 µm diameter Pt UME.[81] The landing position and movement of fluorescent microbeads at the electrode surface are tracked by fluorescent microscopy. At the same time, the Pt UME is held at +0.5 V vs. Ag/AgCl at which 1,1'-ferrocendimethanol (FcDM) molecule is oxidized under diffusion-controlled mass transfer limit. A series of numbered micrographs show the numbered collisions of polystyrene beads at the surface of Pt, together with the simultaneous *i-t* trace (see Figure 1.34). For example, bead 1 hits the surface of Pt (see frame 1 in Figure 1.34a) and produce a staircase-shaped current decrease (see Figure 1.34b); bead 2 first lands closer to the electrode center (about 2.2 µm away from the edge) and then moves to the edge while bead 3 simultaneously hits the surface, producing a large coupled current step (Figure 1.34c); double beads 7 and 8 appear to oscillate at the electrode surface shortly after landing at the surface of Pt (frames 7-8 in Figure 1.34a), resulting in a large baseline noise in the *i-t* trace (Figure 1.34d).

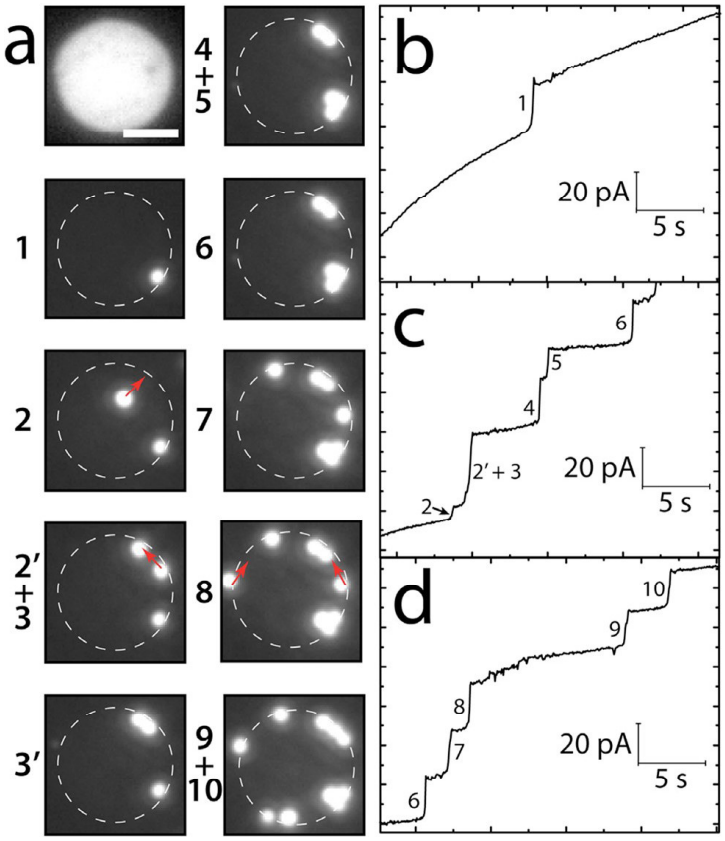

Figure 1.34. Simultaneous opto-electrochemical measurements of particle collisions at a 10 μm Pt UME. (a) A group of optical micrographs shows a discrete of bead collisions on the surface of Pt (dash circle). The optical microscopy tracks the landing positions of beads (each frame) or the movement of beads (indicated by the red arrow) on the surface of Pt. (b-d) Simultaneous *i-t* trace corresponding to movie frames in numbers in each panel of (a). The current convention shows decreasing oxidation current upward, and thus bead collisions result in a current decrease from FcDM oxidation. Note that after collisions of double beads 7-8, beads move on the surface along the direction of red arrows and produce a large background noise in the *i-t* trace between the interval of beads 8 and 9 in part (d). Reproduced from Ref. [81]. Copyright 2013, American Chemical Society.

Correlated opto-electrochemical measurements confirm the oscillating behaviors of beads at the electrode surface. The authors further correlate the magnitude of current steps to the corresponding landing positions observed optically at the surface of Pt by fluorescent microscopy. Figure 1.35A plots the average magnitude of current steps versus the indicated colliding positions from the center of UME, together with the simulated relation between the magnitude of current steps and the colliding positions. For the same size of bead, the current step magnitude can differ by a factor of around 4 times, depending on if it collides on the edge of Pt (where the flux is the highest) or at the center of Pt (where the flux is the lowest), which matches well with the simulated current step i_{step} along with the radial direction. For disk-shaped UMEs, the diffusion flux along the radial direction is not uniformly accessible. In other words, the edge effect exists on the surface of disk-shaped UMEs. The edge effect is emphasized in Figure 1.35 B and C, during which the closer to the edge, the more flux of FcDM molecules is blocked; thus, the magnitude of current steps is higher than other locations away from the edge (inside the UME).

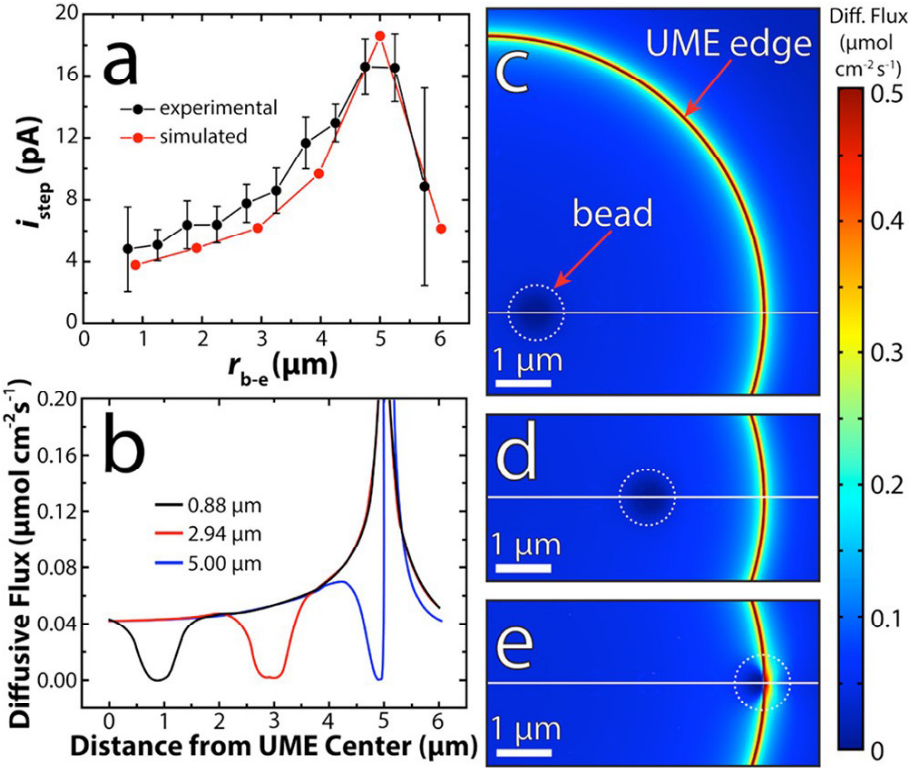

Figure 1.35. Opto-electrochemical evidence showing the relation between the magnitude of current steps i_{step} and the corresponding landing positions r_{b-e}. (a) Plot of i_{step} versus r_{b-e}. The black symbols with the error bars (95% confidence interval) represent the experimental results that are binned into increments of 0.5 μm, as a comparison with the red dotted line from the simulation results. The simulated i_{step} is the difference in the steady-state current measured at a particle (1.03 μm in diameter) centered at the indicated distance from the electrode center versus the steady-state current at the bare electrode (10 μm in diameter). (b) Simulated diffusive flux profiles across the length of the electrode radius for various values of r_{b-e}. The simulated maximum flux is 4.2 $\mu mol \cdot cm^{-2} \cdot s^{-1}$, but the scale is shortened in order to better compare the effect of the insulating beads. (c-e) Diffusive flux over a portion of the electrode surface for r_{b-e} = 0.88 μm (c), 2.94 μm (d), and 5.00 μm. The white dash circle and white line indicate the location of the spheres and the electrode radius. Reproduced from Ref. [81]. Copyright 2013, American Chemical Society.

1.3.5 Other experimental considerations

The frequency of collision of individual analytes (either conducting or non-conducting analytes) with a UME is considered as a measure of their concentration. However, for an ultralow concentration of below 1 fM, a thousand seconds are required to observe few collisions. Thus, the concentration determination by statistical collision frequencies would be a lengthy process. Boika and Bard proposed an alternative method, time of first arrival (TFA), to estimate the ultralow concentration of analytes (e.g., spheres, nanoparticles, macromolecules) below 1 fM. TFA is defined as the duration from the moment of recording to the first observed collision event, as shown in Figure 1.36A. The use of TFA as a concentration indicator of analytes relies on the assumption that the distance of analytes traveling at the timescale of TFA is comparable (but not equal) to the interspecies separation distance (a) in solution. The interspecies separation distance is estimated by the following equation:

$$a = (CN_A)^{-1} \tag{1.11}$$

Where C is the concentration of analytes and N_A is the Avogardo constant. The values of a for various analyte concentrations are given in Figure 1.36B. It is noted that when the concentration is on the order of fM or below, the separation distance exceeds the typical dimensions of microelectrodes. They separately studied the method of TFA for the determination of analyte concentration, where mass transfer of analytes is solely predominately either by migration or by diffusion.

(i) If the transport of analytes is only by migration, then time of first arrival (t_{1m}) is described by:

$$t_{1m} = \frac{4}{3}\frac{\kappa}{\mu I}(0.62a)^3 \tag{1.12}$$

Where κ, μ, and I are the electrical conductivity of the solution, the mobility of the analytes, and the steady-state current. The term of $0.62a$ represents the average traveling distance of analytes at the timescale of TFA. The derivation of the Eq. (1.12) is solid only when the transport of analytes is dominated by migration.[80, 142] Then, the fundamental relation between the analyte concentration can be established by combining the Eq. (1.10), given by:

$$C = \frac{4}{3}\frac{(0.62a)^3\kappa}{\mu I N_A}{t_{1m}}^{-1} \tag{1.13}$$

Thus, at migration-controlled mass transfer, the concentration of analytes scales linearly with the inverse TFA. Figure 1.36C shows experimental and theoretical results for TFA versus the concentration of analytes. The theoretical result (open squares in Figure 1.36C) obtained using the Eq. (1.13) matches well with the experimental observation.

(ii) If the transport of analytes is only controlled by diffusion (i.e., the analyte is not charged or the concentration of supporting electrolyte is sufficiently high such that migration is negligible), TFA is measured by the change in OCP of Au immersed in 15 mM hydrazine solution. The uncharged Pt NPs act as the analyte and once Pt NP diffuses to the surface of Au and catalyzes the oxidation of hydrazine. Then the OCP of Au shifts to a more negative potential, resulting in a noticeable OCP change. The simulated relation of TFA expressed by a factor f_N versus the concentration of analytes is given below:

$$f_N = \frac{1}{\sqrt{2\pi}} DCN_A r_{el} \tag{1.14}$$

Where $\frac{1}{\sqrt{2\pi}}$ is the normalized constant and r_{el} is the electrode radius, and other parameters are the same meaning as defined. A linear relation is expected in the experimental data shown in Figure 1.36D, but the wide standard deviation bars are observed, possibly due to the uncertainty of stochastic collision. However, for mixed modes of transport in the presence of both migration and diffusion, no straightforward information for analyte concentration by TFA analysis was provided.

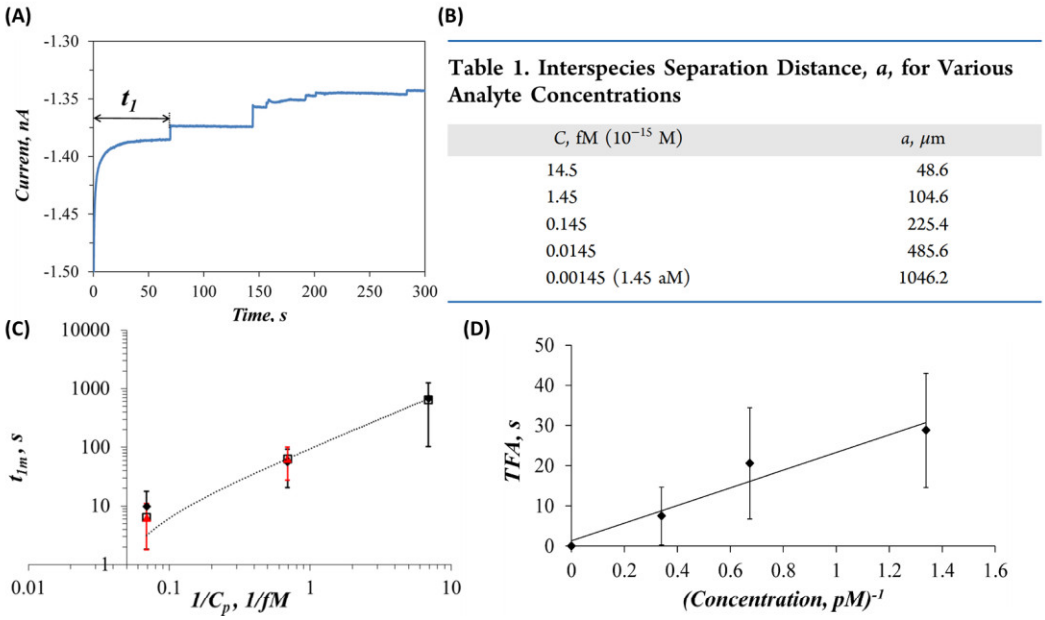

Figure 1.36. A measure of the ultralow concentration of analytes by the method of TFA at a UME. (A) *i-t* trace shows a discrete of decreasing current steps in the presence of insulating particles recorded at a 5 μm Pt UME in 2 mM FcMeOH. TFA (indicated by t_1) is measured by the duration between zero time and the first observed collision event. (B) The interspecies separation distance for an ultralow concentration of analytes. (C) Experimental results of TFA by migration versus the inverse particle concentration (C_p^{-1}). The TFA is measured by adsorption of the first insulating sphere (1 μm diameter) at the surface of Pt held at a sufficient potential to achieve FcMeOH oxidation at mass-transfer limit. Black diamonds (◆) represent experimental data with error bars obtained from at least ten individual measurements. Red triangles (▲) represent the simulation results. Analytical solutions obtained by the Eq. (1.12) are given by open squares (□). (D) Experimental results of TFA by diffusion as a function of the concentration of Pt NPs in power (-1) recorded at a 10 μm Au UME. The solution contains 15 mM hydrazine and 5 mM PBS solution (pH = 7). The TFA value of collisions was determined by the change in the OCP value. Reproduced from Ref. [146]. Copyright 2015, American Chemical Society.

1.4 The objective of the thesis

This dissertation is aiming to develop the methodology of electrochemical blocking, establishing an elegant and straightforward methodology into a versatile and quantitative analytical tool for single particle detection. First, a hemispherical UME was fabricated to remove the edge effect on disk-shaped UMEs in order to perform accurate size measurements during particle collisions and simultaneously the total concentration of beads in suspension. Using finite element simulations, the relationship between the distribution of current step magnitudes and the size distribution of the bead will be considered. Besides, the frequency of collision for a given size of a bead will be related to the concentration of bead in solution. The respective contributions of migration and diffusion to the frequency of collision will be discussed.

Second, the concept of electrochemical blocking for single particle detection will be extended from insulating particles to conducting particles. In this work, we propose a methodological development of the electrochemical blocking that we called “electro-catalytic depression” (ECD). This method enables the detection of particles that are electric conductors but catalytically inert such as carbonaceous particles. The ECD method takes advantage of the difference in kinetics of electron transfer for a given inner-sphere reaction to block the current at the surface of a particle made of a material having poor catalytic properties compared to the material of the electrode. We use ECD to detect individual graphene nanoplatelets (GNPs) of a few μm long and 15 nm thick blocking the oxidation of hydrazine on a 5 μm radius Pt UME. We will show how the analysis of a “blocking-type” signal originally developed for insulating beads can be extended to the detection of conducting particles. The size distribution of the current steps, the stacking of multiple GNPs on the UME, and the frequency of collisions are studied and compared to models developed for single particle collision.

The last work is the correlated optical and electrochemical measurements. The collision behaviors between a two-dimensional (2D) object with the UME surface are not always a simple collision event (e.g., bouncing, colliding, leaving). From the analysis of current-time trace, complex transient current behaviors were observed during opto-electrochemical measurement. These complex electrochemical responses are then investigated by coupling optical microscopy and electrochemical measurements to correlate current and position/movement of the entities on the UME during collisions. A new kind of dynamic information of a 2D object laying on an electrified surface, at the single entity level, will be investigated.

1.5 Reference

1. Baker, L. A., Perspective and Prospectus on Single-Entity Electrochemistry. *Journal of the American Chemical Society* **2018,** *140* (46), 15549-15559.

2. Crooks, R. M., Concluding remarks: single entity electrochemistry one step at a time. *Faraday Discussions* **2016,** *193*, 533-547.

3. Chang, P. R.; Jian, R.; Yu, J.; Ma, X., Fabrication and characterisation of chitosan nanoparticles/plasticised-starch composites. *Food Chemistry* **2010,** *120* (3), 736-740.

4. Guo, Y. G.; Hu, J. S.; Wan, L. J., Nanostructured materials for electrochemical energy conversion and storage devices. *Advanced Materials* **2008,** *20* (15), 2878-2887.

5. Gao, M.-R.; Xu, Y.-F.; Jiang, J.; Yu, S.-H., Nanostructured metal chalcogenides: synthesis, modification, and applications in energy conversion and storage devices. *Chemical Society Reviews* **2013,** *42* (7), 2986-3017.

6. Chen, C.; Geng, J.; Pu, F.; Yang, X.; Ren, J.; Qu, X., Polyvalent nucleic Acid/Mesoporous silica nanoparticle conjugates: dual stimuli-responsive vehicles for intracellular drug delivery. *Angewandte Chemie International Edition* **2011,** *50* (4), 882-886.

7. Guo, S.; Li, D.; Zhang, L.; Li, J.; Wang, E., Monodisperse mesoporous superparamagnetic single-crystal magnetite nanoparticles for drug delivery. *Biomaterials* **2009,** *30* (10), 1881-1889.

8. Yáñez-Mó, M.; Siljander, P. R.-M.; Andreu, Z.; Bedina Zavec, A.; Borràs, F. E.; Buzas, E. I.; Buzas, K.; Casal, E.; Cappello, F.; Carvalho, J., Biological properties of extracellular vesicles and their physiological functions. *Journal of extracellular vesicles* **2015,** *4* (1), 27066.

9. Marzluff, W. F.; Wagner, E. J.; Duronio, R. J., Metabolism and regulation of canonical histone mRNAs: life without a poly (A) tail. *Nature Reviews Genetics* **2008,** *9* (11), 843-854.

10. Dick, J. E., Electrochemical detection of single cancer and healthy cell collisions on a microelectrode. *Chemical Communications* **2016,** *52* (72), 10906-10909.

11. Gooding, J. J., Single entity electrochemistry progresses to cell counting. *Angewandte Chemie International Edition* **2016,** *55* (42), 12956-12958.

12. Tomaszewska, E.; Soliwoda, K.; Kadziola, K.; Tkacz-Szczesna, B.; Celichowski, G.; Cichomski, M.; Szmaja, W.; Grobelny, J., Detection Limits of DLS and UV-Vis Spectroscopy in Characterization of Polydisperse Nanoparticles Colloids. *Journal of Nanomaterials* **2013,** *2013*, 10.

13. Poon, W. C. K.; Weeks, E. R.; Royall, C. P., On measuring colloidal volume fractions. *Soft Matter* **2012,** *8* (1), 21-30.

14. Gallego-Urrea, J. A.; Tuoriniemi, J.; Hassellöv, M., Applications of particle-tracking analysis to the determination of size distributions and concentrations of nanoparticles in environmental, biological and food samples. *TrAC Trends in Analytical Chemistry* **2011,** *30* (3), 473-483.

15. Dick, J. E.; Hilterbrand, A. T.; Boika, A.; Upton, J. W.; Bard, A. J., Electrochemical detection of a single cytomegalovirus at an ultramicroelectrode and its antibody anchoring. *Proceedings of the National Academy of Sciences* **2015,** *112* (17), 5303-5308.

16. Xiao, X.; Bard, A. J., Observing single nanoparticle collisions at an ultramicroelectrode by electrocatalytic amplification. *Journal of the American Chemical Society* **2007,** *129* (31), 9610-9612.

17. Xiao, X.; Fan, F.-R. F.; Zhou, J.; Bard, A. J., Current transients in single nanoparticle collision events. *Journal of the American Chemical Society* **2008,** *130* (49), 16669-16677.

18. Ying, Y. L.; Long, Y. T., Nanopore-Based Single-Biomolecule Interfaces: From Information to Knowledge. *Journal of the American Chemical Society* **2019,** *141* (40), 15720-15729.

19. Kim, B.-K.; Boika, A.; Kim, J.; Dick, J. E.; Bard, A. J., Characterizing Emulsions by Observation of Single Droplet Collisions--Attoliter Electrochemical Reactors. *Journal of the American Chemical Society* **2014,** *136* (13), 4849-4852.

20. Dick, J. E.; Renault, C.; Kim, B. K.; Bard, A. J., Simultaneous detection of single attoliter droplet collisions by electrochemical and electrogenerated chemiluminescent responses. *Angewandte Chemie International Edition* **2014,** *53* (44), 11859-11862.

21. Zhang, X.-W.; Hatami, A.; Ewing, A. G., Simultaneous Quantification of Vesicle Size and Catecholamine Content by Resistive Pulses in Nanopores and Vesicle Impact Electrochemical Cytometry. *Journal of the American Chemical Society* **2020,** *142* (9), 4093-4097.

22. Lebègue, E.; Anderson, C. M.; Dick, J. E.; Webb, L. J.; Bard, A. J., Electrochemical detection of single phospholipid vesicle collisions at a Pt ultramicroelectrode. *Langmuir* **2015,** *31* (42), 11734-11739.

23. Toh, H.; Compton, R., Electrochemical detection of single micelles through 'nano-impacts'. *Chemical science* **2015,** *6* (8), 5053-5058.

24. Dick, J. E.; Renault, C.; Bard, A. J., Observation of single-protein and DNA macromolecule collisions on ultramicroelectrodes. *Journal of the American Chemical Society* **2015,** *137* (26), 8376-8379.

25. Lee, J. Y.; Kim, B.-K.; Kang, M.; Park, J. H., Label-free detection of single living bacteria via electrochemical collision event. *Scientific reports* **2016,** *6*, 30022.

26. Degiacomi, M. T.; Iacovache, I.; Pernot, L.; Chami, M.; Kudryashev, M.; Stahlberg, H.; Van Der Goot, F. G.; Dal Peraro, M., Molecular assembly of the aerolysin pore reveals a swirling membrane-insertion mechanism. *Nature Chemical Biology* **2013,** *9* (10), 623-629.

27. Parker, M. W.; Buckley, J. T.; Postma, J. P.; Tucker, A. D.; Leonard, K.; Pattus, F.; Tsernoglou, D., Structure of the Aeromonas toxin proaerolysin in its water-soluble and membrane-channel states. *Nature* **1994,** *367* (6460), 292-295.

28. Freedman, K. J.; Otto, L. M.; Ivanov, A. P.; Barik, A.; Oh, S.-H.; Edel, J. B., Nanopore sensing at ultra-low concentrations using single-molecule dielectrophoretic trapping. *Nature communications* **2016,** *7* (1), 1-9.

29. Ren, R.; Zhang, Y.; Nadappuram, B. P.; Akpinar, B.; Klenerman, D.; Ivanov, A. P.; Edel, J. B.; Korchev, Y., Nanopore extended field-effect transistor for selective single-molecule biosensing. *Nature communications* **2017,** *8* (1), 1-9.

30. Bell, N. A.; Chen, K.; Ghosal, S.; Ricci, M.; Keyser, U. F., Asymmetric dynamics of DNA entering and exiting a strongly confining nanopore. *Nature communications* **2017,** *8* (1), 1-8.

31. Dekker, C., Solid-state nanopores. *Nature nanotechnology* **2007,** *2* (4), 209.

32. Hall, A. R.; Scott, A.; Rotem, D.; Mehta, K. K.; Bayley, H.; Dekker, C., Hybrid pore formation by directed insertion of α-haemolysin into solid-state nanopores. *Nature nanotechnology* **2010,** *5* (12), 874.

33. Liu, L.; Yang, C.; Zhao, K.; Li, J.; Wu, H.-C., Ultrashort single-walled carbon nanotubes in a lipid bilayer as a new nanopore sensor. *Nature communications* **2013,** *4*, 2989.

34. Geng, J.; Kim, K.; Zhang, J.; Escalada, A.; Tunuguntla, R.; Comolli, L. R.; Allen, F. I.; Shnyrova, A. V.; Cho, K. R.; Munoz, D., Stochastic transport through carbon nanotubes in lipid bilayers and live cell membranes. *Nature* **2014,** *514* (7524), 612-615.

35. Garaj, S.; Hubbard, W.; Reina, A.; Kong, J.; Branton, D.; Golovchenko, J., Graphene as a subnanometre trans-electrode membrane. *Nature* **2010,** *467* (7312), 190-193.

36. Gu, L.-Q.; Braha, O.; Conlan, S.; Cheley, S.; Bayley, H., Stochastic sensing of organic analytes by a pore-forming protein containing a molecular adapter. *Nature* **1999,** *398* (6729), 686-690.

37. Kasianowicz, J. J.; Brandin, E.; Branton, D.; Deamer, D. W., Characterization of individual polynucleotide molecules using a membrane channel. *Proceedings of the National Academy of Sciences* **1996,** *93* (24), 13770-13773.

38. Valpuesta, J. M.; Carrascosa, J. L., Structure of viral connectors and their function in bacteriophage assembly and DNA packaging. *Quarterly Reviews of Biophysics* **1994,** *27* (2), 107-155.

39. Ji, Z.; Wang, S.; Zhao, Z.; Zhou, Z.; Haque, F.; Guo, P., Fingerprinting of peptides with a large channel of bacteriophage Phi29 DNA packaging motor. *Small* **2016,** *12* (33), 4572-4578.

40. Piguet, F.; Ouldali, H.; Pastoriza-Gallego, M.; Manivet, P.; Pelta, J.; Oukhaled, A., Identification of single amino acid differences in uniformly charged homopolymeric peptides with aerolysin nanopore. *Nature communications* **2018,** *9* (1), 1-13.

41. Cao, C.; Ying, Y.-L.; Hu, Z.-L.; Liao, D.-F.; Tian, H.; Long, Y.-T., Discrimination of oligonucleotides of different lengths with a wild-type aerolysin nanopore. *Nature nanotechnology* **2016,** *11* (8), 713.

42. Shi, W.; Friedman, A. K.; Baker, L. A., Nanopore sensing. *Analytical Chemistry* **2017,** *89* (1), 157-188.

43. Lin, Y.; Ying, Y.-L.; Long, Y.-T., Nanopore confinement for electrochemical sensing at the single-molecule level. *Current Opinion in Electrochemistry* **2018,** *7*, 172-178.

44. Bard, A. J.; Zhou, H.; Kwon, S. J., Electrochemistry of single nanoparticles via electrocatalytic amplification. *Israel Journal of Chemistry* **2010,** *50* (3), 267-276.

45. Wang, Y.; Shan, X.; Tao, N., Emerging tools for studying single entity electrochemistry. *Faraday Discussions* **2016,** *193*, 9-39.

46. Lemay, S. G.; Kang, S.; Mathwig, K.; Singh, P. S., Single-molecule electrochemistry: present status and outlook. *Accounts of Chemical Research* **2013,** *46* (2), 369-377.

47. Ying, Y.-L.; Wang, J.; Leach, A. R.; Jiang, Y.; Gao, R.; Xu, C.; Edwards, M. A.; Pendergast, A. D.; Ren, H.; Weatherly, C. K. T., Single-entity electrochemistry at confined sensing interfaces. *Science China Chemistry* **2020**, 1-30.

48. Peng, Y. Y.; Qian, R. C.; Hafez, M. E.; Long, Y. T., Stochastic collision nanoelectrochemistry: a review of recent developments. *ChemElectroChem* **2017,** *4* (5), 977-985.

49. Brasiliense, V.; Berto, P.; Combellas, C.; Tessier, G.; Kanoufi, F. d. r., Electrochemistry of single nanodomains revealed by three-dimensional holographic microscopy. *Accounts of Chemical Research* **2016,** *49* (9), 2049-2057.

50. Laborda, E.; Molina, A.; Batchelor-McAuley, C.; Compton, R. G., Individual Detection and Characterization of Non-Electrocatalytic, Redox-Inactive Particles in Solution by using Electrochemistry. *ChemElectroChem* **2018,** *5* (3), 410-417.

51. Stevenson, K. J.; Tschulik, K., A materials driven approach for understanding single entity nano impact electrochemistry. *Current Opinion in Electrochemistry* **2017,** *6* (1), 38-45.

52. Fan, Y.; Anderson, T. J.; Zhang, B., Single-molecule electrochemistry: From redox cycling to single redox events. *Current Opinion in Electrochemistry* **2018,** *7*, 81-86.

53. Goines, S.; Dick, J. E., Electrochemistry's Potential to Reach the Ultimate Sensitivity in Measurement Science. *Journal of the Electrochemical Society* **2020,** *167* (3), 037505.

54. McKelvey, K.; German, S. R.; Zhang, Y.; White, H. S.; Edwards, M. A., Nanopipettes as a tool for single nanoparticle electrochemistry. *Current Opinion in Electrochemistry* **2017,** *6* (1), 4-9.

55. Edwards, M.; Robinson, D.; Ren, H.; Cheyne, C.; Tan, C.; White, H., Nanoscale electrochemical kinetics & dynamics: the challenges and opportunities of single-entity measurements. *Faraday Discussions* **2018,** *210*, 9-28.

56. Zhou, M.; Dick, J. E.; Bard, A. J., Electrodeposition of Isolated Platinum Atoms and Clusters on Bismuth Characterization and Electrocatalysis. *Journal of the American Chemical Society* **2017,** *139* (48), 17677-17682.

57. Zhou, M.; Bao, S.; Bard, A. J., Probing size and substrate effects on the hydrogen evolution reaction by single isolated Pt atoms, atomic clusters, and nanoparticles. *Journal of the American Chemical Society* **2019,** *141* (18), 7327-7332.

58. Jin, Z.; Bard, A. J., Atom-by-atom electrodeposition of single isolated cobalt oxide molecules and clusters for studying the oxygen evolution reaction. *Proceedings of the National Academy of Sciences* **2020,** *117* (23), 12651-12656.

59. Park, J. H.; Boika, A.; Park, H. S.; Lee, H. C.; Bard, A. J., Single collision events of conductive nanoparticles driven by migration. *The Journal of Physical Chemistry C* **2013,** *117* (13), 6651-6657.

60. Kim, J.; Kim, B.-K.; Cho, S. K.; Bard, A. J., Tunneling ultramicroelectrode: Nanoelectrodes and nanoparticle collisions. *Journal of the American Chemical Society* **2014,** *136* (23), 8173-8176.

61. Guo, Z.; Percival, S. J.; Zhang, B., Chemically resolved transient collision events of single electrocatalytic nanoparticles. *Journal of the American Chemical Society* **2014,** *136* (25), 8879-8882.

62. Evers, M. V.; Bernal, M.; Roldan Cuenya, B.; Tschulik, K., Piece by Piece—Electrochemical Synthesis of Individual Nanoparticles and their Performance in ORR Electrocatalysis. *Angewandte Chemie International Edition* **2019,** *58* (24), 8221-8225.

63. Kahk, J. M.; Rees, N. V.; Pillay, J.; Tshikhudo, R.; Vilakazi, S.; Compton, R. G., Electron transfer kinetics at single nanoparticles. *Nano Today* **2012,** *7* (3), 174-179.

64. Zhou, Y. G.; Rees, N. V.; Compton, R. G., The electrochemical detection and characterization of silver nanoparticles in aqueous solution. *Angewandte Chemie International Edition* **2011,** *50* (18), 4219-4221.

65. Oja, S. M.; Robinson, D. A.; Vitti, N. J.; Edwards, M. A.; Liu, Y.; White, H. S.; Zhang, B., Observation of multipeak collision behavior during the electro-oxidation of single Ag nanoparticles. *Journal of the American Chemical Society* **2017,** *139* (2), 708-718.

66. Ma, W.; Ma, H.; Chen, J.-F.; Peng, Y.-Y.; Yang, Z.-Y.; Wang, H.-F.; Ying, Y.-L.; Tian, H.; Long, Y.-T., Tracking motion trajectories of individual nanoparticles using time-resolved current traces. *Chemical science* **2017,** *8* (3), 1854-1861.

67. Haddou, B.; Rees, N. V.; Compton, R. G., Nanoparticle–electrode impacts: the oxidation of copper nanoparticles has slow kinetics. *Physical Chemistry Chemical Physics* **2012,** *14* (39), 13612-13617.

68. Ngamchuea, K.; Tschulik, K.; Compton, R. G., Magnetic control: Switchable ultrahigh magnetic gradients at Fe 3 O 4 nanoparticles to enhance solution-phase mass transport. *Nano Research* **2015,** *8* (10), 3293-3306.

69. Fernando, A.; Parajuli, S.; Alpuche-Aviles, M. A., Observation of individual semiconducting nanoparticle collisions by stochastic photoelectrochemical currents. *Journal of the American Chemical Society* **2013,** *135* (30), 10894-10897.

70. Ma, H.; Ma, W.; Chen, J.-F.; Liu, X.-Y.; Peng, Y.-Y.; Yang, Z.-Y.; Tian, H.; Long, Y.-T., Quantifying visible-light-induced electron transfer properties of single dye-sensitized ZnO entity for water splitting. *Journal of the American Chemical Society* **2018,** *140* (15), 5272-5279.

71. Kwon, S. J.; Fan, F.-R. F.; Bard, A. J., Observing iridium oxide (IrO x) single nanoparticle collisions at ultramicroelectrodes. *Journal of the American Chemical Society* **2010,** *132* (38), 13165-13167.

72. Sardesai, N. P.; Andreescu, D.; Andreescu, S., Electroanalytical evaluation of antioxidant activity of cerium oxide nanoparticles by nanoparticle collisions at microelectrodes. *Journal of the American Chemical Society* **2013,** *135* (45), 16770-16773.

73. Sepunaru, L.; Sokolov, S. V.; Holter, J.; Young, N. P.; Compton, R. G., Electrochemical red blood cell counting: one at a time. *Angewandte Chemie International Edition* **2016,** *55* (33), 9768-9771.

74. Cheng, W.; Compton, R. G., Investigation of Single-Drug-Encapsulating Liposomes using the Nano-Impact Method. *Angewandte Chemie International Edition* **2014,** *53* (50), 13928-13930.

75. Kim, B.-K.; Kim, J.; Bard, A. J., Electrochemistry of a single attoliter emulsion droplet in collisions. *Journal of the American Chemical Society* **2015,** *137* (6), 2343-2349.

76. Zhang, B.; Fan, L.; Zhong, H.; Liu, Y.; Chen, S., Graphene nanoelectrodes: fabrication and size-dependent electrochemistry. *Journal of the American Chemical Society* **2013,** *135* (27), 10073-10080.

77. Poon, J.; Batchelor-McAuley, C.; Tschulik, K.; Compton, R. G., Single graphene nanoplatelets: capacitance, potential of zero charge and diffusion coefficient. *Chemical science* **2015,** *6* (5), 2869-2876.

78. Park, J. H.; Thorgaard, S. N.; Zhang, B.; Bard, A. J., Single particle detection by area amplification: single wall carbon nanotube attachment to a nanoelectrode. *Journal of the American Chemical Society* **2013,** *135* (14), 5258-5261.

79. Stuart, E. J.; Tschulik, K.; Batchelor-McAuley, C.; Compton, R. G., Electrochemical observation of single collision events: Fullerene nanoparticles. *ACS nano* **2014,** *8* (8), 7648-7654.

80. Boika, A.; Thorgaard, S. N.; Bard, A. J., Monitoring the electrophoretic migration and adsorption of single insulating nanoparticles at ultramicroelectrodes. *The Journal of Physical Chemistry B* **2013,** *117* (16), 4371-4380.

81. Fosdick, S. E.; Anderson, M. J.; Nettleton, E. G.; Crooks, R. M., Correlated electrochemical and optical tracking of discrete collision events. *Journal of the American Chemical Society* **2013,** *135* (16), 5994-5997.

82. Bonezzi, J.; Boika, A., Deciphering the magnitude of current steps in electrochemical blocking collision experiments and its implications. *Electrochimica Acta* **2017,** *236*, 252-259.

83. Coulter, W. H., Means for counting particles suspended in a fluid. Google Patents: 1953.

84. Henriquez, R. R.; Ito, T.; Sun, L.; Crooks, R. M., The resurgence of Coulter counting for analyzing nanoscale objects. *Analyst* **2004,** *129* (6), 478-482.

85. DeBlois, R.; Bean, C., Counting and sizing of submicron particles by the resistive pulse technique. *Review of Scientific Instruments* **1970,** *41* (7), 909-916.

86. DeBlois, R. W.; Wesley, R., Sizes and concentrations of several type C oncornaviruses and bacteriophage T2 by the resistive-pulse technique. *Journal of Virology* **1977,** *23* (2), 227-233.

87. Sun, L.; Crooks, R. M., Single carbon nanotube membranes: a well-defined model for studying mass transport through nanoporous materials. *Journal of the American Chemical Society* **2000,** *122* (49), 12340-12345.

88. Wang, H. Y.; Ying, Y. L.; Li, Y.; Long, Y. T., Peering into Biological Nanopore: A Practical Technology to Single-Molecule Analysis. *Chemistry–An Asian Journal* **2010,** *5* (9), 1952-1961.

89. Ying, Y.-L.; Long, Y.-T., Nanopore-based single-biomolecule interfaces: From information to knowledge. *Journal of the American Chemical Society* **2019,** *141* (40), 15720-15729.

90. Yu, R. J.; Ying, Y. L.; Gao, R.; Long, Y. T., Confined nanopipette sensing: from single molecules, single nanoparticles, to single cells. *Angewandte Chemie International Edition* **2019,** *58* (12), 3706-3714.

91. Neher, E.; Sakmann, B., Single-channel currents recorded from membrane of denervated frog muscle fibres. *Nature* **1976,** *260* (5554), 799-802.

92. Chen, P.; Zhou, X.; Andoy, N. M.; Han, K.-S.; Choudhary, E.; Zou, N.; Chen, G.; Shen, H., Spatiotemporal catalytic dynamics within single nanocatalysts revealed by single-molecule microscopy. *Chemical Society Reviews* **2014,** *43* (4), 1107-1117.

93. Yi-Lun, Y.; Jiajun, W.; Rose, L. A.; Ying, J.; Rui, G.; Cong, X.; Martin, E.; Hang, R.; Terry, W. C. K.; Wei, W., Single-Entity Electrochemistry at Confined Sensing Interfaces. *SCIENCE CHINA Chemistry* **2020**.

94. Bard, A. J.; Fan, F. R. F.; Kwak, J.; Lev, O., Scanning electrochemical microscopy. Introduction and principles. *Analytical Chemistry* **1989,** *61* (2), 132-138.

95. Ebejer, N.; Güell, A. G.; Lai, S. C.; McKelvey, K.; Snowden, M. E.; Unwin, P. R., Scanning electrochemical cell microscopy: a versatile technique for nanoscale electrochemistry and functional imaging. *Annual Review of Analytical Chemistry* **2013**.

96. Kang, M.; Perry, D.; Kim, Y.-R.; Colburn, A. W.; Lazenby, R. A.; Unwin, P. R., Time-resolved detection and analysis of single nanoparticle electrocatalytic impacts. *Journal of the American Chemical Society* **2015,** *137* (34), 10902-10905.

97. Gao, R.; Edwards, M. A.; Qiu, Y.; Barman, K.; White, H. S., Visualization of Hydrogen Evolution at Individual Platinum Nanoparticles at a Buried Interface. *Journal of the American Chemical Society* **2020**.

98. Brasiliense, V.; Patel, A. N.; Martinez-Marrades, A.; Shi, J.; Chen, Y.; Combellas, C.; Tessier, G.; Kanoufi, F., Correlated Electrochemical and Optical Detection Reveals the Chemical Reactivity of Individual Silver Nanoparticles. *Journal of the American Chemical Society* **2016,** *138* (10), 3478-83.

99. Patel, A. N.; Martinez-Marrades, A.; Brasiliense, V.; Koshelev, D.; Besbes, M.; Kuszelewicz, R.; Combellas, C.; Tessier, G.; Kanoufi, F., Deciphering the elementary steps of transport-reaction processes at individual Ag nanoparticles by 3D superlocalization microscopy. *Nano Letters* **2015,** *15* (10), 6454-6463.

100. Hao, R.; Fan, Y.; Zhang, B., Imaging Dynamic Collision and Oxidation of Single Silver Nanoparticles at the Electrode/Solution Interface. *Journal of the American Chemical Society* **2017,** *139* (35), 12274-12282.

101. Fang, Y.; Wang, W.; Wo, X.; Luo, Y.; Yin, S.; Wang, Y.; Shan, X.; Tao, N., Plasmonic imaging of electrochemical oxidation of single nanoparticles. *Journal of the American Chemical Society* **2014,** *136* (36), 12584-12587.

102. Shan, X.; Díez-Pérez, I.; Wang, L.; Wiktor, P.; Gu, Y.; Zhang, L.; Wang, W.; Lu, J.; Wang, S.; Gong, Q., Imaging the electrocatalytic activity of single nanoparticles. *Nature nanotechnology* **2012,** *7* (10), 668-672.

103. Syal, K.; Iriya, R.; Yang, Y.; Yu, H.; Wang, S.; Haydel, S. E.; Chen, H.-Y.; Tao, N., Antimicrobial susceptibility test with plasmonic imaging and tracking of single bacterial motions on nanometer scale. *ACS nano* **2016,** *10* (1), 845-852.

104. Wang, S.; Shan, X.; Patel, U.; Huang, X.; Lu, J.; Li, J.; Tao, N., Label-free imaging, detection, and mass measurement of single viruses by surface plasmon resonance. *Proceedings of the National Academy of Sciences* **2010,** *107* (37), 16028-16032.

105. Cheng, H.-Y.; Schenk, J.; Huff, R.; Adams, R., In vivo electrochemistry: behavior of micro electrodes in brain tissue. *Journal of Electroanalytical Chemistry and Interfacial Electrochemistry* **1979,** *100* (1-2), 23-31.

106. Wightman, R. M., Microvoltammetric electrodes. *Analytical Chemistry* **1981,** *53* (9), 1125A-1134A.

107. Fleischmann, M.; Pons, S., The behavior of microelectrodes. *Analytical Chemistry* **1987,** *59* (24), 1391A-1399A.

108. Engstrom, R. C.; Weber, M.; Wunder, D. J.; Burgess, R.; Winquist, S., Measurements within the diffusion layer using a microelectrode probe. *Analytical Chemistry* **1986,** *58* (4), 844-848.

109. Liu, H. Y.; Fan, F. R. F.; Lin, C. W.; Bard, A. J., Scanning electrochemical and tunneling ultramicroelectrode microscope for high-resolution examination of electrode surfaces in solution. *Journal of the American Chemical Society* **1986,** *108* (13), 3838-3839.

110. Zhou, H.; Park, J. H.; Fan, F.-R. F.; Bard, A. J., Observation of single metal nanoparticle collisions by open circuit (mixed) potential changes at an ultramicroelectrode. *Journal of the American Chemical Society* **2012,** *134* (32), 13212-13215.

111. Percival, S. J.; Zhang, B., Fast-scan cyclic voltammetry allows determination of electron-transfer kinetic constants in single nanoparticle collision. *The Journal of Physical Chemistry C* **2016,** *120* (37), 20536-20546.

112. LabordeC; PittinoF; Verhoeven, H. A.; Lemay, S. G.; SelmiL; Jongsma, M. A.; Widdershoven, F. P., Real-time imaging of microparticles and living cells with CMOS nanocapacitor arrays. *Nat Nano* **2015,** *10* (9), 791-795.

113. Lemay, S. G.; Laborde, C.; Renault, C.; Cossettini, A.; Selmi, L.; Widdershoven, F. P., High-Frequency Nanocapacitor Arrays: Concept, Recent Developments, and Outlook. *Accounts of Chemical Research* **2016**.

114. Gao, R.; Ying, Y. L.; Li, Y. J.; Hu, Y. X.; Yu, R. J.; Lin, Y.; Long, Y. T., A 30 nm nanopore electrode: facile fabrication and direct insights into the intrinsic feature of single nanoparticle collisions. *Angewandte Chemie International Edition* **2018,** *57* (4), 1011-1015.

115. Liu, Q.; Zhang, Z., Platinum single-atom catalysts: a comparative review towards effective characterization. *Catalysis Science & Technology* **2019,** *9* (18), 4821-4834.

116. Lang, R.; Xi, W.; Liu, J.-C.; Cui, Y.-T.; Li, T.; Lee, A. F.; Chen, F.; Chen, Y.; Li, L.; Li, L., Non defect-stabilized thermally stable single-atom catalyst. *Nature communications* **2019,** *10* (1), 1-10.

117. Wan, G.; Yu, P.; Chen, H.; Wen, J.; Sun, C. j.; Zhou, H.; Zhang, N.; Li, Q.; Zhao, W.; Xie, B., Engineering Single‐Atom Cobalt Catalysts toward Improved Electrocatalysis. *Small* **2018,** *14* (15), 1704319.

118. Xiao, X.; Fan, F.; Bard, A. J.; Xiaoyin Xiao, F.-R., Jiping Zhou, and Allen J. Bard, Current Transients in Single Nanoparticle Collision Events. *Journal of the American Chemical Society* **2008,** *130*, 16669–16677.

119. Kleijn, S. E.; Lai, S. C.; Miller, T. S.; Yanson, A. I.; Koper, M. T.; Unwin, P. R., Landing and catalytic characterization of individual nanoparticles on electrode surfaces. *Journal of the American Chemical Society* **2012,** *134* (45), 18558-18561.

120. Kleijn, S. E.; Serrano-Bou, B.; Yanson, A. I.; Koper, M. T., Influence of hydrazine-induced aggregation on the electrochemical detection of platinum nanoparticles. *Langmuir* **2013,** *29* (6), 2054-2064.

121. Robinson, D. A.; Kondajji, A. M.; Castañeda, A. D.; Dasari, R.; Crooks, R. M.; Stevenson, K. J., Addressing colloidal stability for unambiguous electroanalysis of single nanoparticle impacts. *The Journal of Physical Chemistry Letters* **2016,** *7* (13), 2512-2517.

122. Defnet, P. A.; Han, C.; Zhang, B., Temporally-Resolved Ultrafast Hydrogen Adsorption and Evolution on Single Platinum Nanoparticles. *Analytical Chemistry* **2019,** *91* (6), 4023-4030.

123. Feng, A.; Cheng, W.; Compton, R. G., Measuring the oxygen content of a single oil droplet. *Chemical science* **2016,** *7* (10), 6458-6462.

124. Thearle, R. A.; Sofer, Z.; Bouša, D.; Pumera, M., Impact Electrochemistry: Detection of Graphene Nanosheets Labeled with Metal Nanoparticles through Oxygen Reduction Mediation. *Chemphyschem: a European journal of chemical physics and physical chemistry* **2016,** *17* (13), 2096.

125. Li, X.; Batchelor-McAuley, C.; Whitby, S. A.; Tschulik, K.; Shao, L.; Compton, R. G., Single nanoparticle voltammetry: contact modulation of the mediated current. *Angewandte Chemie International Edition* **2016,** *55* (13), 4296-4299.

126. Jiao, X.; Lin, C.; Young, N. P.; Batchelor-McAuley, C.; Compton, R. G., Hydrogen Oxidation Reaction on Platinum Nanoparticles: Understanding the Kinetics of Electrocatalytic Reactions via "Nano-Impacts". *The Journal of Physical Chemistry C* **2016,** *120* (24), 13148-13158.

127. Xiang, Z. p.; Deng, H. q.; Peljo, P.; Fu, Z. y.; Wang, S. l.; Mandler, D.; Sun, G. q.; Liang, Z. x., Electrochemical dynamics of a single platinum nanoparticle collision event for the hydrogen evolution reaction. *Angewandte Chemie International Edition* **2018,** *130* (13), 3522-3526.

128. Zhou, H.; Fan, F.-R. F.; Bard, A. J., Observation of discrete Au nanoparticle collisions by electrocatalytic amplification using Pt ultramicroelectrode surface modification. *The Journal of Physical Chemistry Letters* **2010,** *1* (18), 2671-2674.

129. Kim, J.; Bard, A. J., Electrodeposition of single nanometer-size Pt nanoparticles at a tunneling ultramicroelectrode and determination of fast heterogeneous kinetics for Ru (NH3) 63+ reduction. *Journal of the American Chemical Society* **2016,** *138* (3), 975-979.

130. Chen, C.-H.; Ravenhill, E. R.; Momotenko, D.; Kim, Y.-R.; Lai, S. C.; Unwin, P. R., Impact of surface chemistry on nanoparticle–electrode interactions in the electrochemical detection of nanoparticle collisions. *Langmuir* **2015,** *31* (43), 11932-11942.

131. Sokolov, S. V.; Eloul, S.; Kätelhön, E.; Batchelor-McAuley, C.; Compton, R. G., Electrode–particle impacts: a users guide. *Physical Chemistry Chemical Physics* **2017,** *19* (1), 28-43.

132. Zhou, Y.-G.; Rees, N. V.; Pillay, J.; Tshikhudo, R.; Vilakazi, S.; Compton, R. G., Gold nanoparticles show electroactivity: counting and sorting nanoparticles upon impact with electrodes. *Chemical Communications* **2011,** *48* (2), 224-226.

133. Suherman, A. L.; Zampardi, G.; Kuss, S.; Tanner, E. E.; Amin, H. M.; Young, N. P.; Compton, R. G., Understanding gold nanoparticle dissolution in cyanide-containing solution via impact-chemistry. *Physical Chemistry Chemical Physics* **2018,** *20* (44), 28300-28307.

134. Ngamchuea, K.; Clark, R. O.; Sokolov, S. V.; Young, N. P.; Batchelor-McAuley, C.; Compton, R. G., Single Oxidative Collision Events of Silver Nanoparticles: Understanding the Rate-Determining Chemistry. *Chemistry–A European Journal* **2017,** *23* (63), 16085-16096.

135. Batchelor-McAuley, C.; Ellison, J.; Tschulik, K.; Hurst, P. L.; Boldt, R.; Compton, R. G., In situ nanoparticle sizing with zeptomole sensitivity. *Analyst* **2015,** *140* (15), 5048-5054.

136. Ustarroz, J.; Kang, M.; Bullions, E.; Unwin, P. R., Impact and oxidation of single silver nanoparticles at electrode surfaces: one shot versus multiple events. *Chemical science* **2017,** *8* (3), 1841-1853.

137. Sun, L.; Wang, W.; Chen, H. Y., Dynamic Nanoparticle-Substrate Contacts Regulate Multi-Peak Behavior of Single Silver Nanoparticle Collisions. *ChemElectroChem* **2018,** *5* (20), 2995-2999.

138. Kanokkanchana, K.; Saw, E. N.; Tschulik, K., Nano impact electrochemistry: effects of electronic filtering on peak height, duration and area. *ChemElectroChem* **2018,** *5* (20), 3000-3005.

139. Little, C. A.; Xie, R.; Batchelor-McAuley, C.; Kätelhön, E.; Li, X.; Young, N. P.; Compton, R. G., A quantitative methodology for the study of particle–electrode impacts. *Physical Chemistry Chemical Physics* **2018,** *20* (19), 13537-13546.

140. Ma, H.; Chen, J.-F.; Wang, H.-F.; Hu, P.-J.; Ma, W.; Long, Y.-T., Exploring dynamic interactions of single nanoparticles at interfaces for surface-confined electrochemical behavior and size measurement. *Nature communications* **2020,** *11* (1), 1-9.

141. Dick, J. E.; Hilterbrand, A. T.; Strawsine, L. M.; Upton, J. W.; Bard, A. J., Enzymatically enhanced collisions on ultramicroelectrodes for specific and rapid detection of individual viruses. *Proceedings of the National Academy of Sciences* **2016,** *113* (23), 6403-6408.

142. Quinn, B. M.; van't Hof, P. G.; Lemay, S. G., Time-resolved electrochemical detection of discrete adsorption events. *Journal of the American Chemical Society* **2004,** *126* (27), 8360-8361.

143. Gorschlüter, A.; Sundermeier, C.; Roß, B.; Knoll, M., Microparticle detector for biosensor application. *Sensors and Actuators B: Chemical* **2002,** *85* (1-2), 158-165.

144. Deng, Z.; Elattar, R.; Maroun, F.; Renault, C., In Situ Measurement of the Size Distribution and Concentration of Insulating Particles by Electrochemical Collision on Hemispherical Ultramicroelectrodes. *Analytical Chemistry* **2018,** *90* (21), 12923-12929.

145. Renault, C.; Lemay, S. G., Electrochemical Collisions of Individual Graphene Oxide Sheets: An Analytical and Fundamental Study. *ChemElectroChem* **2020,** *7* (1), 69-73.

146. Boika, A.; Bard, A. J., Time of first arrival in electrochemical collision experiments as a measure of ultralow concentrations of analytes in solution. *Analytical Chemistry* **2015,** *87* (8), 4341-4346.

2. Chapter 2 Experiments and fundamentals

2.1 Experimental section

2.1.1 Chemicals and reagents

In chapter 3, amine-functionalized polystyrene beads of 0.5 and 1 µm radius (product numbers: L1030 and L9529, respectively), sodium nitrate ($NaNO_3$), mercury nitrate ($Hg(NO_3)_2$), hexaammineruthenium (III) chloride ($[Ru(NH_3)_6]Cl_3$), acetate acid (CH_3COOH) and sodium acetate ($C_2H_3NaO_2$) were purchased from Sigma-Aldrich (Saint Louis, USA). Acetate buffer (pH = 5) was prepared by mixing 59 ml of 0.1 M acetic acid and 141 ml of 0.1 M sodium acetate. The solutions were kept at room temperature.

In chapters 4 and 5, GNPs (≈ 5 µm particle size, 15 nm thickness, Sigma Aldrich), hydrazine monohydrate (N_2H_4 64-65%, > 98%, Sigma Aldrich), ferrocene methanol (FcMeOH, 97%, Sigma Aldrich) and Sodium hydroxide (0.1 M NaOH solution, Fluka) were used without further purification. Milli-Q water with the resistance of 18.2 $M\Omega.cm^{-1}$ was used throughout the experiment. The GNP suspension was kept at room temperature and should be sonicated right before collision measurements.

2.1.2 Fabrication of disk-shaped Pt UMEs and C-fiber UMEs

The 5 µm radius disk Pt UMEs were fabricated by heat-sealing a 5 µm radius Pt wire (hard tempered, Goodfellow) inside the borosilicate glass capillary (2 mm outer diameter, 1.16 mm inner diameter, Sutter Instrument, Novato USA). The Pt disk was polished with abrasive disks (600, 800, 1200 grit) and alumina slurry (1, 0.3 and 0.05 µm, Buehler, Lake Bluff, USA) until a mirror-like surface is observed under an optical microscope. The connection between a platinum wire and a tungsten wire (0.25 µm diameter, ChemPure, Karlsruhe, Germany) was made with a conductive silver paste (RS Components, Northants, UK).

C-fiber UMEs was fabricated by first gluing a c.a. 1 cm long 3.5 µm radius C-fiber (XAS quality, Goodfellow) on a tungsten wire with conducting Ag epoxy and then, casting the fiber and a portion of the tungsten wire into a hard epoxy (EpoHeat, Buehler) contained within a plastic pipette cone. The C-fiber UME is polished following the same procedure as the Pt UME.

2.1.3 Electrochemical measurements

The electrochemical measurements were carried out with a two-electrode setup represented in Figure 2.2. A potential form (e.g., controlled-potential experiments, triangular-wave form) is applied between the two electrodes with the analogue potential output of a National Instrument USB 6212 acquisition card. The current between the UME and the reference electrode is measured using a DDPCA-300 (Femto, Germany) variable gain trans-impedance amplifier. The gain of the amplifier and the output voltage are set/read with the National Instrument card. A relay placed between the reference electrode (Ref in Figure 2.2) and the National Instrument card is controlled by the card and can be used to open the circuit after an experiment. A home-made Labview code (Labview 2013 Pack 1, National Instruments) installed on a PC is used to control the National Instrument card, record the data and plot them. Typical experiments involve a current in the nA range and thus, a gain of 10^9 V/A was set. The data are acquired at 150 Hz (the bandwidth of the amplifier) and averaged in order to plot a point every 50 ms. No further treatment of the signal was performed. The experimental setup is designed to minimize the noise. The electrochemical cell (home-made Teflon cell of 5 - 10 mL, Piranha cleaned between experiments) and

the amplifier are housed in a Faraday cage in order to suppress interferences from external electric fields. The connections to the acquisition card are made with coaxial cables. The amplifier is operated with 12V batteries in order to avoid noise from the electric outlet. The Faraday cage is sitting on a floating table to suppress mechanical vibrations and covered with expended Styrofoam to provide acoustic and thermal insulation.

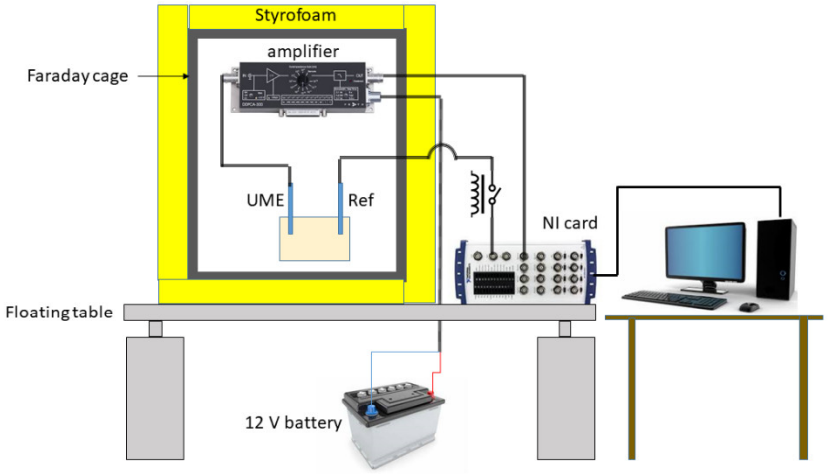

Figure 2.1. Schematic illustration of low noise experimental setup used for the electrochemistry.

All electrochemical measurements were performed using a home-made two-electrode setup placed in a Faraday cage. A 2 mm diameter leakless miniature Ag/AgCl 3 M KCl reference electrode (ref: ET072, EDAQ, Warsaw, Poland) was used as the reference/counter electrode. Prior to use, stock solutions of beads were centrifuged and re-dispersed in Milli-Q water three times. The cell is kept under an Ar blanket at all-time. The cell was stirred by bubbling Ar in a solution for approximately 10 s right before running chronoamperometry measurements in order to ensure a homogeneous concentration. The Ar inlet was then raised above the surface of the liquid right before the measurement to minimize convection. Chronoamperograms are recorded for 120 s for each run. Before the addition of beads in solution, chronoamperograms are recorded over 120 s to ensure that no steps are observed.

The analysis of the current steps on the chronoamperograms was carried out with a semi-automatic procedure and a home-made code written in Labview (2013). A screenshot of the program is shown in Figure 2.2. The code was used to correct the baseline and then search for the presence of peaks using the analysis of the derivative (top and bottom panels on the left in Figure 2.2). The window width and the step width are normally set as 2 s and 1.0 s. When the time interval between two peaks is quite close (within 1 s), the step width is manually adjusted to find the optimized result. Finally, the operator can select the peaks found by the program and input them in an analysis window (top right in Figure 2.2) that will automatically cut the step in three segments (before, during and after a collision) and then subtract a linear baseline on the two segments before and after a collision. Finally, a step-like (logistic) function is automatically fitted in order to determine the amplitude, initial current and temporal position of the step.

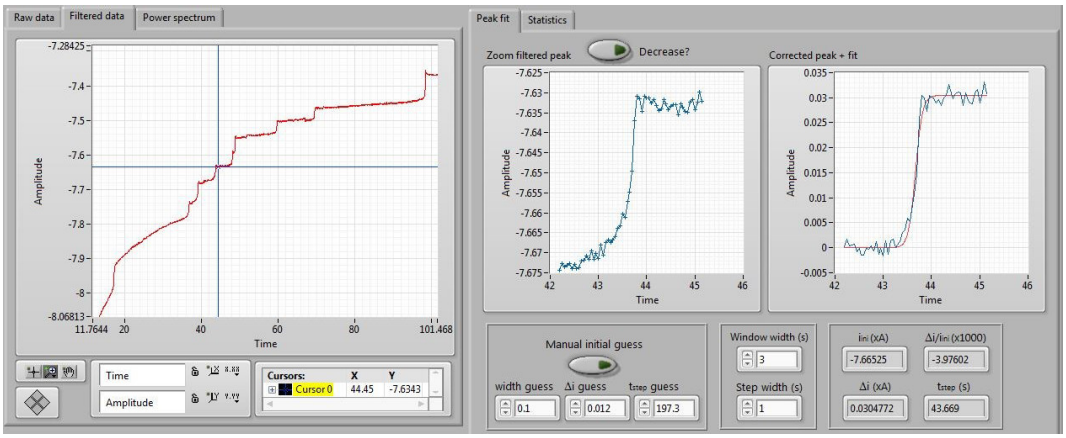

Figure 2.2. Screenshot of the Labview interface made to analyze semi-automatically the current steps.

2.1.4 Correlated otpo-electrochemical measurements

The setup shown in Figure 2.3 is used to monitor simultaneously by optical microscopy and electrochemistry the adsorption of individual GNPs on an electrified gold surface. A movie of the Pt surface is acquired under bright field illumination (THA-200, Olympus) using an inverted microscope (ix-73 Olympus) equipped with a 40x or 20x objective focused on the surface of a 10 µm diameter Pt UME. The frames are acquired at a rate of 20 frames per second by a digital CMOS camera (Orca Flash v4, Hamamatsu). The objective of 20X (UCPLFLN20X, Olympus) magnification has a working distance of 6.60-7.80 mm and a numerical aperture of 0.45, while the objective of 40X (LUCPLFLN40X, Olympus) magnification has a working distance of 2.70-4.00 mm and a numerical aperture of 0.6. The UME is positioned at about 300 µm from the bottom of the cell (150 µm thick coverslip, n°1.5H, Thorlabs), and the Ag/AgCl 3M reference electrode crosses through the Teflon cell to construct a two-electrode system. The solution contains 0.9 mM of FcMeOH and 15 fM of GNP having an average size of 4.2 µm (the characterization of their size is provided in Ref. [1]). The current is recorded by a low-noise current amplifier (LCA-2K-2G, Femto Gmbh) with a gain of 2 GV/A. Correlated microscopy videos were collected at 20 Hz by a home-made program (Labview) and image stacks were subsequently exported for analysis using ImageJ. The temporal resolution for all correlated opto-electrochemical measurements is 50 ms. The acquisition of the video and the *i-t* trace is synchronized by the external trigger of the camera.

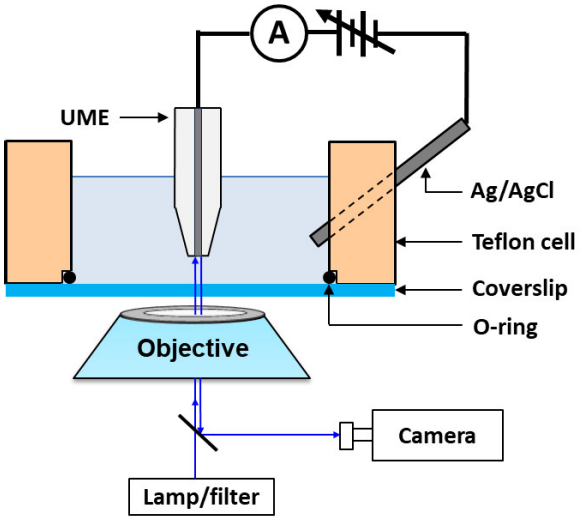

Figure 2.3. Schematic illustration of the opto-electrochemical setup used to track the landing position of individual GNPs. The thickness of the coverslip is 175 µm and the working distance between the electrode and the is set as about 300 µm.

A 100 μg/ml stock solution of GNPs in 10 μM NaOH was first sonicated for 10 minutes, followed by sedimentation for 6 hours. After sedimentation, the top half volume of GNP suspension with a small size was sucked out by pipette, and the remaining volume of GNP suspension with a large size was further sonicated for 10 minutes right before opto-electrochemical collision measurements. Following injection into the electrochemical cell, the solution was manually sonicated by using a pipette to ensure homogenization. The GNPs dispersed in solution appear in the movie as black moving objects of few microns. For all opto-electrochemical measurements, a Pt UME is chosen as the working electrode and biased at a potential of 0.45 V vs. Ag/AgCl.

2.2 Electrochemical methods used throughout experiments

2.2.1 Chronoamperometry

Chronoamperometry is the controlled-potential electrochemical technique that the potential of the working electrode is stepped to a certain potential, and the resulting current from the faradaic processes flows through the electrode as a function of time. Consider an analytical system in which species O is electrochemically inactive at E_1 and the potential of the working electrode is stepped to a potential (E_2) where O is reduced at a diffusion-limited rate: $O \pm e^- \rightleftharpoons R$, as shown in Figure 2.4A. The theoretical expression for the concentration profile of species O near the electrode surface is obtained by solving Fick's second law of diffusion subject to boundary conditions.[2]

(i) For a planar electrode (one-dimensional case), the mass transport equation is given by:

$$\frac{\partial C_O(x,t)}{\partial t} = D_O \frac{\partial^2 C_O(x,t)}{\partial x^2} \tag{2.1}$$

where $C_O(x,t)$ is the concentration of species O at the distance x from the electrode surface at time t, and D_O is the diffusion coefficient of species O. The boundary conditions are:

$$C_O(x \geq 0,0) = C_O^* \tag{2.2}$$

$$\lim_{x\to\infty} C_O(x,t) = C_O^* \tag{2.3}$$

$$C_O(0, t > 0) = 0 \tag{2.4}$$

Solving this differential equation gives the current-time response:

$$i_d(\mathrm{t}) = \frac{nFAD_O^{1/2}C_O^*}{\pi^{1/2}t^{1/2}} \tag{2.5}$$

where n is the number of electrons exchanged per molecule, F is the Faraday's constant, and A is the geometric area of the electrode. The Eq. (2.5) is also known as the *Cottrell equation*. The concentration profile of species O as a function of the distance near the electrode is given by:

$$C_O(x,t) = C_O^*\left[1 - \mathrm{erfc}\left(\frac{x}{2(D_O t)^{1/2}}\right)\right] \tag{2.6}$$

Plots of current responses versus time and the concentration of species O versus the distance near the electrode are shown in Figure 2.4 B and C, respectively.

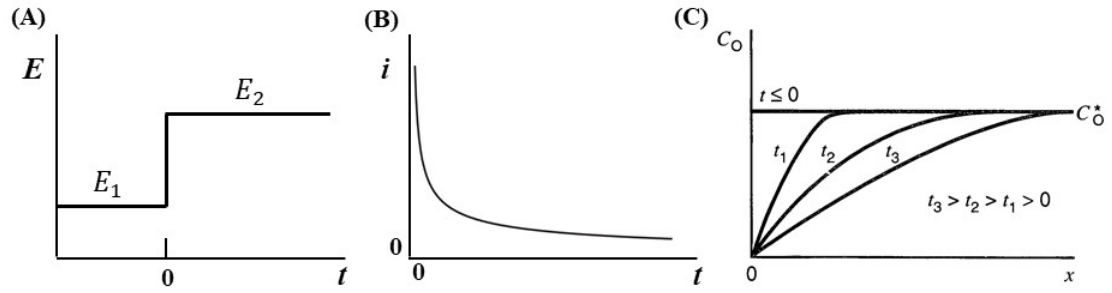

Figure 2.4. Controlled-potential step experiment at a UME. (A) the UME is stepped from a potential (E_1) in which species O is electro-inactive to a potential (E_2) in which O is reduced at a diffusion-limited rate. (B) time-dependent current response. (C) the concentration profile for various times in the vicinity of the electrode surface. Adapted with permission from Ref. [2]. Copyright 2002,

(ii) If the electrode is spherical rather than planar (the hemispherical Hg UME in chapter 3), one must consider a spherical diffusion field. The concentration gradient is obtained by solving Fick's 2nd law in spherical coordinates:

$$\frac{\partial C_O(r,t)}{\partial t} = D_O\left(\frac{\partial^2 C_O(r,t)}{\partial x^2} + \frac{2}{r}\frac{\partial C_O(r,t)}{\partial r}\right) \tag{2.7}$$

Where r is the radial distance from the electrode center. The concentration profile of species O near the hemispherical electrode is obtained by solving the Eq. (2.7) subject to the boundary conditions:

$$C_O(r,t) = C_O^*\left[1 - \frac{r_0}{r}\operatorname{erfc}\left(\frac{r-r_0}{2(D_O t)^{1/2}}\right)\right] \tag{2.8}$$

where r_0 is the electrode radius. The flux of reactants near the electrode surface is deduced by

$$j = D\left(\frac{\partial C}{\partial r}\right)_{r=r_0} \tag{2.9}$$

The resulting diffusion current is given by:

$$i(t) = \frac{nFAD_O^{1/2}C_O^*}{\pi^{1/2}t^{1/2}} + \frac{nFAD_O C_O^*}{r_0} \tag{2.10}$$

The diffusion current for the spherical electrodes is just that for the linear situation plus a constant term. At long times, the steady-state limiting current for a spherical electrode is given by

$$i_{ss} = \lim_{t\to\infty} i = \frac{nFAD_O C_O^*}{r_0} = 4\pi nFD_O C_O^* \tag{2.11}$$

Or the hemispherical electrode,

$$i_{ss}(\text{hemisphere}) = \lim_{t\to\infty} i = \frac{nFAD_O C_O^*}{r_0} = 2\pi nFD_O C_O^* r_0 \tag{2.12}$$

(iii) For a disk UME, the diffusion occurs in two dimensions that are radial with respect to the axis of symmetry and normal to the electrode plane. This case is much more complicated since the flux is no longer uniform over the electrode surface. The detailed description of the form of the diffusion equation, the boundary conditions and general expression of the current-time response can refer to the literature. At long times, the steady-state current for the disk is given by

$$i_{ss}(\text{disk}) = \frac{4nFAD_O C_O^*}{\pi r_0} = 4nFD_O C_O^* r_0 \tag{2.13}$$

The Eq. (2.13) has the same functional form as for the hemisphere, but with a smaller i_{ss} (by a factor of $2/\pi$) than a hemisphere with the same radius (see the Eq. (2.12)).

2.2.2 Cyclic voltammetry

Cyclic voltammetry (CV) is considered as one of the most important and most widely employed techniques in the entire field of electrochemistry.[2-4] It is a reversal technique that the potential is linearly swept from the initial potential (E_1) to the switching potential (E_2), and then swept back to the initial potential, as shown in Figure 2.5. The CV experiment records the current flowing through the working electrode (WE) versus the applied potential. A plot of current versus potential (known as the voltammogram) is shown in Figure 2.6. The shape of the observed voltammograms depends on the rate constant (k^0), the diffusion coefficients of the reactants, the voltage sweep rate together with the voltages E_1 and E_2, as well as the dimensions of the electrode (macro-electrodes or ultra-microelectrodes).

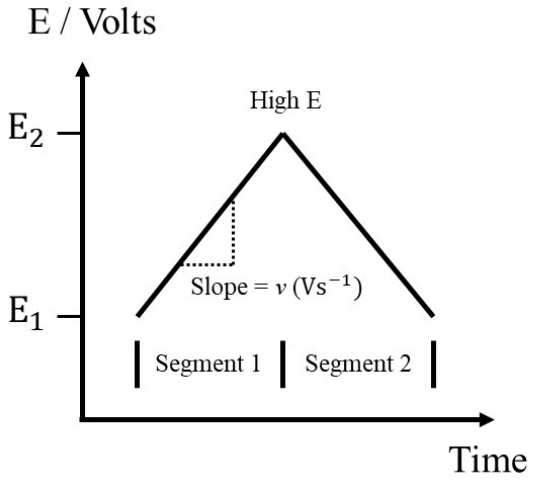

Figure 2.5. The potential waveform applied to the working electrode in a typical cyclic voltammetric experiment.

The microelectrode is an electrode that has its characteristic dimension on the scale of micrometers (less than 100 μm), while a macroelectrode usually have a characteristic dimension on the scale of millimeters or centimeters. Although microelectrodes may appear merely the difference in the smaller size compared to macroelectrodes, their small size causes characteristically different electrochemical behaviors.[5] The mass transport of redox species to a macroelectrodes occurs perpendicular to the electrode surface, known as the planar diffusion shown in the left in Figure 2.6A, and the edge effects can be ignored; in contrast, the flux of redox species are transported to/from the microelectrode in all directions, known as the radial diffusion shown in the right in Figure 2.6A, while the flux at the perimeter of the microelectrode surface is higher than at the center (called edge effects). Compared to planar diffusion, radial diffusion makes microelectrodes enjoy much faster transport rates and current densities, facilitating the measurement of faster processes. The difference in mass transport is apparent from the observed voltammograms recorded between a macroelectrode and a microelectrode (see Figure 2.6B). A typical peak-shaped voltammogram with a diffusional tail is observed at macroelectrodes. The peak occurs at the macroelectrode since after the peak potential the current is controlled by diffusion, with the depletion of redox species near the electrode, the redox species have to be transported to the electrode from increasingly further distances, leading to the growth of the diffuse layer. The current drop follows the same behavior as predicted by the *Cottrell equation*. However, microelectrodes show a typical voltammogram in which the current does not decay but rather to a steady-state value because of constant flux to a microelectrode from radial diffusion. The steady-state current or the limiting current at long times can be calculated by

$$i_{ss} = m_o nFAC_O^* \tag{2.14}$$

where m_o is the geometry-dependent mass transfer coefficient. The values of m_o for the disk, hemisphere and sphere are $4D_O/\pi r_0$, D_O/r_0 and D_O/r_0, respectively. The form of the steady-state

current is as predicted in the controlled potential analysis (at long times) as described in the previous section.

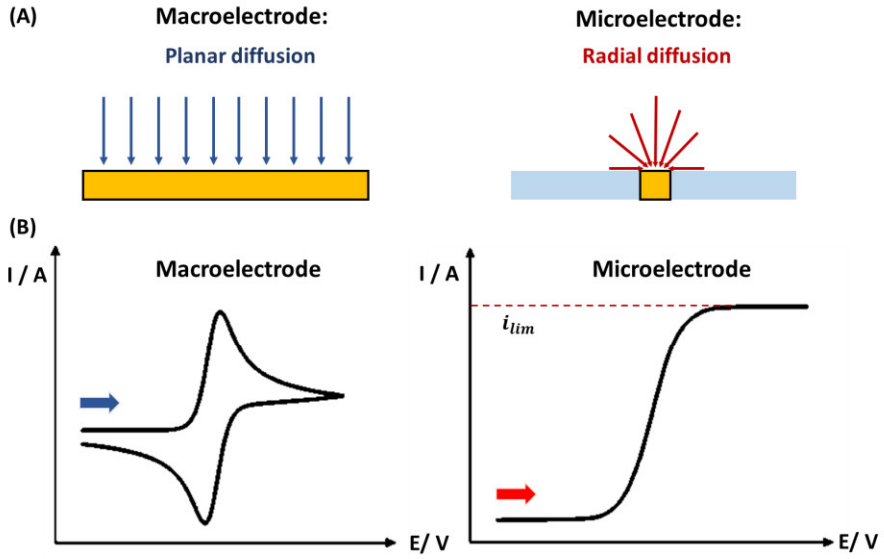

Figure 2.6. (A) Schematic illustration of the difference in mass transport to a microelectrode (planar diffusion) and a microelectrode (radial diffusion). (B) Resulting cyclic voltammograms observed at macroelectrodes and microelectrodes for a representative reversible electrochemical reaction. The blue and red arrows represent the potential-scanning directions.

In this dissertation, the experiments with ultra-microelectrodes (disk UMEs or hemispherical UMEs) are mainly operating in the steady-state regime in which redox species are oxidized or reduced at a mass-transfer limit. The value of steady-state current is proportional to the electrode radius and the concentration of redox species, as well as the geometry of the electrode.

2.3 Reference

1. Deng, Z.; Elattar, R.; Maroun, F.; Renault, C., In Situ Measurement of the Size Distribution and Concentration of Insulating Particles by Electrochemical Collision on Hemispherical Ultramicroelectrodes. *Analytical Chemistry* **2018,** *90* (21), 12923-12929.

2. Faulkner, L. R.; Bard, A. J., *Electrochemical methods: fundamentals and applications, 2nd Edition*. John Wiley and Sons: 2002.

3. Sandford, C.; Edwards, M. A.; Klunder, K. J.; Hickey, D. P.; Li, M.; Barman, K.; Sigman, M. S.; White, H. S.; Minteer, S. D., A synthetic chemist's guide to electroanalytical tools for studying reaction mechanisms. *Chemical science* **2019,** *10* (26), 6404-6422.

4. Elgrishi, N.; Rountree, K. J.; McCarthy, B. D.; Rountree, E. S.; Eisenhart, T. T.; Dempsey, J. L., A practical beginner's guide to cyclic voltammetry. *Journal of Chemical Education* **2018,** *95* (2), 197-206.

5. Compton, R. G.; Banks, C. E., *Understanding voltammetry*. World Scientific: 2018.

3. Chapter 3 Simultaneous measurement of size and concentration of individual insulating particles using hemispherical UMEs

3.1 Introduction

In electrochemical blocking, one of the most considerable limitations is the difficulty to simultaneously measure the size and concentration of colliding species. Several attempts were made to determine the size and concentration of colliding species separately in solution by the analysis of current steps.[1-3] In this introduction, we will review the important results achieved between 2004 and 2020.

In 2004, Lemay and coworkers provided a relation between the concentration of bead and the experimental frequency of collision for a situation where diffusion is neglectable, and solely migration ensures the transport of the beads from the bulk solution toward the electrode surface:[1]

$$J_{mig} = \frac{1}{\Delta t} \approx \frac{I c_{bead}}{e c_{KCl}} \left(\frac{\mu_{bead}}{\mu_{K^+} + \mu_{Cl^+}} \right) \tag{3.1}$$

where J_{mig} is the frequency of collision (Hz) due to migration, I is the current response, e is the unit of charge, c_{bead} and c_{KCl} are the concentrations of the bead and supporting electrolyte, respectively, and μ_i is the mobility of the ions "i" in solution. The equation describes the portion of current supported by the migration of an ion i in the solution, the term in bracket being an approximation of the transference number of the beads when the concentration of bead is sufficiently low to neglect its overall contribution to the total current.[1] The authors evidence the effect of migration by varying the ionic strength, as shown in Figure 3.1. The frequency of collision increases from 5 mHz at 50 mM KCl to 100 mHz and 430 mHz for 5 and 0.5 mM KCl, respectively. These values are in quantitative agreement with the results estimated from Eq. (3.1). (3 mHz at 50 mM KCl, 60 mHz and 500 mHz at 5 and 0.5 mM KCl, respectively).

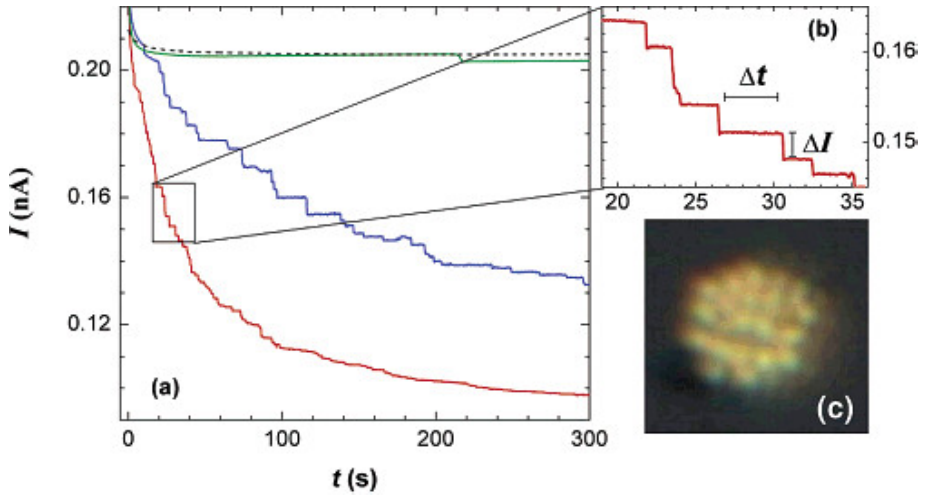

Figure 3.1. (a) Current-time transients for the diffusion-limited oxidation of 0.31 mM FcMeOH (black line) at a 2.5 μm diameter Au microdisk electrode showing discrete current step decreases in the presence of 0.5 μm radius carboxylated latex beads at 0.5 (red line), 5 (blue line), and 50 mM (green line) KCl supporting electrolyte concentrations. (b) Details of panel a. (c) Ex-situ optical micrograph taken after the amperometric measurements showing the electrode surface covered by beads. Reproduced from Ref[1]. Copyright 2004, American Chemical Society.

In their model, Lemay and coworkers consider that the flux of bead toward the surface is dominated by migration, neglecting the flux by diffusion. Intuitively one can understand that migration will dominate over diffusion if the ionic strength is low and the bead is large and heavily charged. For small particles such as nanoparticles, diffusion may become the predominant mechanism of mass transfer, while migration is negligible. This situation is opposite to the case shown previously. Then, the frequency of collision is described by Eq. (3.2):[2]

$$f_{diff} = 4D_s C_s r_0 \tag{3.2}$$

where f_{diff} is the frequency of collision due to diffusion, D_s is the diffusion coefficient of bead in cm^2/s, C_s is the number concentration of bead in particles/cm^3, and r_0 is the radius of the electrode in cm. This formula was initially given by Bard and coworkers in the context of electrocatalytic amplification (ECA) with Pt NPs of ~3.6 nm diameter dispersed in a supporting electrolyte of 50 mM phosphate buffer.[4-5] The ECA strategy produces small background current, and thus, migration is not expected to play a significant role in mass transport. We can recognize that Eq. (3.2) is simply the stationary part of the solution of Fick's equation for a disk electrode. Thus, Eq. (3.2) is valid only for a disk-shaped electrode inlaid in an infinite sheath with beads sticking only on the electrode surface but not on the sheath.

The presence of the sheath surrounding the electrode can change the frequency of collision in the case of diffusion. Compton and coworkers showed that the adsorption of particles on the large (mm^2) surface of the sheath can significantly decrease the concentration of bead near the sheath and thus the electrode.[6] Consequently, the frequency of collision should decrease and may also lose its steady-state characteristic because of 1D semi-infinite diffusion of the beads toward the sheath. Compton and co-workers also proposed to take into account the effect of near-wall hindered diffusion.[7] Indeed, the presence of near-wall hindered diffusion would lower the diffusion coefficient of particles, both parallel and perpendicular to the wall. The diffusion coefficient $D_\perp(x)$ of particle movement describing the diffusive motion perpendicular to the wall is given by[7-8]

$$D_\perp(x) = \frac{6x^2 + 2xr}{6x^2 + 9xr + 2r^2} D_{bulk} = \lambda(x) D_{bulk} \tag{3.3}$$

where x is the closest distance between the particle and the wall, r is the radius of the particle and D_{bulk} is the bulk diffusion coefficient. The effect of near-wall diffusion on the bulk diffusion coefficient is described by the factor λ(x). From Figure 3.2 we can note that this factor is significant only very close to the electrode (tens of nm at most) and thus is more relevant for nanoparticles than microbeads.

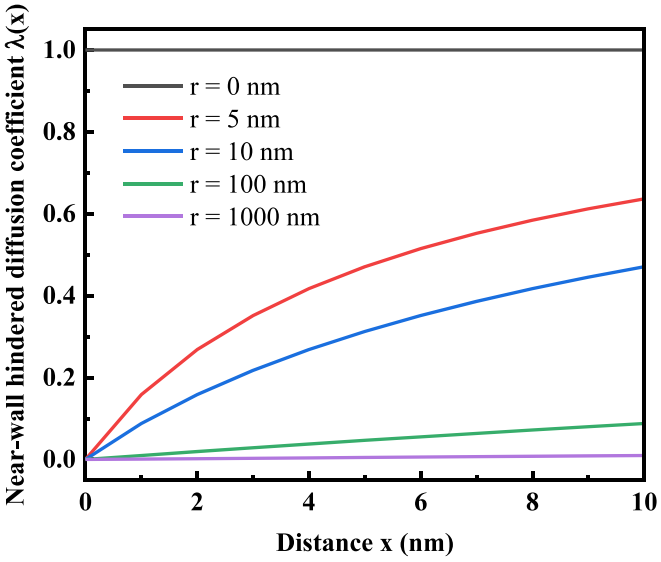

Figure 3.2. Near-wall hindered diffusion coefficient factor *λ(x)* as a function of particle-wall distance for various nanoparticle radii, calculated from Eq. (3.3).

In the two previous cases, the frequency of collision is measured by averaging multiple intervals between two collisions, and the precision on the frequency will increase with the number of collisions. The standard deviation on the average value (for a given confidence interval) decreases with the inverse of the square root of the number of measurements.[9] For this reason, the attempt of Boika and coworkers to deduce the concentration of particle from one or few measurements of time of first arrival (the time interval between the moment that the UME is dipped in the bead solution and the first collision recorded) only allowed gaining time at the expense of the certainty on the deduced concentration.[10]

For any mixed situation where both diffusion and migration play a role, it is not possible to use the Equations (3.1) and (3.2) to determine the concentration. Numerical simulations can be used to solve the Poisson-Nernst-Planck equation describing mass transport under both migration and diffusion. The collision frequency of nanoparticles, microbeads and Graphene oxide (GO) sheets has been modeled with success using this approach.[11-13] We note that solving simultaneously Poisson and Nernst-Planck equations can become extremely resource-demanding in particular when solving in 2D or 3D geometries as often the case for UMEs. To alleviate this problem, one could consider that a single bead does not significantly perturbate the electric field near the UME (in other words, neglect the influence of the bead on the electrostatic forces) and solve Poisson equation in the absence of beads first. The solution of the Poisson equation could then be used to solve the transport equation for the beads. We also note that a simplification made in all the simulations mentioned above is the existence of only one population of size. In other words, the size distribution of the particles obeys the Dirac delta function. This is obviously not the case in practice, and we will see later that the transport of the bead displays a complex dependency with the size of the beads.

We will now focus on the analysis of the step size made to deduce the size of a bead. Lemay and coworkers measured the relative current step size as a function of the ratio of the bead radius divided by the electrode radius for a range of 0.2 to 0.8 (i.e., beads range between 20% and 80% of the size of the electrode).[1] They claim to observe a linear relation. Nonetheless, a closer examination of the data seems to indicate a relationship closer to a square root rather than a straight line between particle size and step size. Boika and coworkers performed numerical simulations of the relative step size of particles landing either at the edge or the center of a UME with relative particle/electrode size comprised of 0.104 and 0.155.[2] They do not discuss the shape of the curve, but clearly, a non-linear dependence is observed. Boika and coworkers further developed a model for the case where solely diffusion controls the arrival of the beads toward the electrode.[3] They assume an equiprobability of the collision over the entire

surface of the electrode (i.e., no edge effect). The probability of landing on a thin annulus centered at a radial position *r* over the electrode is then proportional to *r*. The effect of the radial position of the bead on the UME on the magnitude of the step size, also known as edge effect, is also evidenced with numerical simulation. Thus, the analysis of the average current step magnitudes does not allow to estimate precisely the size of the insulating particles. Crooks and coworkers experimentally confirmed that the size of the current step magnitude is not solely a function of the bead size on a disk UME.[14] They correlated fluorescence microscopy with electrochemistry to track the landing position of beads on the disk UME, while simultaneously recording the magnitude of the current step. The result showed that the current step magnitudes of a bead landed at the edge is around four to seven times larger than that at the center. As a matter of fact, the edge effect comes from the inhomogeneous flux of the reporter molecule. Consequently, the existence of edge effect makes it difficult to measure the size of collision species without knowing the landing position of colliding species on the UME.

On the other hand, for the case where there is not enough supporting electrolyte to carry the current, the bead would undergo significant migration and the frequency of collision is not solely proportional to the bead concentration. For example, the oxidation of ferrocene methanol at the electrode surface would produce a positively charged species (hydroxyl-methyl ferrocenium ion, A^+).[15] In order to keep the electro-neutrality in the vicinity of the electrode surface, all the anions will be attracted by migration. If there is not enough supporting electrolyte to neutralize the charge imbalance, there is a potential drop in the electrolyte and all charges carriers (including the beads) undergo significant migration. Due to the existence of inhomogeneous flux on a disk, the probability for a bead lands at a certain position on a disk-shaped UME is not identical everywhere but depends on the local flux of reporter molecule, the surface charge of an analyte, and their size. Consequently, it is difficult to estimate precisely the concentration of colliding species under migration without knowing the size distribution.

In brief, the prerequisite of measuring the concentration of colliding species is the measurement of their size distribution, while the prerequisite of knowing the size distribution of colliding species is of tracking their landing positions at a disk-shaped UME. However, tracking of statistically-significant number (approximately c.a. 200) of beads dramatically increase the difficulty of the measurement and also brings into additional experimental errors due to readings of the radial distance of colliding species from the UME center. Here is an alternative way of thinking. Could we remove the edge effect by using a specific UME with the homogenous flux of the reporter molecule on its surface?

We simulated the concentration profiles of the reporter molecule being oxidized or reduced at mass transfer limit at a disk and a hemispherical UME, as shown in Figure 3.3A. The grey and light blue colors represent the electrode and the glass sheath, respectively. The color map indicates the concentration of the redox reporter above the electrode. For the disk-shaped UME, the flux profile of the reporter molecule is not homogenous: the closer to the edge, the higher the flux, and the closer to the center, the lower the flux. On the contrary, the flux profile on a hemisphere is homogenous, indicating that all the collision positions are equivalent. Furthermore, the corresponding flux of reporter molecule is obtained by the concentration gradient on the electrode surface, according to Fick's first law. Figure 3.3B shows the corresponding simulated flux of redox molecule at a disk-shaped UME and hemispherical UME. The flux at the edge of a disk-shaped UME is about seven times larger than that at its center, which is consistent with previously reported simulations.[14] On the other hand, the flux at a hemisphere UME is identical everywhere. Thus, using a hemispherical UME instead of a disk-shaped UME allows, in theory, measuring precisely the size distribution of colliding species, thereby determining the corresponding concentration.

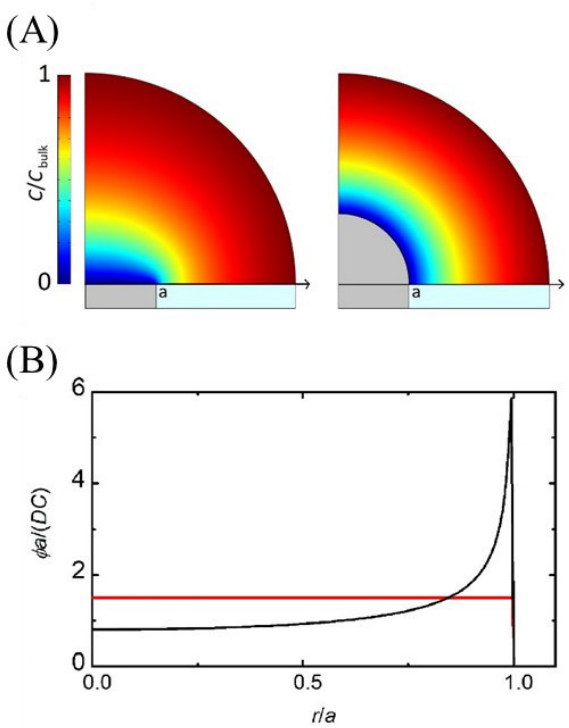

Figure 3.3. (A) Simulated concentration profiles of a redox molecule being oxidized/reduced at mass transfer-limit on a disk and a hemispherical UME. The grey and light blue colors represent the electrode and the glass sheath, respectively. The concentration of redox reporter above the electrode is indicated by the color map. (B) The black and red traces correspond to the dimensionless flux simulated at a disk and a hemispherical UME, respectively. The radial position is normalized by the radius *a* of the UME. The letters *Φ*, *D,* and *C* correspond to the flux, the diffusion coefficient, and the concentration of the redox reporter, respectively.

3.2 Fabrication of hemispherical Hg UMEs

Hemispherical UMEs are fabricated by electrodepositing mercury on a 5 µm radius Pt disk UME under constant potential (potentiostatic mode, E_{WE} = -0.1 V vs. Ag/AgCl) according to a protocol published by Bard and coworkers.[16] The liquid Hg surface ensures a perfectly smooth surface and can be easily fabricated in our laboratory. The drawback is the short potential window where Hg is stable (< 0.5 V in the absence of Cl^- in the electrolyte).

Note that we use Pt electrodes instead of Au electrodes to avoid the formation of an amalgam with Hg. The electrodeposition bath is composed of 10 mM $Hg(NO_3)_2$ and 100 mM $NaNO_3$ (the supporting electrolyte). Before each electrodeposition, the Pt UME is sequentially polished with 1, 0.3 and 0.05 µm alumina slurry (followed by a gentle wiping of the surface with a wet micro cloth to remove alumina particles), dipped in a Piranha solution for ten seconds and finally rinsed with DI water. This procedure ensures a reproducible Pt surface. Ar was bubbled to remove oxygen throughout the experiment. The Pt UME is biased at -0.1 V for around 172 s, and a total of charge of 5.94 µC on average passes the electrode before disconnecting the electrode. The maximum deposition time stays at 180 s based on experimental experiences. The subsequent steady-state current measurement is performed to check the hemisphere. A typical chronocoulogram is shown in Figure 3.4A. The slope of the chronocoulogram is not constant but increases monotonically, revealing a transition from a disk to a hemispherical shape. The theoretical charge necessary to form a 5 µm radius Hg hemisphere, 3.415 µC, is calculated with the Eq. (3.4):[17]

$$Q = nFN_A = nF\frac{m_{hemi}}{M_r} = nF\frac{\rho V_{hemi}}{M_r} = \frac{2\pi nF\rho r_{elec}^3}{3M_r} \tag{3.4}$$

where Q is the charge passing through the electrode, n is the number of electrons transferred (n equals to 1), F is the Faraday's constant (96487 C mol^{-1}), ρ is the density of mercury (13.56 g/cm^3), M_r is the molar mass of the mercury (200.59 g/mol), r_{elec} is the radius of the Pt UME, N_A is the Avogadro constant, m_{hemi}, and V_{hemi} are the moles, mass and volume of the deposited mercury, respectively. In practice, a charge of 5.997 ± 0.257 µC (on average) is necessary to form a hemisphere. The faradaic yield is thus 57%. The loss of charge is possibly introduced by the deposited mercury volume large than a normal hemisphere. Indeed, the charge having a cubic relation with the radius, and the ratio of increment will reach 33% even with a radius of 10% larger than the radius of a perfect hemisphere. After electrodeposition, the Hg hemisphere is checked by optical microscopy. Figure 3.4 B and C show optical micrographs of a bare Pt UME and a Hg hemispherical UME. The micrographs are taken in the air after gently rinsing the UME in DI water and drying under ambient temperature. The change of color on the micrographs is caused by the light source and color settings of the camera changing between measurements. While the Pt UMEs presents scratches caused by mechanical polishing, the Hg UME displays a smooth surface in a different focal plane than the glass sheath, as expected for a 5 µm tall hemisphere and 40X magnification. One can observe that the Hg stays confined on the Pt surface and does not spread on the glass.

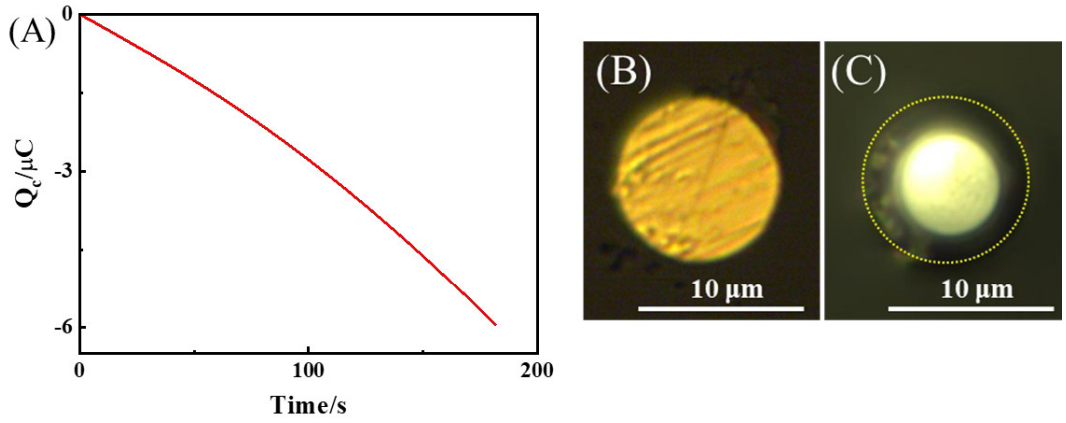

Figure 3.4 (A) Chronocoulogram recorded during the electrodeposition of Hg on a 10 µm diameter Pt electrode. The UME is biased at -0.1 V in a 10 mM $Hg(NO_3)$ in a 100 mM $NaNO_3$ aqueous solution. Optical micrographs of (B) a bare platinum UME and (C) a Hg hemispherical UME. The surface of the UME was observed by optical microscopy with a 100X magnification.

The actual size of the Hg hemisphere is measured by cyclic voltammetry of the couple $Ru(NH_3)_6^{3+}/Ru(NH_3)_6^{2+}$. This redox couple is chosen because of its fast electron transfer rate constant and its low formal potential ($E^{\theta\prime}_{Ru(NH_3)_6^{3+}/Ru(NH_3)_6^{2+}}$ = ~ -0.18 V vs. Ag/AgCl) compatible with the potential window where Hg is stable. Figure 3.5 shows typical voltammograms obtained with a UME before (black trace) and after (red trace) electrodeposition of the Hg hemisphere. The steady-state current of the hemispherical UME is larger than that of the disk UME. One also notices that the capacitive current of the Hg hemisphere seems slightly larger the capacitance of the Pt disk, indicating an increase of surface. Most importantly, the steady-state current is a function of the shape of the UME, with the theoretical ratio of 1.57 ($2\pi/4$) between a hemisphere and a disk having the same radius.

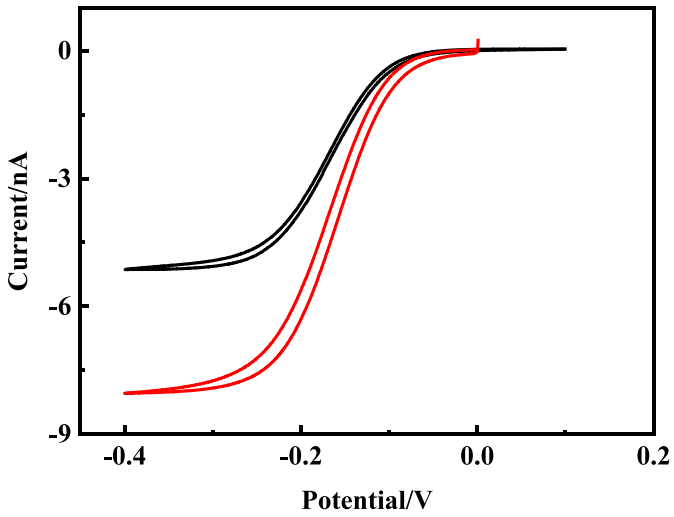

Figure 3.5. The steady-state current measured with a disk UME (black) and a hemispherical UME (red). The solution contains 3 mM $Ru(NH_3)_6^{3+}$ and 1 mM acetate buffer (pH = 5). The solution is bubbled with Ar for a few minutes to remove the oxygen before the measurement.

For all hemispherical Hg UMEs, we typically obtain ratios between 1.55 and 1.74, with difference of less than 10% between the optimum and experimental ratio. The impact of this difference on the shape of UMEs was estimated by performing numerical simulations of the steady-state current at a 5 µm radius UME having a shape comprised between a disk and a sphere, as shown in Figure 3.6A. The steady-state current is plotted in Figure 3.6B versus the shape of the UME. It can be seen that ratios between 1.55 and 1.74 correspond to electrodes having a height comprised between 4.8 and 6.2 µm.

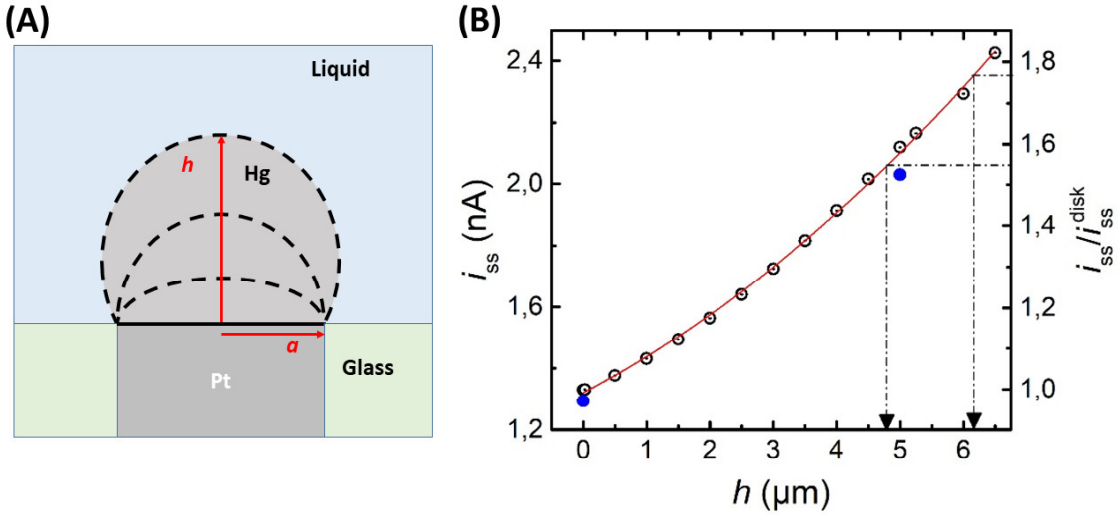

Figure 3.6. (A) The geometry of the UME. The dashed lines represent three different cases where the UME is smaller than a hemisphere, exactly a hemisphere and larger than a hemisphere. The area of contact between the Hg and the Pt is kept constant (Hg does not wet glass) while the height, *h*, of the Hg droplet progressively increases. The droplet keeps a spherical aspect of minimizing the energy of the Hg/water interface. (B) Steady-state current simulated with COMSOL in 2D axial geometry for the UME (a = 5 µm) shown on the left assuming a diffusion-limited current. The current is simulated as a function of the height of the droplet. The blue points correspond to the analytical solution for a disk (h = 0 µm) and a hemisphere (h = 5 µm). The red line is the least-square fit of the function $y = ax^2+bx+c$ with the coefficients a, b and c being 1.321, 0.107 and 0.010, respectively (R^2 =0.999). [redox molecule] = 1 mM, D_{redox} is taken as 6.7 cm^2/s. The time-dependent solution obtained at 5 s is considered to be sufficiently close from the steady-state solution (less than 1% of variation). The deviation between the simulation and the analytical solution is less than 5%. The black arrows represent the experimental minimum and maximum values of the $i_{ss,hemi}/i_{ss,disk}$ measured for the Hg UMEs. These values lead to a height varying between 4.8 and 6.2 µm (i.e., between - 4% and + 24% of nominal height).

3.3 Collisions on hemispherical UMEs

3.3.1 Schematic collision experiments on Hg hemispherical UMEs

A schematic experimental setup is shown in Figure 3.7. A hemispherical Hg UME is dipped in a solution containing the redox species of $Ru(NH_3)_6^{3+}$. Once adding insulating beads in solution, these beads latter can diffuse/migrate toward the electrode surface and adsorb irreversibly. The bead will partially block the flux of redox molecule by blocking the volume above the electrode (not only the electrode surface), [13] producing a discrete decrease of the steady-state current in the *i-t* curve.

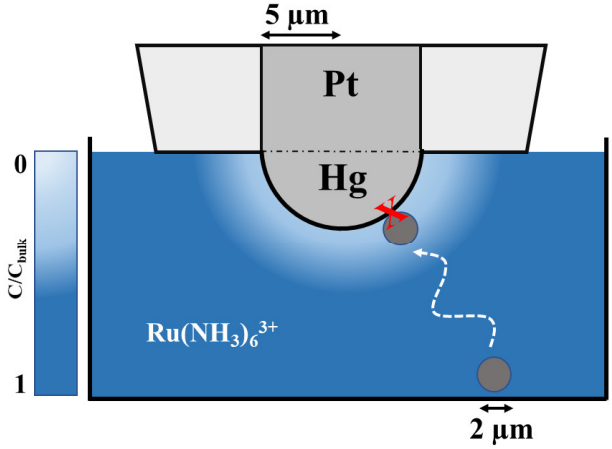

Figure 3.7. Scheme of the experimental setup. The polystyrene beads move toward the electrode from the bulk solution by diffusion/migration (white arrow). If the insulating polystyrene bead sticks to the surface of the UME, then the flux of $Ru(NH_3)_6^{3+}$ toward the electrode (white arrow) is partially hindered, and a discrete decrease of current is recorded. Under the diffusion-limited process, the concentration of $Ru(NH_3)_6^{3+}$ at the electrode surface is close to zero, and a concentration gradient of the reporter molecules forms as sketched by the color map.

Figure 3.8 A and B show typical chronoamperograms recorded in the absence (black trace) and presence (red trace) of 1 µm and 0.5 µm radius amine-functionalized polystyrene beads, respectively. The presence of amine groups on the surface of the beads ensures a large value of zeta-potential (+ 40 mV at pH of 5), increasing the stability of the beads in solution and more importantly favoring their migration toward the UME where a cathodic reaction is taking place (hence positive counter-ions are attracted to balance the charge). The solution contains 3 mM $Ru(NH_3)_6Cl_3$ and 1 mM acetate buffer (pH = 5). We purposely keep the concentration of $Ru(NH_3)_6Cl_3$ and buffer low to keep the ionic strength as low as possible and maximize the migration of the beads. The reduction of $Ru(NH_3)_6Cl_3$ at mass transfer limit leads to a quasi-steady-state current, as shown in both black traces in Figure 3.8. The red traces in both figures evidence discrete step-like current transients that are not observed in both black traces. These step-like current events are caused by the irreversible adsorption of beads on the UME surface. This phenomenon is consistent with the previous observations of negatively charged carboxylated latex beads, silica and polystyrene spheres on electrodes (with ferrocene methanol being oxidized at the electrode).[1-3, 15]

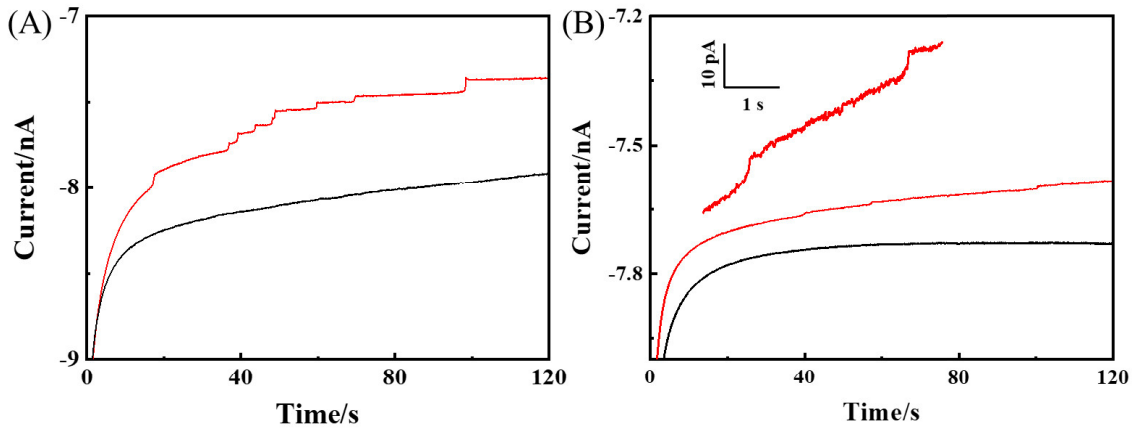

Figure 3.8. Chronoamperograms recorded in the absence (black traces) and presence (red traces) of (A) 1 µm and (B) 0.5 µm radius amine-functionalized polystyrene beads. The inset in (B) is an enlarged zone. The concentrations of 1 µm and 0.5 µm radius polystyrene beads are 100 fM and 25 fM, respectively. The solution contains 3 mM $Ru(NH_3)_6Cl_3$ and 1 mM (acetate buffer pH = 5). The 5 um radius Hg hemispherical UME is biased at -0.4 V.

Further evidence of the origin of current steps is provided by the examination of the UME under optical microscopy right after the collision experiment. Figure 3.9A shows polystyrene beads on the electrode. We attempted to clean the beads in order to re-use the same electrode for several collision experiments. Figure 3.9B shows that sonication of the UME in DI water for ten minutes can entirely remove the beads. Note that polystyrene beads on the surface are occasionally partially removed after sonication shown in Figure 3.9C. Thus, it is necessary to check the hemisphere by optical microscopy after sonication and do the sonication again if necessary. Besides, for a new day of the experiment, the electrode needs to be polished, and a new Hg hemisphere needs to be electrodeposited.

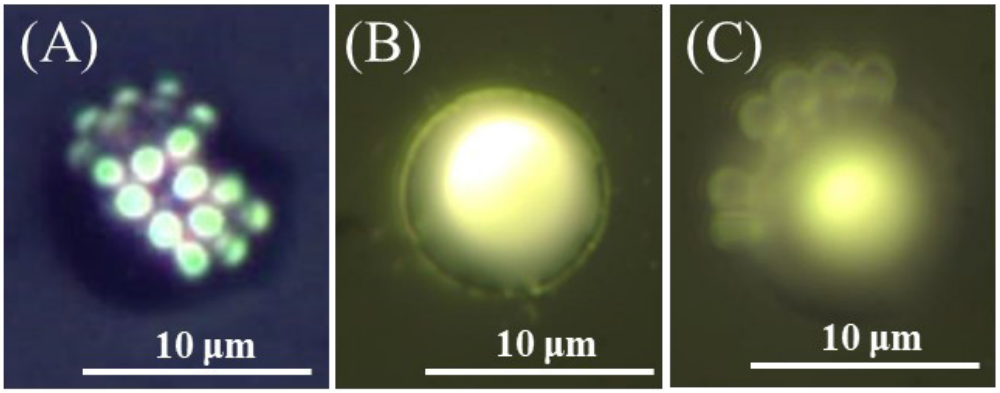

Figure 3.9. (A) Optical micrographs of a Hg hemispherical UME after multiple collisions showing the electrode surface covered by 1 µm radius beads. Optical micrographs of the same electrode as in (A) after ultra-sonication in DI water for 10 minutes (B). (C) the same procedure with (B), but beads are only partially removed. The surface of the UME was observed, in the air, by optical microscopy with a 100X magnification.

The dimensions of the polystyrene beads were measured by SEM in order to determine precisely their size distribution. A typical SEM image of 1 µm radius polystyrene beads drop cast on a Si wafer is shown in Figure 3.10A. The size distribution was determined through the analysis of several images. The analysis comprises a clean-up of the picture with ImageJ (thresholding, binary mask, rolling ball filter, color inversion, see Figure 3.10B) followed by an automated search of the beads with a Matlab script (red circles Figure 3.10C).

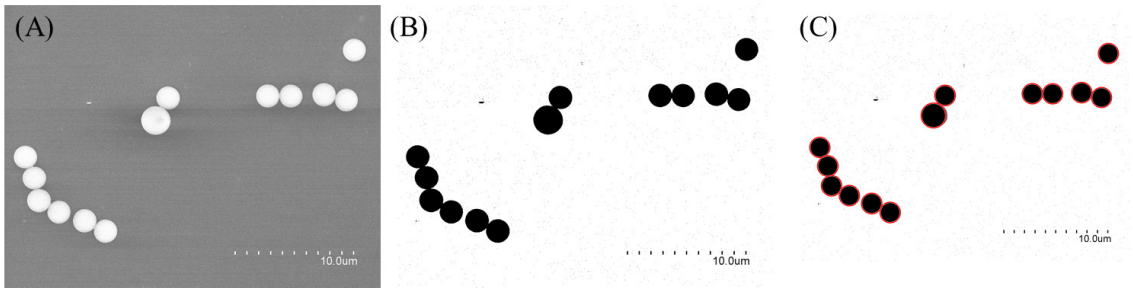

Figure 3.10. The procedure used to calculate the diameter of beads by using SEM images (A) filtered with Image J (B) and finally analyzed with MATLAB (C). The code in Matlab 2012R is shown below:

```
>> Rgb = imread ('file_name.tif');
   Figure imshow (rgb)
   [centers, radii] = imfindcircles (rgb, [20 50], 'ObjectPolarity', 'dark', 'Sensitivity', 0.95) ;
   Viscircles (centers, radii) ;
```

The size distribution obtained from the SEM images is shown in Figure 3.11 A and B for the 0.5 µm and 1 µm radius beads, respectively. The average radius of the 0.5 µm and 1 µm beads are 0.51 µm and 0.97 µm in good agreement with the specifications of the provider.

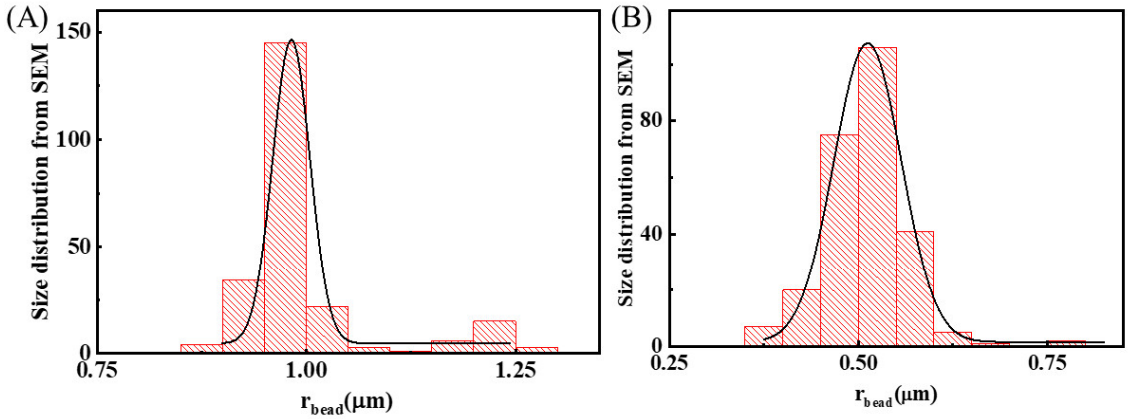

Figure 3.11. The size distribution of the 1 µm (A) and 0.5 µm (B) radius polystyrene beads found by SEM. The total number of bead analyzed is 194 and 303, respectively. The black lines are the best fits of a Gaussian function. The center, standard deviation and R^2 of the Gaussians fitted on the distributions of the 1, and 0.5 µm beads are: 0.97 µm, 0.03 µm, 0.988, and 0.51 µm, 0.04 µm, 0.995, respectively.

3.3.2 Size distribution of the current step

During amperometric measurements of 1 µm radius polystyrene beads, for each measurement a newly-electrodeposited or sonicated Hg hemisphere was used. Among all chronoamprograms, a maximum of 13 collisions is counted, and the average number of collisions recorded per *i-t* trace is 10. The probability of having a collision, between a bead absorbed on the electrode surface and a particle coming from the solution, is roughly estimated by dividing the projected area of a bead (multiplied by the compacity of hexagonally-arranged spheres on a flat surface) by the surface of the hemisphere. After 13 collisions of 1 µm radius beads on a 5 µm radius Hg UME, the probability of having a collision between a bead coming from the bulk solution and a bead already present on the hemisphere is 26% at most. Figure 3.12(A_1-A_3) shows three examples of current steps recorded for 1 µm radius beads the Hg UME, where each segment corresponds to one trial (120 s each chronoamperogram). Between each trial, the Hg UME is sonicated in water for ten mins to remove the beads from the previous trial, in order to make sure those beads absorbed on the electrode surface are independent. The number of collisions is 10 on average for each trial. During the analysis of collision data, three conditions are taken into consideration, including the frequency of collision, the changing trend of relative current step with successive trials, and the range of relative current step. In practice, the collision data is regarded: (i) when the number of

collisions is among majority ranges (≥ 5 collisions each chronoamperogram), as shown in Figure 3.12A$_1$. For the other minority cases, the chronoamperograms are disregarded, only a few cases with the number of collisions less than 5; (ii) when there is no obvious changing trend during one experiment (the first two trials in Figure 3.12A$_2$), the other increasing or decreasing data is disregarded (shown in black arrow in Figure 3.12 A$_2$ and A$_3$); (iii) when the range of relative current step mainly sits between 3 ‰ and 7 ‰, corresponding to the radius of bead between 0.79 μm and 1.15μm, respectively.

Concerning 0.5 μm radius polystyrene beads, the number of collisions is 3 collisions per trial on average. Considering the relatively low frequency of collisions, for each newly-electrodeposited Hg UME, a maximum of 20 collisions is continuously recorded without further sonication to remove beads between trials, as shown in Figure 3.12(B$_1$-B$_3$). The total bead coverage is less than 10% on the electrode surface. The size of relative current steps is not varying significantly during the course of the experiment (around one thousand seconds in total). Thus, all the data fitting the conditions is regarded for further analysis.

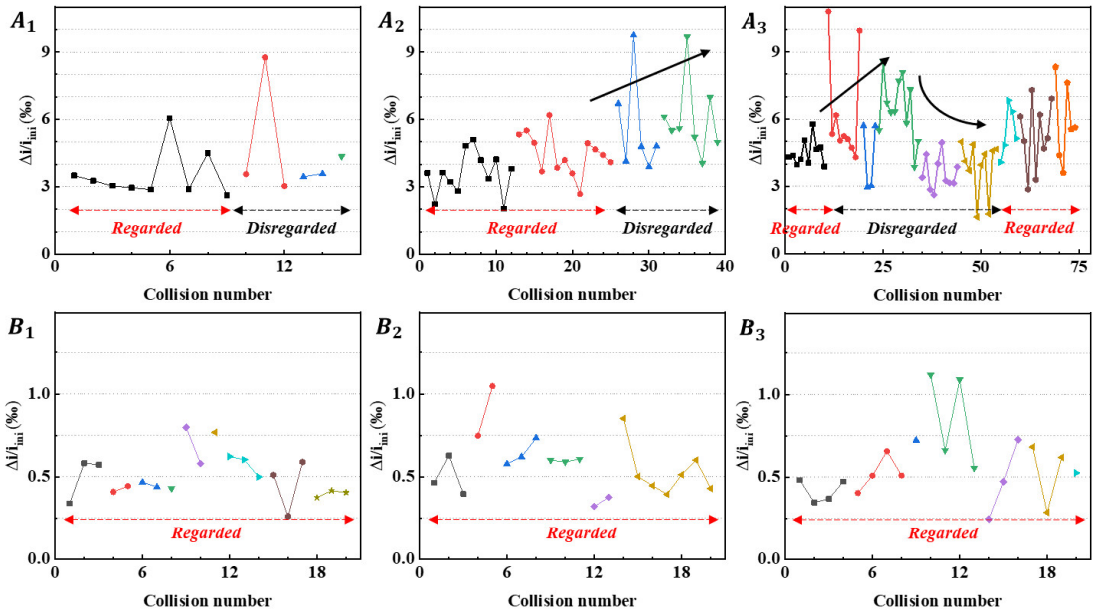

Figure 3.12. The magnitude of the step size as a function of collision number present on the Hg UME. Each segment of line+symbol shown in different colors represents an individual trial, and one graph corresponds to a newly-electrodeposited Hg UME. (A$_1$-A$_3$), (B$_1$-B$_3$) Examples of the current steps recorded for (i) 1.0 μm, (ii) 0.5 μm radius polystyrene beads, respectively. (i) For 1.0 μm radius beads, the Hg UME is sonicated in water for ten mins to remove the beads from the previous trial due to the much higher collision frequency (10 collisions on average). (ii) For 0.5 μm radius bead, however, considering the low-collision frequency (3 collisions on average), the next trial is continuously recorded once the previous trial stops, without further sonication to remove beads. A maximum of 20 collisions for one newly-electrodeposited Hg UME is recorded. The selected data used for further analysis is underlined by the red dash line, while the other data is disregarded (black dash line).

The histograms of relative current steps for 1 μm and 0.5 μm radius polystyrene beads are shown in Figure 3.13 A and B, respectively. For the sake of comparison, collision measurement was also performed with a disk-shaped UME, and the results are shown with the black bars in Figure 3.13 A and B, respectively. For 1 μm radius polystyrene beads, the size distribution of current steps obtained on a hemispherical UME spans from 2 ‰ to 8 ‰, while it spans over about a 2 – 3 times broader range (3 ‰ and 22 ‰) for a disk-shaped UME. Both distributions have an asymmetrical shape with a tailing toward a large step size. This tailing is much more pronounced for the disk-shaped UME due to the edge effect. This phenomenon is similar for 0.5 μm radius polystyrene bead shown in Figure 3.13B, where the step size distribution at a hemispherical UME and a disk-shaped UME ranges from 0.25 ‰ to 3.25 ‰ and 0.75 ‰ to 8.25 ‰, respectively.

As explained in the introduction, a disk-shaped UME is expected to create a broader distribution of current steps due to the edge effect compared to hemispherical UMEs. These large current steps obtained on the disk UME are caused by the beads colliding near the perimeter of the disk UME, where the diffusive flux of electroactive molecules is the largest. On the contrary, these large steps are not observed on hemispherical UMEs. Thus, we conclude that hemispherical UMEs can effectively reduce the edge effect.

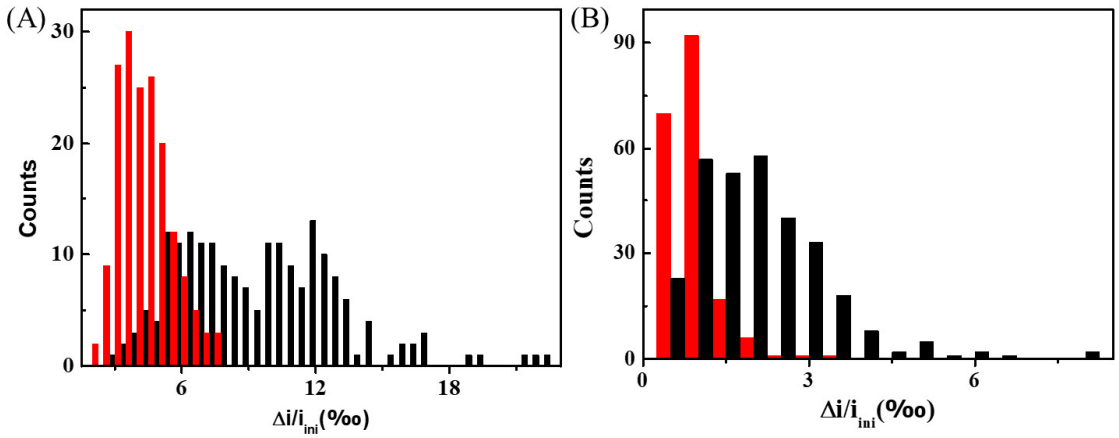

Figure 3.13. Distribution of the amplitudes of the current steps corresponding to the collision of (A) 1 μm radius and (B) 0.5 μm radius amine-functionalized polystyrene beads on a 5 μm radius Hg hemispherical UME (red bar) and a 5 μm radius disk Pt UME (black bar). (A): red bars, 170 counts; black bars, 194 counts. (B): red bars, 189 counts; black bars, n = 303 steps.

However, the reduction of the edge effect does not allow a direct comparison of current step distribution and bead size distribution, not to mention the bead concentration. In the next section, we will introduce numerical simulation to determine the current step produced by a bead of a given radius, thereby converting current step distribution into bead size distribution. After knowing the bead size distribution, we will show how to determine the bead concentration using the collision frequency.

3.4 The determination of radius and concentration of beads

3.4.1 Convert current step size to bead radius

In order to convert the relative current step into a bead radius, we proceed as follows. We first use numerical simulations to simulate the current step size produced by a bead of a given radius. Using this simulated calibration curve, we transform the distribution of current steps into a bead size distribution. Details about the numerical simulations are provided in Appendix Section 1. Several simulations were performed with beads of various radii in order to generate the calibration curve shown in Figure 3.14, where the black circles correspond to the simulation points for a given radius, and the red curve is a least-square fitting of a polynomial. The bead radius is normalized by the electrode radius and plotted in %, while the step size is normalized by the steady-state current and plotted in ‰. From the calibration curve, we can see that the current step size is not a linear function of bead size but second-order polynomial relation: $Ax^2 + Bx$. The coefficients A and B equal 0.0187 and -0.1012, respectively (R^2 = 0.999). This relation holds for any ratio of bead/electrode (e.g., 0.05 μm radius bead/0.5 μm radius electrode) shown in Figure 3.12. In the above polynomial function, the quadratic component dominates. In other words, the current step size depends mainly on the projected area of the bead. Note that the quadratic dependence of the step size with bead radius implies that an initially symmetrical distribution of the bead size should lead to an asymmetric distribution of the current step size. Similar quadratic behavior was also observed when simulating a disk-shaped UME, suggesting that the shape of the UME is not at the origin of this kind of relationship.[3]

The calibration curve in Figure 3.14 indicates that a relative step size of 0.5 ‰, the minimum step that could be distinguished experimentally, corresponds to a bead with a radius of 8.3 % of the radius of

the UME. The range of radius that can be detected by a UME of a given size spans typically between ≈ 8% to 30% of the radius of the UME. For a 5 µm radius UME, beads between 0.4 and 1.5 µm radius could be detected. This range is imposed by the signal-to-noise ratio (S/N) of the experiment and a minimum number of collisions that can be recorded with one UME before completely covering its surface. It is indeed preferable to avoid multilayers as the analysis becomes complicated. In some specific conditions, particles with a size down to 0.05% of the size of the UME can also be detected by blocking. For example, single proteins of a few nm in radius were detected using 80 nm radius nanoelectrode and extremely high concentrations of redox reporter (300 mM).[18] Thanks to this large concentration of redox reporter, a large steady-state current was obtained, and thus the S/N ratio of the experiment increased enough to detect tiny particles. However, high concentrations of charged redox molecules can easily destabilize colloidal suspensions and thus is not compatible with most of the particles (such as polystyrene beads).

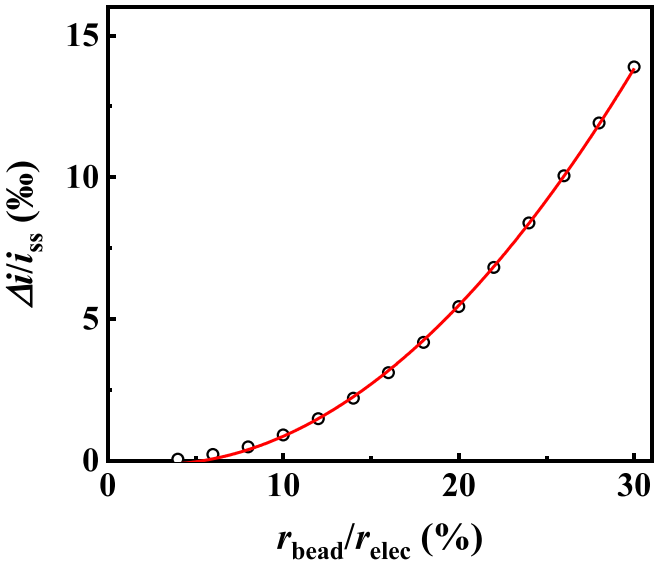

Figure 3.14. Simulated calibration curve of the step size vs. bead size. Details about the simulation are shown in Appendix Section 1. The red line corresponds to a least-square fitting of a second-order polynomial: Ax^2+Bx. The coefficients A and B equal 0.0187 and -0.1012, respectively (R^2 = 0.999).

In order to determine the analytical limits of the electrochemical blocking, the precision of the bead size, corresponding to the minimum change in step size that we can observe experimentally, needs to be discussed. The precision of the bead size is fixed by the precision of our electrochemical measurement, the precision of the simulated calibration curve, and the bead/electrode size ratio. (i) The precision of the current measurement is fixed by our setup at 0.5 pA and is constant over all the current ranges. This value represents a trade-off between the gain of the amplifier (10^9 V/A) and a reasonable bandwidth (10 ms for our low noise trans-impedance amplifier). If we consider that a signal (step height) should be at least three times larger than the noise (about 0.5 pA) then, the closest current step we can measure is 2 pA. These steps would correspond to relative steps of 0.2 ‰ and 0.3 ‰, respectively (steady-state current ≈ 7.5 nA). (ii) The precision of the numerical simulation is about 0.2 ‰ for the smallest ratio of bead/electrode radii. Thus, we can distinguish at best 0.2 ‰ from 0.4 ‰ steps. From the simulated calibration curve, one estimate that a change of 0.2 ‰ to 0.4 ‰ in relative current step produces a change of 6 % to 8 % in the bead/electrode size ratio. In other words, for 0.5 µm radius polystyrene beads, we could distinguish a bead of 0.3 µm radius from a bead of 0.4 µm radius. The precision is 0.1 µm. (iii) A similar calculation provides a precision of 0.05 µm for 1.0 µm radius polystyrene beads. The precision will increase for a large bead because of the quadratic dependence of the step size with bead size. In other words, the slope (red curve in Figure 3.14) will increase for a larger bead than a smaller bead. In summary, the precision of the bead size is 100 nm and 50 nm for 0.5 µm and 1.0 µm radius polystyrene beads, respectively.

Once the radius of the bead is obtained, it is then possible to convert the frequency of collision steps to the concentration of the bead in mol/L. In Appendix section 2, we can see how the frequency of collision steps is converted into the bead concentration in mol/L. Also, the respective contribution by diffusion and/or migration will be discussed in the next subsection.

3.4.2 Convert the frequency of collision steps to the bead concentration

In the absence of convection, the frequency of collision steps, $f(r_{bead})$, (defined as the average time interval between current steps) for a bead of radius r_{bead} consists of two contributions: i) the frequency of diffusion, f_{dif}, and ii) the frequency of migration, f_{mig}, are shown in Eq. (3.5) left and right terms in brackets, respectively. If we consider a 100% sticking probability, the frequency of collision is related to the concentration of bead, their size, and other experimental parameters by the relation (see Appendix Section 2):

$$f_{bead} = 2\pi N_a r_{elec} C_{bead} \left(\frac{\alpha}{r_{bead}} + \beta r_{bead} \right) \tag{3.5}$$

The quantities N_a, r_{elec}, and C_{bead} are the Avogadro's constant, the radius of the electrode, and the concentration of bead, respectively. The coefficients α and β are defined as follows:

$$\alpha = \frac{kT}{6\pi\eta} \tag{3.6}$$

$$\beta = D_{redox} C_{redox} \frac{2\sigma_{bead}}{3\eta} \sum \frac{1}{C_i \mu_i} \tag{3.7}$$

where k, T, η, D_{redox}, C_{redox}, σ_{bead}, μ_i and C_i are the Boltzmann constant, the temperature, the dynamic viscosity of the medium, the diffusion coefficient of the redox reporter, the concentration of the redox reporter, the surface charge density of the bead, the mobility of the ions "i" in solution and their concentration, respectively. These two coefficients are weighting the respective contribution of diffusion (α) and migration (β) on the frequency of collision for beads of a given size. They depend solely on known experimental parameters, and the surface charge density of the beads measured independently (see Appendix Section 2).

The respective contribution of diffusion and migration to the collision frequency is obtained as a function of the size of the bead, plotted in Figure 3.15. In order to better compare the frequency of collision as a function of the radius, the diffusion and migration frequencies are normalized by the concentration of the bead and the radius of the electrode. Note that these frequency values are specific to the condition used here. Figure 3.15 highlights that, under our experimental conditions (low concentration of supporting electrolyte), migration dominates the flux of bead. The flux by migration is around 100 times larger than the flux by diffusion on the whole range of bead size used in this work (0.5 - 1 μm radius). This is the reason why we choose a reduction reaction to attract positively charged amine-functionalized polystyrene beads (ζ-potential is around 44 mV). Besides, Eq. (3.5) reveals that diffusion and migration have opposite trends with respect to the size of the beads. The smaller the bead is, and the faster it diffuses; the bigger the bead is and the faster it migrates. Thus, it is necessary to calculate the migration and diffusion flux for a given set of experimental conditions and the size of the bead.

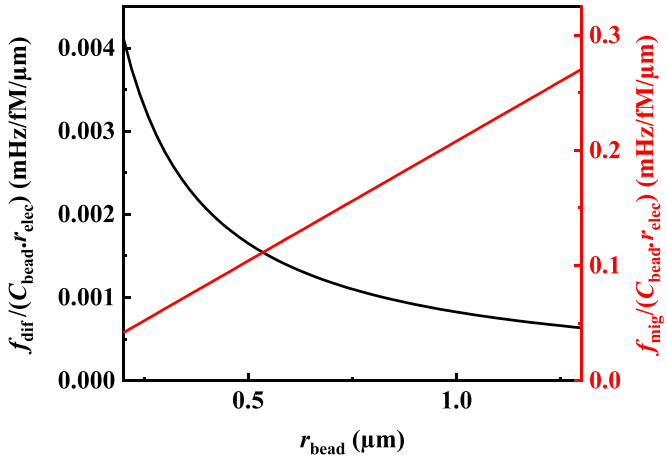

Figure 3.15. Normalized collision frequencies as a function of the radius of the bead. The diffusion and migration components are shown in the black curve and red lines, respectively. These frequencies are calculated using Eqs. (3.1-3.3) and the experimental parameters: r_{elec} = 5.3 μm, $D_{[Ru(NH_3)_6]^{3+}}$ = 8.4 x 10^{-6} $cm^2 \cdot s^{-1}$, [$Ru(NH_3)_6^{3+}$] = 3 mM, [acetate buffer] = 1 mM, [Cl^-] = 9 mM, [Na^+] = 1 mM, $\mu_{Ru^{3+}}$ = 9.82 x 10^{-8} $m^2 \cdot V^{-1} \cdot s^{-1}$, $\mu_{acetate\ buffer}$= 4.24 x 10^{-8} $m^2 \cdot V^{-1} \cdot s^{-1}$, μ_{Cl^-} = 7.92 x 10^{-8} $m^2 \cdot V^{-1} \cdot s^{-1}$, μ_{Na^+} = 5.19 x 10^{-8} $m^2 \cdot V^{-1} \cdot s^{-1}$, σ_{bead} = 36 μC·m^{-2}, η = 8.9 x 10^{-5} Pa·s, T = 293 K.

In summary, using the calibration curve in Figure 3.14, we can convert the distribution of the magnitude of current steps to the distribution of bead size. Once knowing the size distribution, we can determine the bead concentration based on the frequency of collisions by using Eq. (3.5).

3.5 Comparison of the size and concentration found by electrochemistry and SEM

Figure 3.16 shows the histogram of the bead radius as well as concentration, which is converted by each bin of the histogram in Figure 3.9, using the calibration curve in Figure 3.13 and the Eq. (3.5). The histogram of the bead radius found by electrochemistry is shown in red while that found by SEM is shown in black. In order to validate the sensitivity of this technique, both 1.0 and 0.5 μm radius polystyrene beads, following the same procedure, are investigated as a parallel experiment. The details of the size distribution of 1.0 and 0.5 μm radius polystyrene beads found by SEM are provided in Figure 3.11. The fitting curves correspond to the least-square fitting of Gaussian functions on the experimental data. The average radius ± standard deviation found by collision and SEM are reported in Table 3.1. The average size of the beads found by electrochemistry and SEM differs by -8% to -9% while the width of the distributions differs by a factor of 1.5 to 3 for the 0.5 and 1 μm radius bead, respectively.

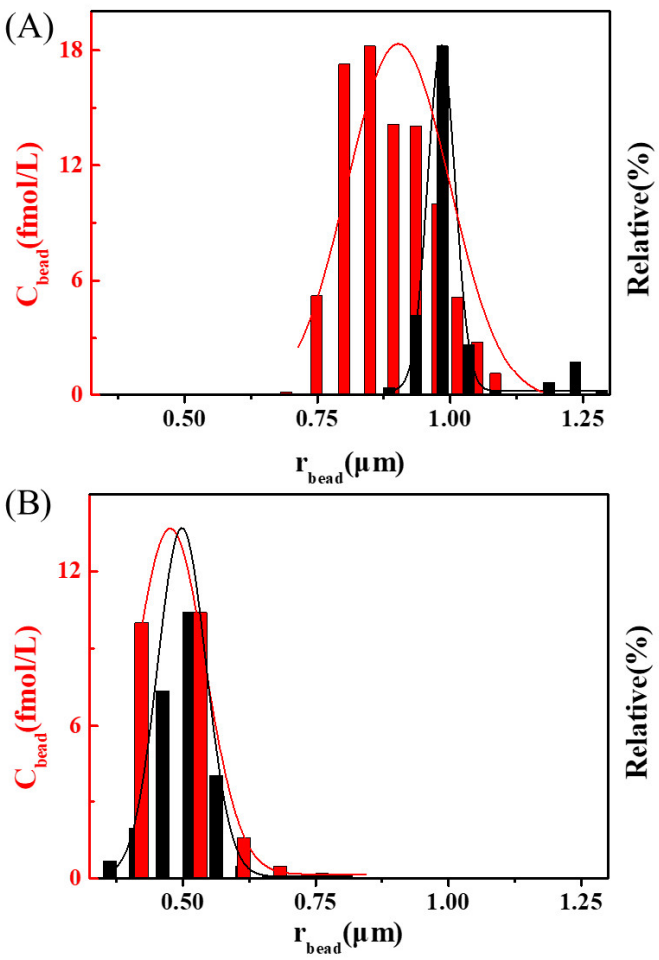

Figure 3.16. Bead size distribution measured by electrochemistry (red) and SEM (black) for 1 µm radius (A) and 0.5 µm radius (B) amine-functionalized polystyrene beads. The curves are the least-square fitting of Gaussian functions of the histograms. For the 1 µm radius beads, the average radius ± standard deviation and R^2 of the electrochemical and SEM data are 0.91 ± 0.09 µm, 0.908 and 0.97 ± 0.03 µm, 0.988, respectively. For the 0.5 µm radius beads the center ± standard deviation and R^2 of the electrochemical and SEM data are 0.47 ± 0.06 µm, 0.997 and 0.51 ± 0.04 µm, 0.995, respectively.

We compare in Table 3.1 (bottom rows) the total number of beads (i.e., all sizes together) initially added in solution and the total number of beads detected by electrochemistry. The sum of the concentration for each bin of the red histogram in Figure 3.14 gives a total concentration of 98 fM (5.902 x 10^7 particle/mL) and 23 fM (1.385 x 10^7 particle/mL) for the 1 µm and 0.5 µm radius beads, respectively. These values found electrochemically are in excellent agreement with the total concentration of bead initially added in solution, 100 fM (6.022 x 10^7 particle/mL), and 25 fM (1.506 x 10^7 particle/mL) for the 1 µm and 0.5 µm radius beads, respectively.

When the flux of bead is dominated by migration, the precision of the bead concentration depends directly on the precision of the surface charge density of the beads (see Eq. (3.5) and (3.7)). In order to determine the surface charge density of the beads, we carried out in an independent measurement of their mobility (by Zetasizer) and then calculated a surface charge density. Details about the measurement and calculations are described in Appendix Section 3. Importantly, the surface charge density is kept constant by the addition of an acetate buffer with a pH of 5, significantly below the *pKa* (=9.5) of the amines decorating the beads.

Table 3.1. Comparison of the size and concentration found by electrochemistry and SEM.

Nominal radius (μm)	0.5		1	
Methods	Echem	Standard*	Echem	Standard*
Mean radius ± SD (μm)	0.47 ± 0.06	0.51 ± 0.04	0.88 ± 0.10	0.97 ± 0.03
Difference in radius (%)	-8		-9	
C_{bead} (fM)*	23	25	98	100
Difference in C_{bead} (%)	-8		-2	

*The average radius was measured by SEM. The concentration was determined by using the concentration of the stock solution given by the provider.

One major advantage of migration over diffusion is the possibility to detect extremely low concentrations of the particle in a reasonable amount of time (< 1 h). Indeed, the limit of sensitivity of the single particle blocking technique is not fixed by the capacity to detect a particle but the time necessary to record statistically meaningful numbers of collisions. Because the flux of the particle is stationary, the limit of sensitivity is directly proportional to the time of the measurement. For example, under our experimental conditions, it takes about 30 min to detect ≈ 200 collisions of 1 μm radius polystyrene beads at 100 fM (6 x 10^7 particle/mL). In principle, we could detect 10 fM (6 x 10^6 particle/mL) of the same beads in 5 h. In the absence of migration (i.e., with the only diffusion), the same measurement would take around 14 days. In order to speed up the collision rate, it is possible to increase the size of the electrode. This strategy has been employed to detect the electro-dissolution of individual Ag nanoparticles on cylindrical carbon fiber UMEs.[19] Concentrations of a few tens of fM (≈ 10^6 particle/mL) were readily detected within a few mins. However, as we saw previously for a detection scheme based on blocking, the size of the electrode has to scale with the size of the beads to keep a reasonable S/N ratio.

The relative difference in the average radius found by electrochemistry and SEM is negative and similar for the two sizes of the bead. For the 0.5 μm radius beads, the width of the distribution found by electrochemistry is close to the width found by SEM. On the other hand, the difference between the width of the distributions found by electrochemistry and SEM is quite large for the 1 μm radius beads. For both sizes of beads, the width of the size distribution is larger in electrochemistry than in SEM. We conclude that, besides the edge effect, there is another phenomenon that biases the size distribution in electrochemical blocking. This bias introduces current steps smaller than expected for a given size of the bead. The smallest current step recorded with the 1 μm radius beads is 1.56 times smaller than the current step predicted from the smallest size of bead found by SEM and our calibration curve in Figure 3.14. Several hypotheses to explain this bias may be pointed out. From the simulated steady-state current as a function of the shape of UME in Figure 3.6B, one can find the variability on the radius of the Hg hemisphere is at most 25% for all experiments and cannot explain a broadening by a factor of three. Also, uncertainties on the values of α and β can affect the symmetry of the distribution but not its width. Eventual numerical errors on the relation between step size and bead size should decrease as the size of the bead gets closer to the size of the UME, and thus we do not expect a significant deviation on the 1 μm radius beads. We could also examine how the presence of beads already adsorbed on the UME will affect the current step size of incoming beads. Indeed, Boika and coworkers reported that a large amount of bead adsorbed on the surface (formation of multilayers) would decrease the average step size.[2] Here, we simulated the step size produced by two beads as a function of the distance between the beads (see Appendix section 1.3). The step size produced by two beads (2 μm diameter) separated by 0.2 μm is 7% larger than two beads far apart from each other (4 μm). In other words, the step size varies only when beads are extremely close to each other (less than a bead's radius) and more importantly, it increases. In our experiments, we observe step size smaller than expected from SEM, and moreover, we keep the probability of observing two beads colliding one on the other very low by limiting the number of collisions on a UME. At this moment, the origin of the broadening remains unknown.

3.7 Conclusion

We report the use of hemispherical UMEs to detect the collision of individual polystyrene beads by electrochemical blocking. We evidenced that the shape of the UME has considerable importance on the size distribution of the current steps. Importantly, the effect of the geometry of the UME on the step size was thoroughly analyzed by numerical simulations, and we showed that the edge effect encountered on disk-shaped UMEs is significantly reduced on hemispherical electrodes. We evidenced the existence of a second bias that tends to overestimate the small current steps. The origin of the bias is not identified yet.

In conclusion, we determine within less than 10% of error the average diameter of polystyrene bead of 0.5 and 1 µm radius. The size distribution of the 0.5 µm radius bead was also correctly determined, while a large deviation is observed for the 1 µm radius beads. The total concentration of bead is found within less than 10% of error for both the 0.5 and 1 µm radius beads. We believe that the quantitative analytical method presented in this work can offer a useful alternative to optical techniques incompatible with opaque samples, for example. The next challenges to be addressed would be the replacement of Hg by another metal, less toxic, and more stable at anodic potentials, as well as the multiplexing of several UMEs of different sizes in order to widen the dynamic range of bead size detectable with one device.

3.8 References

1. Quinn, B. M.; van't Hof, P. G.; Lemay, S. G., Time-resolved electrochemical detection of discrete adsorption events. *Journal of the American Chemical Society* **2004,** *126* (27), 8360-8361.

2. Boika, A.; Thorgaard, S. N.; Bard, A. J., Monitoring the electrophoretic migration and adsorption of single insulating nanoparticles at ultramicroelectrodes. *The Journal of Physical Chemistry B* **2013,** *117* (16), 4371-4380.

3. Bonezzi, J.; Boika, A., Deciphering the magnitude of current steps in electrochemical blocking collision experiments and its implications. *Electrochimica Acta* **2017,** *236*, 252-259.

4. Xiao, X.; Bard, A. J., Observing single nanoparticle collisions at an ultramicroelectrode by electrocatalytic amplification. *Journal of the American Chemical Society* **2007,** *129* (31), 9610-9612.

5. Xiao, X.; Fan, F.-R. F.; Zhou, J.; Bard, A. J., Current transients in single nanoparticle collision events. *Journal of the American Chemical Society* **2008,** *130* (49), 16669-16677.

6. Eloul, S.; Kätelhön, E.; Compton, R. G., When does near-wall hindered diffusion influence mass transport towards targets? *Physical Chemistry Chemical Physics* **2016,** *18* (38), 26539-26549.

7. Kätelhön, E.; Sokolov, S. V.; Compton, R. G., Near-wall hindered diffusion: Implications for surface-based sensors. *Sensors and Actuators B: Chemical* **2016,** *234*, 420-425.

8. Bevan, M. A.; Prieve, D. C., Hindered diffusion of colloidal particles very near to a wall: Revisited. *The Journal of Chemical Physics* **2000,** *113* (3), 1228-1236.

9. Taylor, J. K.; Cihon, C., *Statistical techniques for data analysis*. CRC Press: 2004.

10. Boika, A.; Bard, A. J., Time of first arrival in electrochemical collision experiments as a measure of ultralow concentrations of analytes in solution. *Analytical Chemistry* **2015,** *87* (8), 4341-4346.

11. Xiong, J.; Chen, Q.; Edwards, M. A.; White, H. S., Ion transport within high electric fields in nanogap electrochemical cells. *ACS nano* **2015,** *9* (8), 8520-8529.

12. Deng, Z.; Elattar, R.; Maroun, F.; Renault, C., In Situ Measurement of the Size Distribution and Concentration of Insulating Particles by Electrochemical Collision on Hemispherical Ultramicroelectrodes. *Analytical Chemistry* **2018,** *90* (21), 12923-12929.

13. Renault, C.; Lemay, S. G., Electrochemical Collisions of Individual Graphene Oxide Sheets: An Analytical and Fundamental Study. *ChemElectroChem* **2020,** *7* (1), 69-73.

14. Fosdick, S. E.; Anderson, M. J.; Nettleton, E. G.; Crooks, R. M., Correlated electrochemical and optical tracking of discrete collision events. *Journal of the American Chemical Society* **2013,** *135* (16), 5994-5997.

15. Allen J. Bard, A. B., Seong Jung Kwon, Jun Hui Park, and Scott N. Thorgaard, Stochastic Events in Nanoelectrochemical Systems. In *Nanoelectrochemistry*, CRC Press, 2015; pp 241-292.

16. Mauzeroll, J.; Hueske, E. A.; Bard, A. J., Scanning electrochemical microscopy. 48. Hg/Pt hemispherical ultramicroelectrodes: fabrication and characterization. *Analytical Chemistry* **2003,** *75* (15), 3880-3889.

17. Harvey, D., Analytical Chemistry 2.0—an open-access digital textbook. *Analytical and Bioanalytical Chemistry* **2011,** *399* (1), 149-152.

18. Dick, J. E.; Renault, C.; Bard, A. J., Observation of single-protein and DNA macromolecule collisions on ultramicroelectrodes. *Journal of the American Chemical Society* **2015,** *137* (26), 8376-8379.

19. Ellison, J.; Batchelor-McAuley, C.; Tschulik, K.; Compton, R. G., The use of cylindrical micro-wire electrodes for nano-impact experiments; facilitating the sub-picomolar detection of single nanoparticles. *Sensors and Actuators B: Chemical* **2014,** *200*, 47-52.

4. Chapter 4 Detection of individual conducting graphene nanoplatelet by electro-catalytic depression

4.1 Introduction

The detection of non-redox active materials that are neither insulators nor good catalysts like carbonaceous materials requires a different strategy. Detection of carbonaceous particles by electrochemical collision is already reported for carbon nanotubes,[1] graphene sheets,[2] and graphene nanoplatelets.[3] The detection of single-wall carbon nanotubes (SWCNTs) relies on area amplification.[4] Bard and coworkers described electrochemical detection of gold NP-decorated single-wall carbon nanotube (Au-SWCNT). The outer-sphere electron-transfer reaction, ferrocenemethanol (FcMeOH) oxidation, was carried out to monitor the nanoparticle attachment at a nanoelectrode. During this simple outer-sphere reaction, neither the reactant nor the product would interact with the electrode surface strongly. Thus, the current increase is caused by the change in the active area for the oxidation of FcMeOH molecule. Figure 4.1A illustrates how a single modified Au-SWCNT is detected, where highly charged Au-SWCNT migrates to a Pt nanoelectrode due to the faradaic current. A representative TEM image of Au-SWCNT is shown in Figure 4.1B. An instantaneous current increment was observed after the attachment of Au-SWCNT to the electrode surface, and the steady-state current is kept constant for over 250 s (Figure 4.1C). The surface area of the nanotube should be large enough in case the current increment by area amplification can be detected. Upon collision of the SWCNT on a nanoelectrode, a discrete increase of current can be evidenced by measuring the electrochemical response of a redox couple in solution. Note that ideal discrete increases of current were observed only for SWCNT modified with gold nanoparticles but not for bare SWCNT.

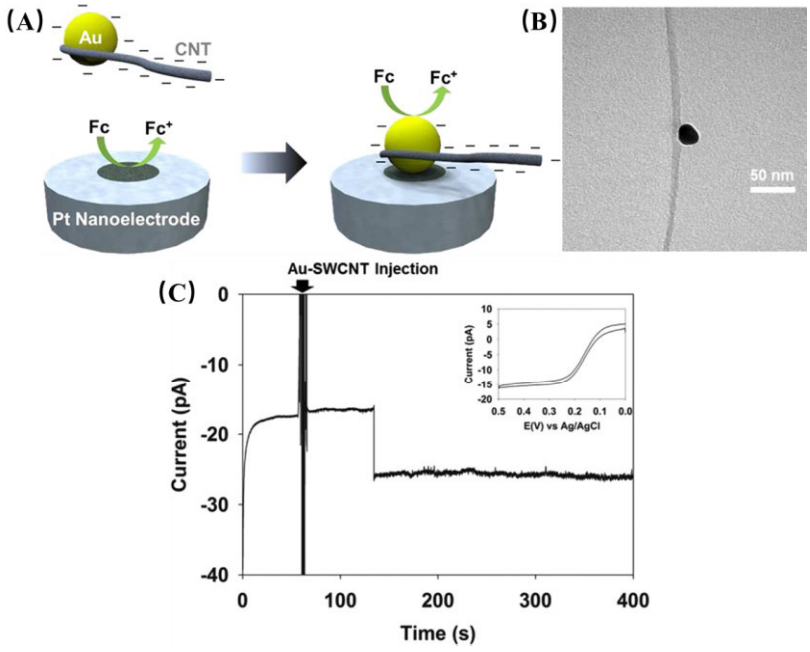

Figure 4.1. (A) Schematic representation of the attachment of an individual Au-SWCNT NP at the Pt nanoelectrode. (B) TEM image of an individual Au-SWCNT. The black dot represents the Au, and the gray band corresponds to the SWCNT. (C) Chronoamperometric curves recorded after the injection of a single Au-SWCNT. The solution contains 4 mM FcMeOH and 100 µM KNO_3. Reproduced, with modification, from Ref. [4]. Copyright 2013, American Chemical Society.

The detection of a single graphene sheet was performed using a "tunneling" strategy, as mentioned in section 1.2.2 in Chapter 1.[2] In this work, the incubation of the electrode in the solution of the graphene sheet was performed blindly, that is without monitoring the collisions. Thus, the adsorption of individual graphene sheets was not observed in real-time and no analysis of the frequency of collision was performed. The third example relies on transient currents recorded upon collision of individual graphene nanoplatelets (GNPs) on a C-fiber UME.[3] The C-fiber UME was polarized either anodically or cathodically, as shown in the left and the right figures in Figure 4.2A. When GNPs impact with the polarized electrode, the authors proposed that GNPs were negatively or positively charged, producing the transient negative or positive current signals due to the capacitance charging (see Figure 4.2B). By altering the applied potential from negative to positive, the potential of zero charge (PZC), at which no excess charge occurred when the electrode was in contact with an electrolyte, was determined by the intersection point from the interpolated reductive and oxidative fitting lines. However, there is no quantitative analysis of the size of the colliding GNPs.

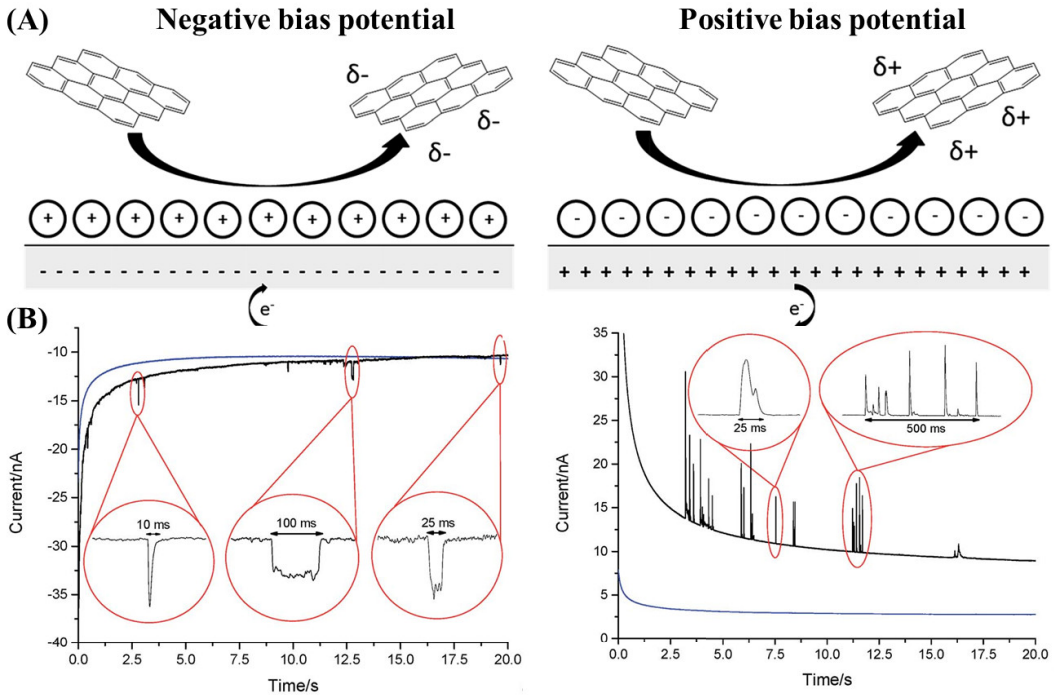

Figure 4.2. (A) Schematic illustration of GNP impacting with the electrode where the applied potential is negative (left) and positive (right) with respect to the potential of zero capacitance (PZC). (B) Chronoamperograms recorded at a 7.0 µm diameter carbon fiber UME at a potential of -1.20 V (left) and +1.20 V (right) in the absence (blue curve) and the presence of (black curve) of 0.59 pM GNP solution. The supporting electrolyte is 0.1 M KCl, 50 mM KH_2PO_4 and 50 mM K_2HPO_4 buffer solution. Reproduced, with modification, from Ref. [3]. Copyright 2015, Royal Society of Chemistry.

Here, we propose an alternative strategy, electro-catalytic depression (ECD), to detect carbonaceous particles. We choose to study GNPs, a material used for a wide range of applications: dye-sensitized solar cells,[5-6] conducting support for loading catalysts,[7-8] supercapacitors,[9] and sensors.[10] In this chapter, commercial GNPs with few microns in width and about 15 nm in thickness are used. We take advantage of the intrinsic difference in kinetics for an inner-sphere reaction, hydrazine oxidation, to drive a current through a microelectrode made of a good catalyst (Pt), while kinetically blocking the current at the surface of a GNP. The frequency of collision versus the concentration of GNP and the potential is investigated. Also, we investigate the distribution of the current step size and the kinetic difference between Pt and GNP as a function of potential

4.2 Principle of electro-catalytic depression

The principle of ECD takes advantage of the intrinsic difference between the kinetics in electron transfer of two different materials. An inner-sphere reaction must be chosen as the redox indicator. By applying a suitable potential, the inner-sphere reaction will occur solely on the Pt electrode while it will remain extremely slow on the particle under investigation. Figure 4.3 illustrates that conducting GNPs are detected by the methodology of ECD, where hydrazine oxidation reaction is chosen as the redox indicator. When conducting GNPs collide on the active electrode, the reaction of hydrazine oxidation is almost quasi-null on the surface of GNP. The collision of GNP is accompanied by an abrupt decrease of the current signal in the *i-t* trace, commonly seen in the type of staircase-shaped steps. The magnitude of current steps can be converted to obtain the size of the GNPs. When GNPs are suspended in solution collides on the Pt UME, the portion of the active surface area of the Pt UME will be blocked (the red cross in Figure 4.3), and a decrease of the current step is expected to be observed, as shown in the right *i-t* trace.

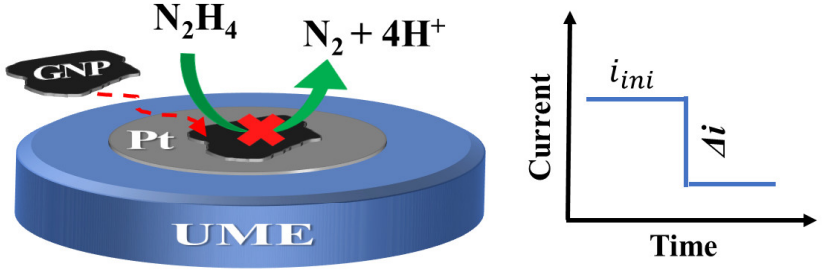

Figure 4.3. Principle of detection of conducting carbonaceous nanoparticles by electro-catalytic depression.

The prerequisite to perform collision studies using ECD is to find a suitable applied potential for an inner-sphere reaction to maximize the difference in kinetics between carbonaceous materials and the underlying electrode. The technique of cyclic voltammetry is a robust and simple way to compare the difference in kinetics of different materials finding the bias potential for further collision studies. Considering the difficulty of fabricating a GNP microelectrode, we use an isomer of GNP, C-fiber UME, to estimate the kinetics of hydrazine oxidation. In the next section, we will compare the kinetics of hydrazine oxidation on Pt UME vs. C-fiber UME.

4.2.1 Kinetics of hydrazine oxidation on Pt UME vs. C-fiber UME

Hydrazine oxidation is an irreversible four-electron reaction, as described in the following chemical equation:

$$N_2H_4 \rightarrow N_2 + 4\,H^+ + 4\,e^-$$

The pKa of hydrazine is 8.1 at 25 °C, and exits in the solution in either protonated (hydrazinium, $N_2H_5^+$) or unprotonated state.[11] In the presence of 10 µM of NaOH in solution, hydrazine is deprotonated and the concentration of $N_2H_5^+$ can be deduced by the base dissociation constant, being ~ 30 µM in aqueous solutions at 298 K. The protonated concentration $N_2H_5^+$ can be quasi-negligible compared to the bulk concentration of hydrazine (1 mM) when counting the steady-state current at a mass-transfer limit.

Figure 4.4 shows typical cyclic voltammograms of hydrazine oxidation on a 3.5 µm radius C-fiber UME (black traces) and a 5 µm radius Pt UME (red traces), along with the corresponding blanks (dashed lines) recorded in the absence of hydrazine. The blanks do not show any faradaic current except the beginning of water oxidation at ca. 1.5 V on the C-fiber UME. In the presence of hydrazine, the current starting at -0.6 V for the Pt UME and 0.1 V for the C-fiber UME is caused by hydrazine oxidation. The cyclic voltammogram recorded with the Pt UME displays two plateaus of current (i_{ss}^1 = 4.5 nA and i_{ss}^2

= 10.8 nA). The plateau of current corresponding to the theoretical diffusion-limited current on a disk UME is given by equation 1:[12]

$$i_{ss} = 4nFD_{\text{redox}}C_{\text{redox}}r_{\text{elec}} \quad (4.1)$$

where n is the number of electrons exchanged per molecule, F is the Faraday's constant, D_{redox} is the diffusion coefficient of the redox molecule, C_{redox} is the bulk concentration of the redox molecule, and r_{elec} is the radius of the electrode. Using our experimental parameters (r_{elec} = 5.0 µm, n = 4, C_{redox} = 1 mM and D_{redox} = 1.4 × 10^{-5} $cm^2 \cdot s^{-1}$) a theoretical limiting current of i_{ss} = 10.8 nA is calculated.[1, 13] Thus, the second plateau at c.a. 10.8 nA on the red cyclic voltammogram in Figure 4.4 is attributed to the diffusion-limited current for hydrazine oxidation. The inflection point of the first and second sigmoids are around -0.4 V and 0.2 V, respectively. These values are close to the apparent standard potential reported for hydrazine oxidation in basic (pH ≈ 8) and acidic (pH ≈ 1-2) conditions, respectively.[14-15]

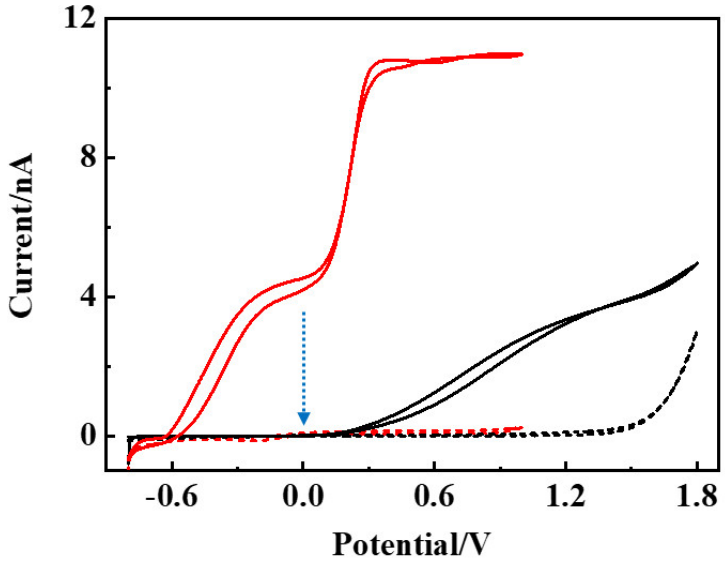

Figure 4.4. Cyclic voltammograms recorded on a 5 µm radius Pt UME (red traces) and a 3.5 µm radius C-fiber UME (black traces). The continuous and dashed lines correspond to cyclic voltammograms recorded in the absence and the presence of 1 mM hydrazine, respectively. [NaOH] = 10 µM, scan rate = 20 mV/s.

The first plateau (c.a. 4.5 nA) on the cyclic voltammogram of the Pt UME is attributed to a local change of pH at the surface of Pt when hydrazine is oxidized (four H^+ are released per molecule of hydrazine) and a subsequent shift of the apparent standard potential.[16] We verified this point by fixing the pH with increasing concentrations of NaOH and observing the complete disappearance of the intermediate plateau when the concentration of NaOH is about five times larger than the concentration of hydrazine, as shown in Figure 4.5. At a high concentration of alkaline electrolyte, the first plateau observed at low concentration (0.01 mM to 0.5 mM) disappeared, indicating the pH does not change significantly at high concentrations of the electrolyte. The limiting current at low concentration of the electrolyte is observed to be lower than that at a high concentration of electrolyte. The possible reason to explain this phenomenon is that the relatively low oxidation current at low concentration of alkaline electrolyte can be related to the ohmic drop and Coulomb repulsion between the positively charged electroactive species $N_2H_5^+$ and the positively charged electrode surface.[14, 17] However, the relative concentration of $N_2H_5^+$ is only ~30 µM, which is impossible to explain the ca. 40% increase in the limiting current. Thus, the mechanism behind the phenomenon remains unclear.

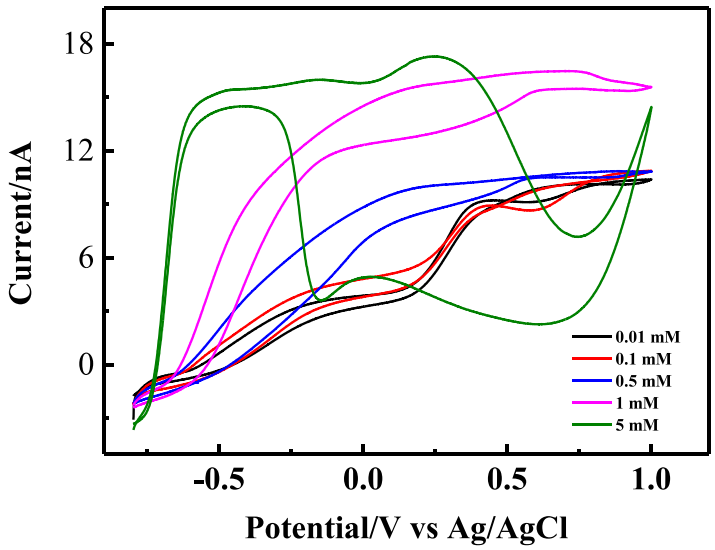

Figure 4.5. Cyclic voltammograms recorded at 20 mV/s on a 5 µm radius Pt ultra-microelectrode (UME) in a solution of 1 mM hydrazine and different concentrations of NaOH. When increasing the concentration of NaOH the intermediate plateau disappears because the pH of the solution does not vary during the potential sweep.

The cyclic voltammogram recorded with the C-fiber UME in Figure 4.4 displays one plateau ($i_{ss} \approx$ 3.8 nA) followed by an increase of the current above 1.5 V. The oxidation of water above 1.5 V masks the second plateau of hydrazine oxidation that should also be observed with the C-fiber UME. Importantly, the oxidation of hydrazine on a C-fiber UME is extremely sluggish, as shown by the width (ca. 1 V) of the sigmoid (black trace in Figure 4.4) and the onset potential of 700 mV more positive on Pt than C-fiber. It is thus possible to find a potential window where the kinetics of hydrazine oxidation is fast on Pt while it remains extremely slow on carbon. For example, at an applied potential of 0 V, the oxidation of hydrazine on Pt will lead to a large steady-state current while on the C-fiber, the current will be quasi-null.

In the following sections, we assume C-fiber and GNPs have similar catalytical properties for hydrazine oxidation. Before performing collision studies of GNP colliding on Pt UMEs, we will show the size distribution and morphology of GNP.

4.2.2 The size distribution of GNP and corresponding morphology

The size and morphology of the GNPs were characterized by scanning electron microscopy (SEM, Hitachi S-4800). The sample is prepared as follows. GNPs are dispersed in a 10 µM NaOH aqueous solution by sonication (10 min, 130-Watt ultrasonic processor bath, Cole-Parmer). Then, a drop of GNP dispersion is deposited onto a glassy carbon substrate and dried in an oven. Multiple SEM images were acquired at different locations on the substrate, and then, the dimension of isolated GNPs was manually measured. Figure 4.6A shows a representative SEM image of GNPs on a glassy carbon substrate. The morphology of the GNP is relatively ill-defined, and thus we quantified their size by averaging the longest and shortest axis of the platelets. Their size distribution is plotted in the histogram Figure 4.6B. The average length is about 4.2 ± 2.5 µm.

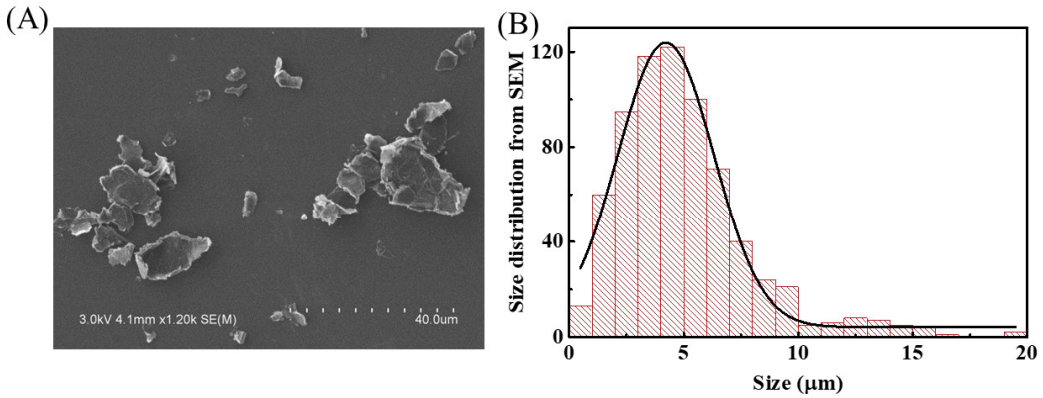

Figure 4.6. (A) Representative SEM image of GNPs on a glassy carbon substrate. (B) The size distribution of GNPs is obtained by SEM. Because GNPs do not have a well-defined geometry, the "size" of each GNP is estimated by averaging the longest and shortest axes. Total number of GNP = 702, bin size = 1 μm. The black line is the best fit of a Gaussian function. The center, standard deviation, and R^2 are 4.2 μm, 2.5 μm, and 0.98, respectively.

4.3 Detection of conducting GNPs by ECD

The concentration of GNP in mg/mL during the preparation process can be converted into molar concentration (C) as follows. We make the approximation that GNPs are disks of 4.2 μm diameter and 15 nm thickness.

$$C = \frac{m}{N_a \rho V_{GNP}} \tag{4.2}$$

where m, ρ, V_{GNP} and N_a are the mass of GNP powder dispersed in 1 L of solution, the true density of GNP (2.3 g·cm^{-3}) and the average volume of one GNP ($V_{GNP} = \pi \times (2.1 \times 10^{-4})^2 \times 15 \times 10^{-7} = 2.08 \times 10^{-13}$ cm^3) and the Avogadro constant. A mass concentration of 10 μg/mL corresponds to a molar concentration of approximately 35 fM. The supporting electrolyte of 10 μM NaOH helps to stabilize carbonaceous particles in water.[18] Concentrations of NaOH larger than 10 μM or GNP concentrations larger than 140 fM induce sedimentation within a few minutes. Although this issue could be addressed by adding surfactants in solution, these latter were not used because of their adverse effect on the oxidation of hydrazine at the Pt surface.

Figure 4.7A shows two typical chronoamperograms obtained with a 5 μm radius Pt UME biased at 0 V in a 1 mM hydrazine and 10 μM NaOH solution in the presence (red trace) and the absence (black trace) of 35 fM GNPs. In the absence of GNP, the oxidation of hydrazine on the Pt UME leads to a quasi-steady-state current (the black trace in Figure 4.7A) of a few nA. Importantly no abrupt change of current is observed. However, in the presence of GNPs, discrete stair-shaped current decays are clearly observed on the red trace in Figure 4.7A. A zoom on typical current steps is shown in Figure 4.7B. Current steps were consistently observed in 19 individual experiments in the presence of GNPs but never in the blanks (i.e., in the absence of GNP). The observation of discrete decreases of current indicates that GNPs are kinetically blocking hydrazine oxidation on the Pt UME at a potential of 0 V.

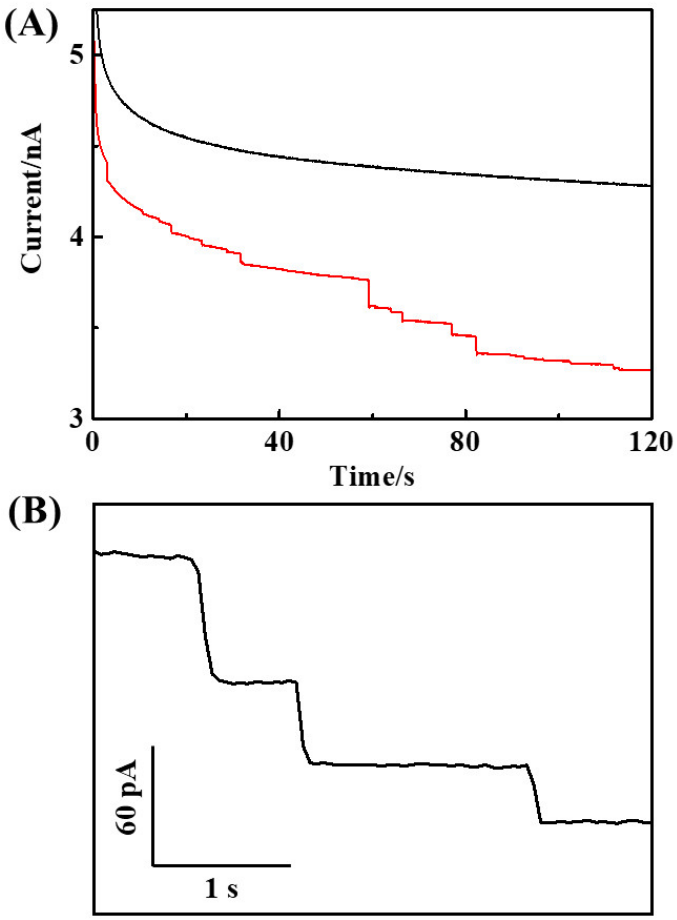

Figure 4.7. (A) Chronoamperograms recorded in the absence (black trace) and the presence (red trace) of 35 fM GNPs on a 5 μm radius Pt UME. The UME is biased at 0 V and the solution contains 1 mM hydrazine and 10 μM NaOH. (B) Zoom on typical current events recorded in the same condition as (A).

Apart from typical stair-shaped events (91% of all events), we also observe in rare occasions square-shaped events (5% of all events) as well as spike-shaped events (4% of all events). Figure 4.8 A, B and C show examples of three types of collision events, staircase-shaped events, square-shaped events, and spike-shaped events, respectively. The staircase-shaped events are attributed to GNPs irreversibly adsorbing on the Pt surface. The square-shaped events are attributed to GNPs that are first adsorbing on the Pt surface and then leaving in solution. These two kinds of events are also observed with polystyrene bead blocking experiments.[19] The spike-shaped events are possibly caused by GNPs bouncing on the UME surface and thus displaying a short residence time (0.13 ± 0.04 s on average). Spike-shaped current events are also reported for gold nanoparticles bouncing at the surface of gold electrodes modified with self-assembled monolayers of alkanethiols.[20]

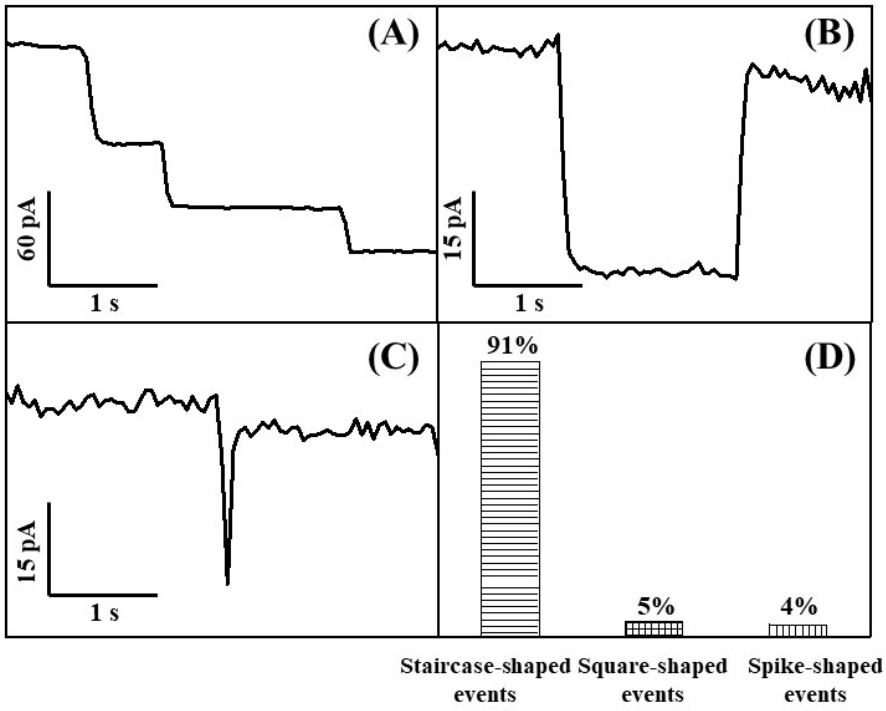

Figure 4.8. Examples of current transients observed during electro-catalytic depression experiments. The shape of these events is attributed to GNPs irreversibly adsorbing (A), absorbing and then desorbing (B), and bouncing (C) on the Pt UME. (D) The proportion of staircase-shaped, square-shaped, and spike-shaped events observed over 363 events (measured over twenty individual experiments).

In order to prove that the blocking does not originate from the poor electrical conductivity of GNP (or contact between the GNP and the Pt surface), we performed a control experiment using an outer-sphere redox molecule, ferroceniummethanol/ferrocenemethanol. Figure 4.9 shows *i-t* trace recorded with a 5 µm diameter Pt UME biased at 0.4 V in a solution of 1 mM FcMeOH in the absence (black trace) and presence of 35 fM of GNP (red trace). No negative current steps are observed. Instead, discrete positive current spikes are observed in the presence of GNP. FcMeOH is oxidized at the GNP surface as it would on the Pt surface. The origin of these spikes will be discussed in detail in Chapter 5.

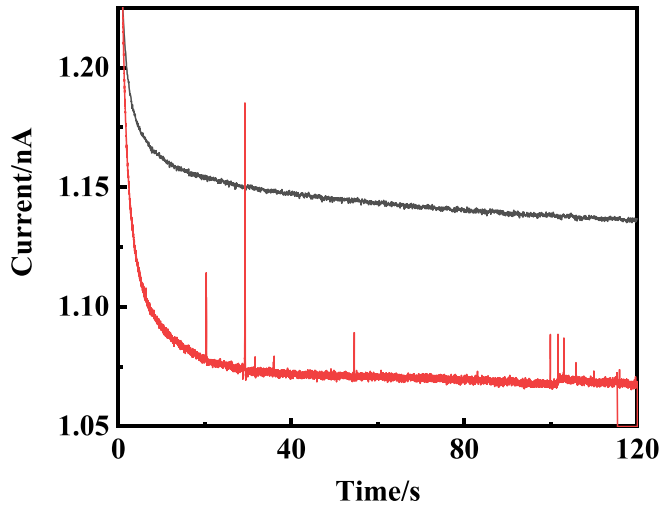

Figure 4.9. A control experiment of the kinetics of ferrocene methanol oxidation on GNP versus Pt UME. Chronoamperograms recorded in the absence (black trace) and presence (red trace) of 35 fM GNPs on a 5 µm radius Pt. The UME is biased at 0.4 V, and the solution contains 1 mM ferrocene methanol and 10 µM NaOH.

In the following sections, we are focusing on the "sticking" GNPs (the majority of the events) that produce negative step-like current transients.

4.3.1 Histogram of current steps

Figure 4.10 presents the histogram of the normalized size distribution of the relative current step, i.e., the current step, Δi, divided by the current right before the step, i_{ini}. Current steps are small variations over a large background, and thus the relative current step size is plotted in ‰. The distribution spans from 1‰ to 55‰, with an average of 8.0‰. Here, the ideal shape of the current events allows a precise measurement of $\Delta i/i_{ini}$. However, the quantitative analysis of the step-size is rendered difficult by the inhomogeneity of the shape and size of the GNPs, as well as the edge effect always present on disk-shaped electrodes (see discussions in Figure 3.3).[21]

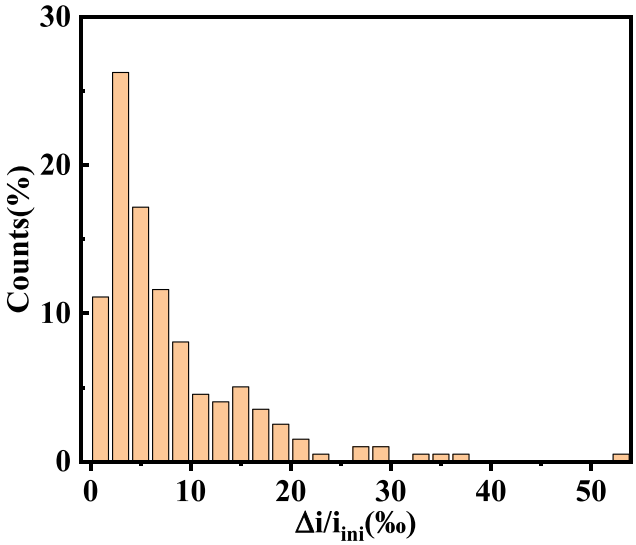

Figure 4.10. Histogram showing the normalized size distribution of the relative current steps caused by GNPs colliding on a 5 µm radius Pt UME. Only the first 6 GNPs colliding on a bare UME are counted to avoid the effect of stacking (vide infra). The UME is cleaned between each run and 198 collisions are counted in total. The concentration of GNP is 35 fM. The UME is biased at 0 V and the electrolyte contains 1 mM hydrazine and 10 µM NaOH.

Taking these considerations into account, we tried to make use of the average distribution to estimate the size of GNPs that cause the steps observed in the histogram. We assume the shape of GNPs is perfect disks infinitely thin. Numerical simulations of these "ideal" GNPs blocking the center and the edge of the UME were carried out. Details about the simulation can be found in Appendix 4. Four simulations (black points) were performed with GNPs of various radii placing in order to generate the calibration curve shown in Figure 4.11. The simulated radii of GNPs were obtained by averaging the simulated radii of GNPs at the center and the edge of the UME in order to suppress the "edge effect" on disk-shaped UMEs. From the calibration curve, we can see that the current step size is not a linear function of GNP size but second-order polynomial relation: Ax^2+Bx. The coefficients A and B equal to 0.022 and 0.1265, respectively ($R^2 = 0.998$). The polystyrene spheres described in Chapter 3 and the flat graphene sheet produces similar non-linear blocking current signals. Indeed, the polystyrene sphere hinders mass transport by rendering the volume above the electrode surface inaccessible, but the flat sheet diminishes current by blocking electron transfer locally at the electrode surface.[22]

Using the relation in the calibration curve, we found that GNPs between 0.5 µm and 3.5 µm in diameter produce the minimum and maximum relative current steps observed in Figure 4.10. This range of size is lower than the size distribution obtained by SEM (c.a. 0.6 – 20 µm) in Figure 4.6. Besides, according to this relation, one can determine that the average relative current step observed in our measurements corresponds to the average diameter of 1.64 µm while the average length found by SEM is 4.2 ± 2.5 µm. Although the assumption of ideal disk-shaped GNPs will introduce errors in the size

determined by electrochemistry, it cannot explain a difference by a factor of more than two. We thus seek for a different explanation.

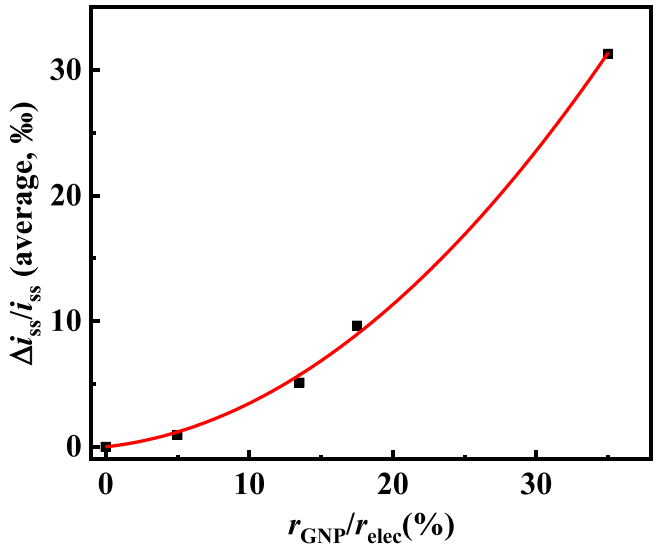

Figure 4.11. Simulated calibration curve of average relative step size vs. GNP radius normalized by the electrode radius. Black points correspond to the simulation result in Table S1.4. The red line corresponds to a least-squares fitting of a second-order polynomial: $Ax^2 + Bx$. The coefficients A and B equal to 0.022 and 0.1265, respectively ($R^2 = 0.998$).

We monitored optically (using bright field microscopy) the solution containing the GNPs directly after dispersion. A droplet of 35 fM GNP (suspended in 10 µM NaOH) was incubated on a glass slide and kept in the oven for 30 minutes. A typical bright field micrograph of the surface of the glass slide is shown in the inset in Figure 4.12. We found that GNPs between 4 and 21 µm sediment within two minutes (time scale of our experiments) on the bottom of the cell, indicating that large sizes of GNPs cannot be detected during the collision experiments. One possible way that can be used to address the sedimentation is to place the electrode surface facing upward.

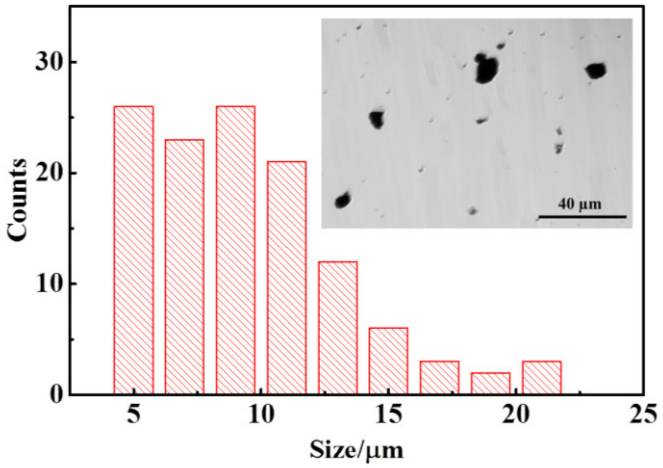

Figure 4.12. The size distribution of GNPs sedimented within two minutes after their dispersion in solution. The inset is a typical optical micrograph of GNPs sedimenting onto the glass substrate within two minutes after sonication. The small blurry black dots on the micrograph are caused by GNPs floating in solution within the field of view of the objective. The total number of GNPs analyzed is 122, and the bin size is set at 2 µm.

4.3.2 Collision frequency vs. concentration of GNPs

Figure 4.13A shows representative chronoamperograms in the presence of various concentrations of GNP from 35 to 280 fM, under the bias potential of 0 V. From Figure 4.13A we can see that the frequency of collision increases with the increase of GNP concentrations. Eleven individual *i-t*

measurements were performed to obtain the average collision frequency. In order to minimize the possible effect of GNP stacking (vide infra) on the electrode, we only counted the first six collisions for each chronoamperogram. The average frequency of collision at 0 V is plotted as a function of the concentration of GNP, as shown in Figure 4.13B. The collision frequency is in the range of 0.2 Hz to 0.8 Hz for concentrations of 35 fM to 280 fM. It increases quasi-linearly with the concentration of GNP and then seems to saturate at a concentration above 140 fM. This saturation can be explained by the precipitation of GNPs in aqueous solution, especially at large GNP concentrations. Because of the existence of both sedimentation and precipitation, the concentration of GNP in suspension is lower than the nominal concentration. Even at a lower concentration (35 fM) we also observed sedimentation of the large GNPs (see Figure 4.12). Such deviation from linearity is also reported for the collision frequency of Pt nanoparticles on Hg UMEs.[23-24] In that case, collision frequencies lower than expected were also explained by the poor stability of the particles.[24] In a nutshell, the stability of the colloidal suspension is of crucial importance to accurately determine the concentration.

The collision frequency is related to the origin of the GNP transport in the electrolyte. In the absence of convection in our system, both migration and diffusion can contribute to the collision frequencies of the GNP transport. The contribution of diffusion to the frequency of collision is given by:[19, 25]

$$f_{diff} = 4N_A D_{GNP} C_{GNP} r_{elec} \tag{4.3}$$

where N_A, D_{GNP}, C_{GNP}, and r_{elec} are Avogadro's constant, the diffusion coefficient of GNP in the solution, the concentration of GNP and the radius of the electrode. If we consider that GNPs are spheres of 2.1 μm radius, their diffusion coefficient can be calculated to be 1.2 x 10^{-9} $cm^2 \cdot s^{-1}$ based on the Stokes-Einstein relation:

$$D = \frac{kT}{6\pi\eta r} \tag{4.4}$$

where k, T and η are the Boltzman constant, the temperature and the dynamic viscosity of the solvent (8.8×10^{-4} Pa·s), respectively. Then, a value of 0.05 mHz is calculated for spherical 4.2 μm diameter GNPs. The arrival of the GNPs to the Pt surface cannot be ensured by diffusion because the estimated value of the collision frequency at 35 fM (0.2 Hz) is of the order of 0.05 mHz at 0 V, which is higher by more than 3 orders of magnitude than the measured value.

On the other hand, GNP migration should then play a major role. Indeed, GNPs are charged and the ionic strength is kept extremely low (40 μM). The frequency of collision caused by the migration of the GNP is estimated as follows. First, we determine the amount of charge per GNP. The charge at the surface of the GNP (σ_{GNP}) can be related to the potential at the outer Helmholtz plane (the slipping plane) can be obtained using the Grahame equation:[26]

$$\sigma_{GNP} = \sqrt{8\varepsilon_r \varepsilon_0 kTN_a C}\sinh\left(\frac{ze\xi}{2kT}\right) \tag{4.5}$$

where ε_r, ε_0, N_a, C^*, z, e and ξ are the relative permittivity, the vacuum permittivity, the Avogadro's constant, the total bulk electrolyte concentration in mol/L (here $C_{NaOH} + C_{N_2H_5 \cdot OH}$ = 40 μM), the charge of the electrolyte, the elementary charge and the zeta potential (-32.5 ± 0.3 mV), respectively. Using the simulated calibration curve between average step size and GNP radius given in Figure 4.11, one can determine that the average radius of GNP detected in our measurements is 0.82 μm. Next, by multiplying the surface charge density by the surface area of a GNP disk, we obtain the amount of charge per GNP (z_{GNP}).

$$z_{GNP} = \sigma_{GNP}\pi r_{GNP}^2 \tag{4.6}$$

Then we can use the Einstein-Smoluchowski equation to calculate the mobility of the GNP:

$$\mu_{GNP} = \frac{z_{GNP} D_{GNP}}{kT} \tag{4.7}$$

Finally, we use the relation to estimate the contribution of migration to the frequency of collision of GNP:[27]

$$f_{mig} = \frac{i_{ss} C_{GNP} \mu_{GNP}}{e} \sum \frac{1}{C_i \mu_i} \tag{4.8}$$

where i_{ss} is the steady-state current and i refers to all the charged species in solution (Na^+, OH^-, $N_2H_5^+$ and GNP).

The expected value of the collision frequency induced by migration at 35 fM is 1.8 Hz estimated by the Eq. (4.8). The theoretical frequency of collision is nine times higher than the experimental frequency of collision (0.2 Hz). This may be due to the sedimentation of GNP decreasing their concentration. Another reason may be a local increase in the ionic strength close to the electrode. Indeed, hydrazine oxidation produces protons that will increase the ionic strength in the diffusion layer around the Pt UME (this increase of proton concentration is observed with the plateau on the cyclic voltammogram in Figure 4.4).

We also measured the average collision frequency (more than twenty individual measurements) at potentials of -0.3 V, 0 V, 0.7 V and 1.0 V, and obtained 0.10 Hz, 0.20 Hz, 0.24 Hz and 0.24 Hz, respectively. We observe a clear increase of the collision frequency with potential, which seems to saturate at 0.7 V. In a migration dominated mass transport, the collision frequency is expected to increase proportionally with the current, from 3.5 nA at -0.3 V, 4.5 nA at 0 V and to 10.8 nA at 0.7 V and 1.0 V. The experimental trend significantly deviates from this linear dependence. In a similar way to what has been shown above, the saturation of the collision frequency may be ascribed to the local increase of the ionic strength due to the proton formation during hydrazine oxidation. The origin of the non-proportionality with the current at the most negative potentials is unclear.

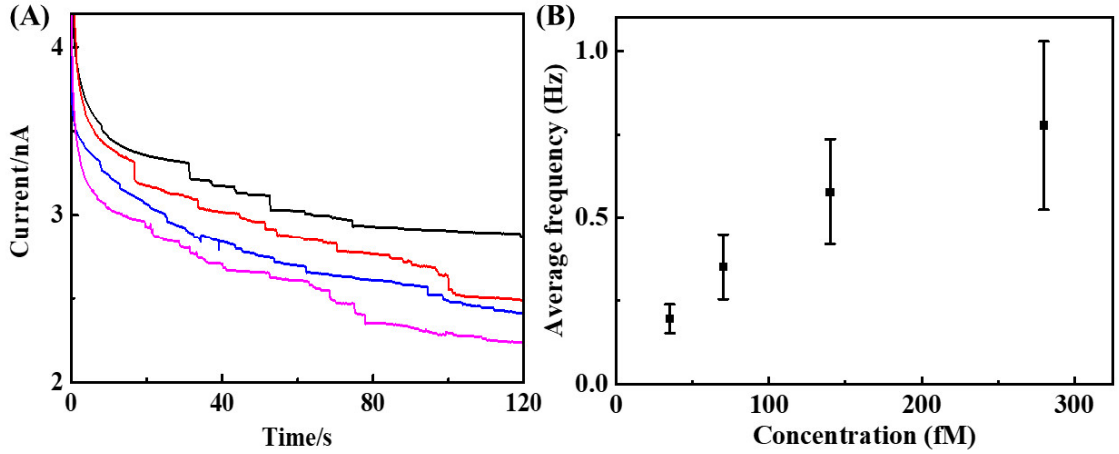

Figure 4.13. (A)Chronoamperograms recorded at different concentrations of GNP. The black, red, blue, and pink traces correspond to concentrations of 35 fM, 70 fM, 140 fM, 280 fM, respectively. (B) The average frequency of collision (the error bars represent the standard deviation of eleven individual experiments) as a function of the concentration of GNP. Only the first six collisions are counted on each chronoamperogram. The 5 µm radius Pt UME was biased at 0 V for all experiments and the solution contains 1 mM hydrazine and 10 µM NaOH.

4.3.3 Stacking of GNPs

In the previous sections, we mentioned that only the first six collisions are counted in order to avoid considering stacking/overlapping GNPs. In this section, we will discuss the effect of stacking GNPs on the relative current step size. When multiple collisions of GNPs are recorded, the stacking of GNPs on top of each other should be considered. Indeed, if we consider an average GNP surface of 13.8 μm^2 (considering an "ideal" GNP as a disk with a diameter of 4.2 µm) and the Pt surface (78.5 μm^2) then, the minimum number of GNPs necessary to pave the Pt surface is about six. In other words, after only six evenly distributed collisions, one should consider overlapping GNPs. We studied how stacking multiple GNPs on the electrode affects the current steps by recording multiple 900 s long collision

experiments. Figure 4.14A shows a representative 900s chronoamperogram with two figures (right) showing the current decay at the beginning of 50 s and the end of the chronoamperogram. The scale of the current step magnitudes at the beginning is more than ten times larger than that at the end of the experiment. In order to make better statistics, we recorded nine individual 900s long chronoamperograms with, on average, 65 ± 12 collision steps per chronoamperogram (see Figure 4.14B). The right histograms show the relative size distribution of the first 15 collisions (light orange) and the last 15 collisions (light green), with the distribution ranges of 4.3‰ to 28‰, and 2.1‰ to 12‰, respectively. The normalized current step size ($\Delta i/i$) of the N^{th} collision was also averaged over the nine chronoamperograms and plotted in Figure 4.14C, during which an adjacent-averaging smoothing (39 points of the window and 'repeat' boundary condition) was applied to emphasize the decreasing trend. Because of the large asymmetry of the two distributions, we characterized the center of the distribution with the average. The average and maximum step size of the black and red distributions are 6.5‰ and 2.7‰ as well as 28‰ and 12‰, respectively. In the presence of GNPs on the electrode surface, the average relative step size is about 2.4 times smaller than for a bare Pt UME and large events (> 12 ‰) completely disappear. The collision of a GNP on a bare Pt UME and an electrode covered with GNPs leads in both cases to a stair-shaped decrease of current. The large scattering of the step size is caused by the size distribution of GNP as well as the edge effect.

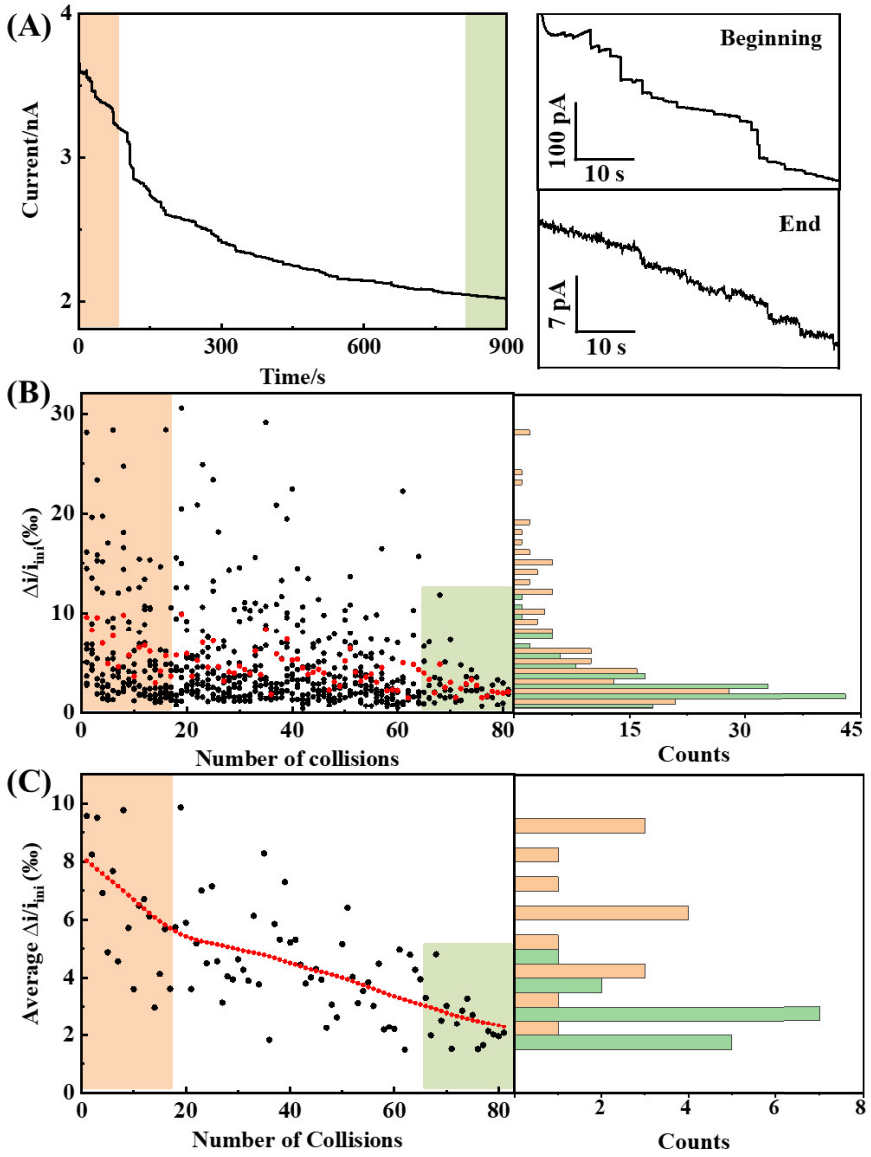

Figure 4.14. (A) Left: Chronoamperogram showing the evolution of the step size as more and more GNPs are stacking on the Pt UME. Right: The right figures correspond to the enlarged curves at the beginning (light orange) and the ending (light green).

[GNP] = 35 fM, [N_2H_4] = 1 mM, [NaOH] = 10 µM; the 5 µm radius Pt UME is biased at 0 V. (B) Left: Relative current step size as a function of the number of GNP present on the UME. These steps from nine independent experiments are plotted in black. The red dots show the average of the nine experiments. Right: Corresponding histograms showing the size distributions of the first (light orange) and last (light green) 15 current steps of long experiments. (C) Left: Average relative current steps recorded by collision sequence in 35 fM GNPs. Black dots represent the average relative current step size and the red discrete trace shows the decreasing trend after a long test. Right: Corresponding histograms showing the average relative size of the first (light orange) and last (light green) 15 current steps of long experiments.

After tens of collisions at the electrode surface, negative current steps are still observed (see the enlarged ending figure in Figure 4.14A) and the current almost levels off at around 2 nA. Among a few cases, we could observe up to 81 successive collisions, a value corresponding to about 13 layers of GNPs evenly distributed on the surface of the electrode. Despite those many layers, the stack of GNP blocks only 40 % of the current. Since hydrazine cannot be oxidized on a GNP at 0 V, the remaining anodic current indicates that some part of the Pt remains in contact with the solution. One possible explanation might be that as GNPs consecutively stacks on the Pt surface, the "effective area" of the colliding particles decreases due to the particle overlapping (see Figure 4.15A). The "effective area" described here is not only the actual surface area of the surface of Pt, but also includes the volume space capable of allowing hydrazine molecules to diffuse or migrate to the Pt surface. Another possibility is that when GNPs are randomly stacking on each other, a tortuous porous network is left between the GNPs and the hydrazine (see Figure 4.15B). In both ways of colliding on the Pt surface, the flux of hydrazine toward the electrode is progressively hindered by the addition of more and more GNPs, and thus the current step size becomes smaller and smaller with the number of GNP present on the surface. Thus, the current step size decreases with the stacking of GNPs on the Pt surface. This kind of behavior was also observed with blocking collisions of polystyrene beads.[19] The key point is that neither the partial overlap or the porous network would block completely the electrode allowing the observation of more collisions than one would expect for a full monolayer of GNPs.

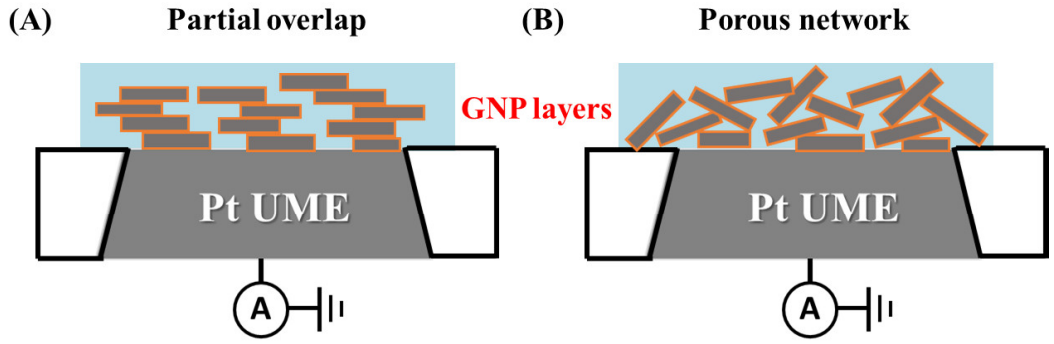

Figure 4.15. Possible ways of GNP stacking, including (A) partial overlap of GNPs and (B) the formation of the porous network on the electrode surface.

4.4 Effects of the potential on the observed current response for individual GNP detection

Figure 4.16 A, B, C and D show representative negative current-time trace recorded in the presence of 35 fM GNPs at potentials of -0.3 V, 0.0 V, 0.7 V, and 1.0 V, respectively. These potentials extend from the first plateau of hydrazine oxidation up to the second plateau at the onset of water oxidation (the black trace in Figure 4.4). This is the reason why the background current (hydrazine oxidation) is increasing from 2 nA (Figure 4.15A) up to 11 nA (Figure 4.16D). All the chronoamperograms display negative current steps over the wide potential window explored here. Such steps are absent in the absence of GNPs in solution (See Figure 4.17).

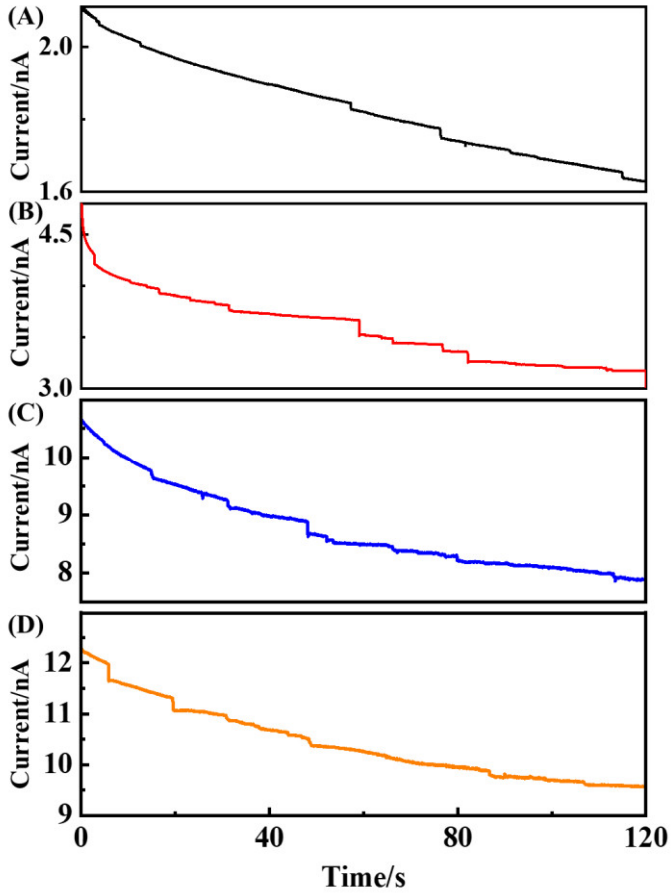

Figure 4.16. Typical chronoamperograms recorded on a 5 μm radius Pt UME at different potentials in the presence of 35 fM GNPs: (A) black trace, -0.3 V; (B) red curve, 0 V; (C) blue curve: 0.7 V; (D) orange curve, 1.0 V. The solution contains 1 mM hydrazine and 10 μM NaOH.

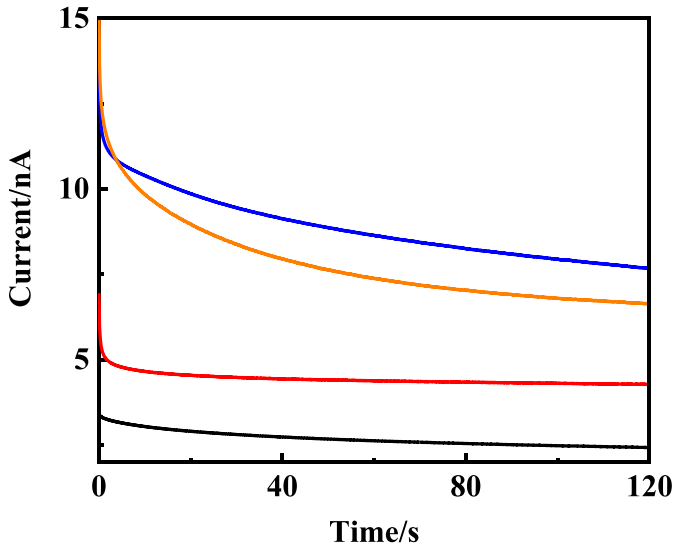

Figure 4.17. Chronoamperograms recorded in the absence of 35 fM GNPs on a 5 μm radius Pt UME at different bias potentials: black trace, -0.3 V; red trace, 0 V; blue trace, 0.7 V; orange trace, 1.0 V. The solution contains 1 mM of hydrazine and 10 μM of NaOH.

About 200 negative steps (for each potential) were recorded to make a statistical description of the effects of the potential on the current step height. Each experiment corresponds to a freshly polished Pt UME. In order to avoid the formation of multilayers, only the first six collisions are counted. The

histograms of the normalized size distribution of the relative current step (i.e., the current step, Δi, divided by the current right before the step, i_{ini}) are plotted in Figure 4.18 for four different potentials.

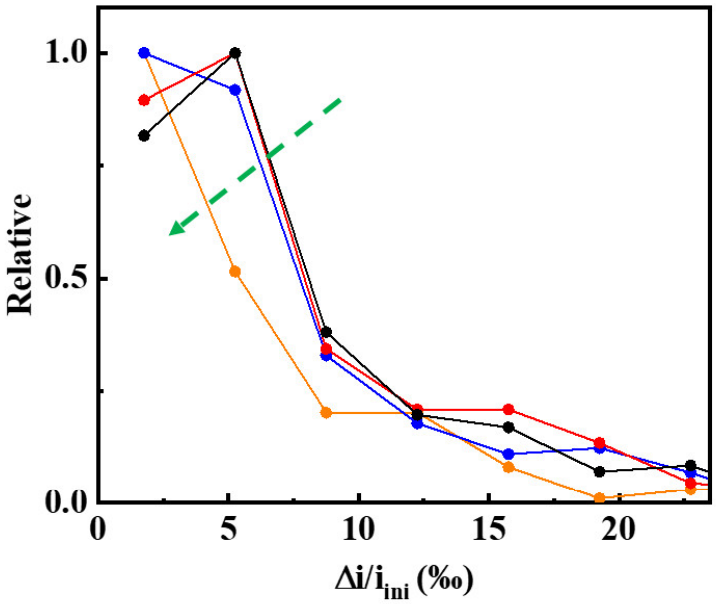

Figure 4.18. Plots showing the normalized size distribution of the relative current steps caused by GNPs colliding on a 5 µm radius Pt UME under different potentials at an orange curve: 1.0 V, 210 counts, blue curve: 0.7 V, 202 counts, red curve: 0 V, 198 counts, black curve: -0.3 V, 201 counts, respectively. Bin size = 3.5, the points show the center of each bin and the maximum range is limited to 24.5‰ in order to better compare the data, accounting for the majority of the data (over 96% of total counts). In each chronoamperogram, only the first 6 GNPs colliding on a bare UME are counted to avoid the effect of GNP stacking. [GNP] = 35 fM in 1 mM hydrazine and 10 µM NaOH.

The trend observed in Figure 4.18 is the shift of the current distribution to lower values with increasing potentials, as indicated by the green dash arrow. This shift is small at 0.7 V (blue symbols) but significant at 1 V (orange symbols). We calculated the average, median, and distribution range obtained for each histogram (Table 1). The average (and median) step size is constant over -0.3 V to 0 V and then decreases by 15% (respectively 24%) as the potential increases from 0 V to 0.7 V (respectively 1 V).

Table 4.1. The statistical description of the magnitude of the negative steps at different bias potentials.

Potentials (V)	Counts	Average (‰)	Median (‰)	*Range (‰)
-0.3	201	8.0	5.3	1 to 55
0	198	8.0	5.4	1.1 to 54
0.7	202	6.8	4.5	0.7 to 42
1.0	210	6.1	3.7	0.6 to 39

* For 95% of the range (for all the potentials) the maximum step is about 21‰.

In order to understand the variation of the average step size, as a function of the potential we will examine the kinetics of hydrazine oxidation on Pt and carbon. As mentioned early, we consider C-fiber a proxy for the surface of the GNPs. This proxy comes from the comparison of the kinetics of hydrazine oxidation on a GNP and C-fiber. Figure 4.19 shows the chronoamperograms in the absence (black) and presence (red) of 35 fM GNPs recorded in the C-fiber UME. The C-fiber UME is biased at 1.2 V in a solution of 1 mM hydrazine and 10 µM NaOH. Without the addition of GNP, a smooth steady-state current is obtained (black trace), while discrete stair-shaped decreases of current are observed after the addition of 35 fM GNPs. Based on this observation, we conclude that (i) GNPs are adsorbing irreversibly on the C-fiber and (ii) the oxidation of hydrazine on the GNPs is much slower than on the C-fiber. This means that the oxidation of hydrazine on a GNP at 0 V is even slower than on a C-fiber, and thus, the current is negligible. Thus, we consider the voltammograms of hydrazine oxidation on C-fiber as a proxy for the surface of GNPs.

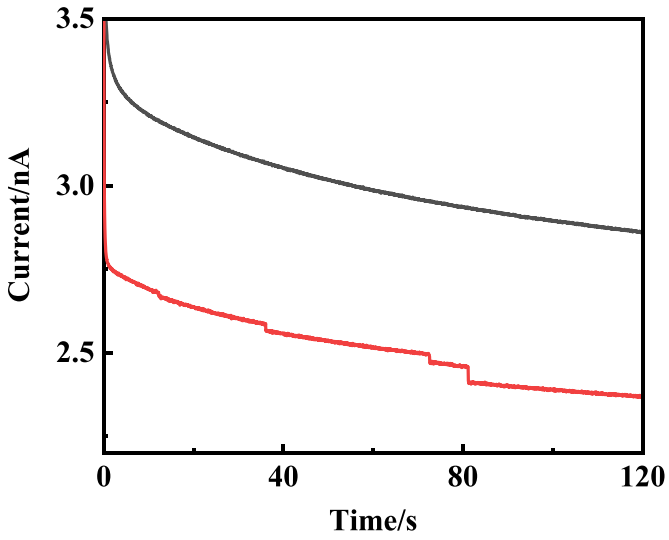

Figure 4.19. Chronoamperogram recorded with a 3.5 µm radius C-fiber UME biased at 1.2 V vs Ag/AgCl 3.4 M KCl in the absence and presence of presence 35 fM GNP. The solution contains 1 mM hydrazine and 10 µM NaOH.

Figure 4.20A shows the adimensional voltammograms (forward scan only) corresponding to hydrazine oxidation on Pt (black curve) and C-fiber (red curve). The adimensional current was obtained by each current divided by the the current measured on Pt, i_{Pt}. The blue curve, Δi, represents the current difference between hydrazine oxidation on Pt and C-fiber. Δi overlaps with the Pt curve from the onset potential of hydrazine oxidation (-0.65 V) to the inflection point (0.25 V). As the potential rises above 0.25 V, this current difference decreases with increasing potentials. In principle, this difference should fall down to zero for sufficiently large potentials where the hydrazine oxidation current becomes limited by diffusion instead of electron transfer.

To correlate the kinetic difference between Pt and GNP (less active than C-fiber) with the change of the current step size as a function of potential, we plot in black in Figure 4.20B the ratio of Δi and the current on Pt (i_{Pt}). The quantity $\Delta i/i_{Pt}$ would correspond to a situation where a 5 µm radius carbon disk completely covers our 5 µm radius Pt UME. The potential range from -0.8 V to -0.65 V is caused by the hydrogen evolution on Pt and the ratio equals to 1 up to 0 V since at low potentials (-0.6 V to 0.1 V), no hydrazine oxidation occurs on C fiber. Thus, the ratio levels off at unity. However, at high potentials (> 0.1 V), hydrazine oxidation occurs on C fiber, and C fiber acts as a partial electron blocker and the kinetic of C fiber increases with increasing potentials. Thus, the ratio decreases with increasing potentials.

The red points in Figure 4.20B represent the average relative step size corresponding to GNPs colliding on the Pt UME. They are associated with the right red scale which was chosen in a way that the average step size at 0 V and -0.3 V coincides with the value of 1 in the black curve and that the relative range is identical to that of the left black scale. This choice of scale allows a comparison of the differences in kinetics independently of the difference in size between the UME and the GNPs. The red line is a logistic function adjusted on our experimental point in order to guide the eyes. The shift between the red points ($\Delta i/i_{ini}$ for GNP collision) and the black curve indicates slower kinetics of hydrazine oxidation on GNP than on C fiber. This observation is in agreement with a separate set of collision experiments of GNPs on C fiber evidencing kinetic blocking of hydrazine oxidation of GNP (see Figure 4.19). Measuring the variation of the amplitude of the negative steps as a function of the potential is a direct means to access the difference in kinetics between a known material (the UME) and the entities under investigation (here the GNPs). Such information is especially difficult to measure on particles.[28-29]

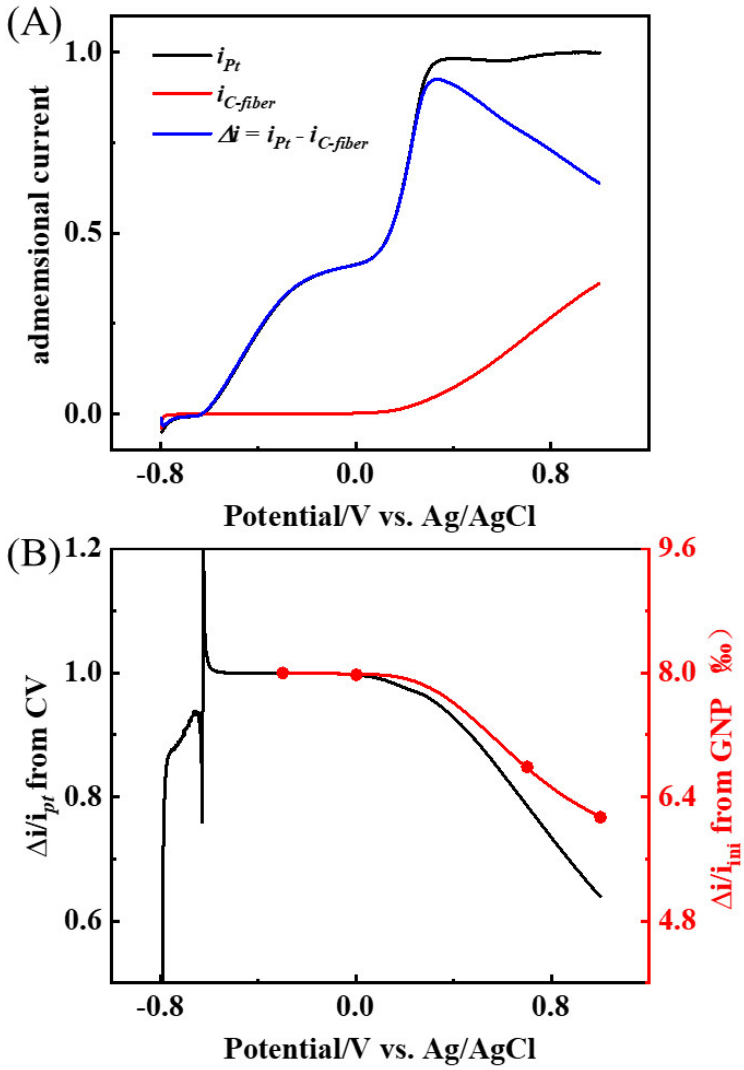

Figure 4.20. (A) Difference between the adimensional linear voltammograms of Pt and C-fiber. Data is taken from Figure 4.4, and normalized by the diffusion-limited steady-state current from Eq. 1. The black curve and the red curve correspond to the hydrazine oxidation occurring on a Pt UME and a C-fiber UME with the same radius as Pt. The Blue curve is the kinetic difference between the adimensional currents measured on Pt (i_{Pt}) and on C-fiber ($i_{C\text{-}fiber}$). (B) Left *y*-axis: The kinetic difference of hydrazine oxidation (Δi) on Pt versus C-fiber is divided by the current on Pt (i_{Pt}). The $\Delta i/i_{Pt}$ varies with the potential. The cross line close to -0.6 V is due to the intersection of non-faradaic currents on Pt and C-fiber. Right *y*-axis: the red points correspond to the relative current step size at different potentials given in Table 1, and the red curve is a fit of a logistic function performed only to guide the eyes.

4.5 Positive current responses at high potentials

When the potential is larger than 0.1 V vs. Ag/AgCl, hydrazine oxidation starts occurring on the surface of GNP and the reaction rate increases with the rise of the potential (see the red trace in Figure 4.20A). Although the kinetics of GNP is still less kinetically active than Pt toward hydrazine oxidation, the difference in kinetics between GNP and Pt decreases with increasing potentials (blue trace in Figure 4.20A). When the potential shifts to a sufficiently positive potential in which noticeable oxidation current occurs on the surface of GNP, two scenarios need to be considered: (i) if a GNP is confined in the surface of Pt, a GNP is partially blocked due to the slow kinetics compared to Pt, as described in the previous sections; (ii) If a GNP hits the perimeter of Pt, the area outside the surface of Pt (area 2# in Figure 4.21) is expected to yield positive current response while the inner area leads to a current decrease (area 1# in Figure 4.21). The sign of current responses (positive or negative) depends on the balance

between the amplification part (signal amplification) and the depression part (partial blocking), as shown in the right bar chart in Figure 4.21.

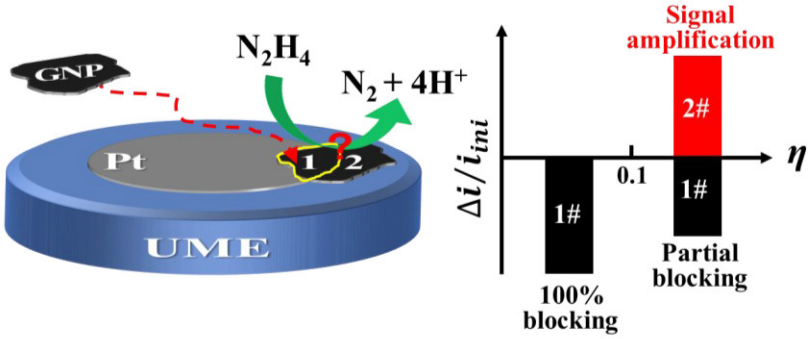

Figure 4.21. Schematic illustration of the proposed principle to explain positive steps at high potentials. At high overpotentials, hydrazine oxidation occurs on GNP, but GNP is still less active than Pt. If a GNP lands on the perimeter of Pt, hydrazine oxidation is partially blocked on the overlapping part (area 1#) while the remaining part (area 2#) will yield a current increase. Thus, the final current sign depends on the balance between the depression area and the area amplification. Areas 1 and 2 represent the overlapping area of GNP/Pt and the remaining part on the glass sheath, respectively.

Figure 4.22 A and B show typical *i-t* trace measured at a 10 μm diameter Pt UME in the presence of 35 fM GNPs at high potentials of 0.7 V and 1.0 V, respectively. Apart from negative current steps, we also observe positive current responses like increasing current steps and spikes. The positive current spikes observed at high potentials are attributed to those GNPs bouncing on the perimeter of Pt while the positive current steps come from the counteract effect where area amplification (area 2#) exceeds the decreased current response by the difference in kinetics of Pt and GNP in the confined area (area 1#). Indeed, GNP laying outside the surface of Pt can access to more volume of diffusion flux of the reporter molecule, resulting in the current enhancement. The current increase by area amplification was already reported in the case of the attachment of Au-SWCNTs to the Pt Nanoelectrode, generating an increasing current step.[4] After adsorption of GNP at the perimeter of Pt, an increase in the background noise is always accompanied by the current step. The increased current noise is emphasized at a higher potential (i.e., 1.0 V vs. Ag/AgCl) than a relatively lower potential (i.e., 0.7 V vs. Ag/AgCl). The large background noise is possibly attributed to the instability of GNP at the surface of Pt after adsorption.

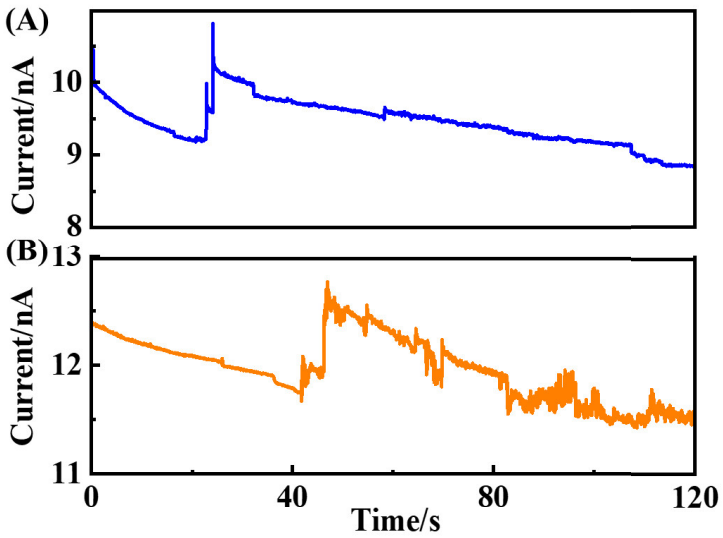

Figure 4.22. Chronoamperograms recorded on a 5 μm radius Pt UME in the presence of 35 fM GNPs at (A) 0.7 V and (B) 1.0 V. Both positive and negative current signals are observed. The solution contains 1 mM hydrazine and 10 μM NaOH.

Over forty individual collision measurements were done in order to obtain the statistical number of collision events. Among these preliminary measurements, positive current responses (current steps and

spikes) account for over 20% of all events. The histograms of the normalized size distribution of the positive relative current steps at potentials of 0.7 V (blue trace) and 1.0 V (orange trace) are shown in Figure 4.23. From the histogram, we can observe that the average magnitude of increasing current steps at 1.0 V is higher than that measured at 0.7 V. We calculated the average, median, and distribution range obtained for positive steps shown in Table 4.2. The distribution range of positive relative current steps spans around 8 ~ 10 times wider than that of the corresponding negative current steps in Table 4.1. The average positive step size for 0.7 V and 1.0 V is 43.1‰ and 50.4‰, respectively, which is around 6-7 times higher than the average negative step size (see Table 4.1).

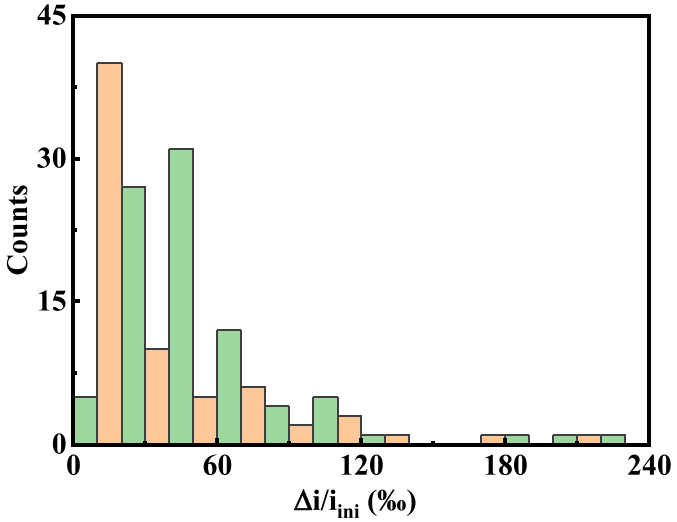

Figure 4.23. Histogram showing the normalized size distribution of the positive relative current steps caused by 35 fM GNPs colliding on a 5 µm radius Pt. The UME is biased at 0.7 V (orange bar) and 1.0 V (green bar). The solution contains 1 mM hydrazine and 10 µM NaOH.

Table 4.2. The statistical description of the magnitude of the positive steps at high bias potentials.

Potentials (V)	Counts	Average (‰)	Median (‰)	Range (‰)
0.7	98	43.1	20.8	4.0 to 422
1.0	88	50.4	35.7	6.1 to 434

In terms of relative current steps, the average is expected to increase due to increasing kinetics of GNP with increasing potentials. However, during pure electrochemical measurements, corresponding surface areas of GNP laying outside the Pt and confined in the Pt are not unknown. It is not possible to use these relative current steps to calculate the kinetics of GNP for hydrazine oxidation. Such a huge range of current distribution for positive current steps are also not clear. Correlated optical and electrochemical measurements will be used to understand the dynamic electrochemical behaviors of GNPs interacting with the electrode surface.

4.5 Conclusion

We report a strategy, electro-catalytic depression, based on the intrinsic difference in kinetics in electron transfer between materials to detect poorly catalytic particles such as GNPs. We show that our approach leads to the detection of individual GNPs of a few µm in length suspended at the concentration of 35 fM. More than 90% of the collisions lead to the irreversible adsorption of the GNP on the Pt surface. The current steps can be analyzed based on models already developed for insulating particles and the variation of their magnitude as a function of the potential can be rationalized with respect to the intrinsic difference in kinetics between the electrode and GNPs. This opens opportunities to quickly measure the kinetics of catalysis on particles in suspension with good statistics and without having to deposit films or use nanoprobes. We also show that despite measuring well-defined current signals (staircase-shape, low noise), a large dispersion of size and shape of the GNP, the poor stability of the GNP suspension,

interactions between GNPs adsorbed on the electrode and the edge effect should be carefully considered before attempting any quantitative analysis of the data.

Besides, at higher potentials (≥ 0.7 V) where the reaction takes place also on GNP, both negative and positive current signals are observed. The average of negative current steps decreases with the increasing potential. The positive steps are possibly caused by the GNP landing on the perimeter of the UME where the negative current steps are counterbalanced by a positive current originating from the GNP area landing outside of the Pt. Owing to lack of optical position information of GNP colliding at the surface of GNP, many issues, the kinetics of GNP versus the bias potential and the origin of large current step distribution as well as average magnitudes, is still unknown. Simultaneous opto-electrochemical measurements might help to unravel this mystery.

4.6 Reference

1. Dudin, P. V.; Unwin, P. R.; Macpherson, J. V., Electro-oxidation of hydrazine at gold nanoparticle functionalised single walled carbon nanotube network ultramicroelectrodes. *Physical Chemistry Chemical Physics* **2011,** *13* (38), 17146-17152.

2. Zhang, B.; Fan, L.; Zhong, H.; Liu, Y.; Chen, S., Graphene nanoelectrodes: fabrication and size-dependent electrochemistry. *J Am Chem Soc* **2013,** *135* (27), 10073-10080.

3. Poon, J.; Batchelor-McAuley, C.; Tschulik, K.; Compton, R. G., Single graphene nanoplatelets: capacitance, potential of zero charge and diffusion coefficient. *Chemical science* **2015,** *6* (5), 2869-2876.

4. Park, J. H.; Thorgaard, S. N.; Zhang, B.; Bard, A. J., Single particle detection by area amplification: single wall carbon nanotube attachment to a nanoelectrode. *J Am Chem Soc* **2013,** *135* (14), 5258-5261.

5. Kavan, L.; Yum, J. H.; Grätzel, M., Optically transparent cathode for dye-sensitized solar cells based on graphene nanoplatelets. *ACS Nano* **2010,** *5* (1), 165-172.

6. Kavan, L.; Yum, J.-H.; Grätzel, M., Graphene nanoplatelets outperforming platinum as the electrocatalyst in co-bipyridine-mediated dye-sensitized solar cells. *Nano letters* **2011,** *11* (12), 5501-5506.

7. Jafri, R. I.; Rajalakshmi, N.; Ramaprabhu, S., Nitrogen doped graphene nanoplatelets as catalyst support for oxygen reduction reaction in proton exchange membrane fuel cell. *Journal of Materials Chemistry* **2010,** *20* (34), 7114-7117.

8. Shao, Y.; Zhang, S.; Wang, C.; Nie, Z.; Liu, J.; Wang, Y.; Lin, Y., Highly durable graphene nanoplatelets supported Pt nanocatalysts for oxygen reduction. *Journal of Power Sources* **2010,** *195* (15), 4600-4605.

9. Han, J.; Zhang, L. L.; Lee, S.; Oh, J.; Lee, K.-S.; Potts, J. R.; Ji, J.; Zhao, X.; Ruoff, R. S.; Park, S., Generation of B-doped graphene nanoplatelets using a solution process and their supercapacitor applications. *ACS Nano* **2012,** *7* (1), 19-26.

10. Zhang, B.; Li, Q.; Cui, T., Ultra-sensitive suspended graphene nanocomposite cancer sensors with strong suppression of electrical noise. *Biosensors and Bioelectronics* **2012,** *31* (1), 105-109.

11. Golabi, S.; Zare, H. R., Electrocatalytic oxidation of hydrazine at glassy carbon electrode modified with electrodeposited film derived from caffeic acid. *Electroanalysis: An International Journal Devoted to Fundamental and Practical Aspects of Electroanalysis* **1999,** *11* (17), 1293-1300.

12. Faulkner, L. R.; Bard, A. J., *Electrochemical methods: fundamentals and applications*. JOHN WILEY & SONS, INC.,: 2002.

13. Chen, C.-H.; Jacobse, L.; McKelvey, K.; Lai, S. C.; Koper, M. T.; Unwin, P. R., Voltammetric scanning electrochemical cell microscopy: dynamic imaging of hydrazine electro-oxidation on platinum electrodes. *Anal Chem* **2015,** *87* (11), 5782-5789.

14. Aldous, L.; Compton, R. G., The mechanism of hydrazine electro-oxidation revealed by platinum microelectrodes: role of residual oxides. *Physical Chemistry Chemical Physics* **2011,** *13* (12), 5279-5287.

15. Yue, G.; Zeng, Q.; Huang, J.; Wang, L., Mechanism studies of hydrazine electro-oxidation by a platinum ultramicroelectrode: Effects of supporting electrolytes. *Journal of Electroanalytical Chemistry* **2018,** *818*, 19-25.

16. Arulrajan, A. C.; Renault, C.; Lai, S. C., How changes in interfacial pH lead to new voltammetric features: the case of the electrochemical oxidation of hydrazine. *Physical Chemistry Chemical Physics* **2018,** *20* (17), 11787-11793.

17. Limon-Petersen, J. G.; Han, J. T.; Rees, N. V.; Dickinson, E. J.; Streeter, I.; Compton, R. G., Quantitative voltammetry in weakly supported media. Chronoamperometric studies on diverse one electron redox couples containing various charged species: dissecting diffusional and migrational contributions and assessing the breakdown of electroneutrality. *The Journal of Physical Chemistry C* **2010,** *114* (5), 2227-2236.

18. Kashyap, S.; Mishra, S.; Behera, S. K., Aqueous colloidal stability of graphene oxide and chemically converted graphene. *Journal of Nanoparticles* **2014,** *2014*.

19. Deng, Z.; Elattar, R.; Maroun, F.; Renault, C., In Situ Measurement of the Size Distribution and Concentration of Insulating Particles by Electrochemical Collision on Hemispherical Ultramicroelectrodes. *Anal Chem* **2018,** *90* (21), 12923-12929.

20. Chen, C.-H.; Ravenhill, E. R.; Momotenko, D.; Kim, Y.-R.; Lai, S. C.; Unwin, P. R., Impact of surface chemistry on nanoparticle–electrode interactions in the electrochemical detection of nanoparticle collisions. *Langmuir* **2015,** *31* (43), 11932-11942.

21. Fosdick, S. E.; Anderson, M. J.; Nettleton, E. G.; Crooks, R. M., Correlated electrochemical and optical tracking of discrete collision events. *J Am Chem Soc* **2013,** *135* (16), 5994-5997.

22. Renault, C.; Lemay, S. G., Electrochemical Collisions of Individual Graphene Oxide Sheets: An Analytical and Fundamental Study. *ChemElectroChem* **2020,** *7* (1), 69-73.

23. Dasari, R.; Tai, K.; Robinson, D. A.; Stevenson, K. J., Electrochemical monitoring of single nanoparticle collisions at mercury-modified platinum ultramicroelectrodes. *ACS nano* **2014,** *8* (5), 4539-4546.

24. Robinson, D. A.; Kondajji, A. M.; Castañeda, A. D.; Dasari, R.; Crooks, R. M.; Stevenson, K. J., Addressing colloidal stability for unambiguous electroanalysis of single nanoparticle impacts. *The Journal of Physical Chemistry Letters* **2016,** *7* (13), 2512-2517.

25. Boika, A.; Thorgaard, S. N.; Bard, A. J., Monitoring the electrophoretic migration and adsorption of single insulating nanoparticles at ultramicroelectrodes. *The Journal of Physical Chemistry B* **2013,** *117* (16), 4371-4380.

26. Faulkner, L. R.; Bard, A. J., *Electrochemical methods: fundamentals and applications, 2nd Edition*. John Wiley and Sons: 2002.

27. Quinn, B. M.; van't Hof, P. G.; Lemay, S. G., Time-resolved electrochemical detection of discrete adsorption events. *Journal of the American Chemical Society* **2004,** *126* (27), 8360-8361.

28. Percival, S. J.; Zhang, B., Fast-scan cyclic voltammetry allows determination of electron-transfer kinetic constants in single nanoparticle collision. *The Journal of Physical Chemistry C* **2016,** *120* (37), 20536-20546.

29. Bentley, C. L.; Kang, M.; Unwin, P. R., Time-resolved detection of surface oxide formation at individual gold nanoparticles: Role in electrocatalysis and new approach for sizing by electrochemical impacts. *Journal of the American Chemical Society* **2016,** *138* (39), 12755-12758.

5. Chapter 5 Understanding complex current responses of individual graphene nanoplatelet collision by correlated opto-electrochemical Measurements

5.1 Introduction

Graphene, as one of the most attractive two-dimensional (2D) materials, has received widespread attention since its first discovery and groundbreaking experiments by Geim and Novoselv in 2004.[1] This Nobel Prize award-winning sparkling material exhibits high charge mobility and carrier concentration, large specific surface area, superior electrical and thermal conductivity, and excellent mechanical strength.[2-5] Graphene nanoplatelet (GNP) belongs to this family of graphene materials and enjoys the advantageous properties of graphene but avoid the poor stability due to its highly ordered graphitic structures.[6-8] GNPs have been proposed as the effective electrocatalyst and the catalyst support for various electrochemical reactions of interest due to high surface-area-to-volume ratio, desirable sp^2 hybridized carbon sites, and excellent stability.[9-11] Despite the intensive efforts that have been made to achieve high performance for catalysis,[12] the mechanism of addressing the fundamental problems of the interactions of GNPs upon contact with the electrode substrate has not yet received enough attention until the contributions from Compton and coworkers.[13-15] As a 2D material with two spatial dimensions in the micrometer range and one spatial dimension in the nanometer range, these nanoplatelets demonstrated significant polydispersity in size and morphology.[15] The high polydispersity blurries difficult the physiochemical properties determined from ensemble measurements. On the other hand, collisions of single GNPs may provide an accurate measurement at the level of a single GNP (i.e., size, morphology and catalytic properties). Another important parameter that has been recently addressed is the question of motion or dynamics of the entity onto/near the surface.[16-20] The complex motion of a particle can lead to new features in the current response.

The combination of single entity electrochemistry and microscopic techniques has been proposed for the analysis of complex current transients.[17-18, 20-21] Fosdick and coworkers directly characterized the edge effect at a UME by correlating simultaneous blocking experiments with fluorescent microscopy using fluorescently labeled polystyrene beads.[21] Zhang and coworkers used fluorescent microscopy to image the dynamic motions of single silver nanoparticles during oxidation at the confined Pt nanoelectrode surface.[18] Tao and coworkers developed the technique of plasmonic-based electrochemical current microscopy to establish a size-dependent relation between localized electrochemical oxidation kinetics of a silver nanoparticle and its size.[17] In these experiments, the colliding entities are spherical such that the entity orientation can be ignored in the analysis. However, for research objects of interest are asymmetric, the issue of reorientation of 2D nanoplatelets presents interesting challenges in single entity electrochemistry. In this chapter, we couple electrochemistry and bright-field microscopy to elucidate how the translation and rotation of GNPs affect the current response.

5.2 Bestiary of current signals: a simple experiment but complex signal

The collision of an object on a surface is by essence a dynamic phenomenon. The convolution of the motion of the object with physicochemical parameters intrinsic to the object (size, shape, charge etc…) as well as parameters of the experiment (inner/outer-sphere redox reporter, edge effects caused by the shape of the electrode, ionic strength and drift/diffusion fluxes) may render the analysis of a current signal extremely difficult. As we saw in Chapter 3 the shape of the electrode can lead to a broadening of the distribution of the current step magnitudes. Kanoufi *et al.*,[20] Zhang *et al.*,[18] and Long *et al.*[19] showed that Ag nanoparticles might rebound several times on the electrode surface leading to multiple collision signals for the same particle. In the case of electrocatalytic amplification, one can find several examples of collisions leading to a spike-shaped current response instead of a stair-case shape.

In this chapter we will examine an experiment that may seem simple in term of electrochemistry but leads to relatively complex current responses. The redox reporter used in this chapter is FcMeOH molecules instead of hydrazine. The current is thus always mass-transfer limited in our experiments. Figure 5.1A shows two typical *i-t* traces measured at a 10 µm diameter Pt UME in the absence (black trace) and presence (red trace) of GNPs in 1 mM FcMeOH and 10 µM NaOH solution. The steady-state current of about 1.1 nA corresponds to the oxidation of FcMeOH at the surface of a bare 10 µm diameter Pt UME. In the absence of GNP in solution, no abrupt current signals are observed (the black trace in Figure 5.1A); in contrast, after the addition of GNPs, a variety of transient current signals are observed on the red trace in Figure 5.1A. The observation of hundreds of current transients reveals several types of current signals. Examples are highlighted in blue, green, orange and yellow colors on the red trace in Figure 5.1A and also magnified in Figure 5.1 (B-E), respectively. We observe negative and positive spikes as well as positive staircase-shape events and multiple combinations. We will attempt to explain this variety of current responses based on both previous modes of collision and new information from the videos.[21-23]

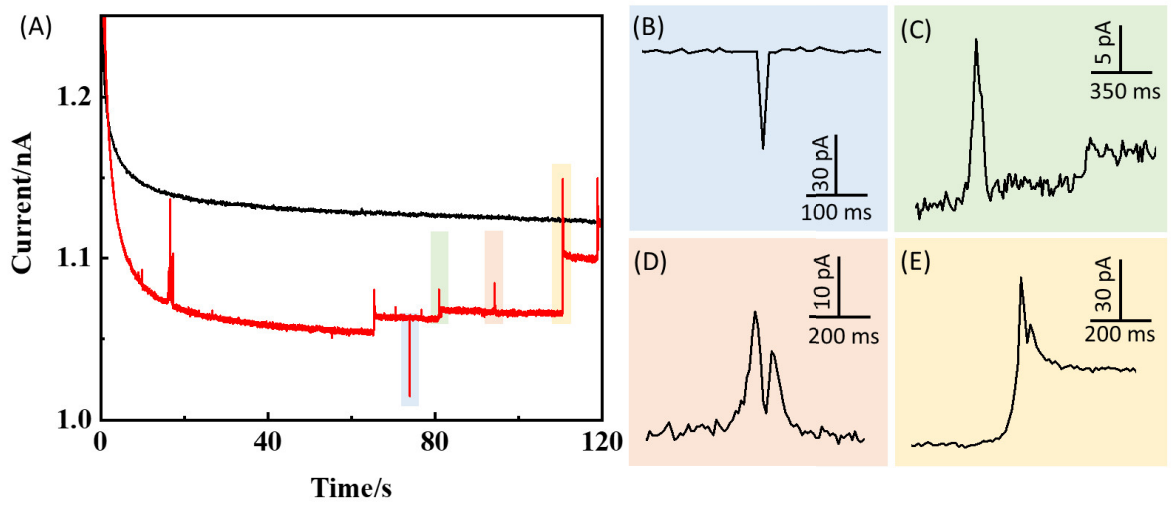

Figure 5.1. Experimental observation of dynamic collision behaviors of GNP at a 10 µm diameter Pt UME. (A) *i-t* trace recorded at a 10 µm diameter Pt UME in the absence (black line) and presence (red line) of 35 fM GNP. The solution contains 1 mM FcMeOH and 10 µM NaOH. The time acquisition is 10 ms. The UME is biased at 0.45 V vs. AgAgCl. The enlarged pictures show the transient current signals marked in (B) blue, (C) green, (D) orange, and (E) yellow.

5.3 Correlated opto-electrochemical measurements of individual GNP collision

Correlated opto-electrochemical measurements were performed with a 10 µm diameter Pt UME positioned atop an inverted microscope in epi-illumination with white light. A video of the surface of the UME in bright-field mode was recorded simultaneously with a chronoamperogram, both with a time

resolution of 50 ms. GNPs were dispersion in a 0.9 mM FcMeOH solution containing 10 μM of NaOH. Details about the experimental setup are provided in Chapter 2. Among preliminary opto-electrochemical measurements, tens of movies were analyzed and show reproducible features. We observe that 79% of all the collision events lead to reversible adsorption (in other words, GNP rebounds at the surface of Pt) while 21% of the GNPs irreversibly absorb at the electrode surface. In the next sub-sections, we will examine in detail remarkable collision events.

5.3.1 Adsorption of individual GNP with permanent amplification

The first exemplar collision event is the movement (rotation + translation) of GNP at the surface of Pt. The *i-t* transients and the enlarged current trace are shown in Figure 5.2 A and B, and snapshots of the movie recorded in synchronization with the *i-t* trace are shown in Figure 5.2C. The enlarged transient current signal consists of three periods, a fast increase, a slight decrease and a plateau. Frame 1 corresponds to the bare Pt (baseline current), and when a GNP approaches above the surface of Pt, a small current increase is observed in the *i-t* trace (from point 1 to point 2). The current reaches a maximum (at point 3) after about 100 ms. If we assume that the GNP is lying flat on the optical micrograph 8 then, the smaller projected area on the micrograph 3 indicates that the GNP stands up (that is on its edge). From the ratio of the long axis (measured on micrograph 8) and the apparent diameter on micrograph 3 we estimate roughly and a dihedral angle of 60° between GNP and the Pt surface. Fifty milliseconds later the GNP lays down at an angle of 30° (frame 4) and the current decreases (point 4). Next, The GNP lays flat at the Pt surface and simultaneously undergoes a translation of 1.3 μm to the edge of Pt (see frames 6-8), and the increased current step appears (from point 5 to point 8). The translation distance is estimated by the difference in the distance from the left side of GNP to the edge of the snapshot in frame 4 and frame 5.

We explain the correlated motions of GNP and current changes as follows. The initial increase of current observed at point 2 is intriguing since the optical micrograph shows a GNP completely out of focus and thus not in contact with the Pt UME. For the time being, we cannot completely exclude that the synchronization of the video and the i-t trace was shifted by one point or a blurring of the image due to the motion of the GNP during the integration of the light (over about 44 ms). In addition, bipolar electrochemistry might occur between the two ends of the GNP when GNP enters the diffusion layer because of the different local concentrations of Fc and Fc^{+}. Such behavior has been observed before especially in SECM measurements where positive current feedback is obtained when the tip approaches very close to the electrode surface.[24]

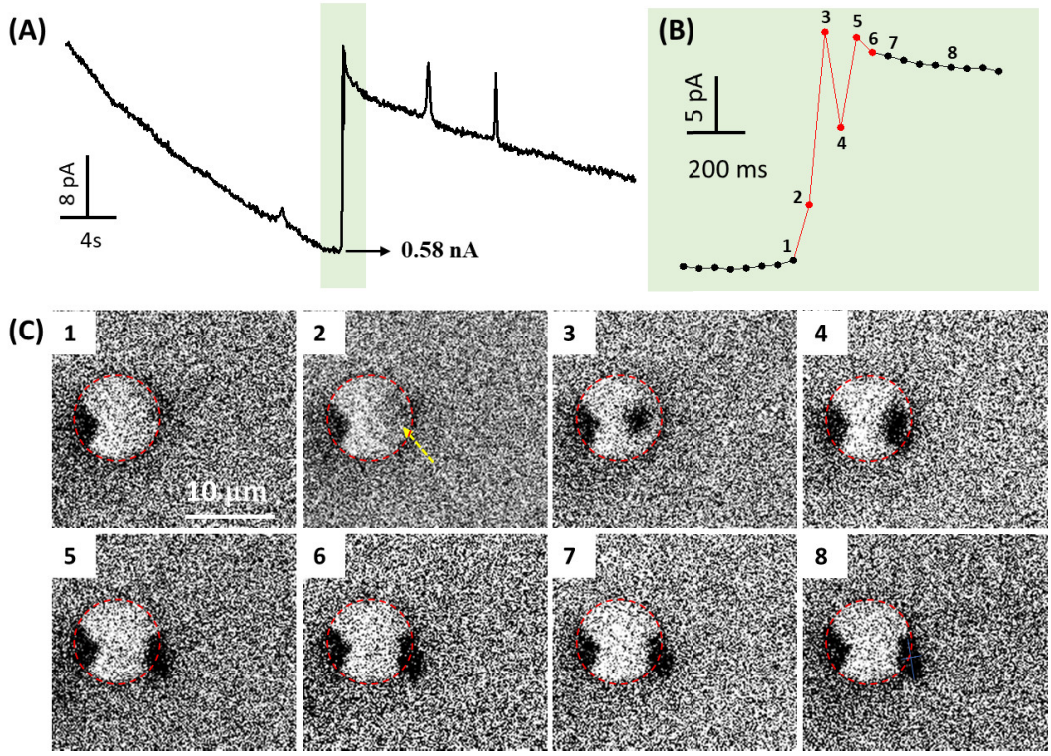

Figure 5.2. Movement of GNP at the surface of Pt. (A) *i-t* transients showing the current signals measured at a Pt UME in the presence of GNP. (B) The enlarged current transients in (A). (C) The numbered optical graphs correspond to the numbered points in (B). Frame 1 represents a bare Pt UME with a GNP already present at the electrode surface. Frames 2 and 3 show the landing process, and frame 4 shows the landing process along with the slight movement of 0.92 µm along the radial direction. The frame 5 shows the dynamic movement of the GNP toward the perimeter of the Pt UME. Then the GNP is kept stable, as shown in frames 6-8. The solution contains 0.45 mM FcMeOH, 15 fM GNP and 10 µM NaOH. The Pt UME is biased at +0.45 V vs. Ag/AgCl.

When the GNP hits the surface of Pt at an angle of 60°, besides the capacitive charging (vide infra), the faradaic oxidation reaction of ferrocenemethanol molecules at the surface of GNP occurs at the mass-transfer limit (we assume that there is no significant drop of potential at the electrical contact between the GNP and the Pt). At this time, the total electroactive area (i.e., surface of Pt and GNP exposed to the solution) is larger than the initial surface of Pt (see Figure 5.3A). Thus, the current is expected to increase. The GNP behaves like an "antenna" reaching FcMeOH deeper in solution. When the GNP progressively lays down, the GNP reaches less of the bulk solution and penetrates more in the diffusion layer originating from the UME, thus the current decreases. When the GNP lays flat at the surface of Pt and simultaneously undergoes a slight translation of 0.92 µm to the edge of Pt (see frame 5), a current increase is observed. Now, a large fraction of the surface of the GNP covers the glass sheath surrounding the UME leading to a permanent increase of the total electroactive surface area and thus the current increases (see Figure 5.3B). This typical current increase is referred as "area amplification".

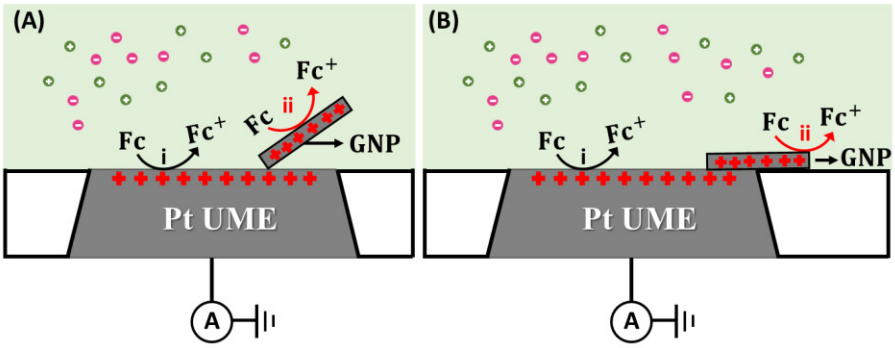

Figure 5.3. (A) When the GNP hits the surface of Pt at a certain angle, the surface of GNP is biased at the same potential as Pt. Ferrocene oxidation occurs at the surface of GNP. (B) The GNP lays flat at the perimeter of electrified Pt UME and can access to more volume of redox molecules than before. The Pt UME is biased at +0.45 V vs. Ag/AgCl.

The second exemplar collision is the observation of the repeated movement of GNP at the electrode surface, as shown in Figure 5.4. The numbered points in the *i-t* trace correspond to micrographs in numbers in Figure 5.4C. The *i-t* trace and corresponding enlarged current transients are shown in Figure 5.4 A and B. In the *i-t* trace, the current increases (intervals 1-3, 100 ms) then partially decays to a quasi-plateau (intervals 3-6, 150 ms) to finally increase again in two steps. The frame 1 corresponds to the bare Pt UME. The image of GNP becomes clear as it lands close to the surface of Pt (see frames 2-5). Note that the entire GNP in frame 2 is blurry and probably not yet in contact with the surface of Pt; the left side of GNP hits earlier at the surface of Pt than the right side (see frames 3-4); when the entire GNP lays flat on the surface of Pt and a clear image of GNP appears in frame 6. Over the landing process, GNP experienced a mixed motion of out-of-plane and in-plane rotation (see frames 2-6), corresponding to the current decrease (see intervals 3-6); note that during frames 3-5, the direction of in-plane rotation is counterclockwise while the direction is reversed to clockwise (see frame 6). In the second period (see intervals 6-9), GNP experiences slight counterclockwise rotation with the angle of from 69.6° (in-plane angle) to 55.0°, together with a slight current increase. The third period (see intervals 9-10) corresponds to the stabilization process at which the GNP is kept stable and the corresponding current does not change. In the fourth period (intervals 10-12), the current climbs to a higher current plateau than the previous steady current, along with the clockwise rotation angle of 18.1° and simultaneous translation of 0.4 μm from the center of the electrode.

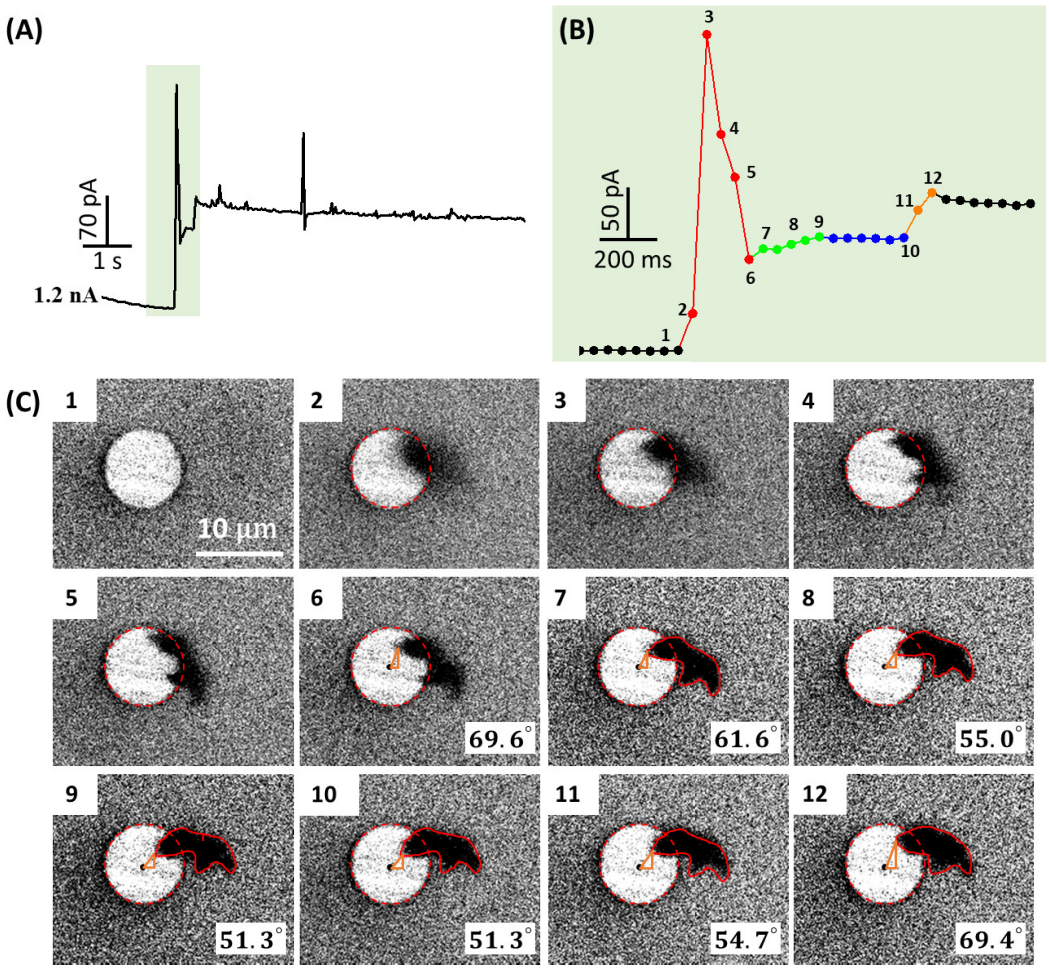

Figure 5.4. Movement of GNP at the surface of Pt. (A) *i-t* transients showing the current signals measured at a Pt UME in the presence of GNP. (B) Enlarged current signals marked in green in (A). The numbers in the *i-t* trace correspond to the numbered movie frames shown in (C). Frame 1 represents the bare Pt UME, and frames 2-5 represents the landing process with the GNP image changing from an obscure view to a clear one. Between frames 3-6, the GNP at the electrode surface undergoes mixed motion (both out-of-plane and in-plane rotation), while during frames 7-12, the GNP only undergoes in-plane rotation. Once the GNP lays completely flat at the electrode surface, the GNP (indicated by red circles) first rotates in the counterclockwise direction (frames 7-9) while during frames 10-12, GNP experiences clockwise rotation along with a slight translation (around 0.4 µm) from the center of the electrode. The apparent angles (orange right triangle) are manually measured by the angle between the center of the electrode (black dot) and the sharp vertex at the top left part. The angles are indicated in the white bar in the bottom right in frames 7-12. The orange dash circles show the perimeter of the Pt UME in order to visually guide the variation of contact area between GNP and Pt UME. The solution contains 0.9 mM FcMeOH, 15 fM GNP and 10 µM NaOH. The Pt UME is biased at +0.45 V vs.Ag/AgCl.

As the GNP progressively lays down at an angle on the edge of Pt UME, the left side of GNP first touches the Pt surface (see frame 3) and is then biased at an equivalent potential to the surface of Pt. The FcMeOH is also oxidized on the surface of GNP. The total electroactive surface area equals to the sum of the surface of Pt and GNP exposed to the solution, which is larger than the initial surface of Pt. The current is thus expected to increase (see point 3). Later, the right side of GNP progressively lays down (see frames 3-6) and covers a part of the UME; thus, the instantaneous current decrease is observed (intervals 3-6). When the GNP completely lays flat on the surface of Pt (frame 6), the transient current is higher than the baseline before the collision. The current increase is attributed to area amplification

During intervals 6-9, the GNP progressively undergoes counterclockwise rotation in the electrode plane and the total electroactive area continuously increases. Thus, the current increases. Note that there is a sharp vertex at the bottom left part of GNP, and after the rotation, the vertex rotates away from the surface of Pt, resulting in the increasing total electroactive surface. Over the stabilization process lasting for 300 ms, no current changes are observed along with no noticeable movement or reorientation of

GNP at the surface of Pt. In the fourth period (see intervals 10-12), the GNP undergoes the clockwise rotation with the angle of 18.1°, simultaneously along with the translation of 0.4 μm from the center of the electrode. The translation distance is measured from the difference in the distance from the center of the electrode (black dot) to the vertex of GNP in frame 10 and frame 12 (this slight translation is relatively clear in the movie). Thus, the contact surface area decreases and the total conducting surface increases, resulting in a current increase to a higher plateau than the baseline current in the stabilization period.

5.3.2 Rebound of a GNP

The third exemplar collision event is a rebound of GNP on the electrode surface. A typical *i-t* transient and the enlarged current transient are shown in Figure 5.5 A and B, respectively. This signal is divided into four periods, including a sharp increase, a slow decay, a stabilization period and a fast slump (see Figure 5.5B). Snapshots of the movie recorded in synchronization with the *i-t* trace are shown in Figure 5.5C, which can be separated into four periods, the approach, rotation, stabilization and departure. The position of the GNP is schematically represented in the right scheme in Figure 5.5C. Because of the GNP having a large size (the surface area is 47.9 μm^2), the GNP moves slowly at a rate of 14.3 μm/s (calculated by the traveling distance divided by the traveling time between frame 1 and frame 2); during this period, no current changes are observed in the *i-t* trace. Later, the GNP (almost parallel to the electrode plane) lays down slowly (see frames 2-3), and the observed area of GNP shrinks. A rapid current increase is observed in the *i-t* trace and the whole process lasts for 100 ms. In the second period (rotation), the current trace shows a slow decay (3.3% of peak current) between intervals 3 and 7 in the *i-t* trace, corresponding to the continuous rotation along the direction indicated by the red arrows in the right scheme. In the third period, the standing GNP is stable and the current (intervals 8-10) remains unchanged. The fourth process is the departure process (see frames 10-12), and the current trace returns to the baseline.

Combining the synchronized optical tracking information and the resulting current changes, we evidence that the rotation of GNP leads to a transient current. Over the rotation process, the progressive current decay might result from the overlap of the diffusion layers originating from the Pt surface and the GNP. One can imagine a competition between these two electrodes to access a certain volume of solution (FcMeOH). Depending on the size of these electrodes and their respective orientation, the total current may vary. A numerical simulation of such systems will be performed to test this hypothesis. One could also raise the hypothesis of a variation of the contact resistance at the junction between the GNP and the Pt that could lead to an ohmic drop. The value of the current flowing through the GNP is typically on the order of few tens of pA and thus a drop of 0.1V would mean a contact resistance of the order of 0.1 Tohm. Typical contact resistance between a 1μm large silver contact pad and a silver nanowire (50 - 130 nm diameter, a proxy for the edge of our GNP) ranges between more than 500 ohm after simple drop-casting of the wires to only 11 ohm after thermal treatments to improve the contact area.[25] It is thus unlikely that contact resistance plays a role in these experiments. In the fourth step, the GNP leaves away from the electrode surface and the current is thus restored to its initial value. The rebound takes about half a second, a rather slow process at the micro-scale. We are currently exploring what are the possible forces in presence that could push away the GNP and the reasons for the slow current decay.

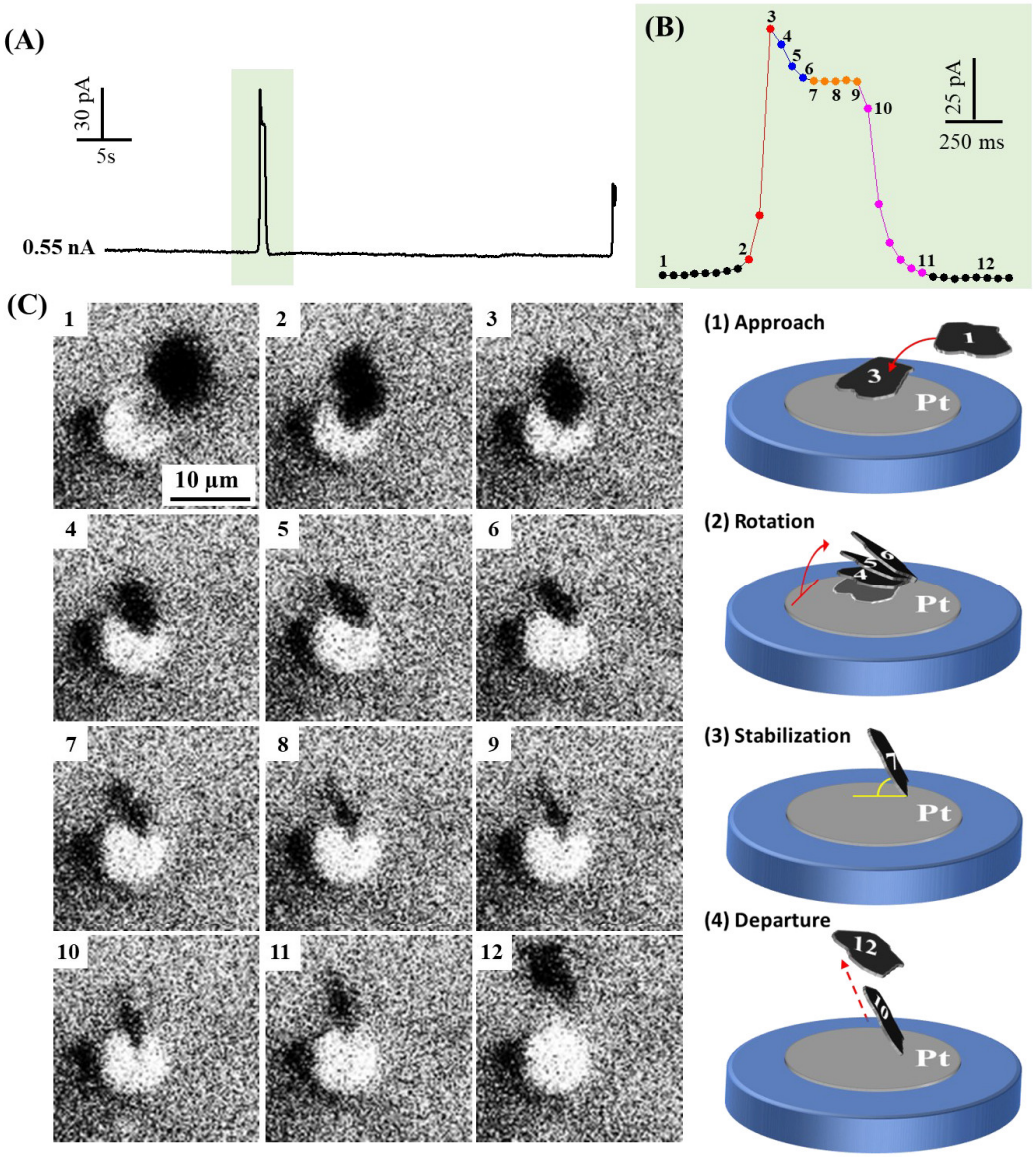

Figure 5.5. Rotation of GNP at the surface of Pt. (A) *i-t* transients showing current signals measured at a Pt UME in the presence of GNP. (B) An enlarged current transient is highlighted in green in (A). (C) The numbered points correspond to the numbers in each movie frame in (C). Frames 1-3 show the approach process of GNP toward the surface of Pt, schematically in the right scheme (1); frames 4-6 represent the rotation process, schematically indicated in (2); frames 7-9 show that GNP is almost kept stable, standing with a certain angle, schematically shown in (3); frames 10-12 show the departure process of GNP from the UME. The solution contains 0.45 mM FcMeOH, 15 fM GNP and 10 µM NaOH. The Pt is biased at 0.45 V vs. Ag/AgCl. The magnification of the objective is 20 X.

5.3.3 Simultaneous collision of two GNPs

The third typical collision event is the almost simultaneous bouncing of two GNPs at the surface of Pt shown in Figure 5.6. The *i-t* transients and the enlarged current transients are shown in Figure 5.6 A and B, respectively. The red dotted line represents the bouncing of the 1st GNP, followed by the blue dotted line being the 2nd GNP bouncing at the surface of Pt. Figure 5.6C shows the synchronized micrographs in numbers. Frame 1 shows the bare Pt UME and frames 2-5 show the landing process of the 1st GNP indicated by the yellow dash arrow. The GNP at frame 2 is at least 3 µm higher than the surface of Pt, and then lays down progressively (frames 3 and 4). The top left side of GNP starts to hit the surface of Pt at a certain angle (see frame 5) and later rebounds on the surface of Pt (frame 6), finally leaving away from the electrode surface (the yellow dash circle in frames 7 and 8). The bouncing event of the 1st GNP lasts for 200 ms, producing a transient current spike. Right after the departure of the 1st

GNP, the 2nd GNP hits the electrode surface (see frames 7 and 8) and then leaves away (frames 9-11) without the reorientation process observed in the 1st GNP. In the *i-t* trace, the peak of the spike is quite clean without the joint points nearby (like point 4 and point 6). The transient current spike is attributed to the instantaneous increase in the total electroactive surface (surface of Pt and GNP exposed to solution). The movement of GNP (frames 4-6) at the surface of Pt leads to additional current signals shown in points 4 and 6 in the *i-t* trace. Due to the fast motions of small GNPs, it is difficult to acquire clear images.

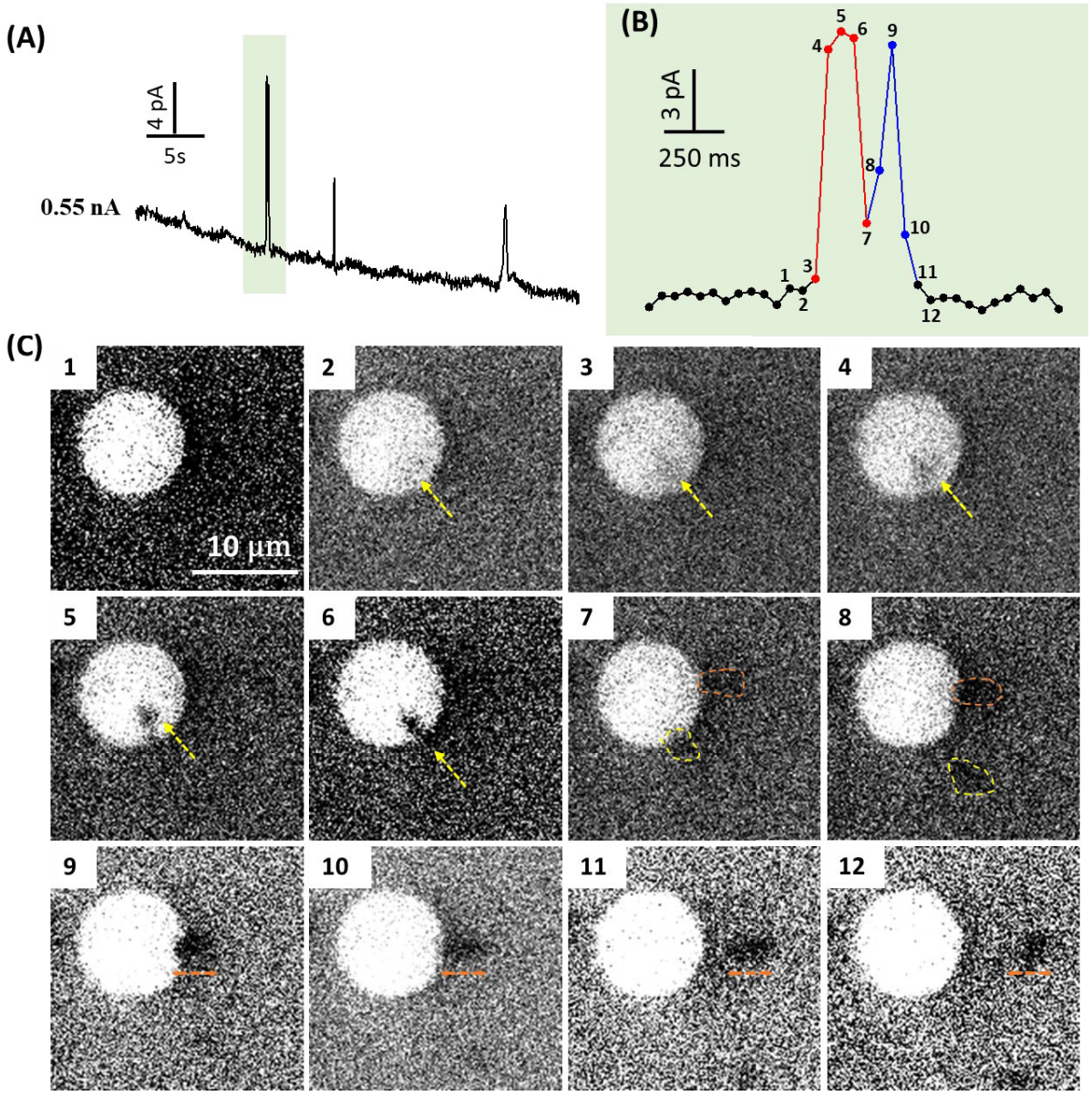

Figure 5.6. Simultaneous bouncing of two GNPs at the surface of Pt. (A) *i-t* transients showing the current signals measured at a Pt UME in the presence of GNP. (B) Complex spike-shaped current transients (highlighted in green in (A) due to the collisions of two GNPs (marked in red and blue respectively) occurring at a very short time interval (less than 50 ms). (C) Frame 1 shows the bare Pt UME; frames 2-4 show the landing process of the 1st GNP marked in the yellow dash arrows, followed by colliding at the electrode surface (frames 5 and 6), and then leaving away from the electrode surface (see the yellow dash circle in frames 7 and 8). Almost at the same time, the 2nd GNP rebounds at the electrode surface, with the approach process (see frames 7 and 8), the colliding at the electrode surface (frame 9), and leaving from the electrode surface (frames 10-12). The solution contains 0.45 mM FcMeOH, 15 fM GNP and 10 µM NaOH. The Pt is biased at 0.45 V vs. Ag/AgCl. The magnification of the objective is 40 X.

5.3 Capacitive charging

When a GNP touches the electrode surface, the potential of the GNP will suddenly jump to the potential of the electrode leading to a transient capacitive current. The question addressed in the present section is whether we can measure it under our experimental conditions. An equivalent circuit for the capacitive charging of the surface of GNP is shown in Figure 5.7, where R_L represents the resistance of solution, and C is the capacitance charging of the surface of GNP. The specific capacitance of GNP will be in a first approximation considered very close from the value (6.0 µF cm^{-2} from Ref. [26]) of exfoliated highly ordered pyrolytic graphite (HOPG). The capacitance for typical GNPs is comprised between 0.6 and 1.62 pF (Table 5.1). The resistance of the electrolytic solution (10 µM NaOH) between the surface of GNP and the counter electrode (assumed to be at infinity in solution) may be approximated by a model of two concentric circles separated by a resistive medium with the outer-sphere (our counter electrode) having a radius much larger than the inner-sphere (the GNP). Then, the resistance simplifies as follows:

$$R_L \approx \frac{\rho}{l} \tag{5.1}$$

where ρ is the solution resistivity and l is the characteristic length of the GNP (assume the spherical shape). The resistivity of the solution is calculated to be 0.2 × 10^6 Ω•cm using the molar conductivity of NaOH (Λ^o, take 249.32 S cm^2 mol^{-1} at 25 °C from Ref. [27]) and the electrolyte concentration (10 µM). For a characteristic length of 10^{-4} cm we obtain a resistance of 2 × 10^9 Ω. If one considers the accumulation of ions in the diffusion layer, we obtain a lower resistance ≈ 10^8 Ω.[28]

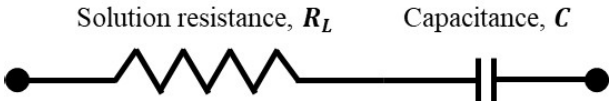

Figure 5.7. An equivalent circuit for the electrochemical charging process at the surface of GNP, composed of elements of the solution resistance and the capacitance at the interface of GNP.

The current transient for charging a RC series circuit is given by:

$$i = \frac{\Delta E}{R_L} e^{-\frac{t}{R_L C}} \tag{5.2}$$

The potential jump may be approximated to be around 0.63 V (the OCP is about -0.185 V (vs. Ag/AgCl) from Ref. [15] and the potential of the working electrode is 0.45 V). The total charge ($C\Delta E$) is estimated to be around few pC (see Table 5.1). The time constant ($R_L C$) is expected to be comprised of 60 - 162 µs. Capacitive charging cannot be resolved with our experimental time resolution of 50 ms and is not expected to affect more than one point in the rise of the transient.

Table 5.1. Summary of the calculated capacitance, charge and time constant, as well as the experimental time to reach the amount of calculated charge (from Figure 5.8).

GNPs	Surface area	Calculated capacitance	Calculated charge	Time constant	Experimental charge time
GNP-1# in Figure 5.2	10 µm^2	0.6 pF	0.38 pC	60 µs	68 ms
GNP-2# in Figure 5.4	21 µm^2	1.26 pF	0.79 pC	126 µs	46 ms
GNP-3# in Figure 5.5	27 µm^2	1.62 pF	1.02 pC	162 µs	103 ms

In order to obtain a better view of the potential contribution of charging to the current response, we shaded in Figure 5.8 the charge calculated in Table 5.1. The hypothetical capacitive charge only accounts for less than half or one-third of the total charge in the initial current increase. More experiments with a

fast temporal solution (1 ms) will be performed to obtain more details in the rising part of the current response.

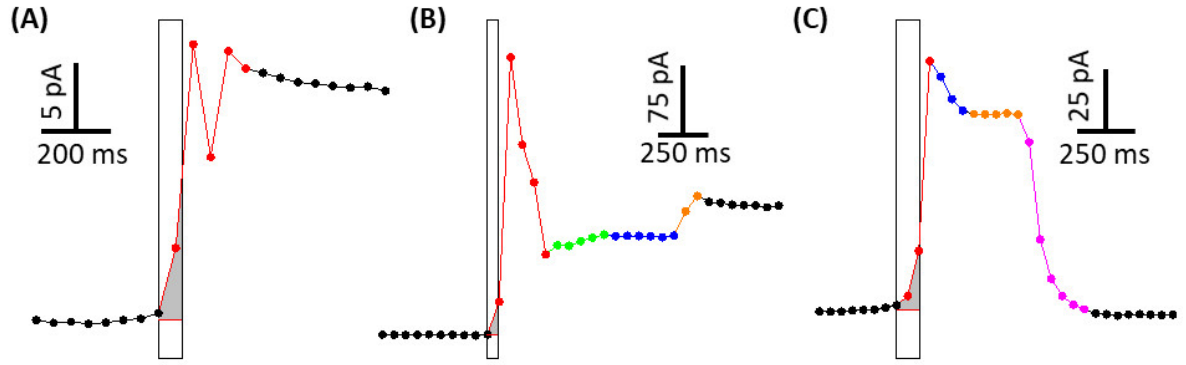

Figure 5.8. Integration of charge (gray color) collected at the initial period of fast current increase for various GNPs, for instance (A) GNP-1# shown in Figure 5.2, (B) GNP-2# shown in Figure 5.4 and (C) GNP-3# in Figure 5.5Figure 5.5. The integration of charge for these GNPs is summarized in Table 5.1. The time necessary to pass the calculated charge (i.e., the time from the beginning to the end of the shaded region) is 68 ms, 46 ms and 103 ms for GNP-1#, GNP-2# and GNP-3#, respectively.

5.4 Conclusion

In this chapter, correlated opto-electrochemical measurements allow insight into complex current transients. During the initial landing process, capacitance charging is not the only factor contributing to the current response rises. Once the GNP touches the surface of Pt, the transient current responses come from the instantaneous increase in the electroactive surface area of GNP. Importantly, the rotation of GNP will cause changes in current. The increased steady-state current plateau is attributed to permanent adsorption of GNPs at the perimeter of the surface of Pt, resulting from the increase in the total effective electroactive surface. A perspective to this work is to use numerical simulations to compare the current transients with the motion of the GNP observed on the videos.

5.5 Reference

1. Novoselov, K. S.; Geim, A. K.; Morozov, S. V.; Jiang, D.; Zhang, Y.; Dubonos, S. V.; Grigorieva, I. V.; Firsov, A. A., Electric field effect in atomically thin carbon films. *science* **2004,** *306* (5696), 666-669.

2. Neto, A. C.; Guinea, F.; Peres, N. M.; Novoselov, K. S.; Geim, A. K., The electronic properties of graphene. *Reviews of modern physics* **2009,** *81* (1), 109.

3. Balandin, A. A., Thermal properties of graphene and nanostructured carbon materials. *Nature materials* **2011,** *10* (8), 569-581.

4. Zhu, Y.; Murali, S.; Cai, W.; Li, X.; Suk, J. W.; Potts, J. R.; Ruoff, R. S., Graphene and graphene oxide: synthesis, properties, and applications. *Advanced Materials* **2010,** *22* (35), 3906-3924.

5. Frank, I.; Tanenbaum, D. M.; van der Zande, A. M.; McEuen, P. L., Mechanical properties of suspended graphene sheets. *Journal of Vacuum Science & Technology B: Microelectronics and Nanometer Structures Processing, Measurement, and Phenomena* **2007,** *25* (6), 2558-2561.

6. Kavan, L.; Yum, J. H.; Grätzel, M., Optically transparent cathode for dye-sensitized solar cells based on graphene nanoplatelets. *ACS nano* **2011,** *5* (1), 165-172.

7. Han, J.; Zhang, L. L.; Lee, S.; Oh, J.; Lee, K.-S.; Potts, J. R.; Ji, J.; Zhao, X.; Ruoff, R. S.; Park, S., Generation of B-doped graphene nanoplatelets using a solution process and their supercapacitor applications. *ACS nano* **2013,** *7* (1), 19-26.

8. Liu, L.; Ryu, S.; Tomasik, M. R.; Stolyarova, E.; Jung, N.; Hybertsen, M. S.; Steigerwald, M. L.; Brus, L. E.; Flynn, G. W., Graphene oxidation: thickness-dependent etching and strong chemical doping. *Nano Letters* **2008,** *8* (7), 1965-1970.

9. Ju, M. J.; Jeon, I.-Y.; Kim, H. M.; Choi, J. I.; Jung, S.-M.; Seo, J.-M.; Choi, I. T.; Kang, S. H.; Kim, H. S.; Noh, M. J., Edge-selenated graphene nanoplatelets as durable metal-free catalysts for iodine reduction reaction in dye-sensitized solar cells. *Science advances* **2016,** *2* (6), e1501459.

10. Liu, X.; Antonietti, M., Moderating black powder chemistry for the synthesis of doped and highly porous graphene nanoplatelets and their use in electrocatalysis. *Advanced Materials* **2013,** *25* (43), 6284-6290.

11. Jeon, I. Y.; Zhang, S.; Zhang, L.; Choi, H. J.; Seo, J. M.; Xia, Z.; Dai, L.; Baek, J. B., Edge-selectively sulfurized graphene nanoplatelets as efficient metal-free electrocatalysts for oxygen reduction reaction: the electron spin effect. *Advanced Materials* **2013,** *25* (42), 6138-6145.

12. Min Song, S.; Yong Kim, T.; Jae Sul, O.; Cheol Shin, W.; Jin Cho, B., Improvement of graphene–metal contact resistance by introducing edge contacts at graphene under metal. *Applied Physics Letters* **2014,** *104* (18), 183506.

13. Krittayavathananon, A.; Li, X.; Batchelor-McAuley, C.; Sawangphruk, M.; Compton, R. G., Electrolyte-Induced Electrical Disconnection between Single Graphene Nanoplatelets and an Electrode. *The Journal of Physical Chemistry Letters* **2018,** *9* (19), 5822-5826.

14. Chen, L.; Tanner, E. E.; Lin, C.; Compton, R. G., Impact electrochemistry reveals that graphene nanoplatelets catalyse the oxidation of dopamine via adsorption. *Chemical science* **2018,** *9* (1), 152-159.

15. Poon, J.; Batchelor-McAuley, C.; Tschulik, K.; Compton, R. G., Single graphene nanoplatelets: capacitance, potential of zero charge and diffusion coefficient. *Chemical science* **2015,** *6* (5), 2869-2876.

16. Ma, H.; Chen, J.-F.; Wang, H.-F.; Hu, P.-J.; Ma, W.; Long, Y.-T., Exploring dynamic interactions of single nanoparticles at interfaces for surface-confined electrochemical behavior and size measurement. *Nature communications* **2020,** *11* (1), 1-9.

17. Fang, Y.; Wang, W.; Wo, X.; Luo, Y.; Yin, S.; Wang, Y.; Shan, X.; Tao, N., Plasmonic imaging of electrochemical oxidation of single nanoparticles. *Journal of the American Chemical Society* **2014,** *136* (36), 12584-12587.

18. Hao, R.; Fan, Y.; Zhang, B., Imaging Dynamic Collision and Oxidation of Single Silver Nanoparticles at the Electrode/Solution Interface. *Journal of the American Chemical Society* **2017,** *139* (35), 12274-12282.

19. Ma, W.; Ma, H.; Chen, J.-F.; Peng, Y.-Y.; Yang, Z.-Y.; Wang, H.-F.; Ying, Y.-L.; Tian, H.; Long, Y.-T., Tracking motion trajectories of individual nanoparticles using time-resolved current traces. *Chemical science* **2017,** *8* (3), 1854-1861.

20. Brasiliense, V.; Patel, A. N.; Martinez-Marrades, A.; Shi, J.; Chen, Y.; Combellas, C.; Tessier, G.; Kanoufi, F., Correlated Electrochemical and Optical Detection Reveals the Chemical Reactivity of Individual Silver Nanoparticles. *Journal of the American Chemical Society* **2016,** *138* (10), 3478-83.

21. Fosdick, S. E.; Anderson, M. J.; Nettleton, E. G.; Crooks, R. M., Correlated Electrochemical and Optical Tracking of Discrete Collision Events. *Journal of the American Chemical Society* **2013,** *135* (16), 5994-5997.

22. Xiao, X.; Bard, A. J., Observing single nanoparticle collisions at an ultramicroelectrode by electrocatalytic amplification. *Journal of the American Chemical Society* **2007,** *129* (31), 9610-9612.

23. Xiao, X.; Fan, F.-R. F.; Zhou, J.; Bard, A. J., Current transients in single nanoparticle collision events. *Journal of the American Chemical Society* **2008,** *130* (49), 16669-16677.

24. Sun, T.; Wang, D.; Mirkin, M. V., Electrochemistry at a single nanoparticle: from bipolar regime to tunnelling. *Faraday Discussions* **2018,** *210*, 173-188.

25. Bellew, A. T.; Manning, H. G.; Gomes da Rocha, C.; Ferreira, M. S.; Boland, J. J., Resistance of single Ag nanowire junctions and their role in the conductivity of nanowire networks. *ACS nano* **2015,** *9* (11), 11422-11429.

26. Zou, Y.; Walton, A. S.; Kinloch, I. A.; Dryfe, R. A., Investigation of the differential capacitance of highly ordered pyrolytic graphite as a model material of graphene. *Langmuir* **2016,** *32* (44), 11448-11455.

27. Bianchi, H.; Corti, H.; Fernandez-Prini, R., Electrical conductivity of aqueous sodium hydroxide solutions at high temperatures. *Journal of Solution Chemistry* **1994,** *23* (11), 1203-1212.

28. Oldham, K. B., Theory of microelectrode voltammetry with little electrolyte. *Journal of Electroanalytical Chemistry and Interfacial Electrochemistry* **1988,** *250* (1), 1-21.

6. Chapter 6 Conclusion and highlights

In the first and second part of this dissertation, we worked on improving the electro-analytical performance of electrochemical blocking for single entity detection. In chapter 3, we reported that the use of hemispherical UMEs enables simultaneous measurements of the concentration and the size distribution of individual insulating particles in suspension. In chapter 4, a new strategy (electro-catalytic depression) is established to detect individual conducting carbonaceous particles. In chapter 5, we couple electrochemistry and bright-field microscopy to elucidate how the translation and rotation of GNPs affect the current response.

(i) Hemispherical Hg UMEs

Owing to the existence of inhomogeneous flux of redox reporter on disk UMEs (edge effect), a bead landing on the perimeter of the disk produces current steps about four to seven times higher than a bead (of similar dimensions) landing on the center. This difference poses a problem when measuring the size of a bead. In order to suppress the edge effect, we described the use of hemispherical UMEs to detect individual polystyrene beads by electrochemical blocking. We evidenced that the shape of the UME has considerable importance on the size distribution of the current steps. Importantly, the effect of the geometry of the UME on the step size was thoroughly analyzed by numerical simulations, and we showed that the edge effect encountered on disk-shaped UMEs is significantly reduced on hemispherical electrodes. The average size of polystyrene beads of 0.5 and 1 μm radius found by electrochemistry and SEM differs within less than 10% of error, but the relative difference is negative and similar for the two sizes of the bead. The size distribution of the 0.5 μm radius bead was also correctly determined, while a large deviation is observed for the 1 μm radius beads. We conclude that apart from the edge effect, there exists a second bias that tends to overestimate the small current steps. We exclude the hypothesis of the variability on the radius of Hg hemisphere (at most 25%), the uncertainties on the values of α and β in our model (that affect the symmetry of the distribution but not its width), as well as the formation of multilayers (see Appendix section 1.3). At this moment, the origin of the broadening is not identified.

Besides, the total concentration of beads found by electrochemistry within less than 10% of error for both the 0.5 and 1 μm radius beads. We believe that the quantitative analytical method presented in this work can offer a useful alternative to optical techniques incompatible with opaque samples. The next challenges to be addressed would be the replacement of Hg by another metal, less toxic, and more stable at anodic potentials, as well as the multiplexing of several UMEs of different sizes in order to widen the dynamic range of bead size detectable with one device.

(ii) The strategy of electro-catalytic depression

In chapter 4, we report a strategy, electro-catalytic depression, based on the intrinsic difference electron transfer kinetics between materials to detect particles that are electrically conducting but catalytically inert, such as carbonaceous particles. We show this new strategy with the detection of individual graphene nanoplatelets of a few μm in length suspended at the concentration of 35 fM. Over tens of individual measurements, more than 90% of the collisions lead to the irreversible adsorption of the GNP on the Pt surface. We evidence that, under 0.1 V vs. Ag/AgCl, electrically conducting GNPs produce discrete negative current steps. These negative current steps can be analyzed based on models already developed for insulating particles. As the potential increases (> 0.1 V vs. Ag/AgCl), where hydrazine oxidation occurs on the GNP, the variation of current step magnitude as a function of the

potential can be rationalized concerning the intrinsic difference in kinetics between the electrode and GNPs. This opens opportunities to measure the kinetics of catalysis on particles in suspension with good statistics and without having to deposit films or use nanoprobes. We also show that despite measuring well-defined current signals (staircase-shape, low noise), a large dispersion of size and shape of the GNP, the poor stability of the GNP suspension, interactions between GNPs adsorbed on the electrode and the edge effect should be carefully considered before attempting any quantitative analysis of the data.

At high potentials (≥ 0.7 V vs. Ag/AgCl), both positive and negative current responses are observed. At this moment, two factors need to be considered, the area of GNP confined in the electrode surface and laying on the glass sheath. The confined area of GNP produces decreasing current responses due to the difference in kinetics between GNP and Pt, while the area of GNP laying outside can generate hydrazine oxidation and produce increasing current responses. We evidence that the average of negative current steps decreases with increasing potentials, while the average magnitude of positive current steps increases with increasing potentials. Owing to lack of optical position information of GNP colliding at the surface of GNP, many issues, the kinetics of GNP versus the bias potential and the origin of large current step distribution as well as average magnitudes, is still unknown. Simultaneous otpo-electrochemical measurements might help to unravel this mystery.

(iii) Correlated opto-electrochemical measurements

In chapter 5, we used correlated opto-electrochemical measurements to elucidate the dynamic motions of GNPs (30 nm in thickness) at the surface of UME. This work originates from interesting complex current transients during GNP collisions at high potentials where blocking is not the mechanism producing the current signal. An outer-sphere reaction, FcMeOH oxidation, is used to investigate dynamic motions of GNP. We used bright-field microscopy to perform real-time monitoring of the motion of GNPs during the oxidation of ferrocenemethanol. Optical microscopy provides the size of GNP, morphology, location of the GNP on the surface of the UME and movement (rotation and translation) at the surface of UME.

We showcase complex current responses and proposed based on the video hypothesis regarding the shape of the current transient. Once the GNP touches the surface of Pt, the transient current responses come from the instantaneous increase in the total electroactive surface area (surface of Pt and GNP exposed to solution). Importantly, the rotation of GNP will cause changes in current transients. The increased steady-state current plateau is attributed to permanent adsorption of GNPs at the perimeter of the surface of Pt, resulting from the increase in the total effective electroactive surface.

Correlated opto-electrochemical measurements with fast temporal resolution can help to capture more position information to better understand the mechanism of current transients, although high temporal resolution will produce large background noise. An alternative way is to increase the viscosity of the solution to slow down the GNP movement. Another perspective is to this work is to use numerical simulations to compare the current transients with the motion of the GNP observed on the videos.

1. Appendix

A.1 Numerical simulations for PSB colliding on hemispherical UMEs

The numerical simulations were performed with a finite element simulation package, COMSOL 4.4, installed on a PC equipped with 16 GB of RAM and an Intel Core i5 processor of 2.70 GHz.

A. 1.1 Estimation of the step size

The step size was estimated by simulating the steady-state current of $Ru[NH_3]_6^{3+}$ reduction at a Hg hemispherical UME in the absence and presence of an insulating bead. In order to reach a sufficient precision for the determination of small relative variation of current (‰), we performed the simulation in a 2D axial geometry with the bead positioned on the top of the hemisphere. As discussed in Section 3.1 in Chapter 3, all positions on the hemisphere are equivalent, and thus it is advantageous to place the bead on top of the electrode to increase the symmetry of the model. Figure S1.1 shows the geometry of the bead/electrode system.

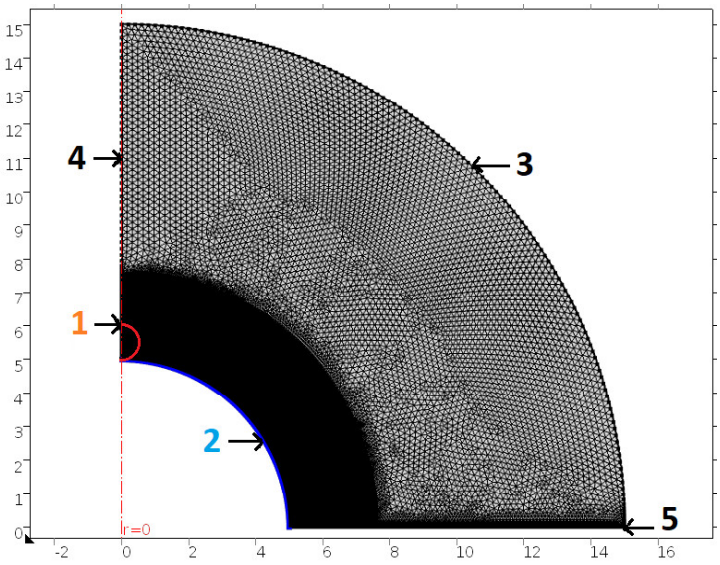

Figure S1.1. 2D axial simulation of a hemispherical electrode (delimited by the blue line) with a bead (red line) sitting on top. The mesh is refined near the electrode surface and the bead where the gradient of concentration is the highest. The lengths are in µm. The radii of the bead and the electrode are 1 and 5 µm, respectively. Near the bead the mesh has a size of about 0.02 µm.

Briefly, we applied concentration boundaries on the electrode (boundary 2) and the wall of the cell (boundary 3) in order to simulate the concentration profile of $Ru[NH_3]_6^{3+}$ when a mass transfer limited steady-state condition is reached. The diffusion of $Ru[NH_3]_6^{3+}$ inside the cell is described by the second Fick's law. The glass sheath (boundary 5), the revolution axis (boundary 4), and the bead (boundary 1) have a no flux boundary. All the boundaries are given in Table S1. The current is obtained by integrating the flux of $Ru[NH_3]_6^{3+}$over boundary 2 in a revolved geometry.

Three crucial innovations were implemented in our simulation. In order to keep the number of elements in the simulation to a reasonable amount (< 100,000), we reduced the size of the cell as much as possible. The following strategy was employed. First, we simulated without bead but with a large

enough cell (50 times the size of the electrode) in order to obtain the concentration profile of $Ru[NH_3]_6^{3+}$ being reduced at a mass transfer limited regime. In this simulation, the walls of the cell are sufficiently far so that the diffusion layer does not reach them. From this simulation, we determined accurately the concentration of $Ru[NH_3]_6^{3+}$ at a distance of three times the radius of the electrode. At this distance, the concentration of $Ru[NH_3]_6^{3+}$ dropped to about two-thirds of its bulk concentration. Then, we made a first simulation where a bead is positioned on top of the Hg hemisphere, and the cell has a size of three times the electrode radius, as explained before a concentration boundary is applied to the wall of the cell. The concentration of $Ru[NH_3]_6^{3+}$ is set to two-thirds of its bulk value, as determined with the previous simulation. Hence, we can drastically reduce the size of the cell (250 µm to 15 µm). Importantly, the size of the bead is much smaller than the size of the electrode, and thus, the perturbation it produces on the diffusion layer does not propagate further than a few times the radius of the bead and does not reach the wall of the cell. The quality of the mesh was estimated by carrying out several simulations and changing the size of the mesh. When the current was found to not change significantly (less than the experimental uncertainty, 0.2 ‰) with the size of the mesh, then we selected this size. As evidenced in Figure S1.1, the mesh is refined near the bead and the surface of the electrode in order to increase the precision of the simulation.

Table S1. Boundary conditions corresponding to the model shown in Figure S1.1.

Boundary	**1**		**2**	**3**	**4**	**5**
Condition	no bead	bead	$C = 0$	$C = C^0$	$dC/dr = 0$	$dC/dr = 0$
	none	$dC/dr = 0$				

Another essential feature of the simulation is a constant mesh of whether or not the particle is present. Simulations are extremely sensitive to the meshing, and thus it is crucial to not modify the mesh between the simulations in the absence and presence of the bead. To do so, we used the “thin impermeable layer” boundary. This boundary is a no flux boundary that can be applied to surface boundaries located inside the volume of the simulation. First, we draw the bead and do not specify any boundary on the surface of the bead. Thus, the bead is entirely transparent to the diffusion of $Ru[NH_3]_6^{3+}$. Then, we apply the “thin impermeable layer” boundary on the surface of the bead in order to simulate its insulating properties.

The last important feature of this simulation is the position of the bead over the surface of the electrode. In our simulation, the bead penetrates the surface by 10% of its diameter. In other words, a 0.5 µm radius bead penetrates over 100 nm inside the mercury hemisphere. This choice is motivated by two reasons. First, it was evidenced for assemblies of silica microbeads that the contact between two beads is not a point but rather a circle with a diameter of roughly 10 to 20% of the diameter of the beads.[1] This can mean that the beads are slightly flexible (as one might expect for polystyrene). Moreover, the mercury is liquid and thus can also slightly deform when in contact with a bead. The second reason motivating the overlap between the bead and the electrode is the absence of singularity or tiny elements in the simulation. These elements, typically created when a sphere is touching a surface with a single point of contact, can render the simulation unstable. We performed two simulations where the bead penetrated by 5% and 15% the electrode and found a difference of current of less than 0.1‰. Thus, we conclude that while improving the robustness of the simulation, the positioning of the bead slightly inside the electrode does not affect the determination of the step size within the precision of our measurements (0.2‰).

A. 1.2 Electrode/sheath boundary

Because the beads have a finite size, they cannot adopt the position depicted in green in Figure S1.2A but have to be above the glass sheath, as shown in red in Figure S1.2A. Thus, a bead located at the edge of the electrode is not perfectly equivalent in terms of symmetry to a bead located on top of the UME. In order to estimate the possible impact of this asymmetry on the step size, we performed numerical

simulations in a 3D geometry with a bead located far from the sheath (φ = 45° in Figure S1.2A) and a bead in contact with both the sheath and the electrode. For this bead, the value of φ is given by:

$$\varphi = \sin^{-1}\left(\frac{0.9b}{0.9b + a}\right) \qquad \text{Eq. S1}$$

where a and b are the radii of the electrode and the bead, respectively. The factor of 0.9 comes from the slight penetration of the bead in the material. For a 0.5 µm radius bead and a 5 µm radius electrode, the value of φ is 8.8°. The simulated system is shown in Figure S1.2B. A procedure similar to the 2D simulations was adopted. For both the 0.5 and 1 µm radius beads, we found that the step size is not affected by the position of the bead within the precision of the simulation (0.2‰).

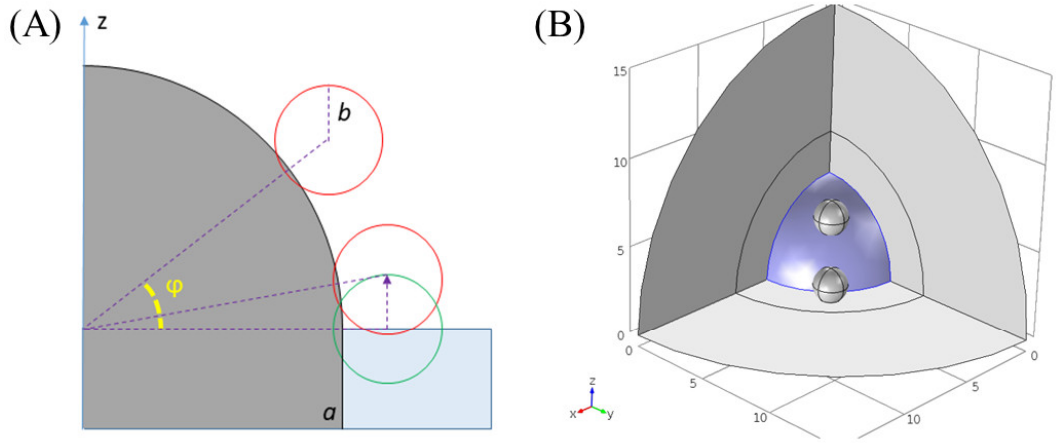

Figure S1.2. (A) The consequence of the finite size of the bead on its position at the electrode/sheath contact. A minimum azimuthal angle, phi, is present, and the proximity of the glass sheath breaks the symmetry locally. (B) 3D simulation of a quarter of a hemispherical electrode (blue surface) with one bead sitting at the electrode/glass sheath junction (φ =8.8°) and another bead at φ =45°.

Hence, we can consider that all the possible positions of a bead on the hemisphere are equivalent in terms of the current step size.

A. 1.3 Step size vs. Bead-to-bead distance

Eventual interaction between the diffusion layers of the redox reporter around the two beads can lead to a current step size that is different from two beads far apart from each other. The goal of this simulation is to estimate how and under what condition such interaction affects the current step size. The simulation was performed in 3D, and a steady-state solution of second Fick's law was computed in the absence and presence of the beads. The main challenge in 3D simulation is to keep the number of elements in the mesh below a reasonable value (1.6 million represents the upper limit for our computer having 4 Go of RAM). As shown in Figure S1.3A, only half of the hemispherical UME is simulated to reduce the number of elements in the mesh. Two beads of 1 µm radius are positioned at 45° from the glass sheath (and the mirror plane) to keep the boundaries as far as possible from the beads. The beads are penetrating the surface of the UME by 10% of their diameter (i.e., 0.2 µm of the beads is buried in the UME) in order to reduce the singularity at the point of contact. The concentration of the redox reporter at the surface of the UME is set to zero. Thus, the flux at the UME surface is the highest (red color in Figure S1.3A). The presence of the bead is simulated by adding a no flux boundary on the surface of the bead while keeping the mesh of the surface and the interior of the bead (these simulations are extremely mesh-dependant and the mesh should not be altered between the calculation of the steady-state current in the absence and presence of the bead). In the absence of the bead, no boundary is applied on the surface of the bead and this latter is "transparent" to the diffusion of the redox molecule. Because we are looking for a difference between two steady-state solutions that is itself proportional to the steady-state solution (in the absence of bead), we can use any value of concentration at the bulk boundary

(i.e., increasing the concentration in the cell and thus the initial current does not change the relative step size). In practice, the pseudo-bulk solution is position at 5 µm from the UME surface and a concentration of 100 mM of redox species (D = 6.7 x 10^{-6} cm^2/s) is used. The mesh is especially refined near the beads by reducing the maximum element size down to 130 nm in the volume of a torus having twice the bead diameter and enveloping the two beads. Despite these refinements, the solutions found in 3D are accurate to about 0.1 % at best.

The relative step size found for two beads separated by 0.1, 0.5, 1 and 2 diameters from each other are shown in Figure S1.3B. These relative step sizes are divided by half of the relative step size simulated with 2 bead diameters between the beads. This quantity represents a deviation from the response of two independent beads. Figure S1.3B shows that the relative step size increases as the beads are closer to each other. When beads are separated by 0.2 µm we calculate an increase of 7% of the relative step size compared to a situation for independent beads. An examination of the flux between the beads (not shown) reveals a drop as if the two beads were equivalent to an ovoidal bead. The increase of the relative step size seems to be in contradiction with previous observations.[2] However, the decrease of relative step size is experimentally evidenced only for a very large amount of bead (equivalent to multiple compact layers) while we are simulating only two beads. It would thus be hazardous to compare these two situations.

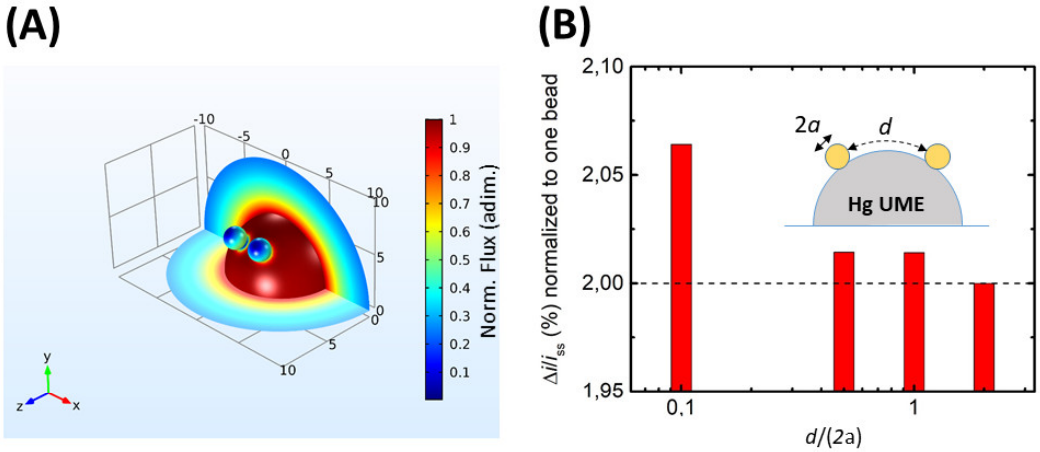

Figure S1.3. (A) Normalized flux calculated for two insulating 1 µm radius beads blocking the oxidation of RuHex on a 5 µm radius hemispherical UME. The glass sheath is in the xOz plane while the yOx plane is a mirror plane. (B) Normalized current step-size simulated for different bead-to-bead separations. The normalized step size is divided by half of the normalized step size for two beads at 4 µm from each other (considered to be two independent beads)

A.2 Derivation of the flux of beads on a hemispherical UME

In the absence of convection, the flux of bead at the electrode, j_{bead}, is governed by the following equation:[3]

$$j_{bead} = D_{bead}\left(\frac{\partial C_{bead}}{\partial r}\right)_{surface} + \mu_{bead} C_{bead}\left(\frac{\partial \varphi}{\partial r}\right)_{surface} \qquad \text{Eq. S2}$$

where D_{bead} is the diffusion coefficient of the bead, C_{bead} is the concentration of bead, μ_{bead} is the mobility of the bead, and φ is the electric potential. The quantity j_{bead} can be separated into two contributions, a diffusion term (j_{dif}) and a migration term (j_{mig}). Because of the spherical symmetry of the problem, the flux has to be constant over the entire surface of the UME, and thus the current of beads equals to:

$$i_{bead} = \int_0^{2\pi}\left(\int_0^{\frac{\pi}{2}}(j_{dif} + j_{mig}) r_{elec}\cos(\theta)\, d\theta\right) d\varphi \qquad \text{Eq. S3}$$

$$= 2\pi r_{elec}(j_{dif} + j_{mig})$$

$$= i_{dif} + i_{mig}$$

In the next section, we will give the expression of these two terms in order to estimate the steady-state current of the bead (i_{bead}) as a function of the concentration, size and zeta potential of the beads as well as parameters independent of beads (e.g., salt concentration, redox reporter concentration). For the sake of convenience, we will transform current into the frequency of experimentally observable collision.

A. 2.1 Diffusion of bead

For a redox couple, the steady-state current at a hemispherical UME is given by:[4]

$$i_{ss} = 2\pi n F D_{redox} C_{redox} r_{elec} \qquad \text{Eq. S4}$$

where n is the number of electrons exchanged per molecule, F is the Faraday constant, D_{redox} is the diffusion coefficient of the redox molecule, C_{redox} is the bulk concentration of the redox molecule, and r_{elec} is the radius of the electrode. If we consider a frequency of collision (1 collision ⇔ 1 step) of bead, f_{bead} (in collision per second), it is possible to rewrite Eq. S4 as:

$$f_{bead}^{dif} = 2\pi N_a D_{bead} C_{bead} r_{elec} \qquad \text{Eq. S5}$$

The Eq. S5 holds only if the boundary conditions for the beads are similar to the boundary conditions for the redox reporter. Beads must adsorb irreversibly on the electrode surface while not adsorb *at all* on the glass sheath. These conditions can be expressed as:

$$C_{bead} = 0 \qquad \text{for} \qquad 0 < r < r_e \qquad \text{Eq. S6}$$

$$\left(\frac{\partial C_{bead}}{\partial r}\right)_{z=0} = 0 \qquad \text{for} \qquad r_{elec} < r \qquad \text{Eq. S7}$$

A representation of the system with the different boundary conditions is shown in Figure S1.4.

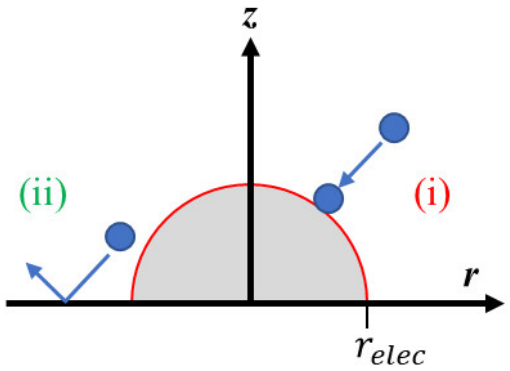

Figure S1.4. Boundary conditions for the beads colliding at the hemispherical UME. Beads irreversibly adsorb on the electrode (i) while they rebound on the glass sheath (ii).

As shown in Figure 3.4C in Chapter 3, the examination of the glass sheath surrounding the electrode with optical microscopy did not reveal any significant adsorption of the polystyrene beads on the glass. Hence, the boundary conditions used in our model are verified.

A. 2.2 Migration of bead

As discussed by Quinn et al., the flux of bead at the electrode is given by[5]

$$f_{bead}^{mig} = \frac{i_{ss} C_{bead} \mu_{bead}}{e} \sum \frac{1}{C_i \mu_i} \qquad \text{Eq. S8}$$

where e, μ, and C are the elementary charge, mobility, and concentration, respectively. The species "i" are all the ions excepted the beads. Eq. S8 indicates that the beads carry only a fraction of the total current passing through the solution. This fraction is proportional to their mobility (and hence radius) as well as their charge.

A. 2.3 Collision frequency as a function of bead size

The diffusion coefficient of the bead is related to its radius by the Stokes-Einstein relation:

$$D_{bead} = \frac{kT}{6\pi\eta r_{bead}} \quad \text{Eq. S9}$$

where k, T, and η are the Boltzman constant, the temperature, and the dynamic viscosity of the solvent, respectively. The larger is a bead, and the slower it diffuses. The mobility of the bead is defined by the Einstein-Smoluchowski equation:

$$\mu_{bead} = \frac{z_{bead} D_{bead}}{kT} \quad \text{Eq. S10}$$

where z_{bead} is the charge of a bead. For a particle much larger than the Debye length, the charge density σ_{bead} on its surface can be considered constant for any given size and thus the total charge on a bead is merely proportional to its surface:

$$z_{bead} = \sigma_{bead} 4\pi r_{bead}^2 \quad \text{Eq. S11}$$

Combining Eqs. S10 and S11 give the mobility as a function of the radius of the bead:

$$\mu_{bead} = \frac{2\sigma_{bead} r_{bead}}{3\eta} \quad \text{Eq. S12}$$

The mobility increases linearly with the size of the bead. It is noteworthy that diffusion and migration show the opposite trend with the size of the bead. While diffusion favors small particles, migration favors large ones. Hence, it is vital to separate the two contributions in order to count particles of different size accurately. The final collision frequency can be expressed as:

$$f_{bead} = 2\pi N_a r_{elec} C_{bead} \left(\frac{\alpha}{r_{bead}} + \beta r_{bead} \right) \quad \text{Eq. S13}$$

with

$$\alpha = \frac{kT}{6\pi\eta} \quad \text{Eq. S14}$$

$$\beta = D_{redox} C_{redox} \frac{2\sigma_{bead}}{3\eta} \sum \frac{1}{C_i \mu_i} \quad \text{Eq. S15}$$

The Eq. S13 allows estimating the relative contribution of diffusion and migration to the total steady-state current of the bead. This equation can be used to weigh the frequency of collision as a function of the bead size for a given set of experimental parameters (Eqs. S14 and S15) and hence access to the value of C_{bead}.

A.3 Determination of the pKa of the amine-functionalized beads

The *pKa* of the amine groups covering the surface of the PSB was determined by measuring the ζ-potential of the beads at different values of pH. Briefly, five solutions of 1 µm diameter amine-functionalized polystyrene beads (25 fM) dispersed in Britton-Robinson buffer (ionic strength ≈ 5 mM) of various pH (3, 5, 7, 9 and 11) were analyzed by Dynamic Light Scattering to determine their ζ-potential. For each solution, the size of the amine-PSB was measured right before the ζ-potential in order to ensure that the particles do not aggregate. The solutions were also sonicated for 5 min right before measuring the ζ-potential. The ζ-potential is plotted as a function of the bulk pH in Figure S1.5 (black dots). The value of ζ-potential and the percentage of protonation of the amines are related as follows. The surface charge of the amine-functionalized polystyrene beads depends on the protonation of the amine groups as described by the acido-basic reaction:

$$\text{bead-NH}_2 + \text{H}^+ \Leftrightarrow \text{bead-NH}_3^+ \quad \text{Eq. S16}$$

with the adsorption constant K_a defined as:

$$K_a = \frac{\Gamma_{\mathrm{NH_3}^+}}{\Gamma_{\mathrm{NH_2}}[\mathrm{H}^+]_{surface}} \quad \text{Eq. S17}$$

where $\Gamma_{\mathrm{NH_2}}$, $\Gamma_{\mathrm{NH_3}^+}$ and $[\mathrm{H}^+]_{surface}$ are the surface concentration of deprotonated and protonated amine, and the volume concentration of protons near the surface, respectively. The Eq. S17 can be rewritten as a function of the protonation ratio, θ, of the amine groups:

$$\theta = \frac{\Gamma_{\mathrm{NH_3}^+}}{\left(\Gamma_{\mathrm{NH_2}} + \Gamma_{\mathrm{NH_3}^+}\right)} = \frac{K_\mathrm{a}[\mathrm{H}^+]_{surface}}{1 + K_\mathrm{a}[\mathrm{H}^+]_{surface}} \quad \text{Eq. S18}$$

This expression, similar to a Langmuir isotherm, can be related to the surface charge density by the following equation:

$$\sigma_{bead} = N_a e\left(\Gamma_0 + \Gamma_{\mathrm{NH_3}^+}\right) \quad \text{Eq. S19}$$

with Γ_0 being surface charges that are not related to amine groups (this charge account for the non-null zeta potential measured on bare polystyrene beads). The charge at the surface of the bead can be related to the potential at the outer Helmholtz plane (that we consider being the shear plane location) and thus the zeta potential by the following equation:[6]

$$\sigma_{bead} = \sqrt{8\varepsilon_r\varepsilon_0 kTN_a C}\,\sinh\left(\frac{z_a e\xi}{2kT}\right) \quad \text{Eq. S20}$$

If we note $\sigma_{bead}^{max} = N_a e\left(\Gamma_0 + \Gamma_{\mathrm{NH_2}} + \Gamma_{\mathrm{NH_3}^+}\right)$ and define a charge coverage $\sigma_{bead}/\sigma_{bead}^{max} = \theta_{charge}$ then:

$$\frac{\sigma_{bead}}{\sigma_{bead}^{max}} = \frac{\sinh\left(\frac{z_a e\xi}{2kT}\right)}{\sinh\left(\frac{z_a e\xi^{max}}{2kT}\right)} = \frac{K_\mathrm{a}[\mathrm{H}^+]_{surf}}{1 + K_\mathrm{a}[\mathrm{H}^+]_{surf}} \quad \text{Eq. S21}$$

The Eq. S21 can be rewritten as a function of pH_{surf} and pKa:

$$\sinh\left(\frac{z_a e\xi}{2kT}\right) = A\frac{10^{pKa-pH_{surf}}}{1 + 10^{pKa-pH_{surf}}} \quad \text{Eq. S22}$$

with $A = \sinh\left(\frac{z_a e\xi^{max}}{2kT}\right)$. Noticing that $\sinh^{-1}(x) = ln\left(x + \sqrt{1 + x^2}\right)$ one can obtain:

$$\xi = \frac{2kT}{z_a e}\ln\left(A\frac{10^{pKa-pH_{surf}}}{1 + 10^{pKa-pH_{surf}}} + \sqrt{1 + \left(A\frac{10^{pKa-pH_{surf}}}{1 + 10^{pKa-pH_{surf}}}\right)^2}\right) \quad \text{Eq. S23}$$

The Eq. S23 establishes the relation between ζ-potential and pH near the surface of a bead. However, the relevant parameter that is varied during our experiment is the bulk pH that can differ significantly from the surface pH.[7] In order to take into account the effect of the electrostatic potential on the concentration of the protons nearby the surface, we calculated the potential at the surface of the bead, ϕ_{surf}, using:[6]

$$\phi_{surf} = \frac{2kT}{e}\sinh^{-1}\left(\frac{\sigma_{bead}}{\sqrt{8\varepsilon_r\varepsilon_0 kTC_{redox}}}\right) \quad \text{Eq. S24}$$

Then, we used a Boltzman distribution to estimate the bulk pH corresponding to a given surface pH:

$$pH_{bulk} = pH_{surf}e^{\frac{e\phi_0}{kT}} \quad \text{Eq. S25}$$

In addition to the shift of surface pH, we added another element to our model. We used a Gaussian distribution of *pKa* to represent variability in the local environment of the amine groups.

$$pKa = \frac{1}{SD_{pKa}\sqrt{2\pi}}e^{-\frac{1}{2}\left(\frac{pH-\overline{pKa}}{SD_{pKa}}\right)^2} \quad \text{Eq. S26}$$

The distribution is centered on an average value $\overline{pKa}$ with a standard deviation SD_{pKa}. This Gaussian distribution of *pKa* introduces a broadening of the ζ-potential/pH curve necessary to describe correctly the experimental data (cf. caption in Figure S1.5).

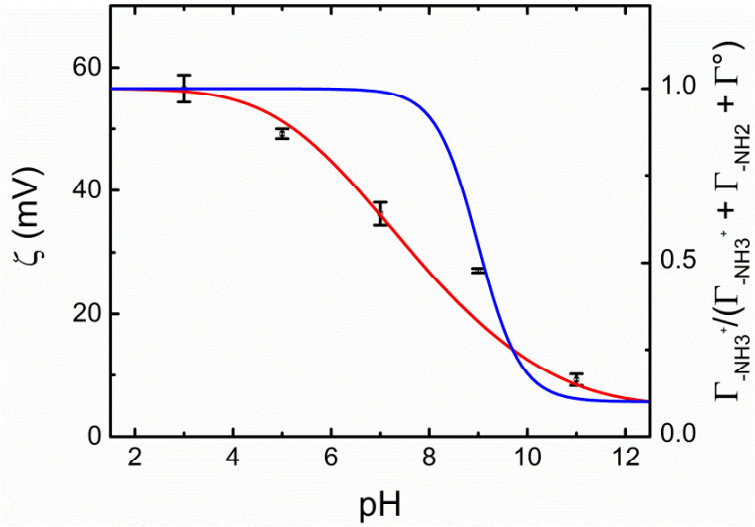

Figure S1.5. Titration curve of the amine groups at the surface of the 1 µm diameter amine-functionalized polystyrene beads as a function of the bulk pH. The error bars correspond to the standard deviation from three measurements. The blue curve corresponds to a standard sigmoidal titration curve. The red line is a titration curve corrected from the pH shift between bulk and surface (Eq. S25) and comprising a Gaussian-shaped distribution (Eq. S26) of *pKa* with an average *pKa* = 9.5 and a standard deviation of 1.5.

A series of titration curves were simulated (using an in-house code in Matlab 2017b), and the parameters were manually adjusted on the experimental data until a good agreement was obtained. The red curve in Figure S1.5 and the set of parameters given in Table S1.1correspond to our best fit of the experimental data (black dots in Figure S1.5). An average *pKa* of 9.5 is measured for the amine groups at the surface of the bead with a Gaussian distribution and taking into account local change of pH at the surface. Note that it corresponds to an apparent *pKa* of 7.9 (half-wave pH in Figure S1.5). This value is relatively high compared to the *pKa* of amine-terminated self-assembled monolayers (SAM) of thiol on gold (*pKa* = 4.5).[8] However, it compares well with the *pKa* of aliphatic secondary amines in solution (typically 11).[9]

Table S1.1. Parameters used to simulate the ζ-potential/pH curve shown in red in Figure S1.5.

	Free Parameter	Fitted value
The total concentration of amine	$\Gamma_{NH_2} + \Gamma_{NH_3}+$	30 (pmol.cm^{-2})
The static concentration of charge on a bead	Γ_0	0.3 (pmol.cm^{-2})
Average *pKa* of an amine	$\overline{pKa}$	9.5
Standard deviation of *pKa*	SD_{pKa}	1.5
	Fixed parameters	**Value**
Concentration of salt (1:1)	C_{salt}	3.6 (mM)
Charge of a protonated amine	z_{amine}	+1
Charge of the salt	z_{salt}	+1/-1

In conclusion, we use an acetate buffer with a pH of 5 to ensure that the charge on the bead is constant and maximum. As explained in the article, fixing the charge is essential to estimate the flux of migration correctly.

Besides, the mobility of the amine-functionalized polystyrene beads was measured with a Zetasizer (Malvern Instruments) in an aqueous solution containing 3 mM $Ru[NH_3]_6^{3+}$ and 1 mM acetate buffer (pH = 5). Hence, we obtain for the 1 µm and 0.5 radius beads a pair of average radius and corresponding mobility. Using Eq. S20, we calculated the density of surface charge. These values are reported in Table S1.2. We used Eq. S12 and σ_{bead} to calculate the mobility for each size of bead in the distribution.

Table S1.2. Charge on the bead obtained by Zetasizer

Nominal bead radius	**0.5 µm**	**1 µm**
***r* (µm)**	0.51	0.97
μ_{bead} (m^2/V/s)*	3.2 x 10^{-8}	2.3 x 10^{-8}
σ_{bead} (µC/m^2)	100	36

* averaged over ten measurement

A.4 Numerical simulations for GNPs colliding on the Pt UME

The numerical simulation was performed with a finite element simulation package, COMSOL 4.4, installed on a PC equipped with 16 GB of RAM and an Intel Core i5 processor of 2.70 GHz. The simulation is performed in 3D, and a steady-state solution is calculated. We want to emphasize that the relative step size is not sensitive to the absolute value of the steady-state current obtained from a simulation (i.e., we could use any value of concentration and calculate currents of several A, but it would not affect the magnitude of the relative step size). The simulation only needs to describe how the diffusion layer of the UME is **locally** affected by the presence of the GNP. Thus, steady-state solutions are employed (instead of resource-intensive and, in this particular situation, useless time-dependent simulations) because the final current is itself a steady-state current, and we make sure that the perturbation of the diffusion layer by the GNP does not extend to the boundary representing the solution. Besides, only half of the UME is modeled in order to reduce the number of elements in the mesh and the duration of the calculation. Figure S1.6A shows a top view of the mesh with the UME delimited by a yellow line. The inner part of the yellow circle represents the Pt surface of the UME (domain 3 indicated by the green arrow), while the other part represents the insulating glass sheath (domain 4 indicated by the blue arrow). The mesh is thinner above the UME to achieve a better precision on the value of the current. The two red circles are two ideal disk-shaped GNPs (domains 1 indicated by the

red arrows) positioned either at the center or the edge of the UME to take into account the change of current induced by the "edge effect". In the absence of the GNP, the boundary inside the red circle is chosen to correspond to a Pt and/or glass surface. In the presence of GNP, the inside of the red circle is set to a no flux boundary. All the boundary conditions are shown in Table S1.3.

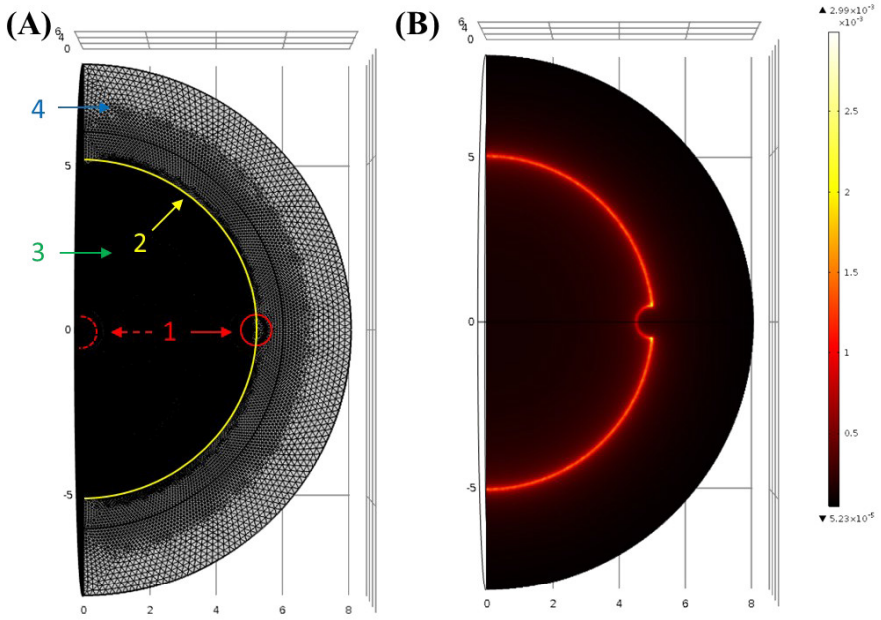

Figure S1.6**.** (A) 3D simulations of a disk electrode (region 3, indicated by the green arrow) with a small disk-shaped GNP (red circles) sitting on the edge (boundary 2) and at the center. The mesh is refined near the electrode surface where the gradient concentration is the highest. The lengths are in µm. The radii of the disk electrode and the disk-shaped GNPs are 5 µm and 0.5 µm, respectively. (B) The simulated flux of hydrazine under diffusion-limited condition. The flux is higher at the perimeter of the electrode than the center of the electrode. This simulation is made with a GNP on the edge of the UME.

The diffusion of hydrazine inside the volume of the cell is described by Fick's first law (steady-state simulation). Firstly, we simulate the mass transfer-limited oxidation of hydrazine on a bare UME (i.e., the surface within the red circle has the properties of Pt). Once the concentration of hydrazine at steady-state is simulated, its gradient can be calculated to obtain the flux of hydrazine at the surface of the UME (as shown in Figure S1.6B). By integrating the flux of hydrazine over the entire surface of the electrode, we calculate a steady-state current, $i^{1/2}$, that represents half of the steady-state current on a bare disk electrode. Secondly, we set the boundary condition of one of the two disks to the "no flux" boundary in order to simulate the presence of a GNP. Then, we calculate the current by integrating the flux over the surface of the UME but not the disk. We repeat this procedure sequentially for the two disks. For a disk positioned at the center or the edge of the UME we calculate $i^{1/2}_{center}$ and $i^{1/2}_{edge}$, respectively. To calculate the total current, i_{ss}, we use the following relations:

$$\text{no GNP:} \quad i_{ss} = 2 \times i^{1/2}$$

$$\text{GNP at the center (symmetric):} \quad i_{ss}(\text{GNP@center}) = 2 \times i^{1/2}_{center}$$

$$\text{GNP at the edge (asymmetric):} \quad i_{ss}(\text{GNP@edge}) = i^{1/2}_{edge} + i^{1/2}$$

For a given size of GNP, the mesh is not modified between the simulation of the current at the bare electrode, and the electrode covered with a GNP on its edge and center. Keeping the same mesh is extremely important because even a minor variation of the mesh can induce variations of few ‰ in the simulated current. The calculation of the steady-state current for a GNP on the edge of the UME implies that we assume no perturbation of the other half of the UME by the presence of the GNP. The distance over which the diffusion layer is perturbed by the GNP is about 1 µm (as measured on the simulated concentration profiles) and thus our assumption is verified. We performed this procedure with GNPs of

different sizes until we find a good agreement between the experimental and simulated relative step size. Table S1.4 gathers currents calculated for disks of different sizes. The simulation shows that disks between 0.5 µm and 3.5 µm in diameter produce relative current steps between ≈ 1‰ to ≈ 38 ‰ covering the range of relative step size observed on the histogram in Figure 4.10, regardless of the maximum relative step size (only one event among around 200 total events).

Table S1.3. Boundary conditions corresponding to the model shown in Figure S1.6A.

Boundary	**1**		**3**	**4**
Condition	no disk	disk	$C = 0$	no flux
	$C = 0$	no flux		

Table S1.4. Values of current simulated for blocking disks of different radii over a 5 µm radius UME with 1 mM of hydrazine in solution and $D = 1.4 \times 10^{-5}$ cm^2/s, and $n = 4$ electrons exchanged.

GNP radius (µm)	**0.250**	**0.675**	**0.875**	**1.75**
$i^{1/2}$ **(nA)**	5.1885	5.1856	5.1864	5.1909
$i^{1/2}_{center}$ **(nA)**	5.1849	5.1666	5.1549	5.0607
$i^{1/2}_{edge}$ **(nA)**	5.1762	5.1184	5.0792	4.8005
i_{ss} **(no GNP, nA)**	10.3771	10.3712	10.3729	10.3818
i_{ss} **(GNP@center, nA)**	10.3698	10.3331	10.3099	10.1214
i_{ss} **(GNP@edge, nA)**	10.3648	10.3040	10.2656	9.9914
Δi_{ss} **(center, nA)**	0.0073	0.0381	0.0315	0.2604
Δi_{ss} **(edge, nA)**	0.0123	0.0672	0.1072	0.3905
$\Delta i_{ss}/i_{ss}$ **(center, ‰)**	0.7	3.7	3	25.1
$\Delta i_{ss}/i_{ss}$ **(edge, ‰)**	1.2	6.5	10.3	37.6
$*\Delta i_{ss}/i_{ss}$ **(average, ‰)**	0.95	5.1	9.65	31.3

$$* \Delta i_{ss}/i_{ss}\,(\text{average}, ‰) = \frac{\Delta i_{ss}/i_{ss}\,(\text{center}, ‰) + \Delta i_{ss}/i_{ss}\,(\text{edge}, ‰)}{2}$$

A.5 Reference

1. Szamocki, R.; Velichko, A.; Mücklich, F.; Reculusa, S.; Ravaine, S.; Neugebauer, S.; Schuhmann, W.; Hempelmann, R.; Kuhn, A., Improved enzyme immobilization for enhanced bioelectrocatalytic activity of porous electrodes. *Electrochemistry Communications* **2007,** *9* (8), 2121-2127.

2. Boika, A.; Thorgaard, S. N.; Bard, A. J., Monitoring the electrophoretic migration and adsorption of single insulating nanoparticles at ultramicroelectrodes. *The Journal of Physical Chemistry B* **2013,** *117* (16), 4371-4380.

3. Bard, A. J.; Faulkner, L. R., Electrochemical Methods: Fundamentals and Applications, 2nd Edition. Wiley: 2000.

4. Faulkner, L. R.; Bard, A. J., *Electrochemical methods: fundamentals and applications, 2nd Edition*. John Wiley and Sons: 2002.

5. Quinn, B. M.; van't Hof, P. G.; Lemay, S. G., Time-resolved electrochemical detection of discrete adsorption events. *Journal of the American Chemical Society* **2004,** *126* (27), 8360-8361.

6. de Rooij, M., Electrochemical methods: Fundamentals and applications. *Anti-Corrosion Methods and Materials* **2003**.

7. Fears, K. P.; Creager, S. E.; Latour, R. A., Determination of the surface p K of carboxylic-and amine-terminated alkanethiols using surface plasmon resonance spectroscopy. *Langmuir* **2008,** *24* (3), 837-843.

8. Molinero, V.; Calvo, E. J., Electrostatic interactions at self assembled molecular films of charged thiols on gold. *Journal of Electroanalytical Chemistry* **1998,** *445* (1-2), 17-25.

9. Christie, A.; Crisp, D., Activity coefficients of the n-primary, secondary and tertiary aliphatic amines in aqueous solution. *Journal of Applied Chemistry* **1967,** *17* (1), 11-14.

List of publication

Peer reviewed journals

1. **Zejun Deng**, Ridha Elattar, Fouad Maroun, and Christophe Renault*. In Situ Measurement of the Size Distribution and Concentration of Insulating Particles by Electrochemical Collision on Hemispherical Ultramicroelectrodes, Analytical Chemistry, 2018, 90 (21), 12923–12929.

2. **Zejun Deng,** Fouad Maroun, Jeffrey E. Dick, and Christophe Renault*. Detection of individual Conducting Graphene Nanoplatelets by Electro-catalytic depression, Electrochimica Acta, 2020, 355, 136805.

3. **Zejun Deng**, Christophe Renault*. Detection of Individual Insulating Entities by Electrochemical Blocking. Current Opinion in Electrochemistry, 2021, 25: 100619.

4. **Zejun Deng**, Fouad Maroun, Jeffrey E. Dick, Christophe Renault*. Understanding Complex Current Responses of Individual Graphene Nanoplatelet Collision by Correlated Opto-electrochemical Measurements. **(Manuscript prepared to be submitted)**

5. Andrew D. Pendergast, **Zejun Deng,** Fouad Maroun, Christophe Renault*, Jeffrey E. Dick*. Dynamics of Individual Graphene Nanoplatelets Irreversibly Adsorbing on an Electrified Interface. **(Manuscript prepared to be submitted)**

Conference poster presentations

1. 14th International Fischer Symposium: a meeting on nanoscale electrochemistry, Kloster Seeon, Germany, May 27-31, 2018.

ECOLE DOCTORALE

Titre : Explorer les concepts de blocage électrochimique pour la détection d'entité unique

Mots clés : électrochimie mono-entité, blocage électrochimique, amplification électro-catalytique, dépression électro-catalytique, mesure opto-électrochimique, nano-électrochimie, nanoplaquette de graphène, ultra-microélectrode

Résumé : Cette thèse est consacrée à l'exploration des concepts autours du blocage électrochimique pour la détection d'entité individuelle. Tout d'abord, nous rapportons l'utilisation d'UME hémisphériques pour détecter la collision de billes de polystyrène par blocage électrochimique. Nous avons mis en évidence que l'effet de bord rencontré sur les UME en forme de disque est considérablement réduit sur les électrodes hémisphériques. Avec ces électrode il est possible de mesurer simultanément la distribution de taille et la concentration des particules en suspension. Nous déterminons avec moins de 10% d'erreur le diamètre moyen de billes de polystyrène de 0.5 et 1 µm de rayon. La concentration totale de ces billes obtenue par électrochimie se trouve en étroite concordance (< 10% d'erreur) avec leurs concentrations nominales (~ 10^{-15} mol/L).

Deuxièmement, nous étendons la stratégie du blocage électrochimique à la détection de particules électriquement conductrices. Cette stratégie, la dépression électro-catalytique, est basée sur la différence intrinsèque de cinétique de transfert électronique entre certains matériaux. Nous utilisons cette stratégie pour détecter des particules nanoplaquettes de graphène (GNP), un materiaux peu actif en electro-catalyse. En fonction du potentiel nous montrons que la collision de GNP plus ou moins bloquer cinétiquement l'oxydation de l'hydrazine sur une UME de Pt et ainsi produire un signal similaire au signal obtenu avec des particules isolantes comme des billes de polystyrène.

Enfin, nous couplons l'électrochimie et la microscopie en champ clair pour élucider comment la translation et la rotation des GNPs affectent la réponse en courant. Une fois que le GNP touche la surface de Pt, le courant transitoire provient de l'augmentation instantanée de la surface électroactive du GNP.

Title : Exploring the concepts of electrochemical blocking for single entity detection

Keywords : single entity electrochemistry, electrochemical blocking, electro-catalytic amplification, electro-catalytic depression, opto-electrochemical measurement, nano-electrochemistry, graphene nanoplatelet, ultra-microelectrode

Abstract : This dissertation is dedicated to exploring the concepts of electrochemical blocking for single entity detection. Currently, the accurate determination of the size of a particle by electrochemical blocking remains an analytical challenge, owing to the uneven current distribution on disk ultramicroelectrodes UMEs (so-called edge effect). The goal of this dissertation is to develop this elegant and straightforward methodology into a versatile and quantitative analytical tool.

First, we report the use of hemispherical UMEs to detect the collision of individual polystyrene beads by electrochemical blocking. We evidenced that the edge effect encountered on disk-shaped UMEs is significantly reduced on hemispherical electrodes. Hemispherical Hg UME enables simultaneous measurements of the *size distribution* and *concentration* of particles in suspension. We determine within less than 10% of error the average diameter of polystyrene bead of 0.5 and 1 µm radius. The total concentration of these polystyrene beads obtained by electrochemistry is found in close agreement (<10% of error) with their nominal concentrations (~10^{-15} mol/L).

Second, we extend the strategy of electrochemical blocking to the detection of electrically conducting particles. This strategy, electro-catalytic depression, is based on the intrinsic difference in electron transfer kinetics between materials to detect poorly catalytic particles such as graphene nanoplatelets (GNPs). Under the potential of 0.1 V vs. Ag/AgCl, GNPs block the oxidation of hydrazine on a 5 µm radius Pt UME, producing staircase-shaped drops of current (negative steps) similar to the signal obtained with insulating particles like polystyrene beads At high potentials (> 0.1 V), where hydrazine oxidation occurs on the GNP, the kinetic difference between GNP and Pt decreases, leading to the decrease of both average and median current step size and the appearance of positive steps.

Finally, we couple electrochemistry and bright-field microscopy to elucidate how the translation and rotation of GNPs affect the current response. Once the GNP touches the surface of Pt, the transient current responses come from the instantaneous increase in the electroactive surface area of GNP. Importantly, the rotation of GNP will cause changes in current transients.

Institut Polytechnique de Paris
91120 Palaiseau, France